Junwei Du
Krzysztof (Kris) Iniewski *Editors*

Gamma Ray Imaging

Technology and Applications

Springer

Gamma Ray Imaging

Junwei Du • Krzysztof (Kris) Iniewski
Editors

Gamma Ray Imaging

Technology and Applications

Springer

Editors

Junwei Du
University of California at Davis
Davis, CA, USA

Krzysztof (Kris) Iniewski
Emerging Technologies CMOS Inc.
Port Moody, BC, Canada

ISBN 978-3-031-30665-5 ISBN 978-3-031-30666-2 (eBook)
https://doi.org/10.1007/978-3-031-30666-2

© The Editor(s) (if applicable) and The Author(s), under exclusive license to Springer Nature Switzerland AG 2023

This work is subject to copyright. All rights are solely and exclusively licensed by the Publisher, whether the whole or part of the material is concerned, specifically the rights of translation, reprinting, reuse of illustrations, recitation, broadcasting, reproduction on microfilms or in any other physical way, and transmission or information storage and retrieval, electronic adaptation, computer software, or by similar or dissimilar methodology now known or hereafter developed.

The use of general descriptive names, registered names, trademarks, service marks, etc. in this publication does not imply, even in the absence of a specific statement, that such names are exempt from the relevant protective laws and regulations and therefore free for general use.

The publisher, the authors, and the editors are safe to assume that the advice and information in this book are believed to be true and accurate at the date of publication. Neither the publisher nor the authors or the editors give a warranty, expressed or implied, with respect to the material contained herein or for any errors or omissions that may have been made. The publisher remains neutral with regard to jurisdictional claims in published maps and institutional affiliations.

This Springer imprint is published by the registered company Springer Nature Switzerland AG
The registered company address is: Gewerbestrasse 11, 6330 Cham, Switzerland

Contents

Nuclear Structure Studies Using Gamma-Ray Spectroscopy and Digital Signal Processing 1
S. K. Tandel

Toward a New Frontier in PET Image Reconstruction: A Paradigm Shift to the Learning-Based Methods 21
Zifeng Tian and Zhaoheng Xie

Cascade Gamma Emission Coincidence Tomography 43
Xiao Liu, Hui Liu, and Yaqiang Liu

Compton Imaging Systems Based on Semiconductor Detectors 65
Mostafa Niknami and Mahdi Valipour

Spatial Localization of Radioactive Sources for Homeland Security 87
Konstantinos Karafasoulis and Aristotelis Kyriakis

Concepts for Solid State Detectors in Space-Based Gamma-Ray Astrophysics 103
Giulio Lucchetta

Radioxenon Detection for Monitoring Subsurface Nuclear Explosion 137
Harish R. Gadey

Shield-Free Directional Gamma-Ray Detector Using Small-Angle Compton Scattering 165
Yoshiharu Kitayama

Materials for Gamma Radiation Sensors 181
Paul M. Johns

Metascintillators for Ultra-Fast Gamma Detectors 209
Georgios Konstantinou

Metal-Loaded Plastic Scintillators Toward Gamma Spectroscopy Applications 231
Yunyun Li and Yuntao Wu

Index 245

Editors Biography

Junwei Du is a scientist at the Department of Biomedical Engineering, University of California at Davis (UC Davis). He obtained his B.S. degree in Applied Physics (2005) and Ph.D. degree in Electronic Science and Technology (2010) from the University of Science and Technology of China. His research focuses on developing high-resolution and high-sensitivity Positron Emission Tomography (H^2RS-PET) for biomedical imaging. Dr. Du has published over 50 peer-reviewed research papers in the biomedical imaging field that cover detectors, electronics, system of PET. Email: jwdu@ucdavis.edu

Krzysztof (Kris) Iniewski is managing R&D development activities at Redlen Technologies Inc., a detector company based in British Columbia, Canada. During his 15 years at Redlen, he has managed development of highly integrated CZT detector products in medical imaging and security applications. Prior to Redlen, Kris hold various management and academic positions at PMC-Sierra, University of Alberta, SFU, UBC and University of Toronto. Dr. Iniewski has published over 150+ research papers in international journals and conferences. He holds 25+ international patents granted in USA, Canada, France, Germany, and Japan. He wrote and edited 75+ books for Wiley, Cambridge University Press, Mc-Graw Hill, CRC Press and Springer. He is a frequent invited speaker and has consulted for multiple organizations internationally. Email: kris.iniewski@gmail.com

Nuclear Structure Studies Using Gamma-Ray Spectroscopy and Digital Signal Processing

S. K. Tandel

1 Introduction

Nuclear spectroscopy involves the use of a variety of radiation detectors, typically either semiconductor or scintillation ones, to record different types of radiations, either charged or neutral particles or photons. A number of different materials have been used for radiation detection over the past several decades. New detector materials and configurations are being constantly developed and evolved. Traditionally, the signals obtained from radiation detectors have been processed using analog instrumentation. It was only around the turn of the century that significant strides were made in the application of digital signal processing to nuclear spectroscopic measurements. The factors driving these developments were the wide availability of fast and precise flash Analog-to-Digital Converters (ADCs) and the increasing complexity of the measurements required. The former allowed more frequent sampling allowing for a better reproduction of the original signal. On account of the latter consideration, analog electronics required for a given application, despite high-density modularization, were becoming increasingly bulky and expensive. Digital pulse processing came in vogue, to begin with, for simpler measurements, and gradually moved towards being the solution of choice in many applications.

This chapter focuses on the detection of photons, both γ and x rays, using a variety of semiconductor and scintillation detectors, and a state-of-the-art digital signal processing (DSP) system. The objective was to accomplish high-resolution energy and fast timing measurements concurrently. In applications involving conventional analog electronics, energy and time parameters are processed through parallel chains of pulse processing units. The implementation of this approach leads to a partial loss

---

S. K. Tandel (✉)
UM-DAE Centre for Excellence in Basic Sciences, University of Mumbai, Mumbai, India
e-mail: sujit.tandel@cbs.ac.in

© The Author(s), under exclusive license to Springer Nature Switzerland AG 2023

J. Du, K. (K.) Iniewski (eds.), *Gamma Ray Imaging*,
https://doi.org/10.1007/978-3-031-30666-2_1

of available information and, in complex applications, can become quite demanding in terms of space and cost. The initial DSP systems were limited in terms of ADC resolution or sampling frequency or both. Limitations in ADC resolution meant that the use of DSP with high-resolution detectors was not feasible, and a lower sampling frequency constrained their adoption in applications involving detectors with a fast time response. With technological developments over the past decade, it is now possible to achieve both high-resolution energy and fast timing measurements with a DSP system. These capabilities and the applications of the diverse measurement techniques with a variety of semiconductor and scintillation detectors used in γ-ray spectroscopy are described in this chapter, along with the results from the study of several physics cases.

2 Detectors for Gamma-Ray Spectroscopy

The detection and measurement of γ rays emitted from the decay of excited nuclear levels is central to nuclear structure studies. These measurements allow for the determination of the excited level structure of nuclei, lifetimes of states, their angular momentum and parity, and many other properties. Semiconductor detectors, wherein a relatively small amount of energy (few keV) is effectively required to create charge carriers from the interaction of incident radiation, are preferred for high-resolution energy measurements. Examples are silicon and germanium detectors, along with materials like CdTe, CZT *etc*. The amount of energy required to effectively generate a charge carrier following the creation of a photon in a scintillation detector is usually much higher (few tens of keV or more), leading to poor energy resolution for inorganic crystals. Organic scintillators, on account of their low atomic number, have a negligible cross section for photoelectric interaction, leading to the absence of photopeaks. Many scintillation detectors, however, have a faster time response in comparison to semiconductor detectors. Consequently, they are preferred for timing applications. Most inorganic scintillators also have a considerably higher detection efficiency for γ rays in comparison to semiconductors [1, 2]. On account of the above considerations, depending on the specific application, different types of detectors may be used for γ-ray spectroscopy. It is highly desirable to have a versatile signal processing system which may be employed with a variety of detectors. Further, γ-ray spectroscopic studies where high sensitivity is required to detect events with low probability, demand either large arrays of detectors or multiple segmented ones. Therefore, data from a large number of channels have to be handled and processed simultaneously. All of these considerations indicate the following preferred characteristics of a DSP system used for γ-ray spectroscopy: (a) high energy resolution, (b) fast timing capabilities, (c) versatility for use with different types of detectors, and (d) ability to process many channels of data simultaneously, or scalability for units, each of which may process a limited number of signals.

3 Digital Instrumentation

The early forays into DSP for spectroscopic studies were aimed at developing suitable hardware and identifying appropriate algorithms [3, 4]. Once prototype DSP systems were constructed, their performance in relation to analog electronics, and with respect to each other, was studied [5, 6]. Later efforts focused on tailoring the DSP systems to optimize them for use with specific types of detectors, either high-resolution x- and γ-ray or fast timing scintillation ones [7–9]. For semiconductor detectors, the applicability of trapezoidal pulse shaping was demonstrated [10]. Refinements in both hardware and software techniques are being constantly realized to exploit the full range of capabilities provided by a variety of radiation detectors, their configurations and applications.

Signal processing with analog instrumentation typically involves analog to digital conversion at the end of a chain of modules far from the detector. With DSP, the conversion to digital is very close to the detector, thus there is minimal loss of information. Additionally, in a DSP system, the functionalities of many analog modules can be embedded on a single board. DSP is particularly suitable in nuclear spectroscopy where multiple parameters like energy, time, pulse shape etc., have to be correlated in the same data stream. Further, DSP systems can be designed for flexibility of the use of the same hardware into which different algorithms may be loaded as required. The DSP algorithms substitute the conventional functionalities of analog electronics like the peak-sensing ADC, time-to-digital converter (TDC), discriminator and others. While data acquisition with analog electronics typically demands the requirement of a trigger (either from an external source or a predefined combination of signals from detectors), it is possible to record data either with a trigger or in triggerless mode using DSP. The latter ensures that all data are saved for further offline analysis. In this case, the data are collected in list mode where the digital pulse processing algorithms are applied online by the Field Programmable Gate Array (FPGA) which operates on a continuous data stream. As soon as one memory buffer is filled with data as per the defined algorithm, these are available for being read out, and data continue to be acquired in another buffer. In this manner, data acquisition is continually possible even at high count rates.

The typical sequence of processing in a DSP system is illustrated in Fig. 1. As mentioned previously, the analog to digital conversion is performed close to the semiconductor detector, immediately after the preamplifier stage. The signal is then split and fed to energy and fast timing filters. The energy filter consists of a trapezoidal shaper for pulse height analysis. Its output has a flat top, with the height being proportional to the amplitude of the input pulse, which in turn is determined by the incident energy. A greater width in time of the flat top leads to improved energy resolution, but in applications involving high count rates, this may result in increased pile-up. Functions like baseline restoration, pile-up rejection *etc*., common to analog electronics, are also implemented. Timing measurements involve the determination of the time of arrival of a pulse with respect to a common reference. A discriminator receives analog pulses and generates a digital signal,

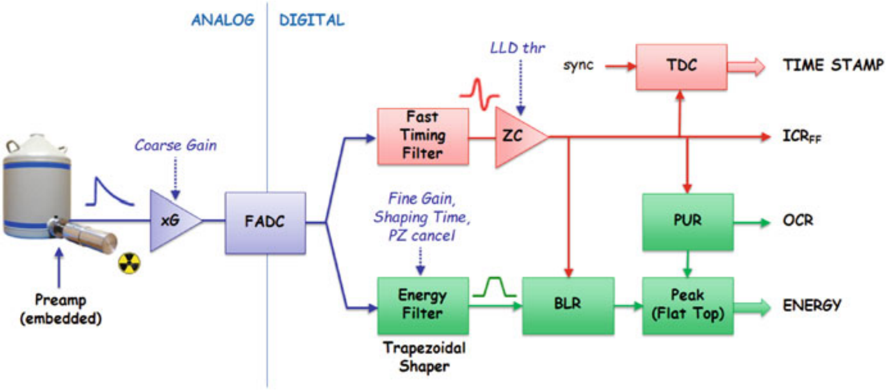

Fig. 1 Scheme of implementation of digital signal processing with a typical semiconductor detector. (Figure courtesy: C. Tintori)

following which a TDC is employed. The digital approach is preferable over the analog one where the discriminator may introduce walk or jitter leading to decreased resolution.

The measurements described in this chapter have, for the most part, been performed with the DT5730 DSP system from CAEN SpA [11]. Others have been performed with large γ-ray detector arrays, with either digital or analog electronics. With the DSP system, data have been collected using semiconductor [high-purity germanium (HPGe) and cadmium telluride (CdTe)] and scintillation [BC501A and NaI(Tl)] detectors. Various radioactive sources emitting both γ and x rays have been used. The ROOT data analysis framework of CERN [12] and the Radware suite of programs [13] have been used for the analysis. The DT5730 system is a flash ADC waveform digitizer. It has 14-bit resolution, a 500 MS/s sampling rate, and eight input channels. With time stamps at fixed intervals of 2 ns, there is potential for limited time resolution, particularly with detectors which have a fast response. This is overcome by online linear interpolation in the FPGA between two time stamps around the zero crossing of the Constant Fraction Discriminator (CFD) curve. This CFD curve is created digitally within the FPGA and allows for fine stamps separated by several picoseconds to be generated in contrast to the coarse time stamps at 2 ns intervals. Therefore, both high-resolution energy and fast timing measurements can be concurrently realized.

4 Energy Measurements with Semiconductor Detectors

Measurements of γ rays and x rays where high resolution is required are typically performed with semiconductor detectors. The materials of choice are germanium and silicon for γ-ray and x-ray detection, respectively, on account of the superior energy resolution they offer. Other materials like CdTe, cadmium zinc telluride (CZT) etc., may also be used. Some measurements using a Canberra-make HPGe detector and an Amptek-make CdTe one with the above DSP system are described here.

In order to achieve precise energy measurements, it is essential that the detector response is extremely linear. The linearity needs to be preserved during signal processing. The excellent linearity obtained with the HPGe detector and DSP system is evident using two standard reference γ-ray sources, ^{152}Eu and ^{182}Ta, where the emitted energies are precisely known. These have been used to validate the linear response of the DSP system. The energy (E) is written in terms of a quadratic expression of the channel number (N):

$$E = a + bN + cN^2 \tag{1}$$

The values of the coefficients obtained are: $a = -0.31$, $b = 0.33$, and $c = -3.77 \times 10^{-8}$. The extremely small value of the quadratic coefficient attests to the linearity of the response.

HPGe detectors with coaxial geometry, similar to the one employed here, are used to detect γ rays with energies ranging from several tens of keV to a few MeV. Those with planar geometry may be used to detect γ rays down to several keV. The energy resolution typically obtained with an HPGe detector and analog instrumentation is <1% at 0.1 MeV and just over 0.1% in the region of 1.3 MeV. Using the DSP system, comparable performance was obtained. This allows for discriminating between γ rays which may be closely spaced in energy. The 79.6 and 81.0 keV γ rays from the ^{133}Ba source [14] are clearly resolved using an HPGe detector with the DSP system. Another example of the advantage provided by good energy resolution is visible from the room background spectrum collected with an HPGe detector. The 2614.5-keV γ ray from the first excited state of ^{208}Pb [14], the final isotope in the ^{232}Th natural radioactive series, has a significant probability for interaction through the pair production process. The resultant positron can be annihilated leading to the emission of two 511-keV photons. If both of these are absorbed in the detector, the full-energy peak is realized. If one or both escape, a single- or double-escape peak at 2103.5 or 1592.5 keV, respectively, is visible. The 1592.5-keV γ ray happens to be close to another one with energy 1588.2 keV, also from the ^{232}Th series. Owing to the good energy resolution, these two peaks are quite clearly resolved.

A further illustration of the utility of the excellent energy resolution obtained is from Doppler broadening measurements of the positron-annihilation peak at 511 keV. When positrons annihilate with an electron in a medium, this gives rise to two 511-keV photons which are emitted in opposite directions. Due to the finite momentum of the $e^+ - e^-$ pair, the annihilation energy of the 511-keV photon is Doppler shifted by a small amount. Integrating over a large number of such events, with different magnitudes and signs of the shifts, leads to a broadened profile for the

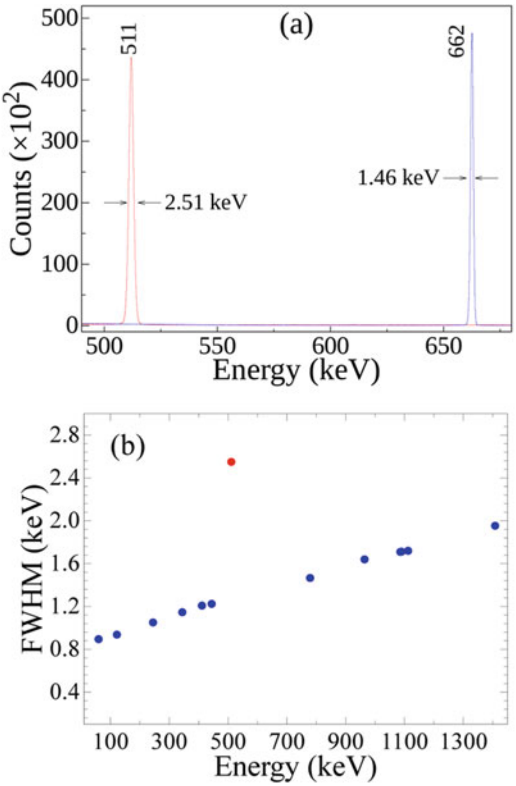

Fig. 2 (**a**) Representation of the Doppler broadening of the 511-keV annihilation photon as measured using an HPGe detector and the DSP system. (**b**) The extent of the Doppler broadening can be precisely quantified by virtue of the excellent energy resolution

511-keV photon. It is possible to precisely quantify this broadening on account of the high energy resolution obtained with the HPGe detector and DSP system. The magnitude of the Doppler broadening is:

$$\Delta E_{DB} = \sqrt{\Delta E^2_{observed} - \Delta E^2_{predicted}} \tag{2}$$

Figure 2a is a spectrum displaying the 511-keV annihilation peak from a ^{22}Na source and the 662-keV one from a ^{137}Cs source. The Full Width at Half Maximum (FWHM) of various γ-ray peaks across a wide range of energy is shown in Fig. 2b. The FWHM of the 511-keV peak from this measurement is clearly much greater (2.51 keV) than that of a γ-ray of a similar energy (1.26 keV, as inferred from Fig. 2b) which would be emitted from a nucleus at rest. The inferred magnitude of the Doppler broadening is 2.17 keV. The extent of the Doppler broadening of the 511-keV peak is utilized in positron-annihilation spectroscopy to study material properties, particularly the presence of defects.

5 Coincidence and Timing Measurements

One of the objectives of γ-ray spectroscopy measurements is to infer the excited level structure of nuclei. For this purpose, coincidence measurements with multiple detectors, either of the same or different types, need to be performed. The correlation in time or lack of it allows for inferring whether or not radiations are emitted in sequence (cascade). The coincidence relationships between different transitions (*e.g.* γ rays) and the relative intensity of each of them is used to construct a level scheme which delineates the location of the energy levels and the transitions feeding or deexciting them. Examples of such coincidence measurements using HPGe and CdTe detectors, along with the DSP system, are described.

5.1 Energy Correlations

Coincidence data of photons (both x and γ rays) emitted from a ^{57}Co source were recorded using HPGe and CdTe detectors, and the DSP system. The radioisotope ^{57}Co undergoes electron capture decay to the second excited state in ^{57}Fe, which has two decay branches: (a) a 136.4-keV transition to the ground state, and (b) a 122.0-keV γ ray to the first excited level, and subsequently a 14.4-keV one to the ground state (Fig. 3a). The 14.4-keV transition, due to its low energy, proceeds mostly by internal conversion, and only partly through γ-ray emission. The 122.0- and 136.4-keV transitions, on the other hand, have predominant γ-ray emission [14]. The energy thresholds for detection of photons in the CdTe and HPGe detector were few keV and few tens of keV, respectively. Consequently, the 14.4-keV γ ray and the 6.4-keV Fe-$K\alpha$ x ray, which is emitted as a natural consequence of electron capture and internal conversion, could only be recorded in the CdTe detector. The higher-energy photons could be observed in both detectors.

The data collected were used to validate the implementation of the coincidence technique in the DSP system as follows. A gate was set on the 6.4-keV Fe-$K\alpha$ line in the CdTe detector (Fig. 3b). As expected, both the 122.0- and 136.4-keV γ rays are visible in coincidence in the HPGe spectrum. In Fig. 3c, with a gate on the 14.4-keV line in the CdTe detector, only the 122.0-keV γ ray is visible in the HPGe spectrum since the 136.4-keV one is not in coincidence. This example provides a simple validation of the coincidence measurement using the DSP system.

The decay scheme of the radioisotope ^{133}Ba, which undergoes electron capture decay to ^{133}Cs, offers a somewhat more detailed validation. The following γ rays, with energies in keV, are emitted: 53.2, 79.6, 81.0, 160.6, 223.2, 276.4, 302.8, 356.0, 383.8 [14]. The relevant level scheme is presented in Fig. 4a. To illustrate that gating on different energies allows for identifying which γ rays are in coincidence with others, spectra were generated with gates on the 302-, 356- and 383-keV γ rays recorded in the HPGe detector. The low-energy γ rays and x rays visible in the CdTe detector are shown in Fig. 4b–d. As expected, the Cs K x rays are visible in

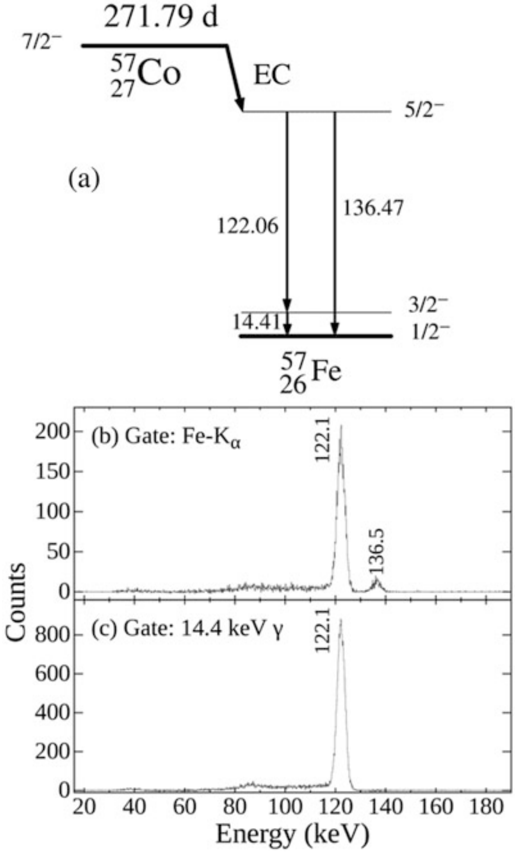

Fig. 3 Coincidence measurement using HPGe and CdTe detectors, and a ^{57}Co source: (**a**) Electron capture decay of ^{57}Co leading to ^{57}Fe. (**b**) Spectrum obtained with a gate on the 14.4-keV γ ray recorded in the CdTe detector. (**c**) Same as (**b**), however, with a gate on the 6.4-keV K x-ray of Fe

all spectra. Consistent with the established level scheme, the 53- and 81-keV γ rays are seen to be coincident with the 302-keV transition (Fig. 4b). With a gate on the 356-keV γ ray (Fig. 4c), only the 81-keV line is visible, since the 53-keV one is not coincident. On the contrary, only the 53-keV line is visible with a gate on the 383-keV γ ray since the 81-keV one is not coincident (Fig. 4d). In this manner, the validity of the coincidence measurements performed with the DSP system is demonstrated.

5.2 *Time Resolution and Lifetime Measurement*

In addition to the high-resolution measurements possible with the 14-bit resolution of the DSP system, the 500 MS/s sampling frequency, and the use of interpolation algorithms, allowed for fast timing studies. This has particular utility in the case of scintillation detectors, some of which have a fast time response. A test of the

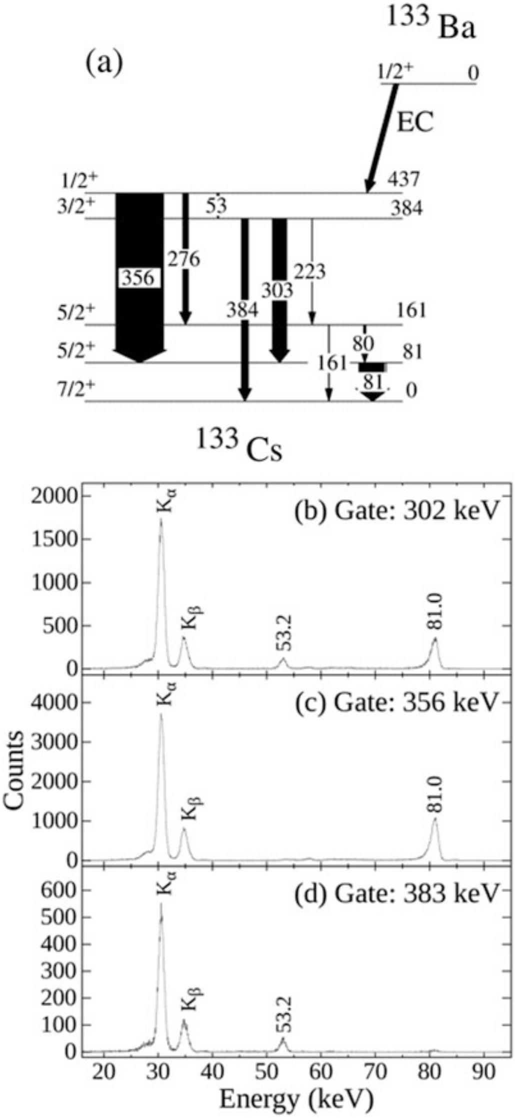

Fig. 4 Coincidence measurement using HPGe and CdTe detectors, and a ^{133}Ba source: (**a**) Electron capture decay of ^{133}Ba leading to ^{133}Cs. Spectra obtained with gates on γ rays recorded in the HPGe detector: (**b**) 302 keV, (**c**) 356 keV, and (**d**) 383 keV

performance of the DSP system in the sub-nanosecond time range was performed through a coincidence measurement using two liquid scintillation, BC501A detectors, and a ^{60}Co source, which emits two coincident γ rays of energy 1.17 and 1.33 MeV [14]. The mean decay time of the fast scintillation component from the BC501A detector is 3.2 ns, thus fast coincidence measurements are possible.

With the sampling frequency of 500 MS/s of the DSP system, time stamps spaced with 2 ns intervals are obtained. To exploit the advantages of the fast time response of BC501A, BaF_2 and other detectors, a linear interpolation was performed

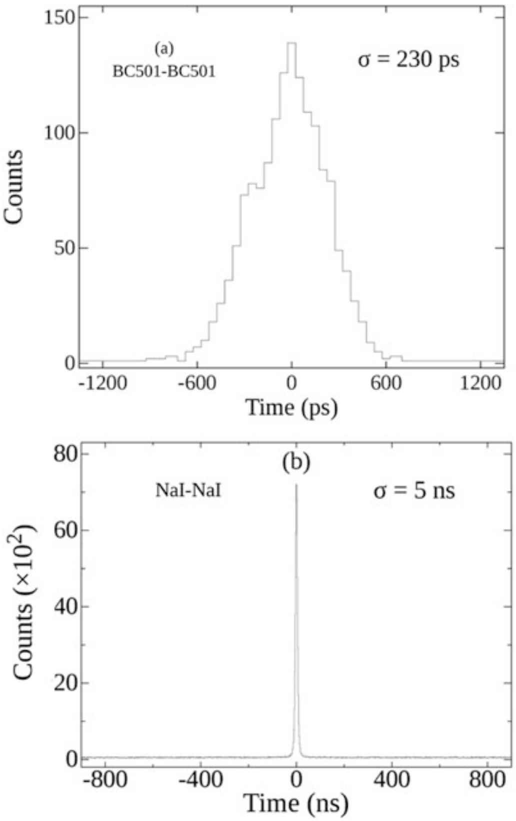

Fig. 5 Time resolution measurement with two: (**a**) BC501A liquid scintillation detectors and the use of fine time stamps from the DSP system. (**b**) NaI(Tl) scintillation detectors and coarse time stamps associated with the sampling frequency. Note the picosecond time scale on (**a**) and the nanosecond one on (**b**)

between two time stamps in the region of zero crossing of the Constant Fraction Discrimination (CFD) curve. A simple interpolation method was utilized since more complex calculations were unfeasible to implement online in the FPGA. With this interpolation, it was possible to obtain fine time stamps spaced by 10 ps, as compared to those at 2 ns intervals characteristic of the sampling frequency. More details about the method may be found elsewhere [15].

The time resolution obtained in the coincidence measurement with two BC501A detectors and a ^{60}Co source was $\sigma = 230(10)$ ps (Fig. 5a) which compares well with the 205(6) ps obtained with analog electronics [15]. In this instance, the fine stamps obtained through the interpolation procedure mentioned earlier, were utilized. With the use of coarse time stamps, a time resolution of $\sigma = 5$ ns was obtained using two NaI(Tl) detectors and the ^{60}Co source (Fig. 5b). This underscores the importance of using appropriate software techniques, along with hardware capable of fast sampling, to exploit the full capabilities of detectors with a fast time response.

Another important aspect of γ-ray spectroscopy is the measurement of lifetimes of excited levels. Lifetimes constitute a measure of the transition probability for the decay from a higher to lower excited state and, therefore, aid in the understanding

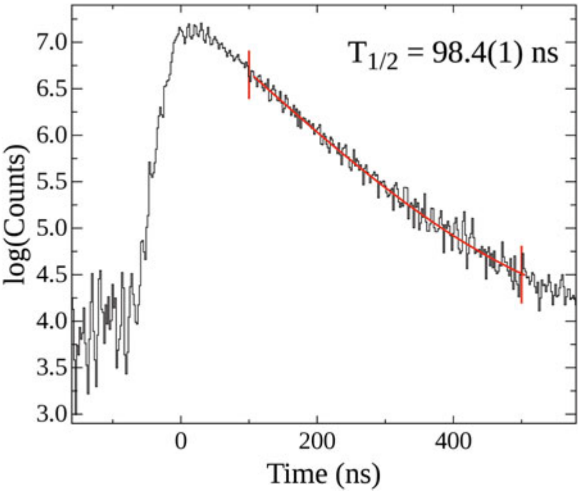

Fig. 6 Lifetime measurement of the first excited level in ^{57}Fe populated in the electron capture decay of ^{57}Co. The time difference between the 14.4- and 122.0-keV γ rays detected in NaI(Tl) detectors is histogrammed. A half-life of 98.4(1) ns is inferred

of the nature of the associated wavefunctions. Using the DSP system and the time stamps on each of the detected γ rays, it was possible to histogram the difference in time of two specific coincident γ rays detected at various points in time. The convolution of these time differences forms an exponential, which when fitted, allows for the extraction of the lifetime of the level intermediate between the feeding and deexciting transitions. Such a measurement was performed using two NaI(Tl) detectors and a ^{57}Co source. The time difference between the 14.4- and 122.0-keV γ rays (Fig. 3a) is displayed in Fig. 6. The half-life for the first excited state in ^{57}Fe is inferred to be 98.4(1) ns, in agreement with the value in the literature. Improved precision is obtained through the present measurement using the DSP system.

6 Selected Results on Nuclear Structure Studies

The γ-ray spectroscopic techniques described above prove to be quite useful in obtaining an understanding of various aspects of nuclear structure. Typical experiments involve γ-ray coincidence measurements with large arrays of high-purity germanium detectors, since many excited states are populated, each of which decays by γ-ray emission. Data on γ-ray energies, along with various time parameters, are recorded, usually with hundreds of millions of coincidence events, and are subsequently sorted offline. Histograms of up to four dimensions, involving energy and time parameters, are generated from the raw data and analyzed to extract the desired nuclear structure information. Some of our recent results on metastable states in nuclei (also known as isomers) and nuclear shapes are described below.

6.1 Nanosecond Isomers in Pt Isotopes

Isotopes of Pt, with even mass numbers, *viz.* ^{192,194,196,198}Pt, were studied through the population of excited states up to high angular momentum, and detecting γ rays emitted in their decay. The level structure of these isotopes was established up to angular momentum, $I = 26\,\hbar$, and the half-lives of isomers were measured. Gamma-ray spectra were generated from a histogram consisting of at least three γ rays in any given coincidence event. To inspect which γ rays are observed in time-correlated coincidence with others, conditions were set such that if two energies of interest are recorded in any two detectors, the γ rays recorded in any of the other detectors in the array could be isolated. Following this procedure for all possible combinations of γ rays of interest, and taking into account the intensity of the photopeaks obtained through Gaussian fitting and appropriate efficiency corrections, the level structure of the isotopes was determined. Typical γ-ray spectra for ^{192}Pt and ^{194}Pt are displayed in Fig. 7. Additionally, the half-lives of the states with spin-parity, $I^{\pi} = 12^{+}$, were measured using the centroid-shift technique [16]. This involves the determination of the centroid of the distribution of the difference in time between the γ rays deexciting and feeding the isomer. The value of this centroid is then compared to the one obtained for two γ rays with similar energies across a short-lived level (with a half-life in the range of picoseconds). The difference in time of the location of the two centroids with respect to each other corresponds to the mean life of the isomer. The half-lives of the $I^{\pi} = 12^{+}$ states in ^{192,194}Pt determined in this manner [$T_{1/2} = 2.8(3)$ ns and 6.6(6) ns] are illustrated in Fig. 7 [16]. The isotope ^{196}Pt was also similarly studied and γ rays from the decay of excited states in this nucleus are displayed in Fig. 8. The half-life of the 12^{+} state in ^{196}Pt was determined using the centroid-shift method described above, and also by fitting the distribution to a convolution of Gaussian and exponential functions as, shown in Fig. 8. The values obtained using the complementary methods were quite similar: $T_{1/2} = 7.7(7)$ ns [17].

The level structure determined for isotopes of Pt could be used to infer the contributions to the total angular momentum from individual nucleons as opposed to that from the collective rotation of the nucleus. When the angular momentum contributed only by the individual nucleons is examined as a function of the rotational frequency of the nucleus, it is evident that similar behavior is observed for all three isotopes ^{192,194,196}Pt, indicating that the same underlying phenomena are at play *i.e.*, the breaking of a pair of neutrons due to the Coriolis force on account of the rotation of the nucleus. The measurement of lifetimes of the 12^{+} states in even-mass Pt isotopes, which deexcite through electric quadrupole ($E2$) γ rays to the lower-lying 10^{+} levels, allows for an inference of the associated reduced transition probabilities [$B(E2)$]. The magnitude of $B(E2)$ with respect to the single-particle value is a measure of the extent of collective behavior in the nucleus. It can be seen from Fig. 9 that the $B(E2)$ values for the γ rays from the 2^{+} to the 0^{+} ground states gradually reduce with an increase in neutron and mass number. The corresponding values for the $E2$ γ rays from the 12^{+} states, however, exhibit a quite different

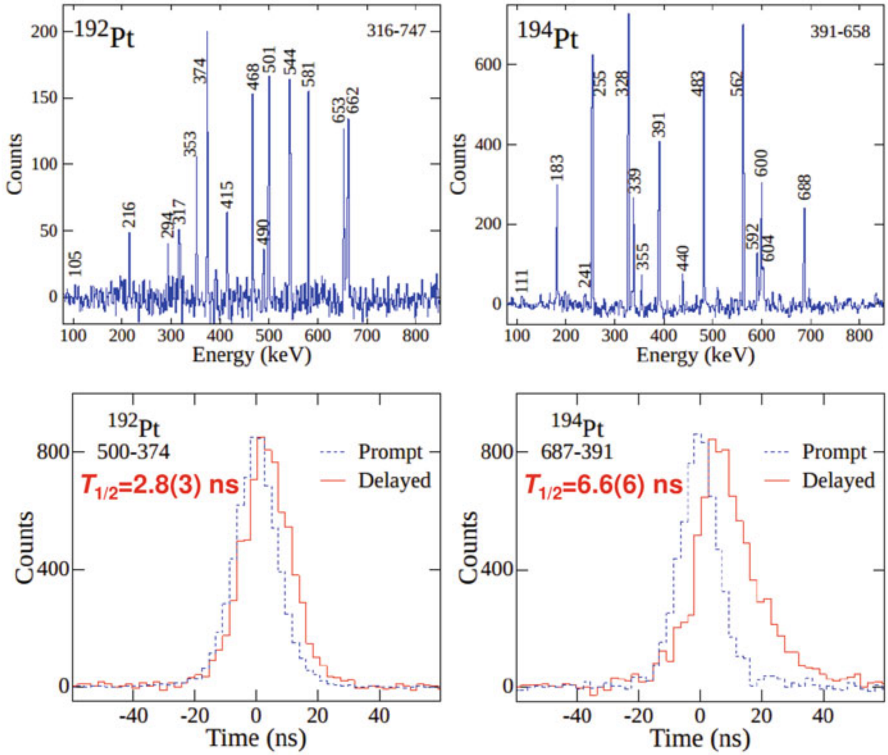

Fig. 7 Gamma rays observed from the decay of excited levels in ^{192}Pt and ^{194}Pt. The half-lives measured for the states with spin-parity 12^+ in these isotopes, using the centroid-shift method, are also indicated

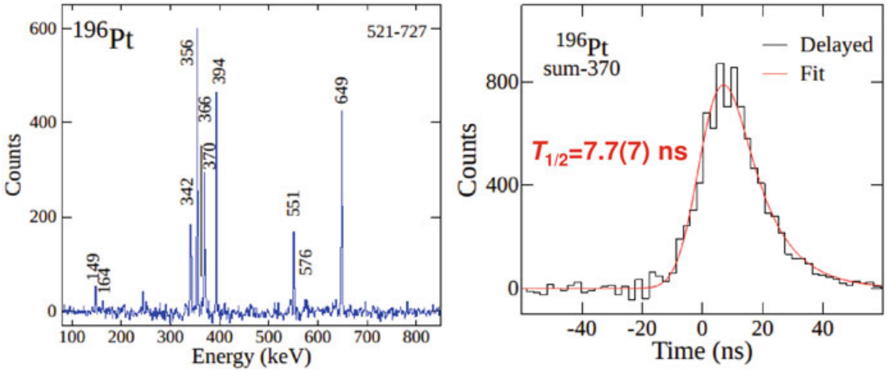

Fig. 8 Gamma rays from ^{196}Pt, and the half-life of the 12^+ state determined by fitting the convolution of Gaussian and exponential functions

Fig. 9 Reduced electric quadrupole transition probabilities, $B(E2)$, in Pt isotopes, inferred from lifetime measurements, demonstrating the reduction in the magnitude of collective behavior with increasing neutron number

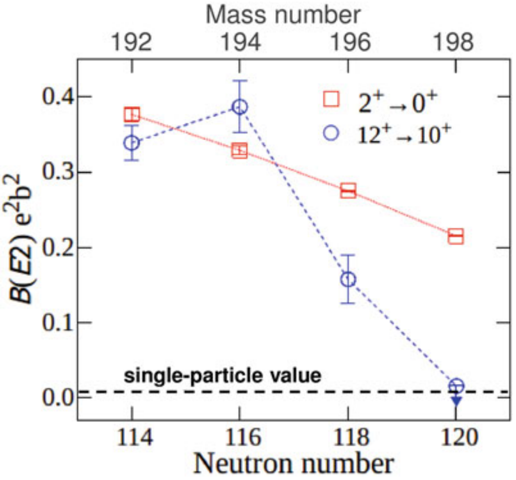

behavior, with an abrupt drop indicated for higher mass numbers, reaching close to the single-particle value, and indicating a loss of collective behavior.

6.2 Microsecond Isomer in ^{180}Hf

The region of the nuclear chart with mass number $A \approx 180$ and atomic number $Z = 70$–76 is characterized by the presence of nuclear isomerism resulting from the symmetry associated with the projection of the intrinsic nucleon angular momentum along the symmetry axis of an axially-symmetric, deformed nucleus (denoted by K). The resultant states with long half-lives are termed K isomers. The nucleus ^{180}Hf ($Z = 72$) is a classic example of K isomerism, with several such states identified [18]. The K-isomeric state with spin-parity 12^+ is discussed here. This isomer is found to de-excite through four distinct γ-ray branches of 222, 539, 832 and 1100 keV which have electric dipole, electric dipole, magnetic quadrupole and electric octupole multipolarity, respectively, as shown in Fig. 10. The half-life of the 12^+ state was determined by constructing several matrices with energy and time difference between distinct γ rays on the two axes, along with the selection of a specific γ ray which is coincident with those incremented in the matrix. The time difference of γ rays feeding and de-exciting the isomeric state were histogrammed and fitted to an exponential function (Fig. 10, top left), and the half-life of the 12^+ state was inferred to be 0.94(11) μs. This state has been associated with the excitation of two protons and two neutrons [18].

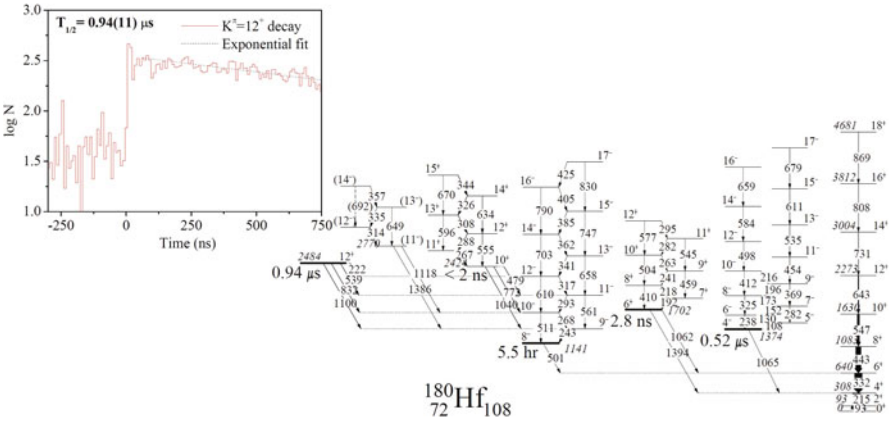

Fig. 10 A partial level scheme of ^{180}Hf illustrating the established isomeric states. The measured half-life of the 12$^+$ state is displayed on the top left

6.3 Metastable State in ^{202}Tl

Nuclei in the vicinity of the doubly-closed shell nucleus, ^{208}Pb ($Z = 82$, $N = 126$), exhibit the presence of metastable states owing to energy-adjacent nucleonic orbitals which have a large difference in their intrinsic angular momentum. The decay of excited states which result from the occupation, by individual nucleons, of such orbitals, is hindered by the angular momentum selection rule, on account of its required large change. The γ rays de-exciting such states have a high multipole order and consequent small transition probability. The associated levels are, therefore, found to have metastable character. Tl isotopes ($Z = 81$) exhibit such metastable states at both low and high excitation. Excited states in ^{202}Tl were studied up to angular momentum, $I = 20\,\hbar$ [19]. Many γ rays, which were previously unobserved, are placed in the level scheme of ^{202}Tl, as shown in Fig. 11. All the γ rays above the 7$^+$ state at 950 keV were determined to have long-lived feeding in the range of hundreds of microseconds. The long half-life was attributed to the state with spin-parity, $I^{\pi} = 20^+$. The value of the half-life was determined by inspecting the variation in integral counts of several de-exciting γ rays as a function of time. An example is shown in Fig. 11, where the integral counts for the 134-keV γ ray de-exciting the 12$^-$ level are fitted to the appropriate exponential function. A value of $T_{1/2} = 215(10)$ μs is determined for the 20$^+$ state at 4148 keV (Fig. 11). This state is inferred to be realized from the excitation of one proton and three neutrons, and the long half-life is attributed to the relatively low-energy 286-keV γ ray carrying angular momentum of three units [19].

Fig. 11 Excited levels in ^{202}Tl which are fed in the decay of the 20^{+} metastable state with half-life, $T_{1/2} = 215(10)$ μs (top panel). Measurement of the half-life of the 20^{+} state in ^{202}Tl by fitting the variation of integral counts of the 134-keV γ ray as a function of time (bottom panel)

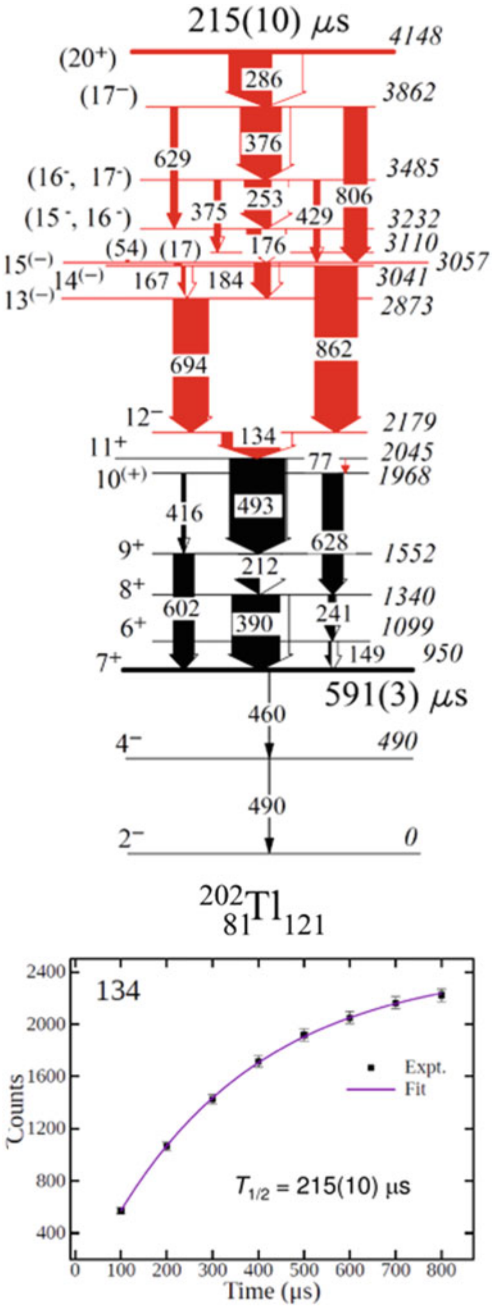

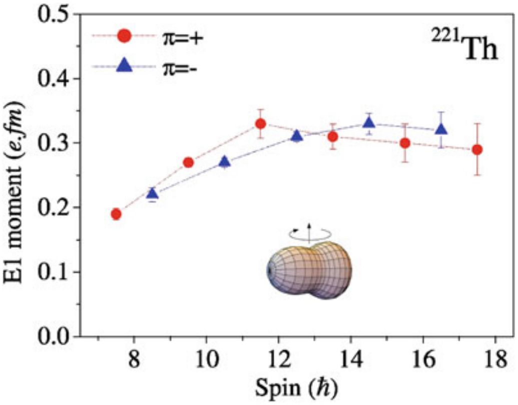

Fig. 12 Inferred intrinsic electric dipole moments in ^{221}Th as a function of total angular momentum, indicating the octupole deformation of this nucleus. The data points in red (blue) correspond to the positive (negative)-parity levels, respectively. The lines are intended to guide the eye

6.4 Octupole Deformation in ^{221}Th

Isotopes of nuclei in the vicinity of closed shells of protons and neutrons are near-spherical in shape, while those far removed from such regions are found to be deformed. Most isotopes in the nuclear chart are deformed, with the deformations ranging from quadrupole (ellipsoidal) to octupole (pear-shaped), and higher-order ones. While quadrupole deformations are observed across the entire nuclear chart, octupole shapes are evident only in specific regions. The region where octupole deformation is most pronounced is the Ra ($Z = 88$) – Th ($Z = 90$) region around mass number, $A = 220$. This is due to the presence of both proton and neutron orbitals which differ by three units in both orbital and total intrinsic angular momentum. Octupole deformed states were established in ^{221}Th [20]. Since this isotope has moderate quadrupole deformation as well, the level structure is characterized by rotational bands, with the associated levels connected by intraband γ rays with electric quadrupole character. Further, rotational bands with both positive and negative parity are observed, which are linked by interband γ rays with electric dipole character. The measured ratio of intensities of these two types of γ rays, along with their associated energies and angular momentum of the states involved, lead to an inference of electric dipole moments for the levels in the bands, as illustrated in Fig. 12. The magnitude of the electric dipole moments is an indirect measure of the extent of octupole deformation of the nucleus. A visualization of such a rotating octupole deformed nucleus is also shown in Fig. 12.

7 Summary

The utility of digital signal processing in different aspects of γ-ray spectroscopy with various semiconductor and scintillation detectors has been demonstrated with the highlight being the concurrent realization of high-resolution energy and fast timing measurements. The performance of the digital system is found to be equivalent to that of conventional analog electronics, but with a much lower cost and footprint. The versatility of the DSP system is evident in terms of the performance obtained with high-resolution semiconductor detectors like HPGe and CdTe, and fast timing ones like BC501A. The linearity is found to be excellent and the energy resolution comparable to that obtained with analog electronics. Coincidence measurements allow for correlations in time to be established between γ rays emitted from radioactive sources, and excited level structures of nuclei to be deduced. Time resolution up to nanoseconds is obtained using the characteristic sampling frequency and up to picoseconds through online interpolation within the FPGA. A precise lifetime measurement has also been performed using the DSP system. The suitability of the digital approach to processing signals from nuclear radiation detectors for spectroscopic studies is established. The structure of numerous nuclei has been studied using the above mentioned techniques. These range from nanosecond isomers in the oblate-deformed Pt isotopes, to K isomers in the prolate-deformed ^{180}Hf. Additionally, a metastable state in the near-spherical ^{202}Tl has also been identified. The level structures of these nuclei have been established through high-fold coincidence measurements involving the simultaneous detection of multiple γ rays in a large array of high-purity germanium detectors. Different techniques have been utilized for determining the half-lives of the above states like the centroid-shift method, fitting a convolution of Gaussian and exponential functions, or alternatively only an exponential function, with either decay or growth. These measurements have yielded important physics insights about the phenomena associated with the excitation of these nuclei. Additionally, octupole-deformed shapes have been investigated in the isotope ^{221}Th, and the intrinsic electric dipole moments have been inferred. These studies illustrate the wide applicability of the γ-ray measurement techniques described in this chapter.

Acknowledgments The author would like to thank M. Venaruzzo, C. Tintori, M. Hemalatha, D.C. Biswas, D. Negi, S.G. Wahid, Saket Suman, Anurag Patel, and many others not listed here, for their contributions.

References

1. Knoll, G. F. (2010). *Radiation detection and measurement* (4th ed.). Wiley.
2. Leo, W. R. (1994). *Techniques for nuclear and particle physics experiments* (2nd ed.). Springer Verlag.
3. Jordanov, V. T., & Knoll, G. F. (1994). Digital synthesis of pulse shapes in real time for high resolution radiation spectroscopy. *Nuclear Instruments and Methods in Physics Research A, 345*, 337.
4. Buckman, S. M., Keightley, J. D., Smith, D., & Woods, M. J. (1998). The validation of a digital coincidence counting system. *Applied Radiation and Isotopes, 49*, 1135.
5. Koskelo, M. J., Koskelo, I. J., & Siela, B. (1999). Comparison of analog and digital signal processing systems using pulsers. *Nuclear Instruments and Methods in Physics Research A, 422*, 373.

6. Reguigui, N., Morel, J., Ben Kraiem, H., & Mahjoub, A. (2002). Characterization of three digital signal processor systems used in gamma ray spectrometry. *Applied Radiation and Isotopes, 56*, 93.
7. Meyer, D. C., & Gawlitza, P. (1999). A new approach of digital signal processing in gamma- and x-ray spectroscopy. *Nuclear Instruments and Methods in Physics Research A, 424*, 470.
8. Nelson, M. A., Rooney, B. D., Dinwiddie, D. R., & Brunson, G. S. (2003). Analysis of digital timing methods with BaF2 scintillators. *Nuclear Instruments and Methods in Physics Research A, 505*, 324.
9. Nakhostin, M., Podolyak, Z., & Regan, P. H. (2014). Digital processing of signals from $LaBr_3$:Ce scintillation detectors. *Journal of Instrumentation, 9*, C12049.
10. Imperiale, C., & Imperiale, A. (2001). On nuclear spectrometry pulses digital shaping and processing. *Measurement, 30*, 49.
11. CAEN SpA. https://www.caen.it/
12. ROOT Data Analysis Framework. https://root.cern.ch/
13. Radford, D. C. (1995). ESCL8R and LEVIT8R: Software for interactive graphical analysis of HPGe coincidence data sets. *Nuclear Instruments and Methods in Physics Research A, 361*, 297.
14. NNDC. *Evaluated nuclear structure data file*. https://www.nndc.bnl.gov/ensdf/
15. Tandel, S. K., Negi, D., Wahid, S. G., Suman, S., Patel, A., Roy, P., Hemalatha, M., Biswas, D. C., Venaruzzo, M., & Tintori, C. (2020). High-resolution energy and fast timing measurements for nuclear spectroscopy using digital signal processing. *Journal of Instrumentation, 15*, P08013.
16. Tandel, S. K., Wahid, S. G., Chowdhury, P., Janssens, R. V. F., Carpenter, M. P., Khoo, T. L., Kondev, F. G., Lauritsen, T., Lister, C. J., Seweryniak, D., & Zhu, S. (2015). Isomers and oblate rotation in Pt isotopes: Delineating the limit for collectivity at high spins. *Physics Letters B, 750*, 225.
17. Wahid, S. G., Tandel, S. K., Chowdhury, P., Janssens, R. V. F., Carpenter, M. P., Khoo, T. L., Kondev, F. G., Lauritsen, T., Lister, C. J., Seweryniak, D., & Zhu, S. (2015). Rotation-aligned isomer and oblate collectivity in ^{196}Pt. *Physical Review C, 92*, 054323.
18. Tandel, S. K., Chowdhury, P., Kondev, F. G., Janssens, R. V. F., Khoo, T. L., Carpenter, M. P., Lauritsen, T., Lister, C. J., Seweryniak, D., Zhu, S., Deacon, A., Freeman, S. J., Hammond, N. J., Jones, G. D., Moore, E. F., & Smith, J. F. (2016). Configurations and decay hindrances of high-K states in ^{180}Hf. *Physical Review C, 94*, 064304.
19. Wahid, S. G., Tandel, S. K., Suman, S., Hemalatha, M., Patel, A., Roy, P., Deo, A. Y., Pragati, Srivastava, P. C., Bhoy, B., Bhattacharjee, S. S., Singh, R. P., Muralithar, S., Chowdhury, P., Janssens, R. V. F., Carpenter, M. P., Khoo, T. L., Kondev, F. G., Lauritsen, T., Lister, C. J., Seweryniak, D., Zhu, S., Rai, S., & Sharma, A. (2020). Metastable states from multinucleon excitations in ^{202}Tl and ^{203}Pb. *Physical Review C, 102*, 024329.
20. Tandel, S. K., Hemalatha, M., Deo, A. Y., Patel, S. B., Palit, R., Trivedi, T., Sethi, J., Saha, S., Biswas, D. C., & Mukhopadhyay, S. (2013). Evolution of octupole collectivity in ^{221}Th. *Physical Review C, 87*, 034319.

Toward a New Frontier in PET Image Reconstruction: A Paradigm Shift to the Learning-Based Methods

Zifeng Tian and Zhaoheng Xie

1 Analytical Methods

In 1979, the Nobel Prize in Physiology or Medicine was awarded jointly to Allan M. Cormack and Godfrey N. Hounsfield "for the development of computer-assisted tomography." In a finite region of a plane, a real function is derived when line integrals along all straight lines intersect the region. From today's perspective, most people are familiar with Cormac's outstanding achievements [1], which had a stronger impact in the Radiology realm. However, Dr. Cormack also demonstrated how to determine the distribution of positron annihilations when there is an inhomogeneous distribution of the positron emitter in the matter. From a mathematical point of view, an unknown, suitably restricted, real function $\boldsymbol{x}$ exists in a finite two-dimensional domain $\boldsymbol{D}$ and is zero outside $\boldsymbol{D}$, when the line integrals of $\boldsymbol{x}$ intersecting $\boldsymbol{D}$ are known. After the invention of PET-scanners, the implementation of the inverse Radon transform has intuitively been reconsidered to reconstruct radioactivity distribution (images) from coincidence events (projection data).

Based on the central slice theorem [2], we know the Radon transform is closely related to the Fourier transform. Specifically, 2D Fourier transform of the image $\boldsymbol{x}$ along a line at the inclination angle α is the Fourier transform of the Radon transform (acquired at angle α). This fact can be used to compute inverse Radon transform. However, no matter how many measurements we use,

---

Z. Tian
Department of Biomedical Engineering, Peking University, Beijing, China

Z. Xie (✉)
Institute of Medical Technology and National Biomedical Imaging Center, Peking University, Beijing, China

Department of Biomedical Engineering, University of California, Davis, CA, USA
e-mail: xiezhaoheng@pku.edu.cn

© The Author(s), under exclusive license to Springer Nature Switzerland AG 2023

J. Du, K. (K.) Iniewski (eds.), *Gamma Ray Imaging*,
https://doi.org/10.1007/978-3-031-30666-2_2

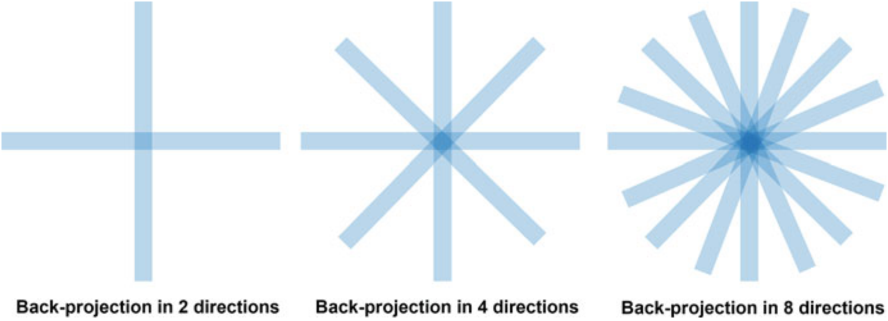
Back-projection in 2 directions
Back-projection in 4 directions
Back-projection in 8 directions

Fig. 1 Analytical methods: simple back-projection of point source

we will still be unable to perfectly recover our image using pure back-projection. As shown in Fig. 1, backprojecting in a few directions is a wildly inaccurate way of recovering a simple point source. However, even if we increase the number of back-projections, the result is still significantly blurry. Instead of direct back-projection, the filtered back-projection (FBP) is the most commonly used inversion formula for the Radon transform that will allow us to recover image $\boldsymbol{x}$.

Since the FBP algorithm is linear ($2\times$ uptake $= 2\times$ intensity in image), the reconstructed images are straightforward to interpret. As recommended by the NEMA standards [3], the spatial resolution of different PET scanners is measured by FBP reconstruction results of a point source, which are independent of activity distribution in the background. Moreover, FBP is computationally fast and easy to implement. We can trade off bias vs. variance of reconstructed images by tuning the filter window.

However, clinical PET scanner typically shows increased noise levels compared to other modalities, such as CT and MRI, due to the limited injected dose or scanning time. For instance, a high flux of X-ray photons roughly gives rise to 0.1% noise in the images, whereas PET, with fewer photons, typically has noise levels of about 10% [4]. The noise from the emission/listmode data was inevitably propagated into the reconstructed images through FBP linear operator. In addition, the inherent properties of PET scanner with ring detection architecture, such as non-uniform spatial resolution and angular-dependent efficiency, would generate non-isotropic patterns in the image reconstruction [5]. Although some pre-calibration could be used to minimize streak artifacts in the FBP reconstructed PET images, the image quality would be compromised in clinical practice. Considering the quantitative reconstructed images of a PET system directly impact the clinical outcome, FBP with sinogram correction is not widely used compared with model-based PET image reconstruction techniques.

2 Model-Based Methods

FBP is one type of inverse Radon transform, but it does not consider the noise distribution in the measurement domain and spatial and temporal heterogeneity of the system response. Therefore, the reconstructed images of FBP suffer from considerable noise. Model-based PET reconstruction algorithms can be decoupled into three main components: the noise model of the Poisson process, the system model of the photon detection process, and image prior model (Fig. 2).

2.1 Noise Model of the Poisson Process

An accurate statistical model of measurements is an essential topic for model-based PET image reconstruction. Since the number of decays in a given time are Poisson distributed, the statistical assumption of the coincidence measurements based on the Poisson model has been studied extensively in the past few decades. In practice, Poisson statistics may be corrupted with electronic noise and physical effects. Beside the Poisson model, the negative binomial distribution model [6] and Gaussian model [7] are used for pre-corrected projection and low-count data, respectively. The discussion about the PET detection system's stochastic nature is beyond this chapter's scope. Readers can find more information in previous studies [8, 9].

Suppose the unknown object is represented by PET activity image $\boldsymbol{x} \in \mathbb{R}^{N \times 1}$, where N is the number of voxels. For detector pair i, the conditional expectation value y_i given $\boldsymbol{x}$ is defined as

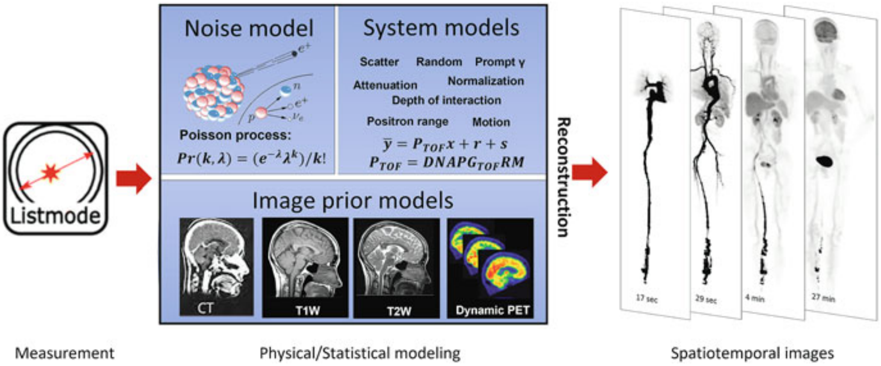

Fig. 2 Model-based PET image reconstruction pipeline

$$y_i = \sum_{j=1}^{N} p_{ij} x_j, \tag{1}$$

where $p_{ij} \in \mathbb{R}^{\mathrm{M} \times \mathrm{N}}$ denotes the probability of detecting emission photon from pixel $j, j \in [1, \ldots, N]$, at detector pair i, $i \in [1, \ldots, M]$. The conditional probability for y_i is

$$Prob\,(y = y_i | x) = e^{-\left(\sum\limits_{j=1}^{N} p_{ij} x_j\right)} \frac{\left(\sum\limits_{j=1}^{N} p_{ij} x_j\right)^{y_i}}{y_i!} \tag{2}$$

Since each detector pair is statistically independent, the probability for the entire detection system is

$$Prob\,(Y|X) = \prod_{i=1}^{M} Prob\,(y_i | x_1, x_2, \ldots, x_N) = \prod_{i=1}^{M} e^{-\left(\sum\limits_{j=1}^{N} p_{ij} x_j\right)} \frac{\left(\sum\limits_{j=1}^{N} p_{ij} x_j\right)^{y_\mathrm{i}}}{y_i!} \tag{3}$$

Prob($Y|X$) is also known as the likelihood function. To obtain the emission distribution from measurement, the expectation-maximization (EM) algorithm is proposed to produce a sequence of estimates of $\boldsymbol{x}$ that converges to $\widehat{\boldsymbol{x}_{ML}}$.

$$\arg \max_{x} Prob\,(Y|X) = \hat{x}_{ML} \tag{4}$$

In the early 1980s, maximum likelihood expectation maximization (MLEM) algorithms [10, 11] were developed for PET reconstruction. Unfortunately, EM methods suffered from noise propagation from the measurements. To mitigate image noise, early stopped is used before it has converged. Later, Hudson and Larkin [12] proposed order subset expectation maximization (OSEM) and considerably decreased the reconstruction time. Some evidence [12, 13] shows that, compared with FBP and MLEM, OSEM gave the best contrast at the cost of increased noise.

2.2 The System Model of the Photon Detection Process

In the past few decades, evolving innovations in instrumentation have improved the timing resolution, spatial resolution, and system sensitivity of PET scanners. To achieve high-precision quantitative images, the point-spread-function (PSF), time-of-flight (TOF) characteristics, depth-of-interaction (DOI), and several physical corrections (random/scatters/attenuation correction and detector dead-time/normalization correction) are developed.

Typically, the measured data can be represented as the sum of three components:

$$\overline{\boldsymbol{y}} = \boldsymbol{P_{TOF}}\,\boldsymbol{x} + \boldsymbol{s} + \boldsymbol{r} \tag{5}$$

where $\boldsymbol{P_{TOF}}\ \boldsymbol{x}$ is the true coincidence, $\boldsymbol{s} \in \mathbb{R}^{\mathrm{M} \times 1}$, denotes the expectation of scattered events, $\boldsymbol{r} \in \mathbb{R}^{\mathrm{M} \times 1}$ denotes the expectation of random events. $\boldsymbol{P_{TOF}}$ is an $\mathrm{M} \times N$ system matrix that can be factored as follows:

$$\boldsymbol{P_{TOF}} = \boldsymbol{DNAG_{TOF}RM}, \tag{6}$$

where ***D, N,*** and $\boldsymbol{A}$ are diagonal $\mathrm{M} \times \mathrm{M}$ matrices that account for detector dead-time, system normalization, and attenuation correction factors, respectively. $\boldsymbol{G_{TOF}}$ is an $\mathrm{M} \times N$ matrix that defines the geometrical relationship between the source volume and the detector pairs. $\boldsymbol{R}$ and $\boldsymbol{M}$ are $\mathrm{N} \times N$ matrices that can model the effects of spatial resolution and motion deformation. It is worth noting that a different factorization scheme of resolution modeling could be applied in the projection domain. Except for attenuation and dead-time factors, the rest of the components are independent of the object, which could be precalculated. Moreover, these computations are very fast, considering each component is very sparse after factorization.

- **Random correction:** Random coincidences are a direct consequence of having a large coincidence timing window. Either a delayed coincidence window or (qualified) singles rate could be used to estimate mean randoms in each line-of-responses (LORs). Modern scanners allow the acquisition of separate channels from the prompt and delayed coincidence. If only the random precorrected data is feasible to collect, exact log-likelihood is intractable. Fessler and his colleagues introduced a “shifted” Poisson model [14, 15], which matches both the model’s first- and second-order moments to the underlying statistics of the precorrected data. Compared with real-time random subtraction that destroys the Poisson statistics [16], post-processing the random estimate could mitigate the variance. The simplest form of variance reduction is to smooth the delayed data. A more accurate method of variance reduction [17] could be derived by using the two LOR fans and dividing by the mean value of all possible LORs between two opposite detector groups.
- **Scatter correction:** As E.J. Hoffman said, “scatter is the enemy,” especially for the recently developed long axial field of view (AFOV) PET scanners. Extended axial coverage increases sensitivity and dramatically lifts scatter fraction, S/(S + T), because there are fewer true coincidences and more substantial object attenuation at larger ring differences. According to anthropomorphic phantom simulation [18], the scatter fraction increased from 28% of the 25 cm ring difference to 50% at the largest ring difference (200 mm). Compared with random estimates, the acquisition system cannot collect scatter estimates

directly. Furthermore, the reconstruction method described above requires the mean scatter sinogram to be known beforehand. A scatter sinogram can be estimated using different ways, such as convolution [19, 20], the dual energy windows [21, 22], analytical methods [23, 24], the Monte Carlo simulation [25, 26], and deep-learning based methods [27, 28]. Among several existing approaches for robust scatter estimation [29], most PET scanners employ a single scatter simulation with tail-fitting scaling for compensating multiple scatter photons. The preparation and tail-fitting scaling process are illustrated in Fig. 3. Currently, deriving accurate scatter estimates in a less computationally intensive way remains challenging. The non-trivial multiple scatters directly impact the estimation of kinetic parameters, especially for voxel-based statistical analysis.

- **Dead-time correction:** PET detector requires a minimum amount of time to deal with each incoming event. Since radioactive decay is a random process, there is a certain probability that more than two events will occur within this minimum time. As an extreme case, the long axial PET encounters a huge number of singles in a short period. To improve quantitative accuracy, the dead time correction model is crucial at a high activity or dose rates. For a given scanner geometry and acquisition system, the nonlinearity of system response depends on the scintillator material and the distribution of activity inside and outside the FOV. The relationship between the incident rate and output rate could be built using calibration acquisitions [30–33]. It should be noted that the dead time is modeled before energy qualification [34]. In other words, singles rate before lower energy-level discriminator (LLD) should be used in deadtime correction. During calibration, similar to upsampled scatter sinogram, singles

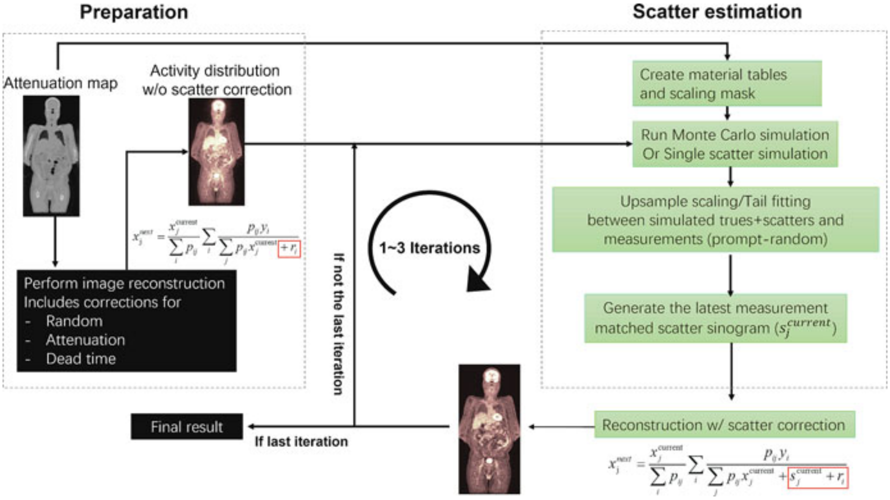
Preparation
Scatter estimation
Attenuation map
Activity distribution w/o scatter correction
$x_j^{next} = \frac{x_j^{current}}{\sum_i p_{ij}} \sum_i \frac{p_{ij} y_i}{\sum_j p_{ij} x_j^{current} \boxed{+r_i}}$
Perform image reconstruction
Includes corrections for
- Random
- Attenuation
- Dead time
If not the last iteration
1~3 Iterations
Create material tables and scaling mask
Run Monte Carlo simulation Or Single scatter simulation
Upsample scaling/Tail fitting between simulated trues+scatters and measurements (prompt-random)
Generate the latest measurement matched scatter sinogram ($s_j^{current}$)
Final result
If last iteration
Reconstruction w/ scatter correction
$x_j^{next} = \frac{x_j^{current}}{\sum_i p_{ij}} \sum_i \frac{p_{ij} y_i}{\sum_j p_{ij} x_j^{current} + \boxed{s_j^{current} + r_i}}$

Fig. 3 Commonly used scatter correction framework in PET image reconstruction

rates were fitted with paralyzable or non-paralyzable model [35] at a block-pairwise level.

- **The attenuation correction (AC)** factor is multiplicative and can easily be incorporated into the EM updates. As shown in Eq. (6). **A** (attenuation) is a diagonal M × M matrix that contains the attenuation correction factors. For PET/CT scanners, aligned CT attenuation information could be converted to linear attenuation values at 511 keV via a bilinear transformation [36, 37]. For PET/MR scanners, template-based approaches, Atlas-based approaches, sequence-based approaches, and state-of-the-art deep learning-based approaches could synthesize μ-map [38, 39]. Besides CT and MRI images, some existing methods, such as MLAA [40] and LYSO intrinsic radiation [41], can be used for whole-body PET AC. Unfortunately, the μ-map cannot be uniquely determined from emission data, even with TOF information. Therefore, the challenge of achieving accurate attenuation in PET reconstruction remains an open question, particularly in the absence of co-registered CT images.
- **Normalization** refers to the process of correcting for differences in the sensitivity of the detector element. This is typically done through a series of calibration scans [42]. In order to model the system completely, a group of component-based normalization methods [43, 44] is proposed to break down the complicated physical effects into separate components, such as intrinsic detector efficiency, block profile factors, geometric factors, misalignment factors, etc. A correction factor is calculated for each component based on the measured data. Ideally, an accurate normalization (diagonal M × M matrix) could compensate for the solid angle effect and crystal non-uniformity, which can cause variations in the measured activity concentrations across the image.
- **The geometric projector** is used in PET reconstruction to map the predefined (grid or blob) image space onto measurement space. Several different (ray-tracing) methods can be used to calculate the probabilities of photons produced by source volume and caught by a pair of detectors. There are three principal approaches, such as single-ray tracing [45], multi-ray tracing [46], and tube-of-response [47], each with its advantages and disadvantages. Most of the computation time is spent executing the forward and backward projection in each EM iteration. The choice of which method to use depends on the specific requirements and goals of the reconstruction, such as the desired level of accuracy, computational efficiency, and flexibility.
- **Resolution modeling**, also known as point-spread-function (PSF) modeling, aims to model the geometrical and detection physics components that degrade resolution within the reconstruction algorithm, such as positron range, photon noncollinearity, photon penetration, inter-crystal scatter, and discrete sampling, etc. [48–50]. Benefits from small crystals and SiPM (silicon photomultipliers) size, the intrinsic spatial resolution PET scanners have been substantially improved in the past few years [49, 51]. PSF modeling aims to create a more accurate and detailed source distribution of smaller structures. It can be performed by incorporating prior knowledge about the spatial resolution characteristics of the PET scanner into the system matrix. There are several

ways to do this [52–54]. One common approach is image-domain PSF, though projection-domain modeling is theoretically appealing. Image-domain PSF modeling methods are particularly suitable for list-mode reconstructions, as all blurring operations are independent of the numbers of LORs. It is worth noting that resolution recovery slows down the convergence speed, and the number of iterations is comparatively higher than its counterpart without PSF modeling [55]. It is important to note that the steps involved in applying projection-based PSF in PET reconstruction can vary depending on the specific PET scanner and software used.

- **Motion correction** can reduce image blurring and motion artifacts, which can improve the accuracy and diagnostic value of PET images. The first step of motion-compensated PET image reconstruction is acquiring cardiac/respiratory/gross body motion signals from external devices or data-driven methods. Let's say the measured data $\boldsymbol{y}$ can be divided into K gate. $\boldsymbol{y}^k$, $k \in [1, 2, \ldots K]$ is the kth gate and $\overline{\boldsymbol{y}}^k$ be the expectation of the measurement. The expectation $\overline{\boldsymbol{y}}^k$ is related to the reference gate PET image $\boldsymbol{x}$ through $\overline{\boldsymbol{y}}^k = \boldsymbol{DNAG_{TOF}R}\cdot \boldsymbol{M}(\boldsymbol{x}, \boldsymbol{\theta}_k) + \boldsymbol{s}_k + \boldsymbol{r}_k$, $\boldsymbol{s}_k \in \mathbb{R}^{\mathrm{M} \times 1}$ and $\boldsymbol{r}_k \in \mathbb{R}^{\mathrm{M} \times 1}$ denote the expectation of scatter and random events for the kth gate. And $\boldsymbol{\theta}_k$ is the deformation field from the reference gate to the k^{th} gate. The second step is to estimate the motion field from a gated PET scan. To obtain an optimized $\boldsymbol{\theta}_k$, an appropriate similarity metric, regularizer, and local invertibility should be considered [56]. Usually, motion-compensated reconstructions were performed by running nest iteration [57]. One outer update contains several inner iterations for deformation field estimation either from the neural network [58] or the iterative approach.

Overall, the quantitative accuracy of the PET scan depends on careful system modeling. Modern PET scanners have hundreds of thousands of tiny crystals with <500 ps TOF resolution, which not only pave the way to achieve high performance but also present challenges for the accurate system model.

2.3 Image Prior Model

Pure maximum-likelihood (ML) methods tend to overfit the data, resulting in images with high noise levels. Therefore, both MLEM and OSEM suffered from excessive noise propagation, particularly in low-count data situations with limited information. To overcome this limitation, prior models are introduced to PET image reconstruction to improve image quality (Fig. 4). One typical type of them are the regularized image reconstruction method [59–62]. The likelihood function and image prior are combined to compute a maximum *a posteriori* (MAP) estimate of the image:

$$\hat{x}_{MAP} = \underset{x}{\arg\max}\,[L(y|x)) - \beta U(x)] \tag{7}$$

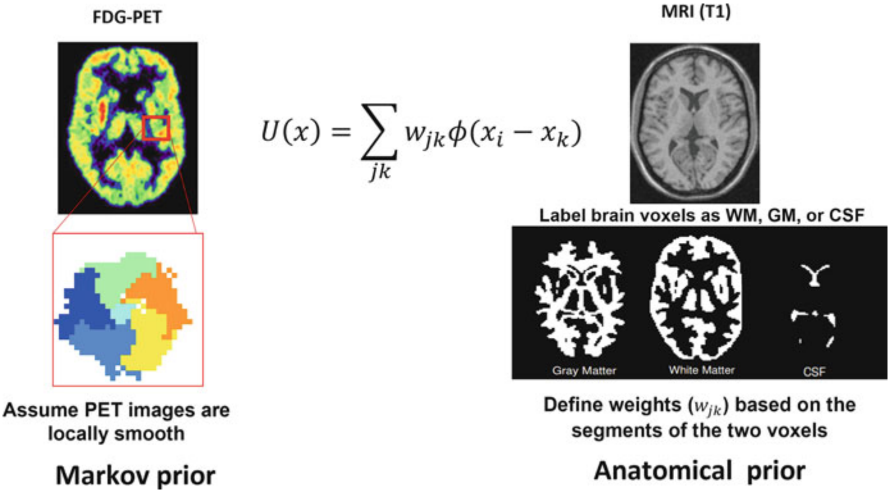
FDG-PET
MRI (T1)
$U(x)=\sum_{jk} w_{jk}\phi(x_i-x_k)$
Label brain voxels as WM, GM, or CSF
Gray Matter
White Matter
CSF
Assume PET images are locally smooth
Markov prior
Define weights (w_{jk}) based on the segments of the two voxels
Anatomical prior

Fig. 4 Prior model in PET image reconstruction

Earlier image prior models, $U(x)$, relied on modifications of the Markov random field, which is defined on pair-wise cliques of neighboring voxels. A global maximum of the above objective function through nonlinear optimization encourages image voxels to be similar to their neighbors. When a larger β is applied, Bayesian methods tend to produce blurry images. To address this issue, other non-quadratic (convex) edge-preserving models [63–65], such as total variation (TV), *p*-Gaussian function, and patch-based penalties, were proposed to preserve sharp edges. Although these image priors have proven to be valuable and convex, they are based on heuristically designed models with limited ability to distinguish an edge from noise. In order to produce even sharper intensity transitions, non-convex priors have also been proposed while it is hard to optimize. The solutions are usually local maxima, which are inherently discontinuous.

Rather than implicitly modeling image boundaries, fairly accurate anatomical boundaries could be revealed in high-resolution MR or CT images [66]. Since the spatial distribution of a radioactive tracer should be associated with anatomical structures, anatomical information from a co-registered CT or MRI can be applied to build an appropriate prior model. The specific form of these priors highly depends on the anatomical images. One challenge is the existence of mismatches between different modalities that measure different morphological or functional information. In the early days, the segmentation-based approaches could encourage boundaries in the functional image or smoothness within the anatomical regions. For example, A-MAP [67] promotes piecewise smoothness on grey matter and uniformity on white matter. Moreover, various segmentation-free anatomical priors have been developed to tackle mismatch problems, such as Bowsher prior, the joint entropy prior, and the level-set prior [68–71].

No matter which prior model is used, a fundamental problem is the selection of the hyperparameters, β, in regularized PET reconstruction. The regularization strength is typically determined empirically. In order to alleviate user intervention, a cross-validation log-likelihood (CVLL) method was proposed to select the optimal regularization strength, yielding images that balance the resolution and noise [72]. Recently, a bootstrap method [73] has been developed to calculate the penalty strength on-the-fly during the reconstruction automatically. Both methods were shown to provide good values of penalty strength across a range of noise levels.

3 Data-Driven/Learning-Based Methods

Although model-based PET reconstruction involves physics, statistical model, or regularization, roughness penalties based on "human-defined" signal models do not fully represent actual prior data. Therefore, it may lead to suboptimal performance and less accurate results when the data does not fit well with predefined models. Additionally, model-based methods, e.g., Monte Carlo-based methods, can be computationally intensive. In contrast, data-driven based methods use machine learning algorithms to learn patterns and features directly from the data without relying on predefined models or assumptions. As a result, data-driven approaches are often more efficient and flexible, allowing them to suit the specific needs of the reconstruction task. Overall, data-driven methods offer improved image quality, reduced noise, and the ability to incorporate "real" prior information into the PET reconstruction process.

3.1 Dictionary Learning and Kernel-Based Methods

An alternative is to find the appropriate signal models by learning from existing images. These methods can be classified as dictionary learning and kernel-based methods (Fig. 5). The dictionary learning based image reconstruction approaches [74–76] are inspired by compressive sensing (CS). CS theory allows a sparse signal to be accurately recovered from insufficient Nyquist sampling measurement. Combining sparse representation and penalized image reconstruction framework, dictionary-based PET reconstruction has proven to achieve good performance in various tasks like low-dose or limited-view scans. To implement a dictionary learning method, we must first obtain an image dataset. This dataset could be adaptively extracted during image reconstruction or existing images, which include a range of different image features. Once the data has been prepared, it can be pre-processed in a suitable format for dictionary learning, e.g., extracting the overlapping patches from the full-size images. Next, a set of over-complete basis functions or a dictionary is generated via the following optimization [77]:

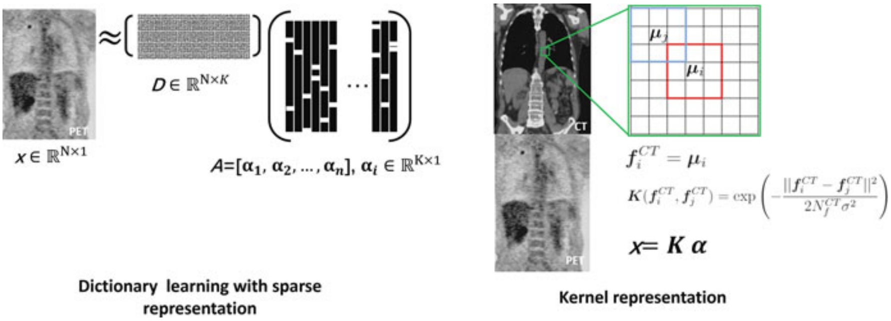
≈
$D \in \mathbb{R}^{N\times K}$
PET
$x \in \mathbb{R}^{N\times 1}$
$A=[\alpha_1, \alpha_2, \dots, \alpha_n]$, $\alpha_i \in \mathbb{R}^{K\times 1}$
CT
μ_j
μ_i
$f_i^{CT} = \mu_i$
$K(f_i^{CT}, f_j^{CT}) = \exp\left(-\frac{\|f_i^{CT} - f_j^{CT}\|^2}{2N_j^{CT}\sigma^2}\right)$
$x = K\alpha$
PET

Dictionary learning with sparse representation

Kernel representation

Fig. 5 Dictionary and kernel-base PET image representation

$$\arg\max_{\mathbf{D},\mathbf{A}} \|\boldsymbol{x} - \mathbf{DA}\|_F^2 \qquad s.t. \quad \|\boldsymbol{\alpha_i}\|_0 \le T, \tag{8}$$

where $\boldsymbol{x}$ and $\mathbf{D}$ are the images (or patches) and dictionary, respectively. $\boldsymbol{\alpha_i}$ is a coefficient vector, which represents the columns of coefficient matrix $\mathbf{A}$. T is a sparsity of the coefficient vector. A dictionary can be identified from the training data using an L1 minimization [78] or K-SVD [79]. Once the dictionary has been learned, we can use it to represent each noisy image as a linear combination of the dictionary atoms. It is worth nothing that the over-complete basis functions (dictionary) learned from existing images or adaptively during image reconstruction. Through the MAP framework, the objective function could be optimized in an alternating manner: (1) image update with a fixed dictionary; (2) Sparse coding with fixed images. For the sparse coding subproblem, algorithms like orthogonal matching pursuits were capable to finds the suitable set of coefficients $\boldsymbol{\alpha_i}$. While dictionary learning can be a helpful tool for PET reconstruction, it is not a perfect solution and has its limitations. One penitential downside is that it may not always be able to accurately capture complex image structures, which can limit its effectiveness in certain situations.

Inspired by kernel regression, a kernel-based method is developed for PET image reconstruction, which exploits prior information from co-registered anatomical images or dynamic PET scans [80–82]. To build a kernel matrix, the patch size, the searching window, and the image size of the reconstruction need to be specified. The kernel-based algorithm uses K-Nearest Neighbor (K-NN) construction to measure the similarity between different patches. It typically explores the distance between one of the N objects and its k^{th} NN and minimizes these K × N functions with the gradient descent method [83]. Once the kernel matrix has been prepared, it can be inserted into any form of EM algorithm. And the optimization process adjusts the coefficients to minimize the reconstruction error. Unfortunately, the kernel method involves additional memory and computation requirements. When no patient-specific prior information is available, the kernel method may not obtain good results.

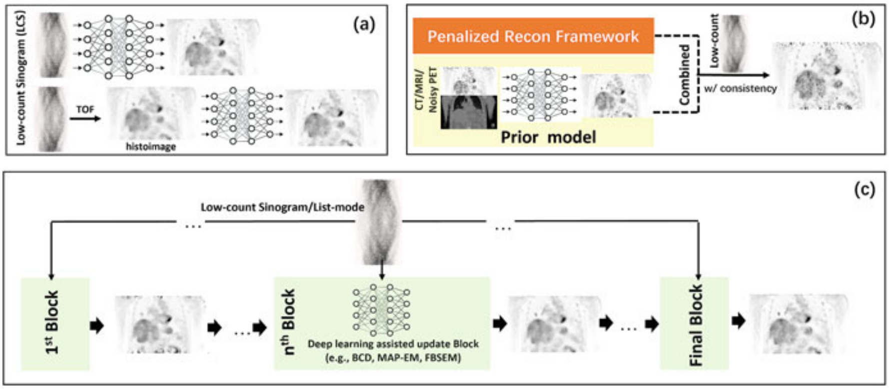

Fig. 6 Three classes of deep learning-based PET image reconstruction methods: (**a**) end-to-end direct reconstruction; (**b**) deep learning-assisted regularized iterative reconstruction; (**c**) unrolled iterative reconstruction

3.2 Deep-Learning Based Methods

PET emission process is not a strict Poisson statistic. Model-based and dictionary-based methods are observed as limited in their ability to learn and adapt to complex patterns in clinical practice. Apart from their empirical success, recently there is a growing amount of work on deep-learning based methods. Nowadays, deep neural networks [84] have dramatically improved the state-of-the-art in visual object recognition, object detection, and many other domains. These successes attracted tremendous attention and led to an explosion of research in the application of machine learning to medical image reconstruction. For PET image reconstruction, deep learning-based methods are also utilized in various methodologies. These methods can be roughly categorized into three classes: end-to-end direct reconstruction, deep learning-assisted regularized iterative reconstruction, unrolled iterative reconstruction methods. This section will discuss deep learning-based PET reconstruction algorithms following these categories (Fig. 6).

3.2.1 Direct End-to-End Reconstruction

The end-to-end direct reconstruction methodology treats the reconstruction as a direct mapping approach. This approach employs deep neural networks as a powerful mapping function or generator that reconstruct the image $\hat{\boldsymbol{x}}$ directly from the measured sinogram or list-mode data $\boldsymbol{m}$. This can be represented as:

$$\hat{\boldsymbol{x}} = F\left(\boldsymbol{m}; \hat{\theta}\right), \tag{9}$$

where F is the deep neural network, and $\hat{\boldsymbol{\theta}}$ is the parameters of F. The direct end-to-end approach uses deep neural networks to model the whole imaging system, which can be beneficial since it avoids the approximation assumptions in conventional reconstruction modeling. The training process is computationally intensive, but it can perform image reconstruction quickly once the model training is completed. Several contributions have been reported using this method. Häggström et al. [85] present a framework named as DeepPET using encoder-decoder structure. The reconstruction processes the sinogram to the PET image directly. The encoder down-samples the interior features into high-dimension, and the decoder reconstructs the features to the PET image. Both simulation and clinical data are evaluated in their research to show the improvement compared with conventional methods. Liu et al. [86] present a generative adversarial network (GAN) framework for PET reconstruction. This framework utilizes U-Net, an encoder-decoder structure with concatenation, as the conditional generator. The authors evaluate their method in phantom experiments. Hu et al. [87] propose a Wasserstein GAN (WGAN) based framework named DPIR-NET as an extension of the DeepPET framework. This framework is also evaluated in simulation and clinical data, showing promising results. Li et al. [88] extend the DeepPET to direct Patlak parametric imaging application. Their framework is an encoder-decoder structure with spatial and channel self-attention modules, mapping the dynamic sinograms directly to the parametric image outputs (Patlak K_i images). Whiteley et al. [89] propose the DirectPET framework, which consists of encoding, radon inversion, and refinement and scaling segments. This framework directly reconstructs whole-body PET sinograms. These authors [90] then proposed a successor framework named FastPET. This framework performs the image generation on the “histoimage” representation of the raw data. This framework can include TOF information in the reconstruction. Clinical and phantom experiments are employed to assess the method’s performance. Feng et al. [91] apply a framework inspired by DirectPET to reconstruct 3D TOF-PET via TOF-histoimage. Their network is a U-Net with only convolutional layers. Kandarpa et al. [92] propose a 3-step reconstruction framework consisting of a U-Net for sinogram denoising, a double U-Net generator for reconstructing, and a Res-Net for super-resolution post-processing. This framework is evaluated using CT and PET data, showing improvement in PET data but not surpassing conventional methods in CT data. Ote and Hashimoto [93] present an approach that better utilizes the “histogram” in TOF-PET reconstruction. They grouped the histogram based on their angular view and fed them into a 3D U-Net to generate the reconstructed image. Their method shows improvement in simulated brain PET data. Ma et al. [94] apply an encoder-decoder network from sinograms in long axial field of view (LAFOV) PET systems. This network contains a U-Net structure for reconstruction and a perceptual loss network. Clinical evaluation was conducted in this research to verify the effectiveness of their proposed method. Liu et al. [95] present a conditional GAN-based method that directly generates the PET image from the sinogram. The result of the simulationed experiment is satisfactory, but the preclinical and clinical experiments are not as well-pleasing. Lv et al. [96] examine the analytical model of 2-D TOF PET and proposed a BPF-like reconstruction algorithm with filtering operation performed with a neural network that reconstructs the PET image directly from list-mode data. The convolutional neural network learns the deconvolution operator in the spatial domain. The simulation experiments show the effectiveness of the proposed BP-Net method.

Although the end-to-end direct reconstruction methodology avoids the approximation assumptions in conventional models, the lack of physics and statistics requires the deep learning-based mapping model to be complex (especially when the reconstruction is in 3-D) and the input dataset to be large and high-quality. The quality of the reconstructed images can satisfy clinical needs.

3.2.2 Deep Learning-Based Regularized Iterative Reconstruction

Due to the disadvantages of end-to-end reconstruction methods, researchers explore the combination of conventional iterative reconstruction methods with deep learning. In the conventional methods, the penalty term methodology is limited by the approximate assumption and compromising the mathematical complexity, and the performance of kernel methodology is heavily dependent on the model designation. Incorporating deep learning with conventional iterative reconstruction can bring powerful learnable modeling tools to improve iterative reconstruction regularization. The reconstruction process benefits from the physical/statistics priors and the flexibility of deep neural network models.

Deep learning can be supervised, unsupervised or semi-supervised. In regularized iterative reconstruction, two primary approaches, supervised and unsupervised deep learning models, are used as penalty terms or image representations. The following part will be organized into two parts: the penalty term method and the representation method.

1) The penalty term methods can be expressed as adding a weighted penalty term to the objective function:

$$\hat{\boldsymbol{x}} = \operatorname{argmin} L\left(\boldsymbol{y}|\boldsymbol{x}\right) + \beta R\left(\boldsymbol{x}\right), \tag{10}$$

where $R(\boldsymbol{x})$ is the penalty term that regularizes the objective function to our dedicated purpose, and β is a hyperparameter that controls the influence of the penalty term. Deep learning-based penalty term methods design the penalty $R(\boldsymbol{x})$ using deep learning.

Kim et al. [97] present a framework consisting of a local linear fitting function module and the denoising convolutional neural network (DnCNN). The optimization utilized the Alternating Direction Method of Multipliers (ADMM) algorithm to decompose the iterations into multiple sub-iterations. Xie et al. [98] present a 3D PET structural convolutional sparse coding (CSC) method. This method combines a quadratic penalty with deep learning. Both simulated and clinical data are applied to evaluate the performance of the proposed method. Li et al. [99] propose a joint reconstruction and motion correction method. The joint estimation is formulated as a regularized optimization problem with a deep neural network. The authors use the ADMM algorithm to solve the constrained optimization problem.

2) The deep learning-based representation method rewrites this formula as $\boldsymbol{x} = f(z; \boldsymbol{\theta})$, where f is a deep learning network, and $\boldsymbol{\theta}$ is the parameters of f. z represents the latent information. The objective function is therefore rewritten as:

$$\hat{\boldsymbol{x}} = \text{argmin}\ L\left(\boldsymbol{y}|\boldsymbol{x}\right), \quad s.t.\boldsymbol{x} = f\left(z; \boldsymbol{\theta}\right) \tag{11}$$

Several articles have been published based on the representation method. Gong et al. [100] propose a CNN representation method that utilizes a 3-D U-Net as the mapping function with frozen parameters and uses ADMM optimization to construct the sub-iteration steps. Xie et al. [101] further improve the generation and representation capability of the network using the GAN-based model, which includes the attention mechanism to enhance the generation performance. Li and Wang [102] apply the deep kernel method in dynamic PET imaging. Their deep kernel representation is a series of deep neural network components. In their work, both simulation and clinical results demonstrated the improvement of the deep kernel method.

The abovementioned approaches are all based on supervised learning, which requireing high-quality ground truths as training labels. However, in many cases, even the ground truth PET images have low SNR. It is difficult for the supervised learning methods to further improve the low SNR ground truth images to a better level. Therefore, unsupervised deep learning algorithms are explored in constrained PET reconstruction. Gong et al. [103] proposed DIP-Recon based on the deep image prior (DIP) method, representing the reconstructed image using deep neural networks. This approach is similar to the kernel method above, but no high-quality ground truths are required. In clinical, the latent information used for representation is CT or MR images collected along with PET scans [104]. Sudarshan et al. [105] utilize a modified Bayesian DIP (BDIP) technique in PET image reconstruction. The BDIP can model the uncertainty tend to prevent the DIP overfitting problem. The authors penalize regions with higher uncertainty, resulting in image quality improvement.

DIP method is further explored [106, 107] in direct parametric reconstruction. The Patlak or Logan parametric imaging is embedded into the deep neural networks. ADMM and optimization transfer algorithms are used to factorize the whole optimization problem into several sub-iterations. Yokota et al. [108] also present a DIP-based method in dynamic PET image reconstruction from both spatial and temporal aspects. Individual U-Nets extract the components of the spatial matrix. Hashimoto et al. [109] incorporate DIP with a forward projection model in reconstruction, which performs unsupervised deep learning-based PET image reconstruction from the sinogram.

3.2.3 Unrolled Deep Learning-Based Iterative Reconstruction

The end-to-end direct and some of the deep learning-based iterative reconstruction still preserve the disadvantages that are derived from their foundational techniques. As mentioned, the end-to-end method ignores the physical and statistical characteristics of the PET system. The system matrix, representing the forward model of the PET system and including abundant information about the PET system, is wasted in the end-to-end method. On the other hand, though the deep learning-based iterative reconstruction method takes the physical and statistical characteristics of the PET system into account, the conventional mathematical assumptions are preserved in the optimization processes. Researchers have explored the unrolled methods and developed several deep learning-based unrolled algorithms for PET image reconstruction to better integrate the advantages of deep neural networks and the iterative reconstruction methodology. Gong et al. propose the MAPEM-Net [110] which is derived from their former work EMNet [111] method. The MAPEM-Net replaces the step of updating the latent input $\mathbf{z}$ in the ADMM optimization with a 3-D U-Net network. Mehranian and Reader [112] propose the FBSEM framework that utilizes the forward-backward splitting algorithm in the optimization process. The FBSEM replaces the update of the regularizer with deep neural networks. Lim et al. [113] employ the BCD-Net [114] in PET image reconstruction. The proposed approach generates an estimation of the PET image using the BCD-Net, and the estimate is utilized as a prior for MAPEM. Using the output of MAPEM as the input of BCD-Net, the estimation is updated again, thus establishing an iterative process for reconstruction. Currently, widespread adoption of unrolled PET reconstruction method has been hampered, partly due to the time-consuming forward and backward projection and a lack of applicable framework in python environment. Some groups establish a direct connection between an established PET reconstruction software (e.g. STIR [115] and SIRF [116]) and PyTorch [117]. This allows for unrolling standard iterative loop of an image reconstruction algorithm into advanced deep learning methodologies.

4 Summary

In this chapter, we introduced three different categories of PET image reconstruction methods. The data-driven PET reconstruction methods offer several advantages over analytical and model-based approaches. For one, they can be more accurate, as they can learn to model complex patterns and structures directly from data. In contrast, analytical and model-based methods rely on predefined mathematical models. Additionally, machine learning or deep learning-based methods are generally easier to use, as they require less expertise in mathematical modeling and can be trained on relatively large amounts of data, allowing them to adapt to different imaging conditions. Overall, deep learning-based PET reconstruction methods offer a powerful tool for improving the quantitative accuracy of PET imaging. However, there are several open questions regarding PET reconstruction: how to construct interpretable, generalizable, data-efficient, and physics-constrained models in PET reconstruction? How can PET reconstruction be integrated with other imaging techniques, such as CT or MRI, to provide more comprehensive and accurate information about the body's structures and functions? In the near future, more evaluations from radiologists/physicians are needed to better understand the clinical outcomes of different approaches.

Acknowledgments The authors would like to thank Prof. Huafeng Liu of Zhejiang University for the valuable discussions and proof-reading. This work was supported by National Natural Science Foundation of China (82061Y0031), Foundation of Beijing Municipal Education Commission (73202Y1022), Shenzhen Science and Technology Program (KQTD20180412181221912, JCYJ20200109140603831), and Start-up Research Fund from the Institute of Medical Technology, Peking University Health Science Center.

References

1. Cormack, A. M. (1963). Representation of a function by its line integrals, with some radiological applications. *Journal of Applied Physics, 34*(9), 2722–2727.
2. Bracewell, R. N. (1956). Strip integration in radio astronomy. *Australian Journal of Physics, 9*, 198.
3. National Electrical Manufacturers Association. (2018). *NEMA Standards publication NU 2-2018: Performance measurements of positron emission tomographs (PET)* (p. 41). National Electrical Manufacturers Association.
4. Razifar, P., et al. (2005). Noise correlation in PET, CT, SPECT and PET/CT data evaluated using autocorrelation function: A phantom study on data, reconstructed using FBP and OSEM. *BMC Medical Imaging, 5*(1), 5.
5. Teymurazyan, A., Riauka, T., Jans, H.-S., & Robinson, D. (2013). Properties of noise in positron emission tomography images reconstructed with filtered-backprojection and row-action maximum likelihood algorithm. *Journal of Digital Imaging, 26*(3), 447–456.
6. Santarelli, M. F., Positano, V., & Landini, L. (2017). Measured PET data characterization with the negative binomial distribution model. *Journal of Medical and Biological Engineering, 37*(3), 299–312.
7. Van Slambrouck, K., et al. (2015). Bias reduction for low-statistics PET: Maximum likelihood reconstruction with a modified Poisson distribution. *IEEE Transactions on Medical Imaging, 34*(1), 126–136.
8. Wilson, D. W., Tsui, B. M., & Barrett, H. H. (1994). Noise properties of the EM algorithm. II. Monte Carlo simulations. *Physics in Medicine & Biology, 39*(5), 847.
9. Barrett, H. H., Wilson, D. W., & Tsui, B. M. (1994). Noise properties of the EM algorithm. I. Theory. *Physics in Medicine & Biology, 39*(5), 833.
10. Lange, K., & Carson, R. (1984). EM reconstruction algorithms for emission and transmission tomography. *Journal of Computer Assisted Tomography, 8*(2), 306–316.
11. Shepp, L. A., & Vardi, Y. (1982). Maximum likelihood reconstruction for emission tomography. *IEEE Transactions on Medical Imaging, 1*(2), 113–122.

12. Boellaard, R., Lingen, A. V., & Lammertsma, A. A. (2001). Experimental and clinical evaluation of iterative reconstruction (OSEM) in dynamic PET: Quantitative characteristics and effects on kinetic modeling. *Journal of Nuclear Medicine, 42*(5), 808–817.
13. Reader, A. J., Visvikis, D., Erlandsson, K., Ott, R. J., & Flower, M. A. (1998). Intercomparison of four reconstruction techniques for positron volume imaging with rotating planar detectors. *Physics in Medicine & Biology, 43*(4), 823–834.
14. Yavuz, M., & Fessler, J. A. (1998). Statistical image reconstruction methods for randoms-precorrected PET scans. *Medical Image Analysis, 2*(4), 369–378.
15. Yavuz, M., & Fessler, J. A. (1997). New statistical models for randoms-precorrected PET scans. In J. Duncan & G. Gindi (Eds.), *Information processing in medical imaging* (Lecture Notes in Computer Science) (Vol. 1230, pp. 190–203). Springer.
16. Brasse, D., Kinahan, P. E., Lartizien, C., Comtat, C., Casey, M., & Michel, C. (2005). Correction methods for random coincidences in fully 3D whole-body PET: Impact on data and image quality. *Journal of Nuclear Medicine, 46*(5), 859–867.
17. Badawi, R. D., Miller, M. P., Bailey, D. L., & Marsden, P. K. (1999). Randoms variance reduction in 3D PET. *Physics in Medicine & Biology, 44*(4), 941–954.
18. Zhang, X., Zhou, J., Cherry, S. R., Badawi, R. D., & Qi, J. (2017). Quantitative image reconstruction for total-body PET imaging using the 2-meter long EXPLORER scanner. *Physics in Medicine & Biology, 62*(6), 2465–2485.
19. Bailey, D. L., & Meikle, S. R. (1994). A convolution-subtraction scatter correction method for 3D PET. *Physics in Medicine & Biology, 39*(3), 411.
20. Lercher, M. J., & Wienhard, K. (1994). Scatter correction in 3-D PET. *IEEE Transactions on Medical Imaging, 13*(4), 649–657.
21. Grootoonk, S., Spinks, T., Sashin, D., Spyrou, N., & Jones, T. (1996). Correction for scatter in 3D brain PET using a dual energy window method. *Physics in Medicine & Biology, 41*(12), 2757.
22. Hamill, J., Efthimiou, N., Karp, J., & Surti, S. (2022). Evaluation of energy-based scatter compensation methods in clinical whole-body PET. *Journal of Nuclear Medicine, 63*(supplement 2), 2395.
23. Watson, C. C. (2000). New, faster, image-based scatter correction for 3D PET. *IEEE Transactions on Nuclear Science, 47*(4), 1587–1594.
24. Ollinger, J. M. (1996). Model-based scatter correction for fully 3D PET. *Physics in Medicine & Biology, 41*(1), 153.
25. Scheins, J. J., Lenz, M., Pietrzyk, U., Shah, N. J., & Lerche, C. W. (2021). High-throughput, accurate Monte Carlo simulation on CPU hardware for PET applications. *Physics in Medicine & Biology, 66*, 185001.
26. Levin, C. S., Dahlbom, M., & Hoffman, E. J. (1995). A Monte Carlo correction for the effect of Compton scattering in 3-D PET brain imaging. *IEEE Transactions on Nuclear Science, 42*(4), 1181–1185.
27. Berker, Y., Maier, J., & Kachelrieß, M. (2018). Deep scatter estimation in PET: Fast scatter correction using a convolutional neural network. In *2018 IEEE nuclear science symposium and medical imaging conference proceedings (NSS/MIC)* (pp. 1–5). IEEE.
28. Qian, H., Rui, X., & Ahn, S. (2017). Deep learning models for PET scatter estimations. In *2017 IEEE nuclear science symposium and medical imaging conference (NSS/MIC)* (pp. 1–5). IEEE.
29. Zaidi, H., & Montandon, M.-L. (2007). Scatter compensation techniques in PET. *PET Clinics, 2*(2), 219–234.
30. Mazoyer, B., Roos, M., & Huesman, R. (1985). Dead time correction and counting statistics for positron tomography. *Physics in Medicine & Biology, 30*(5), 385.
31. Guérin, B., & El Fakhri, G. (2008). Realistic PET Monte Carlo simulation with pixelated block detectors, light sharing, random coincidences and dead-time modeling. *IEEE Transactions on Nuclear Science, 55*(3), 942–952.
32. Bailey, D. L., Meikle, S. R., & Jones, T. (1997). Effective sensitivity in 3D PET: The impact of detector dead time on 3D system performance. *IEEE Transactions on Nuclear Science, 44*(3), 1180–1185.

33. Issa, A. S. M., et al. (2022). A detector block-pairwise dead time correction method for improved quantitation with a dedicated BrainPET scanner. *Physics in Medicine & Biology, 67*, 235004.
34. Guez, D., Bataille, F., Comtat, C., Honore, P. F., Jan, S., & Kerhoas, S. (2008). Counting rates modeling for PET scanners with GATE. *IEEE Transactions on Nuclear Science, 55*(1), 516–523.
35. Knoll, G. F. (2000). *Radiation detection and measurement*. Wiley.
36. Carney, J. P. J., Townsend, D. W., Rappoport, V., & Bendriem, B. (2006). Method for transforming CT images for attenuation correction in PET/CT imaging. *Medical Physics, 33*(4), 976–983.
37. Kinahan, P. E., Townsend, D. W., Beyer, T., & Sashin, D. (1998). Attenuation correction for a combined 3D PET/CT scanner. *Medical Physics, 25*(10), 2046–2053.
38. Wagenknecht, G., Kaiser, H. J., Mottaghy, F. M., & Herzog, H. (2013). MRI for attenuation correction in PET: Methods and challenges. *Magma, 26*(1), 99–113.
39. Hofmann, M., et al. (2011). MRI-based attenuation correction for whole-body PET/MRI: Quantitative evaluation of segmentation- and atlas-based methods. *Journal of Nuclear Medicine, 52*(9), 1392.
40. Rezaei, A., et al. (2012). Simultaneous reconstruction of activity and attenuation in time-of-flight PET. *IEEE Transactions on Medical Imaging, 31*(12), 2224–2233.
41. Omidvari, N., et al. (2022). Lutetium background radiation in total-body PET—A simulation study on opportunities and challenges in PET attenuation correction. *Frontiers in Nuclear Medicine, 2*, 963067.
42. Defrise, M., Townsend, D., Bailey, D., Geissbuhler, A., & Jones, T. (1991). A normalization technique for 3D PET data. *Physics in Medicine & Biology, 36*(7), 939.
43. Badawi, R. D., & Marsden, P. (1999). Developments in component-based normalization for 3D PET. *Physics in Medicine & Biology, 44*(2), 571.
44. Bai, B., et al. (2002). Model-based normalization for iterative 3D PET image reconstruction. *Physics in Medicine & Biology, 47*(15), 2773.
45. Wu, X. (1991). An efficient antialiasing technique. *ACM SIGGRAPH Computer Graphics, 25*(4), 143–152. ACM.
46. Zhou, J., & Qi, J. (2011). Fast and efficient fully 3D PET image reconstruction using sparse system matrix factorization with GPU acceleration. *Physics in Medicine & Biology, 56*(20), 6739–6757.
47. Terstegge, A., Weber, S., Herzog, H., Muller-Gartner, H., & Halling, H. (1996). High resolution and better quantification by tube of response modelling in 3D PET reconstruction. In *1996 IEEE nuclear science symposium. Conference record* (Vol. 3, pp. 1603–1607). IEEE.
48. Moses, W. W. (2011). Fundamental limits of spatial resolution in PET. *Nuclear Instruments and Methods in Physics Research Section A: Accelerators, Spectrometers, Detectors and Associated Equipment, 648*, S236–S240.
49. Stickel, J. R., & Cherry, S. R. (2005). High-resolution PET detector design: Modelling components of intrinsic spatial resolution. *Physics in Medicine & Biology, 50*(2), 179.
50. Rahmim, A., Qi, J., & Sossi, V. (2013). Resolution modeling in PET imaging: Theory, practice, benefits, and pitfalls. *Medical Physics, 40*(6), 064301.
51. Chen, S., Hu, P., Gu, Y., Yu, H., & Shi, H. (2020). Performance characteristics of the digital uMI550 PET/CT system according to the NEMA NU2-2018 standard. *EJNMMI Physics, 7*(1), 1–14.
52. Tong, S., Alessio, A. M., Thielemans, K., Stearns, C., Ross, S., & Kinahan, P. E. (2011). Properties and mitigation of edge artifacts in PSF-based PET reconstruction. *IEEE Transactions on Nuclear Science, 58*(5), 2264–2275.
53. Lee, K., Kinahan, P. E., Fessler, J. A., Miyaoka, R. S., Janes, M., & Lewellen, T. K. (2004). Pragmatic fully 3D image reconstruction for the MiCES mouse imaging PET scanner. *Physics in Medicine & Biology, 49*(19), 4563.
54. Zeng, T., et al. (2020). A GPU-accelerated fully 3D OSEM image reconstruction for a high-resolution small animal PET scanner using dual-ended readout detectors. *Physics in Medicine & Biology, 65*(24), 245007.

55. Gong, K., Cherry, S. R., & Qi, J. (2016). On the assessment of spatial resolution of PET systems with iterative image reconstruction. *Physics in Medicine & Biology, 61*(5), N193–N202.
56. Chun, S. Y., & Fessler, J. A. (2009). Joint image reconstruction and nonrigid motion estimation with a simple penalty that encourages local invertibility. In *Medical imaging 2009: Physics of medical imaging* (Vol. 7258, pp. 288–296). SPIE.
57. Blume, M., Martinez-Moller, A., Keil, A., Navab, N., & Rafecas, M. (2010). Joint reconstruction of image and motion in gated positron emission tomography. *IEEE Transactions on Medical Imaging, 29*(11), 1892–1906.
58. Li, T., Zhang, M., Qi, W., Asma, E., & Qi, J. (2020). Motion correction of respiratory-gated PET images using deep learning based image registration framework. *Physics in Medicine & Biology, 65*(15), 155003.
59. Mumcuoglu, E. U., Leahy, R., Cherry, S. R., & Zhou, Z. (1994). Fast gradient-based methods for Bayesian reconstruction of transmission and emission PET images. *IEEE Transactions on Medical Imaging, 13*(4), 687–701.
60. Qi, J. Y., & Leahy, R. M. (1999). A theoretical study of the contrast recovery and variance of MAP reconstructions from PET data. *IEEE Transactions on Medical Imaging, 18*(4), 293–305.
61. Leahy, R. M., & Qi, J. Y. (2000). Statistical approaches in quantitative positron emission tomography. *Statistics and Computing, 10*(2), 147–165.
62. Fessler, J. A., & Hero, A. O. (1995). Penalized maximum-likelihood image-reconstruction using space-alternating generalized EM algorithms. *IEEE Transactions on Image Processing, 4*(10), 1417–1429.
63. Ahn, S., & Leahy, R. M. (2008). Analysis of resolution and noise properties of nonquadratically regularized image reconstruction methods for PET. *IEEE Transactions on Medical Imaging, 27*(3), 413–424.
64. Wang, C., Hu, Z., Shi, P., & Liu, H. (2014). Low dose PET reconstruction with total variation regularization. In *2014 36th annual international conference of the IEEE Engineering in Medicine and Biology Society* (pp. 1917–1920). IEEE.
65. Wang, G., & Qi, J. (2012). Penalized likelihood PET image reconstruction using patch-based edge-preserving regularization. *IEEE Transactions on Medical Imaging, 31*(12), 2194–2204.
66. Mehranian, A., et al. (2017). PET image reconstruction using multi-parametric anato-functional priors. *Physics in Medicine & Biology, 62*(15), 5975.
67. Vunckx, K., et al. (2012). Evaluation of three MRI-based anatomical priors for quantitative PET brain imaging. *IEEE Transactions on Medical Imaging, 31*(3), 599–612.
68. Cheng-Liao, J., & Qi, J. (2011). PET image reconstruction with anatomical edge guided level set prior. *Physics in Medicine & Biology, 56*(21), 6899–6918.
69. Schramm, G., et al. (2018). Evaluation of parallel level sets and Bowsher's method as segmentation-free anatomical priors for time-of-flight PET reconstruction. *IEEE Transactions on Medical Imaging, 37*, 590–603.
70. Tang, J., & Rahmim, A. (2009). Bayesian PET image reconstruction incorporating anato-functional joint entropy. *Physics in Medicine & Biology, 54*(23), 7063.
71. Bowsher, J. E., et al. (2004). Utilizing MRI information to estimate F18-FDG distributions in rat flank tumors. In *IEEE symposium conference record nuclear science 2004* (Vol. 4, pp. 2488–2492). IEEE.
72. Zhang, M., Zhou, J., Niu, X., Asma, E., Wang, W., & Qi, J. (2017). Regularization parameter selection for penalized-likelihood list-mode image reconstruction in PET. *Physics in Medicine & Biology, 62*(12), 5114–5130.
73. Reader, A. J., & Ellis, S. (2020). Bootstrap-optimised regularised image reconstruction for emission tomography. *IEEE Transactions on Medical Imaging, 39*(6), 2163–2175
74. Chen, S., Liu, H., Shi, P., & Chen, Y. (2015). Sparse representation and dictionary learning penalized image reconstruction for positron emission tomography. *Physics in Medicine & Biology, 60*(2), 807.
75. Tahaei, M. S., & Reader, A. J. (2016). Patch-based image reconstruction for PET using prior-image derived dictionaries. *Physics in Medicine & Biology, 61*(18), 6833.

76. Tang, J., Yang, B., Wang, Y., & Ying, L. (2016). Sparsity-constrained PET image reconstruction with learned dictionaries. *Physics in Medicine & Biology, 61*(17), 6347.
77. Rubinstein, R., Bruckstein, A. M., & Elad, M. (2010). Dictionaries for sparse representation modeling. *Proceedings of the IEEE, 98*(6), 1045–1057.
78. Gribonval, R., & Schnass, K. (2010). Dictionary identification—Sparse matrix-factorization via ℓ_1-minimization. *IEEE Transactions on Information Theory, 56*(7), 3523–3539.
79. Aharon, M., Elad, M., & Bruckstein, A. (2006). K-SVD: An algorithm for designing overcomplete dictionaries for sparse representation. *IEEE Transactions on Signal Processing, 54*, 4311–4322.
80. Wang, G., & Qi, J. (2015). PET image reconstruction using kernel method. *IEEE Transactions on Medical Imaging, 34*(1), 61–71.
81. Hutchcroft, W., Wang, G., Chen, K. T., Catana, C., & Qi, J. (2016). Anatomically-aided PET reconstruction using the kernel method. *Physics in Medicine & Biology, 61*(18), 6668–6683.
82. Gong, K., Cheng-Liao, J., Wang, G., Chen, K. T., Catana, C., & Qi, J. (2018). Direct Patlak reconstruction from dynamic PET data using the kernel method with MRI information based on structural similarity. *IEEE Transactions on Medical Imaging, 37*(4), 955–965.
83. Wei, D., Charikar, M., & Kai, L. (2011). Efficient k-nearest neighbor graph construction for generic similarity measures. In *International conference on World Wide Web*. ACM.
84. Lecun, Y., Bengio, Y., & Hinton, G. (2015). Deep learning. *Nature, 521*(7553), 436–444.
85. Haggstrom, I., Schmidtlein, C. R., Campanella, G., & Fuchs, T. J. (2019). DeepPET: A deep encoder-decoder network for directly solving the PET image reconstruction inverse problem. *Medical Image Analysis, 54*, 253–262.
86. Liu, Z. Y., Chen, H., & Liu, H. F. (2019). Deep learning based framework for direct reconstruction of PET images. In *Medical image computing and computer assisted intervention – MICCAI 2019, Pt III* (Vol. 11766, pp. 48–56).
87. Hu, Z. L., et al. (2021). DPIR-Net: Direct PET image reconstruction based on the Wasserstein generative adversarial network. *IEEE Transactions on Radiation and Plasma Medical Sciences, 5*(1), 35–43.
88. Li, Y., et al. (2023). A deep neural network for parametric image reconstruction on a large axial field-of-view PET. *European Journal of Nuclear Medicine and Molecular Imaging, 50*(3), 701–714.
89. Whiteley, W., Luk, W. K., & Gregor, J. (2020). DirectPET: full-size neural network PET reconstruction from sinogram data. *Journal of Medical Imaging, 7*(3), 032503.
90. Whiteley, W., Panin, V., Zhou, C. Y., Cabello, J., Bharkhada, D., & Gregor, J. (2021). FastPET: Near real-time reconstruction of PET histo-image data using a neural network. *IEEE Transactions on Radiation and Plasma Medical Sciences, 5*(1), 65–77.
91. Feng, T., et al. (2021). Deep learning-based image reconstruction for TOF PET with DIRECT data partitioning format. *Physics in Medicine & Biology, 66*(16), 165007.
92. Kandarpa, V. S. S., Bousse, A., Benoit, D., & Visvikis, D. (2021). DUG-RECON: A framework for direct image reconstruction using convolutional generative networks. *IEEE Transactions on Radiation and Plasma Medical Sciences, 5*(1), 44–53.
93. Ote, K., & Hashimoto, F. (2022). Deep-learning-based fast TOF-PET image reconstruction using direction information. *Radiological Physics and Technology, 15*(1), 72–82.
94. Ma, R. Y., et al. (2022). An encoder-decoder network for direct image reconstruction on sinograms of a long axial field of view PET. *European Journal of Nuclear Medicine and Molecular Imaging, 49*(13), 4464–4477.
95. Liu, Z. Y., Ye, H. H., & Liu, H. F. (2022). Deep-learning-based framework for PET image reconstruction from sinogram domain. *Applied Sciences-Basel, 12*(16), 8118.
96. Lv, L., et al. (Apr 2022). A back-projection-and-filtering-like (BPF-like) reconstruction method with the deep learning filtration from listmode data in TOF-PET. *Medical Physics, 49*(4), 2531–2544.
97. Kim, K., et al. (Jun 2018). Penalized PET reconstruction using deep learning prior and local linear fitting. *IEEE Transactions on Medical Imaging, 37*(6), 1478–1487.

98. Xie, N. B., et al. (2022). Penalized-likelihood PET image reconstruction using 3D structural convolutional sparse coding. *IEEE Transactions on Biomedical Engineering, 69*(1), 4–14.
99. Li, T. T., Zhang, M. X., Qi, W. Y., Asma, E., & Qi, J. Y. (2022). Deep learning based joint PET image reconstruction and motion estimation. *IEEE Transactions on Medical Imaging, 41*(5), 1230–1241.
100. Gong, K., et al. (2019). Iterative PET image reconstruction using convolutional neural network representation. *IEEE Transactions on Medical Imaging, 38*(3), 675–685.
101. Xie, Z. H., et al. (2020). Generative adversarial network based regularized image reconstruction for PET. *Physics in Medicine & Biology, 65*(12), 125016.
102. Li, S. Q., & Wang, G. B. (2022). Deep kernel representation for image reconstruction in PET. *IEEE Transactions on Medical Imaging, 41*(11), 3029–3038.
103. Gong, K., Catana, C., Qi, J. Y., & Li, Q. Z. (2019). PET image reconstruction using deep image prior. *IEEE Transactions on Medical Imaging, 38*(7), 1655–1665.
104. Cui, J. N., et al. (2019). PET image denoising using unsupervised deep learning. *European Journal of Nuclear Medicine and Molecular Imaging, 46*(13), 2780–2789.
105. Sudarshan, V. P., Reddy, K. P. K., Singh, M., Gubbi, J., & Pal, A. (2022). Uncertainty-informed Bayesian PET image reconstruction using a deep image prior. In N. Haq, P. Johnson, A. Maier, C. Qin, T. Würfl, & J. Yoo (Eds.), *Machine learning for medical image reconstruction. MLMIR 2022* (Lecture Notes in Computer Science) (Vol. 13587, pp. 145–155).
106. Gong, K., et al. (2022). Direct reconstruction of linear parametric images from dynamic PET using nonlocal deep image prior. *IEEE Transactions on Medical Imaging*, *41*(3), 680–689.
107. Cui, J. N., Gong, K., Guo, N., Kim, K., Liu, H. F., & Li, Q. Z. (2022). Unsupervised PET logan parametric image estimation using conditional deep image prior. *Medical Image Analysis, 80*, 102519.
108. Yokota, T., Kawai, K., Sakata, M., Kimura, Y., & Hontani, H. (2019). Dynamic PET image reconstruction using nonnegative matrix factorization incorporated with deep image prior. In *2019 IEEE/CVF international conference on computer vision (ICCV 2019)* (pp. 3126–3135). IEEE.
109. Hashimoto, F., Ote, K., & Onishi, Y. (2022). PET image reconstruction incorporating deep image prior and a forward projection model. *IEEE Transactions on Radiation and Plasma Medical Sciences, 6*(8), 841–846.
110. Gong, K., et al. (2019). MAPEM-Net: An unrolled neural network for fully 3D PET image reconstruction. In *15th international meeting on fully three-dimensional image reconstruction in radiology and nuclear medicine* (Vol. 11072, p. 110720O). SPIE.
111. Gong, K., et al. (2019). EMnet: An unrolled deep neural network for PET image reconstruction. In *Medical imaging 2019: Physics of medical imaging* (Vol. 10948, p. 1094853). SPIE.
112. Mehranian, A., & Reader, A. J. (2021). Model-based deep learning PET image reconstruction using forward-backward splitting expectation-maximization. *IEEE Transactions on Radiation and Plasma Medical Sciences, 5*(1), 54–64.
113. Lim, H. K., Chun, I. Y., Dewaraja, Y. K., & Fessler, J. A. (2020). Improved low-count quantitative PET reconstruction with an iterative neural network. *IEEE Transactions on Medical Imaging, 39*(11), 3512–3522.
114. Chun, I. Y., & Fessler, J. A. (2018). Deep BCD-Net using identical encoding-decoding CNN structures for iterative image recovery. In *Proceedings 2018 IEEE 13th image, video, and multidimensional signal processing workshop (IVMSP)*. IEEE.
115. Thielemans, K., et al. (2012). STIR: Software for tomographic image reconstruction release 2. *Physics in Medicine & Biology, 57*(4), 867.
116. Ovtchinnikov, E., et al. (2020). SIRF: Synergistic image reconstruction framework. *Computer Physics Communications, 249*, 107087.
117. Paszke, A., et al. (2019). Pytorch: An imperative style, high-performance deep learning library. In H. Wallach, H. Larochelle, A. Beygelzimer, F. d'Alché Buc, E. Fox, & R. Garnett (Eds.), *Advances in neural information processing systems* (Vol. 32, pp. 8024–8035). Curran Associates, Inc.

Cascade Gamma Emission Coincidence Tomography

Xiao Liu, Hui Liu, and Yaqiang Liu

1 Introduction

Cascade gamma emission coincidence tomography is an imaging approach proposed primarily for assessing the delivery integrity of radiopharmaceuticals in nuclear medicine. Its working principle is that coincident events formed by cascade gamma photons consist of information that can be used to pinpoint the emission location of the photons, that is, where the radiopharmaceutical molecule is. Cascade gamma emission coincidence tomography (CGECT) is an imaging modality different from the conventional emission coincidence tomography (ECT) technology, which can create a distribution of cascade radiation nuclides using coincidence events emitted.

1.1 The Inadequacy of Standard Imaging Approach

In the single-photon emission computerized tomography (SPECT) and positron emission tomography (PET) detection process, for a decay event, only the LOR of a decaying nuclide can be determined, and the specific location of the nuclide cannot be obtained. This will make it hard to locate the nuclide's position and aggravate the noise of the reconstruction image. To obtain three-dimensional information on nuclide distribution, SPECT needs to perform multi-angle rotation sampling, while PET resolves this issue by being equipped with ring-shape detectors. Furthermore, in both scenarios, the three-dimensional distribution of radionuclides can be recon-

---

X. Liu (✉) · H. Liu · Y. Liu
Department of Engineering Physics, Tsinghua University, Beijing, China

© The Author(s), under exclusive license to Springer Nature Switzerland AG 2023

J. Du, K. (K.) Iniewski (eds.), *Gamma Ray Imaging*,
https://doi.org/10.1007/978-3-031-30666-2_3

structed only after accumulating data for a certain period of time in every detection angle, which leads to a big challenge for real-time imaging.

1.2 The Opportunity for Cascade Coincidence Imaging

Certain radionuclides used in nuclear medicine offer a unique opportunity for imaging. The two most widely used radionuclides in radiopharmaceutical therapy, Indium-111 and Lutetium-177, emit cascade gamma photons besides alpha and beta particles in their decay scheme. For these radionuclides, cascade gamma emission coincidence tomography becomes an optional approach for imaging the radio-agent distribution.

1.2.1 The Physics of Cascade Emission

The physical definition of cascade radiation is that when a nuclide decays, through the transition of energy level from high to low, two or more gamma photons of specific energy can be emitted in a very short time in sequence. As shown in the decay diagram of Indium-111 in Fig. 1, it has a high probability of decaying to the excited state of 417 keV of cadmium-111 after one decay occurs, and then

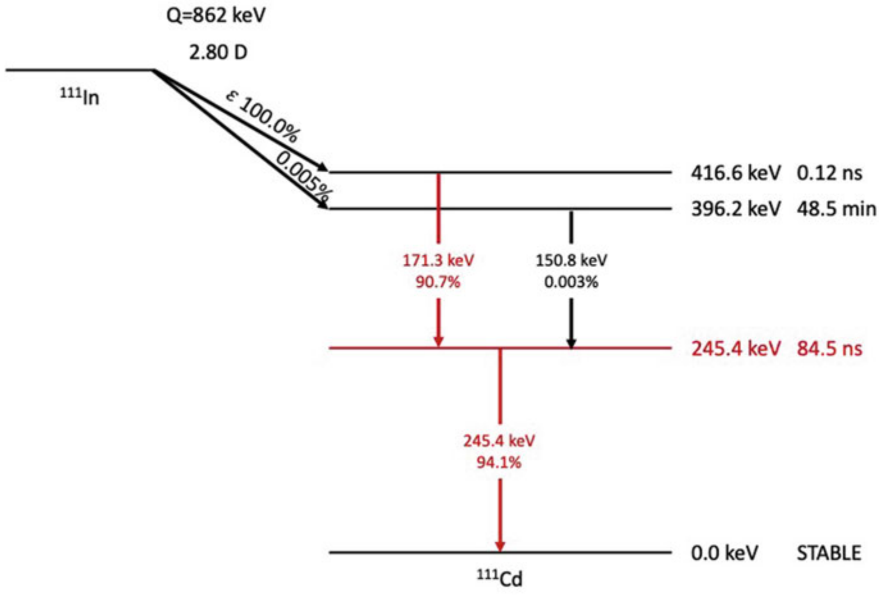

Fig. 1 The decay diagram of Indium-111

decays to 245 keV excited state and emits gamma photons of 171 keV. This 245 keV excited state is also called the cascade radiation intermediate state. After that, after experiencing a half-life of 84.5 ns, it de-excited to the ground state and emitted gamma photons of 245 keV. This process is called cascade radiation, and the successively emitted gamma photons of 171 keV and 245 keV form a pair of cascade radiation photons.

1.2.2 Cascade Photon Coincidence

Cascade radiating nuclides have cascade branches, which can generate cascade gamma photon pairs for the same decay. In nature, there are many such nuclides, but due to various reasons, not every cascade radiation nuclide is suitable for use in nuclear medicine.

Cascade radiation photon pairs have a good correlation in time, position, and emission angle, hence, the position information of nuclide can be directly included. Usually, the half-life of the cascade intermediate state corresponding to the cascade radiation gamma photon is sufficiently small, for example, less than 10 ns [1, 2], it is quite a short time compared considering the slow moving speed of the radionuclide molecule (normally several hundred meters per second), and it can be considered that the nuclide molecule is still during this period of time. Thus, each pair of cascaded radiation gamma photons can be considered from the same location. At the same time, the intervals of emission angles in each cascaded radiation photon pair are generally not parallel, so the above-mentioned positions can be directly determined by the intersection of their emission trajectories.

In general, as shown in Fig. 2, if the cascade radiation photon pair can be found according to the detection time, and the emission trajectories of the two photons can be obtained, according to the intersection of the emission trajectories, the position of the nuclide is directly obtained for imaging. It can be seen that the localization information contained in the coincident events is much better than that of the single-photon events, they can obtain Point-of-Response rather than Line-of-Response. This is the basic concept of cascade gamma coincidence imaging.

An ideal cascade radionuclide that can be used for cascade gamma photon coincidence imaging should have the following properties:

1. The total luminous intensity of the cascaded branches is high: for a decay event, it is hoped to emit as many cascaded photon pairs as possible. The more cascade radiation gamma photon pairs, the more detectable true coincidence events produced by the same number of decay events, which means less detection time and less damage to the imaging object.
2. Energy suitable for imaging: If the emitted gamma photon energy is too low, it is easy to be blocked by obstacles such as imaging objects and cannot be detected, and due to the negative correlation between energy resolution and energy, its energy resolution is relatively low. If the energy of the gamma photon is too high, it will easily penetrate the detector directly, which will also lead to undetectable.

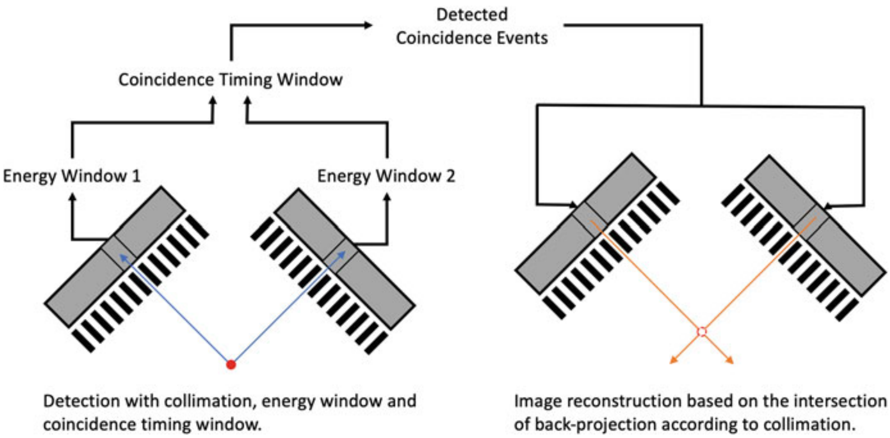
Detected
Coincidence Events
Coincidence Timing Window
Energy Window 1
Energy Window 2
Detection with collimation, energy window and coincidence timing window.
Image reconstruction based on the intersection of back-projection according to collimation.

Fig. 2 Detection and image reconstruction conception of CEGCT

Therefore, for the current nuclear medicine imaging system, it is hoped that the emitted gamma photon energy is between 50–200 keV.

3. Cascade branches with a high degree of discrimination: In the detection of a specific cascade branch, it is hoped that the cascade radiation gamma photons of this branch can be distinguished from other gamma photons as much as possible. On the one hand, in the mono-energy branch corresponding to the cascade branch, the proportion of cascaded radiation gamma photons needs to be high. On the other hand, the energy of the mono-energy branch corresponding to the cascade branch needs to be quite different from other branches and could be discriminated by the detector to reduce contamination between energy windows.
4. Shorter half-life of cascade intermediate states: The shorter the half-life of intermediate states, the narrower the coincidence timing window that can be used, which can better limit random coincidence events and make the image quality better.
5. Cascade radiation photon pairs with non-parallel emission: If the emission directions of the cascaded gamma photon pairs are all parallel, the location positioning of the radionuclide will degenerate to a line, and there is no way to achieve precise positioning. Cascading nuclides generally satisfy this point.

Energy Resolution (ER) is a very important parameter in cascade gamma coincidence imaging, just like other modalities in nuclear medicine imaging. In the detected photon energy spectrum, the concerned photon all-energy peak E will have a certain broadening ΔE, then ER can be defined as $ER = \frac{\Delta E}{E} \times 100\%$. Generally, the ER is inversely proportional to the square root of the energy, which means the higher the energy, the smaller the ER. Since photons are likely to undergo Compton scattering with substances during transportation, resulting in inaccurate localization information, how to distinguish between full energy peak photons and Compton scattered photons is crucial: if the ER is good enough, a narrower Energy Window

(EW) can be used, which excludes a large number of scattering events, thereby improving image quality and quantitative accuracy.

In general, ER is mainly related to the crystal and electronics of the detector. In the PET system, for 511 keV photons, its ER is generally 10–20%. In the SPECT system, a variety of nuclides will be targeted, and the ER of the most used Technetium-99 m is generally 10%. In the CGECT, photons' energy is close to that in SPECT, the energy resolution should be nearly the same.

1.2.3 Advantages: Higher Information Quality, Real-Time Imaging

Compared with traditional PET or SPECT imaging, cascaded gamma photon coincidence imaging can directly locate a decay event, thus having unique real-time imaging advantages, which have very prominent clinical value.

In addition to this, statistical noise is suppressed, and each pixel within the FOV is no longer affected by statistical errors from farther pixels on the LOR. It can be proved that, if a uniform cylinder of radius D is imaged, and the coincidence event can locate the decay position in the area of diameter d, then the signal-to-noise ratio of the image can be increased by $\sqrt{D/d}$.

At last, the CGECT must first detect the single photons just like SPECT, and then coincide them to obtain coincidence events. This means the CGECT can use not only coincidence events for imaging but also use those single events that cannot be coincided, behaving just like SPECT.

1.2.4 Potential Application & Nuclides

CGECT is proposed primarily for assessing the delivery integrity of radiopharmaceuticals and there is also plenty of potential use in the nuclear medical imaging field. Nuclear medical imaging is mainly based on the principle of isotope tracing, which introduces radioisotopes into organic organisms to form a certain three-dimensional dose distribution in the body and carry out non-invasive disease diagnosis, treatment and research on organic organisms [3]. Gamma photons from these nuclides already have good applications in imaging, but additional knowledge about cascade radiation might take it to the next level. Table 1 shows the cascade radiation information of some nuclides already used in nuclear medicine.

2 Design Issues that Are Unique to CGECT Systems

In this section, we will first go through the whole cascade gamma coincidence imaging process, and then discuss the factors in each part that govern the system performance. As shown in Fig. 2, a typical imaging generation process using coincident gamma cameras has several steps:

Table 1 Some cascade radiation nuclides used in nuclear medicine

Nuclide	Half-life	Cascade branch energy (keV)[a]	Corresponding single energy branch light intensity (%)[a]	Cascade intermediate state half-life	Decay mode
Lutetium-177	6.65 d	208.4/112.9	10.36/6.17	0.537 ns	β^-
Iodine-131	8.03 d	284.3/80.2	6.12/2.62	0.454 ns	β^-
Indium-111	2.8 d	171.3/245.4	90.7/94.1	84.5 ns	ε
Terbium-161	6.89 d	48.9/25.7	17.0/23.2	29.5 ns	β^-
Copper-67	2.58 d	91.3/93.3	7.0/16.1	9.10 μs	β^-
Arsenic-72	1.08 d	629.9/834.0	8.07/81	–	ε
Gallium-67	3.26 d	300.2/93.3	16.64/38.81	9.07 μs	ε
Samarium-153	1.94 d	69.7/103.2	4.67/29.14	3.9 ns	β^-
Cobalt-60	5.27 y	1173.2/1332.5	99.85/99.98	0.9 ps	β^-
Iodine-124	4.18 d	722.8/602.7	10.36/62.9	–	ε
Selenium-75	119.8 d	136/264.7	58.5/58.9	11.2 ps	ε
Th-227	18.68 d	235.96/50.13	12.9/8.4	0.63 ns	α

[a] According to the order of cascade radiation, the information of photons emitted first is shown in the former position

1. The cascade radiation nuclide decays, emitting several pairs of cascaded gamma photons and several non-cascade gamma photons. For simplicities, we only consider one cascade photon pair scenario, whose energy is marked E_1 and E_2. The multi-pairs case can be divided into single-pair cases.
2. These gamma photons then interact with the matter on their flying trajectory after they are emitted, and finally caught by the detector. This part includes the decay of the imaging object itself, the pass possibility of the collimator, the penetration of detector, etc.
3. The coincident gamma camera sets up two energy windows (EWs), EW1 for E_1 photons and EW2 for E_2 photons, only those photons whose energy is within the EW are selected.
4. The coincident gamma camera then sets up a coincidence timing window (CTW), tries to coincide every E_1 photons with every E_2 photons. Only when the detection time difference between one E_1 photon and one E_2 photon is within the CTW, these two photons are coincided and considered as a coincidence event. Those photons that cannot be coincided are treated as single photon events.
5. Use coincidence events or single photons or even both of them to build the image of nuclide distribution based on reconstruction algorithm.

In the following description, we focus on the unique issues of CGECT system design and skip well-known design considerations about gamma cameras.

2.1 Detector's Timing Resolution

The detectors of CGECT are essentially gamma camera detectors with event timing measurement capability. We skip descriptions on the gamma camera for its established status and focus only on the timing aspect of the detector.

We describe useful knowledge about detectors from the perspective of timing resolution: what is better timing resolution, why, how (what scintillator or technique) to make it happen, what are the better ones available, etc.

2.2 System Detection Efficiency

Coincidence detection has a significant impact on system detection efficiency. The main factors that affect the detection efficiency are the geometric design of the system and the inherent detection efficiency of the detector. For SPECT and CGECTs, the collimator is also an important factor affecting the detection efficiency. At present, the detection efficiency of clinical SPECT is generally 0.01–0.03%, and the detection efficiency of clinical PET is generally 2–10%.

For the CGECT, there are single photon detection efficiency and coincidence events detection efficiency, the latter could be roughly expressed as the square of the former one, yet the angular correlation issue between the two cascade gammas will cause some fluctuation. In general, the emission angular spacing distribution of cascaded radiation photon pairs satisfies [4–7]

$$W(\theta) = \sum_k A_k P_k(\cos\theta)$$

Where A_k is a positive or negative parameter related to each cascade radiation pair, P_k is a k order Legendre polynomial. Obviously, $W(\theta)$ should be symmetric for 90 degrees, therefore the parameter corresponding to the odd Legendre inequality should be equal to 0, i.e. $A_k = 0$ for any odd k. This equation indicates that the distribution of the cascade photon at a certain angular interval is bigger than others, which may be useful for the system design. For example, for Lu177's 113/208 keV cascade photon pairs, $W(\theta) = 1 - 0.16\left(\frac{3\cos^2\theta - 1}{2}\right)$, which means that if we put the two detectors at 90 degrees, we will get 1.29 times more true coincidence events than 180 degrees.

2.3 Image Generation

We describe several CGECT specific tasks in the image generation process of CGECT .

2.3.1 Choose a Coincidence Timing Window: NECR Analysis

Generally, different source activities and different CTWs will lead to changes in the proportion of detected coincident events of various types, which in turn affects the quality of reconstructed images. In order to select the best CTW for a specific source activity, analysis and study of the coincident event components are required.

The coincidence events detected by the cascade gamma coincidence system can be roughly divided into three types: true coincidence events, scatter coincidence events, and random coincidence events. Among them, only the true coincidence event is the real concern of the research institute, and the correct positioning information can be obtained. For the scatter coincidence event, the two photons also come from the same decay event, but some or even all of the cascaded photons in the coincidence event have undergone Compton scattering, resulting in refraction in the emission trajectory, resulting in inaccurate positioning information. The photons in the random coincidence event do not come from the same decay event, but the time difference falls within the coincidence time window, which is misjudged as a coincidence event by the system. Figure 3 shows a schematic diagram of three coincidence events in CGECT. Both scatter coincidence events and random coincidence events will generate incorrect positioning information.

In the PET system, the two 511 keV photons from the same decay event are emitted at the same time. While in the CGECT, there are time gaps between these cascade photons, and the value varies based on the natural property of the cascade

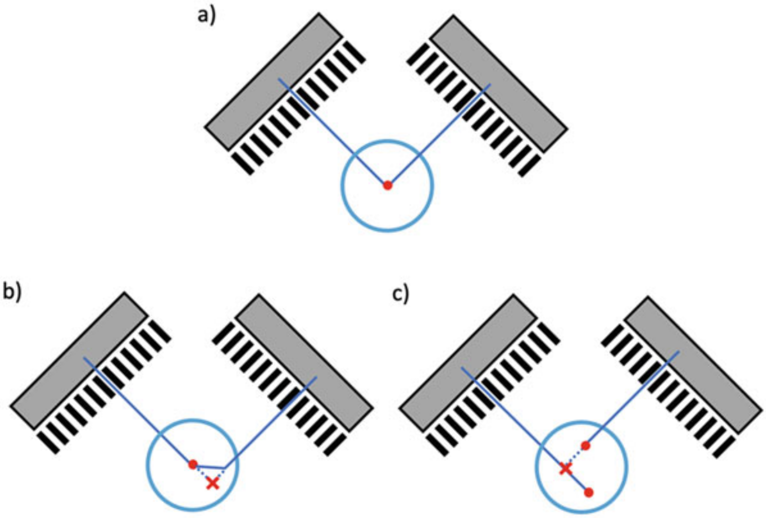

Fig. 3 Schematic diagrams of three coincidence events: (**a**) true coincident event; (**b**) scatter coincident event; (**c**) random coincident event. The red dot is the location of the decay event, and the red cross is the location of the error location

nuclide, which makes the situation more complicated. Next, we will do a theoretical derivation analysis for CTW choosing in the CGECT.

Let T, S, and R be the count rates of true coincidence events, scattered coincidence events, and random coincidence events, respectively. S is generally related to matter in space and needs to be discussed on a case-by-case basis, so it will not be discussed here. For T and R, it can be described using the following formula [3]

$$T = K \cdot (A \cdot b_c) \cdot d_c$$

$$R = CTW \cdot (A \cdot b_1) \cdot (A \cdot b_2) \cdot d_c$$

where subscripts 1, 2 and c represent monoenergetic branch 1, monoenergetic branch 2 and cascade branch, respectively, b represents branch luminescence intensity, d represents system detection efficiency, A represents source activity, and K is the impact of CTW that

$$K = 2 \cdot CDF\left(2.355 \cdot \frac{CTW}{2 \cdot CTR}\right) - 1$$

where CDF is the standard normal distribution cumulative distribution function. The values of b_1, b_2 and b_c are source specific properties.

In order to reduce the negative effects of scattering coincidence and random coincidence as much as possible, and to study the best experimental conditions, this study introduces the concept of maximizing the Noise Equivalent Count Rate (NECR) [3, 8, 9]. NECR is a surrogate metric for the time-to-event signal-to-noise ratio and is widely used to evaluate the performance of PET and can be directly promoted to the CGECT. The higher the NECR value the better. The specific definition of NECR is as follows:

$$NECR = \frac{T^2}{T + S + R}$$

When S is negligible compared to T and R, NECR approximately has

$$NECR \approx \frac{K}{1/A + CTW/(K \cdot B)} \cdot b_c \cdot d_c$$

where $B = \frac{b_c}{b_1 b_2}$. It can be seen that NECR is positively correlated with d_c, B, b_c and d_c, and negatively correlated with CTR. In order to make the NECR larger, the nuclides with larger B and b_c should be selected as much as possible, while reducing the CTR as much as possible. Generally speaking, when other values are fixed, NECR will first increase and then decrease with the increase of CTW. Therefore, an appropriate CTW should be selected to maximize NECR.

2.3.2 Sampling Completeness

Sampling completeness is a crucial issue for every medical imaging system, which determines whether the image of each pixel can be accurately reconstructed. This includes complicated Mathematics. Generally speaking, if every detected event can be traced back to a decay event within a FOV voxel, the decay event counts in every voxel can be perfectly estimated. However, if one detected event could be emitted from several voxels and one cannot directly locate it, voxels may not have enough information to reconstruct this event. In CEGCT, sampling completeness could be easily satisfied based on the PORs given by each coincidence event, every FOV voxel's value could be reconstructed perfectly as long as it could be detected by the coincident gamma cameras.

On the contrary, in conventional medical imaging systems like PET and SPECT, only LORs are obtained, thus they have to find ways to address this issue. In PET systems, they solve this by ring-shape design, while in most of the SPECT systems they are designed to orbit in a certain trace.

However, not every CGECT can fully exploit the coincidence events' information, they might only get LOR, plane-of-respond, or even volume-of-respond instead of POR due to some specific reason, such as using a complex collimation and detection method or trying to get a higher detection efficiency. When a coincidence event no longer corresponds to a point, we need to put the sampling completeness back on the table. Besides, there are also single photons that cannot be coincided with in the CGECT. Each single-photon event can utmost get one LOR, which is just like SPECT. Therefore, if we still want to use this part of information to do reconstruction, it is necessary to conduct in-depth research on the sampling completeness of single photon events to verify whether they can perform accurate 3D reconstruction of imaged objects.

The completeness of sampling for such projected data has been studied for a long time. Tuy and Smith [10, 11] in the 1980s deduced the sampling completeness for cone beam projection data, while Orlov et al. [12] in 1976 proposed the Orlov condition for sampling completeness for parallel beam projection observations. Based on their works, Metzler et al. [13] integrated these two conditions and proposed a Tuy condition similar to Orlov's expression: If an imaging point can be accurately imaged, the trajectory of the intersection of each projection direction and the Orlov sphere from this point intersects with all the great circles of the Orlov sphere, which is shown in Fig. 4. This condition is no longer limited to parallel beam or cone beam, and allows sampling completeness analysis for every point within the FOV. Systems with complicated collimation and detection methods could use the numerical algorithm [13] to assess the sampling completeness.

2.3.3 System Matrix

In the generation of the system matrix, it is necessary to model the probability of one gamma photon from each FOV pixel being detected by each detector

Fig. 4 Orlov sphere diagram

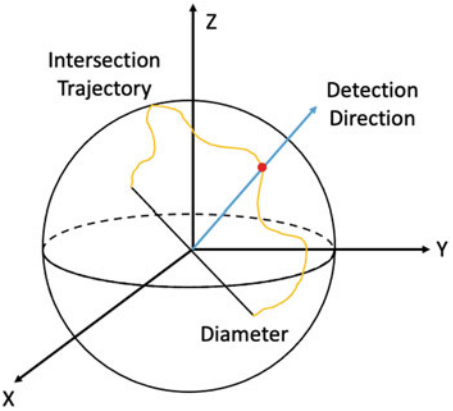

unit, and the accuracy of its modeling plays a decisive role in the quality of the reconstructed image. The system matrix can be calculated by online generation methods such as geometric analysis and Monte Carlo simulation etc. [14–19], or it can be obtained through offline experimental collection [20, 21]. In addition, CGECTs always involve at least one coincident branch and two mono-energy branches, it is necessary to expand the definition of the system matrix in traditional nuclear medicine imaging. In this part, we mainly introduced the geometric analytic numerical simulation, which is widely used to generate the system matrix for CGECT.

For the CGECT, there are single photons and coincidence events, so it is necessary to calculate two sets of different system transmission matrices. The generation of the system matrix is mainly divided into two steps: first, for each FOV pixel, solving the detection probability of the single photon emitted by this pixel on each detector unit, and considered this probability as the single photon system matrix; then, for each FOV pixel, the probability that a coincident event emitted in this pixel is detected on a pair of detector units is equal to the product of the probabilities that the single photon emitted by this FOV pixel is detected by these two detectors separately, and use the nuclide's angular distribution probability for normalized weighting, as the system matrix of the coincident event.

The system matrix c_{ij} of a branch is defined as the probability of a decay event occurring at the i element within the FOV space, and the branch event is detected by the j element in the detection space. For the system matrix of a mono-energy branch, the FOV space refers to the collection of all pixels in the image, the detection space refers to the collection of all detection units of the detector, and the branch event refers to the single photon event. For the system matrix of coincidence branch, the FOV space refers to the same thing, while the detection space refers to the set of all detection units paired in the detector, and the branch event refers to the coincidence event. Based on this definition, c_{ij} can be disassembled in the order of the detection process as follows:

$$c_{ij} = P_{intensity} \cdot P_{energy} \cdot P_{time} \cdot P_{ij,decay} \cdot P_{ij,collimator} \cdot P_{ij,detector} \cdot g_{ij}$$

The three parameters $P_{intensity}$, P_{energy} and P_{time} in parentheses are discussed first. In general, for non-quantitative imaging of a single energy branch, these three parameters are the same and do not need to be considered. However, in the CGECT, these three parameters are different in each branch, so it is necessary to consider their impact.

$P_{intensity}$: The luminous intensity of the branch, i.e., the probability of the branch event occurring in each decay.

P_{energy}: The probability that the energy of the event is in the energy window. In the mono-energy branch it can be expressed as $P_{energy} = 2\Phi\left(2.355 \cdot \frac{EW}{2 \cdot ER}\right) - 1$; In the coincidence branch, the cascaded photons are separated and each one is processed with one energy windows, so it can be expressed as the square of that in mono-energy branch case.

P_{time}: The probability that the time difference of the cascade gamma from the one coincidence event is in the coincidence time window CTW. The mono-energy branch does not have the concept of coincidence, this item is directly set to 1. For the coincidence branch, it can be expressed as $P_{time} = 2\Phi\left(2.355 \cdot \frac{CTW}{2 \cdot CTR}\right) - 1$.

For the three items $P_{ij,\,decay}$, $P_{ij,\,collimator}$ and $P_{ij,\,detector}$ in square brackets, they are essentially the interaction and energy deposition of gamma photons with matter during flight. When photons pass through various substances, some will be absorbed by the object, and the amount of absorption depends on the linear attenuation coefficient μ of the object for this energy gamma photon and the flight distance in the object [3], which is

$$I = I_0 \cdot e^{-\int \mu(x)dx}$$

Where I_0 and I are the light intensity before and after the attenuation, respectively, x is the flight path, and $\mu(x)$ is the linear attenuation coefficient at x.

$P_{ij,\,decay}$: The probability that this branch event is not absorbed by matter other than the detector and collimator during the flight from the i FOV element to the j detection element, which can be expressed as $e^{-\int_{x_i}^{x_j} \mu_{decay}(x)dx}$.

$P_{ij,\,collimator}$: The probability that this branch event passes the collimator during its flight from the i FOV element to the j detection element, which can be expressed as $e^{-\int_{x_i}^{x_j} \mu_{collimator}(x)dx}$.

$P_{ij,\,detector}$: The probability that the branch event is detected by the detector after the flight from the i FOV element to the j detection element, which can be expressed as $1 - e^{-\int_{x_i}^{x_j} \mu_{detector}(x)dx}$.

The last item g_{ij} is the geometric contribution factor between the i FOV element and the j detector element. Different modeling methods define this item differently. For example, in the SPECT line tracing method, it is defined as the length of the line segment of the detection line within the FOV element i. g_{ij} could also contain the angular correlation correction described in II.D.

$P_{ij,\,decay}$, $P_{ij,\,collimator}$, $P_{ij,\,detector}$ and g_{ij} are the main parameters of the general system transmission matrix, and their values will change with the change of the FOV space element i and the detection space element j, and are related to the system geometry design and collimator parameter design.

2.3.4 Reconstruction Algorithms

Direct Back-Projection

The direct back-projection based on coincidence events is widely used in cascade gamma coincidence imaging studies [22–26]. Its biggest advantage is that it does not require complex modeling and continuing iteration, hence, its reconstruction speed is much faster than the MLEM algorithm and thus has the potential for real-time imaging.

In the process of reconstructing the image, the back-projection algorithm starts from the position of the detection event on the detector, and performs back-projection in the FOV space through the collimator. For each coincident event, an intersection coordinate can be obtained. In the entire FOV space, each pixel counts the number of intersections in it, so as to directly obtain the histogram with one pixel as a bin for detecting the coincident event, thereby obtaining the reconstruction image. Since different pixels have different coincident event detection efficiencies, the histogram of detection data needs to be corrected for coincident event detection efficiency, which means it still needs to use the system matrix to calculate the coincidence event detection efficiency of each pixel for correction.

MLEM

In the field of nuclear medical imaging, iterative reconstruction algorithms based on probability theory may be more suitable to suppress the statistical noise in data [3]. In the reconstruction of nuclear medicine images, the number of unknowns required to be solved is large, and it is very hard to solve the problem directly by solving the linear equation system. For this type of problem, Dempster et al. [27] proposed an expectation maximization (EM) algorithm, which uses incomplete data for maximum likelihood estimation. Later, Shepp [28] and Lange [29] introduced the EM algorithm into nuclear medicine reconstruction imaging, and finally proposed the maximum likelihood expectation maximization (MLEM) algorithm commonly used today.

The data in nuclear medical imaging generally satisfy the Poisson distribution [3, 30]. Let the projection data of the FOV voxel i on the detection element j be z_{ij}, the prior probability is

$$g\left(z_{ij}|\lambda_{ij}\right) = e^{-\lambda_{ij}}\frac{{\lambda_{ij}}^{z_{ij}}}{z_{ij}!}$$

Where $\lambda_{ij} = c_{ij} \bullet f_i$, c is the system matrix, f is the image value, the subscript i represents the FOV voxel index, and the subscript j represents the detection element index, ! is the factorial operator. Taking the logarithm of the joint probability of all prior probabilities as the likelihood function, and ignoring the constant $\sum_{i,j} \log(z_{ij}!)$ that does not contain f_i, the likelihood function of MLEM algorithm is

$$L_{MLEM} = \log\left[\prod_{i,j} g\left(z_{ij}|\lambda_{ij}\right)\right] = \sum_{i,j}\left[z_{ij}\log\left(c_{ij}f_i\right) - c_{ij}f_i\right]$$

After obtaining the likelihood function, it is hoped to determine f_i by solving its maximum likelihood solution. However, z_{ij} in the above formula is still a random variable, and the maximum likelihood solution cannot be obtained. Therefore, in MLEM, the expectation of its value under the condition of the current image value f_i is used to replace z_{ij}, and then iteratively solves the solution. Since z_{ij} still satisfies the Poisson distribution, let the total detection count on the detection unit j be p_j, then the expected value of z_{ij} can be expressed as

$$E\left(z_{ij}|f_i\right) = \frac{c_{ij}f_i}{\sum_j c_{ij}f_i} \cdot p_j$$

Use $E(z_{ij}|f_i)$ instead of z_{ij}, let the solution of $\frac{\partial L_{MLEM}}{\partial f_i} = 0$ be the image value $f_i^{(n)}$ after the n iteration, the final iterative formula of MLEM can be obtained as follows

$$f_i^{(n)} = \frac{f_i^{(n)}}{\sum_j c_{ij}}\sum_j c_{ij}\frac{p_j}{\sum_j c_{ij}f_i^{(n-1)}}$$

For the formula, it can guarantee the non-negativity of f_i in the iteration, and its convergence has been proved [27–29], i.e., after each iterative update, the value of the likelihood function L_{MLEM} will not become smaller, and the final image will converge to the maximum value of L_{MLEM}.

The MLEM algorithm is generally a very good algorithm. Compared with analytical reconstruction algorithms such as FBP, its advantage is that it can use the system matrix for more accurate modeling, and it is also an asymptotic unbiased estimation algorithm with small variance. But in addition to the disadvantage of slow convergence speed, it also has the problem of being more sensitive to data, and it is easy to continuously amplify the noise of the data during the iteration. Therefore, in actual use, it is generally necessary to stop the iteration in advance [31–33] or post-smoothing [34, 35] to suppress noise.

What is worth noticing is that, since CGECT systems can detect coincidence events and single photon in the same time, they could use MLEM to do the reconstruction using both of these events based on their corresponding system matrix. That is to says, CGECT systems can use coincidence events are used as the input of MLEM, and reonconstruct the image based the system matrix of the coincident event. Meanwhile, it is also possible to use single photon events and the system matrix of single photon event in MLEM to obtain recontruction images.

3 CGECT Systems in the Literature

Over the past 50 years, there have been many research groups [22–26, 36–51] worked on the imaging of cascade radiation. In the early years, some research groups hoped to add another detector to the parallel hole SPECT, and add coincidence electronics to develop a CGECT, which once had the possibility of replacing PET. However, because its performance is slightly worse than that of PET, it has not become the mainstream only as a low-cost alternative to PET. Nowadays, with the rapid development of high performance detector and new system design, CGECT seems to become more promising.

In the following section, we introduce CGECT system designs with different collimation and detection methods in the literatures.

3.1 CGECT Systems with Collimators

1. Parallel-hole collimator & SPECT head

   Pahlka et al. [23] reported the performance of an Indium-111 based Monte Carlo simulation cascaded gamma-conformance imaging system. Shimazoe et al. [22] also completed a GAGG crystal and silicon photomultiplier tube based cascade gamma coincidence imaging experimental setup. Both of these works were based on SPECT detectors and were able to get POR using parallel-hole collimators. This collimation method can guarantee the spatial resolution of the system, but greatly limits the coincidence event detection efficiency. For example, the spatial resolution of the system reported by Pahlka et al. is better than 7.2 mm, but its coincident event detection efficiency is only 6×10^{-8} [23].
2. Pinhole-slit collimator & SPECT head

   Recently, Xiao et al. [26] built an experimental setup using two commercial SPECT detectors and a combination of pinhole and slit plate-shaped collimators and detected coincidence events from Lu-177. They were able to get POR inside a limited FOV with good performance, 3.8×10^{-6} coincidence event detection efficiency and 7.0 mm spatial resolution was achieved. However, they still needed a long detection time to get a low-noise image.

3.2 CGECT Systems Without Collimators

1. Scanner & Coincidence detector

   In fact, related research on cascade coincidence imaging has been carried out for a long time, and it can be traced back to the scanner plus slit collimator coincidence detector system using Se-75 proposed in 1970 [36]. In this system, the FOV is a 2D plane. Each pixel of the plane is scanned by the scanner for a certain time. Meanwhile, the coincidence detectors, which are NaI detectors, use slit collimators to monitor the whole plane. When both the scanner and the detector get a signal inside a timing window, it will be considered that a coincidence event emitted from this pixel was detected, and then used to create the image. However, such a pixel-by-pixel scanning machine is obviously time consuming, thus lacks practicality.
2. TOF-PET

   Besides, Chiang et al. [25] conducted a Monte Carlo simulation study and introduced the TOF DuPECT to collect coincidence events from Se-75. Instead of collimation, information from two cascade photons is used to derive the cascade emission location. They reported a very promising coincidence detection efficiency of 2×10^{-3} with a poor spatial resolution of around 40 mm limited by the current's TOF-PET 200 ps CTR. Even considering the ideal CTR equal to 0, the lower limit of its spatial resolution can only reach 20 mm. It also suffers from the collimation methods, which could only obtain a Plane-of-Response.
3. Multiple Compton cameras

   Another group evaluated the feasibility of Compton-camera-based cascade gamma coincidence imaging using In-111 and GAGG crystals coupled with SiPM [24, 39]. The system achieved a higher coincidence detection efficiency of 3.56×10^{-6}, but at a very poor spatial resolution of 28 mm. Besides, Compton cameras can only locate the decay position in the intersecting line of the two conical surfaces, or even the intersecting volume of the two thick conical surfaces due to the bad angular resolution of the Compton camera, which means losing the ability to direct positioning.

3.3 Performance Summary

In Table 2, the collimation and detection methods and related performances of some existing cascaded gamma photon coincidence imaging systems are summarized. Based on the above analysis, it can be seen that the current cascaded gamma photon coincidence imaging system is still far from practical clinical application. It is hoped to propose a cascaded gamma photon coincidence imaging system capable of real-time imaging, which can keep the spatial resolution less than 10 mm, while the coincidence event detection efficiency exceeds the existing research level, at least reaching 10^{-6} order of magnitude in the future.

Table 2 Performance comparison of CGECTs for different detection methods

Collimaition and Detection Method	Cascade Nuclides	Coincidence Event Detection Efficiency	Spatial Resolution	Data Respond
Compton cameras [24, 39]	In-111	3.56×10^{-6}	28 mm	Line/Volume
TOF-PET [25]	Se-75	2.0×10^{-3}	20 mm	Plane
Parallel-hole SPECT [23]	In-111	6×10^{-8}	7.2 mm	Point
Pinhole-slit SPECT [26]	Lu-177	3.8×10^{-6}	7 mm	Point

4 Discussion

Although each coincidence event is highly effective toward image reconstruction, the low detection efficiency remains the key deficiency of CGECT. This results in a long detection time for the CGECT to get a good-quality, low-noise image. There are several approaches that can help with this issue. We have already discussed the factors that govern the system performance of CGECT in Sect. 2, we will discuss how these factors will affect the image quality one by one and their potential development directions.

4.1 More Suitable Nuclides

We have already named the theoretically ideal properties of cascade radiation nuclides in II.A., all of them are helpful for improving the image quality. Great luminous intensity can increase the NECR under the same source activity. Short intermediate half-life means that there is more true coincidence event under the same CTW, which will also increase the NECR. The full energy peak photons of the cascade event should be suitable for detection and easily discriminated for other photons, thus the random and scatter coincidence events could be suppressed and NECR could be increased. The distribution of the angular difference between each gamma in the coincidence event is expected to be as close to 90 degrees as possible, which can contain more precise position information. However, CGECT is a new type of imaging modality, its manufacturing technology of radiopharmaceuticals is still under exploration. An ideal CEGCT cascade radiation nuclide, which is cheap and easy to be labeled is hoped to be found someday.

4.2 New Detectors

The rapid development of detection technology will also further promote the performance improvement of the CGECT. The timing and energy performance of these detectors will continue to improve, which means that we could easily obtain more true coincidence events and suppress random and scatter events.

4.3 New System Design

How to design and develop a collimation-detection method that is more conducive to the CGECT is still under research. We have seen two kinds of CEGCT in Sects. 3.1 and 3.2, corresponding to CGECT system with or without collimators. The former kind has better spatial resolution but poor sensitivity, while the latter one is on the contrary. An ideal collimation-detection method is to ensure high detection efficiency and high spatial resolution, and at the same time able to obtain POR directly through each coincidence event and thus have real-time imaging capabilities. Based on a FOV of a certain size, through the design of the geometric parameters of the collimator, there is only one possible position within the FOV, which is the POR, for each coincident event. Recently, new research called self-collimation was proposed by Tianyu et al. [52], they used multi-Layer interspaced mosaic detectors to collimate the gamma photon by the detector itself, thus can greatly improve detection efficiency. This kind of new research could also be introduced to the CGECT to lift up the detection efficiency.

Besides, increasing the detection solid angle is an obvious approach. Every coincidence event needs to detect two single photons at the same time, thus its detection efficiency is proportional to the square of the single photon detection efficiency. Increasing the detection solid angle can lead to a linear growth of single photon detection efficiency, which leads to a squared growth of coincidence event detection efficiency. Besides, lots of the CGECTs are based on two perpendicular-placed detectors [22, 23, 26], which is asymmetrical to the whole FOV. This will result in uneven detection efficiency of pixels, the farther the pixels are to the two detectors, the lower their detection efficiency and the higher statistical noise, and causes problems to image reconstruction. By increasing the detection solid angle, it is also possible to design a more symmetrical detection method, thereby improving image quality.

4.4 Reconstruction with Both Singles and Coincidence Events

Another direction to explore is to find a joint reconstruction method using both coincidence events and single photons. If only the coincident events are used for reconstruction, the large number of single-photon events with low noise will be discarded directly, and the information contained in this part will be wasted. Therefore, we hope to reduce statistical noise and improve image quality by using the information on single-photon events in the process of coincident event reconstruction. It is worth noting that, unlike coincidence events that can obtain POR, single photons can only obtain LOR, so it may need to further discuss the sampling completeness, which is also a major challenge for joint reconstruction methods. There have been many studies on the MLEM algorithm using multiple sets of mixed events. Zhou et al. [53] conducted a correlation derivation through the Fisher information matrix of the data, and demonstrated that the image quality obtained by mixing two sets of Poisson distribution data is better than the case of using any set of data alone, and Jiang et al. [54, 55] also obtained the same result in the experiment. The above work is mainly concentrated on the PET study. In cascade gamma coincidence imaging, Xiao et al. [45] have also tried to introduce joint reconstruction methods using both single photons and coincidence events.

4.5 Other Possible Points

In cascaded gamma coincidence imaging, the information contained in the coincidence events is essentially the same as the coincidence events in TOF-PET, and both have the ability to locate the position of the decay nuclide in decay in a smaller range of positions, so the above advantages of TOF-PET imaging are also true for cascaded gamma coincidence imaging. Even further, the existing PET technology can only obtain a spatial resolution of 30–120 mm by relying solely on TOF information, while cascaded gamma-coherence imaging can use a certain collimation technology to directly achieve a real-time spatial resolution of less than 10 mm.

In addition, the way in which cascaded gamma photon coincidence imaging can directly locate the imaging also makes it free from some limitations of traditional nuclear medicine imaging in image reconstruction. In PET and SPECT, since only LOR can be obtained, it is generally necessary to accumulate a large amount of LOR, and then use an iterative image reconstruction algorithm to reconstruct the image, which will bring some issues. The first issue is that a large amount of LOR needs to be accumulated, which is difficult to achieve for some imaging applications with high real-time requirements and rapid changes. This requires sufficient detection time. For non-annular SPECT, it is even necessary to quickly switch between detection angles and complete detection for sufficient time at each detection angle, not to mention that the high-speed movement of the detector will give opportunities. The design accuracy and practicability of the rack bring challenges, and it is also a big challenge to detection efficiency. Secondly, in terms of the reconstruction algorithm of PET and SPECT, since the noise will continue to amplify in the later stage of the iteration, it is necessary to stop the iteration as soon as possible to prevent the noise from being too large, but the image may not converge to the convergence point at this time, and the iterative reconstruction algorithm will give priority to reconstruction of low frequency part, the reconstruction of important high frequency parts may not be perfect. For cascaded gamma photon coincidence imaging, back-projection can be directly selected for real-time imaging, thereby avoiding the defects of traditional nuclear medicine image reconstruction.

5 Summary

The CGECT system is an emerging nuclear medicine imaging technique still developing. It can exploit the coincidence photon events emitted by the cascading radiation phenomenon that exists widely in nuclear medicine, to obtain more accurate nuclide localization information. This could benefit the reconstruction of nuclide distribution images, and have potential advantages such as real-time imaging with prominent clinical value. At present, the development of the CGECT system is still in the experimental stage. Several researchers are still trying to design the CGECT system with high spatial resolution and high coincidence event detection efficiency simultaneously, to obtain high signal-to-noise ratio and high-resolution images so that the CGECT system can have better application potential in clinical medical imaging in the future.

References

1. Butz, T. (1996). Nuclear quadrupole interactions studied by time differential perturbed angular correlations of γ-rays. *Zeitschrift für Naturforschung A, 51*(5–6), 396–410.
2. Hemmingsen, L., Sas, K. N., & Danielsen, E. (2004). Biological applications of perturbed angular correlations of γ-ray spectroscopy. *Chemical Reviews, 104*(9), 4027–4062.
3. Cherry, S. R., Sorenson, J. A., & Phelps, M. E. (2012). *Physics in nuclear medicine e-Book*. Elsevier Health Sciences.
4. Hamilton, D. R. (1940). On directional correlation of successive quanta. *Physical Review, 58*(2), 122.
5. Brady, E., & Deutsch, M. (1950). Angular correlation of successive gamma-rays. *Physical Review, 78*(5), 558.
6. Biedenharn, L. C., & Rose, M. (1953). Theory of angular correlation of nuclear radiations. *Reviews of Modern Physics, 25*(3), 729.
7. Rose, M. (1953). Angular correlation of nuclear radiations. *Science, 118*(3074), 635–642.
8. Strother, S., Casey, M., & Hoffman, E. (1990). Measuring PET scanner sensitivity: Relating countrates to image signal-to-noise ratios using noise equivalents counts. *IEEE Transactions on Nuclear Science, 37*(2), 783–788.
9. Watson, C. C. (2004). Count rate dependence of local signal-to-noise ratio in positron emission tomography. *IEEE Transactions on Nuclear Science, 51*(5), 2670–2680.
10. Tuy, H. K. (1983). An inversion formula for cone-beam reconstruction. *SIAM Journal on Applied Mathematics, 43*(3), 546–552.
11. Smith, B. D. (1985). Image reconstruction from cone-beam projections: Necessary and sufficient conditions and reconstruction methods. *IEEE Transactions on Medical Imaging, 4*(1), 14–25.

12. Orlov, S. (1976). Theory of three dimensional reconstruction. I. Conditions for a complete set of projections. *Soviet Physics Crystallography, 20*, 312–314.
13. Metzler, S., Bowsher, J., & Jaszczak, R. (2002). Geometrical similarities of the Orlov and Tuy sampling criteria and a numerical algorithm for assessing sampling completeness. In *2002 IEEE nuclear science symposium conference record*. IEEE.
14. Floyd, C. E., Jaszczak, R. J., & Coleman, R. E. (1985). Inverse Monte Carlo: A unified reconstruction algorithm for SPECT. *IEEE Transactions on Nuclear Science, 32*(1), 779–785.
15. Veklerov, E., Llacer, J., & Hoffman, E. (1988). MLE reconstruction of a brain phantom using a Monte Carlo transition matrix and a statistical stopping rule. *IEEE Transactions on Nuclear Science, 35*(1), 603–607.
16. Qi, J., et al. (1998). Fully 3D Bayesian image reconstruction for the ECAT EXACT HR+. *IEEE Transactions on Nuclear Science, 45*(3), 1096–1103.
17. Parra, L., & Barrett, H. H. (1998). List-mode likelihood: EM algorithm and image quality estimation demonstrated on 2-D PET. *IEEE Transactions on Medical Imaging, 17*(2), 228–235.
18. Laurette, I., et al. (2000). A three-dimensional ray-driven attenuation, scatter and geometric response correction technique for SPECT in inhomogeneous media. *Physics in Medicine & Biology, 45*(11), 3459.
19. Beekman, F. J., de Jong, H. W., & van Geloven, S. (2002). Efficient fully 3-D iterative SPECT reconstruction with Monte Carlo-based scatter compensation. *IEEE Transactions on Medical Imaging, 21*(8), 867–877.
20. Formiconi, A., Pupi, A., & Passeri, A. (1989). Compensation of spatial system response in SPECT with conjugate gradient reconstruction technique. *Physics in Medicine & Biology, 34*(1), 69.
21. Panin, V. Y., et al. (2006). Fully 3-D PET reconstruction with system matrix derived from point source measurements. *IEEE Transactions on Medical Imaging, 25*(7), 907–921.
22. Shimazoe, K., et al. (2017). Double photon emission coincidence imaging using GAGG-SiPM pixel detectors. *Journal of Instrumentation, 12*(12), C12055.
23. Pahlka, R. B., Kappadath, S. C., & Mawlawi, O. R. (2018). A Monte Carlo simulation of coincidence detection and imaging of gamma-ray cascades with a scintillation camera. *Biomedical Physics & Engineering Express, 4*(5), 055012.
24. Uenomachi, M., et al. (2020). Double photon emission coincidence imaging with GAGG-SiPM Compton camera. *Nuclear Instruments and Methods in Physics Research Section A: Accelerators, Spectrometers, Detectors and Associated Equipment, 954*, 161682.
25. Chiang, C.-C., et al. (2020). Time of flight dual photon emission computed tomography. *Scientific Reports, 10*(1), 1–13.
26. Liu, X., et al. (2021). A 3-dimensional stationary cascade gamma-ray coincidence imager. *Physics in Medicine & Biology, 66*(22), 225001.
27. Dempster, A. P., Laird, N. M., & Rubin, D. B. (1977). Maximum likelihood from incomplete data via the EM algorithm. *Journal of the Royal Statistical Society: Series B (Methodological), 39*(1), 1–22.
28. Shepp, L. A., & Vardi, Y. (1982). Maximum likelihood reconstruction for emission tomography. *IEEE Transactions on Medical Imaging, 1*(2), 113–122.
29. Lange, K., & Carson, R. (1984). EM reconstruction algorithms for emission and transmission tomography. *Journal of Computer Assisted Tomography, 8*(2), 306–316.
30. Rockmore, A. J., & Macovski, A. (1976). A maximum likelihood approach to emission image reconstruction from projections. *IEEE Transactions on Nuclear Science, 23*(4), 1428–1432.
31. Veklerov, E., & Llacer, J. (1987). Stopping rule for the MLE algorithm based on statistical hypothesis testing. *IEEE Transactions on Medical Imaging, 6*(4), 313–319.
32. Coakley, K. J. (1991). A cross-validation procedure for stopping the EM algorithm and deconvolution of neutron depth profiling spectra. *IEEE Transactions on Nuclear Science, 38*(1), 9–15.
33. Johnson, V. E. (1994). A note on stopping rules in EM-ML reconstructions of ECT images. *IEEE Transactions on Medical Imaging, 13*(3), 569–571.

34. Llacer, J., et al. (1993). Statistical analysis of maximum likelihood estimator images of human brain FDG PET studies. *IEEE Transactions on Medical Imaging, 12*(2), 215–231.
35. Silverman, B., et al. (1990). A smoothed EM approach to indirect estimation problems, with particular reference to stereology and emission tomography. *Journal of the Royal Statistical Society: Series B (Methodological), 52*(2), 271–303.
36. Schmitz-Feuerhake, I. (1970). Studies on three-dimensional scintigraphy with gamma-gamma-coincidences. *Physics in Medicine & Biology, 15*(4), 649.
37. Von Boetticher, H., et al. (1982). Advances in γ-γ-coincidence scintigraphy with the scintillation camera. *Physics in Medicine & Biology, 27*(12), 1495.
38. Liang, Z., & Jaszczak, R. (1990). Comparisons of multiple photon coincidence imaging techniques. *IEEE Transactions on Nuclear Science, 37*(3), 1282–1292.
39. Yoshihara, Y., et al. (2017). Evaluation of double photon coincidence Compton imaging method with GEANT4 simulation. *Nuclear Instruments and Methods in Physics Research Section A: Accelerators, Spectrometers, Detectors and Associated Equipment, 873*, 51–55.
40. Akamatsu, G., et al. (2019). Modified NEMA NU-2 performance evaluation methods for a brain-dedicated PET system with a hemispherical detector arrangement. *Biomedical Physics & Engineering Express, 6*(1), 015012.
41. Shimazoe, K., Uenomachi, M., & Takahashi, H. (2022). Imaging and sensing of pH and chemical state with nuclear-spin-correlated cascade gamma rays via radioactive tracer. *Communications on Physics, 5*(1), 1–8.
42. Accorsi, R. (2001). *Design of a near-field coded aperture cameras for high-resolution medical and industrial gamma-ray imaging*. Massachusetts Institute of Technology.
43. Uenomachi, M., Shimazoe, K., & Takahashi, H. (2022). Double photon coincidence crosstalk reduction method for multi-nuclide Compton imaging. *Journal of Instrumentation, 17*(04), P04001.
44. Chung, V., et al. (1980). Multiple photon coincidence tomography. In *Seminars in nuclear medicine*. Elsevier.
45. Liu, X., et al. (2020). An MLEM reconstruction method with mixed events based on a cascade gamma emission imager system. In *2020 IEEE nuclear science symposium and medical imaging conference (NSS/MIC)*. IEEE.
46. Powell, M. (1989). Multiphoton, time-of-flight three-dimensional radionuclide imaging. *Medical Physics, 16*(5), 809–812.
47. Lin, C.-S., et al. (2016). Application of the intraoperative dual photon emission computed tomography system in sentinel lymph node detection: A simulation study. *IEEE Transactions on Nuclear Science, 63*(1), 108–116.
48. Nellemann, P., et al. (1995). Performance characteristics of a dual head SPECT scanner with PET capability. In *1995 IEEE nuclear science symposium and medical imaging conference record*. IEEE.
49. Kunze, W.-D., Baehre, M., & Richter, E. (2000). PET with a dual-head coincidence camera: Spatial resolution, scatter fraction, and sensitivity. *Journal of Nuclear Medicine, 41*(6), 1067–1074.
50. Schelper, L. F., et al. (2006). Performance comparison of two dual-head coincidence cameras of the first and latest generation. *Medical Physics, 33*(2), 329–336.
51. Luo, W., & Cao, Z. (2003). Monte Carlo simulation for coincidence detection of In-111 cascaded photons with innovative data processing. In *2003 IEEE nuclear science symposium. conference record (IEEE Cat. No. 03CH37515)*. IEEE.
52. Ma, T., et al. (2021). Self-collimating SPECT with multi-layer interspaced mosaic detectors. *IEEE Transactions on Medical Imaging, 40*(8), 2152–2169.
53. Zhou, J., & Qi, J. (2010). Adaptive imaging for lesion detection using a zoom-in PET system. *IEEE Transactions on Medical Imaging, 30*(1), 119–130.
54. Jiang, J., et al. (2019). Augmented whole-body scanning via magnifying PET. *IEEE Transactions on Medical Imaging, 39*(11), 3268–3277.
55. Jiang, J., et al. (2019). A second-generation virtual-pinhole PET device for enhancing contrast recovery and improving lesion detectability of a whole-body PET/CT scanner. *Medical Physics, 46*(9), 4165–4176.

Compton Imaging Systems Based on Semiconductor Detectors

Mostafa Niknami and Mahdi Valipour

1 Introduction

Nowadays, nuclear imaging systems are widely used for detection, diagnosis, therapy, and other applications. There are two main procedures in nuclear imaging that can be distinguished based on the type of radioactive source used. Single-photon emission computed tomography (SPECT) and the Compton imaging system are two well-known examples based on single-photon imaging of radioactive nuclei that decays by emitting a gamma-ray [1, 2]. Another method known as positron emission tomography (PET) uses positron-emitting radioisotopes as radioactive material [3].

In recent years in nuclear imaging systems, using electronic collimators instead of mechanical collimators has received more attention due to the limitations of mechanical collimators. A mechanical collimator is used in SPECT to determine the direction of incoming gamma rays. PET detects the coincidence of two 511 keV gamma rays emitted in opposing directions when a positron annihilates with an electron using positron-emitting nuclides [4]. On the other hand, the Compton camera is an imaging system based on an electronic collimator [5]. The Compton imaging system can perform multi-nuclide imaging without requiring a mechanical collimator. Several researchers have reported in vivo multi-tracer imaging [6–8]. A wide range of detectors and geometries were recommended for Compton cameras in various applications for high energy resolution, angular resolution, spatial resolution, efficiency, and fast reading systems.

The Compton imaging method was first used to detect gamma rays with scintillation detectors in the mid-twentieth century [9], developed in 1961 and 1964 as the Compton telescope and Compton spectrometer [10, 11]. The Compton

---

M. Niknami (✉) · M. Valipour
Department of Energy Engineering, Sharif University of Technology, Tehran, Iran
e-mail: mostafa.niknami13@sharif.edu; Mehdi.valipour@energy.sharif.ir

© The Author(s), under exclusive license to Springer Nature Switzerland AG 2023
J. Du, K. (K.) Iniewski (eds.), *Gamma Ray Imaging*,
https://doi.org/10.1007/978-3-031-30666-2_4

telescope was used in astronomy between 1973 and 1976 to detect incoming rays [12, 13]. COMPTEL became the first Compton telescope to orbit the Earth [14–18]. COMPTEL, which is very successful, still had its limitations that led to the design of other models of Compton telescopes [19]. The NCT balloon-borne Compton telescope (COSI) is different from other Compton telescopes [20]. Compton cameras, due to their application for detection, are being developed in astrophysics [21].

However, the Compton imaging system's application in other fields came to be recognized; Compton cameras were first suggested by Everett and his colleagues in nuclear medical imaging [22]. The initial prototype was built in 1983 by Singh et al. with semiconductor and NaI(TL) detectors [23]. Later research allowed for the imaging of three-dimensional cylindrical test phantoms [24]. Due to their increased efficiency, silicon detectors (a stack of silicon pad detectors or silicon drift detectors) became more popular in Compton cameras in the coming years [25–27]. The Compton cameras were also used for multiple molecular simultaneous imaging in a living mouse [28]. Compton cameras were also suggested to treat radioisotope with alpha particles [29, 30]. A system combining a pinhole and a Compton camera was designed to detect both X-rays and gamma-rays in the same application region [31]. In other studies, the Compton and PET cameras were used for imaging [32, 33]. Comparing Compton camera with PET and SPECT in terms of economic effectiveness and appropriate performance in medical applications proved that Compton camera has high capability in these situations in most studied investigations [34–36]. Several research groups have also investigated the application of Compton cameras in ion beam therapy, using both scintillation and semiconductor detectors [37–39].

Another usage of Compton cameras is for safety and security from any disasters or contaminations caused by human or natural interactions. For this purpose, portable Compton cameras are often used to measure the dose in these areas [40, 41]. Hmissi et al. tested a portable Compton camera using CeBr3 scintillation crystals and digital photon counter detectors with time-of-flight (TOF) capabilities in the Lab, with acceptable results for energy and angular resolutions [42]. Gamma-ray detection was performed to recognize and characterize such material assemblies [43]. In Fukushima, a Compton camera was built and tested to lessen noise on gamma-ray images by adding a Pb layer to the rear panel [44].

A similar approach was also discussed using a Compton camera (1.5 kg) installed on a drone system with a diagonal base. The prototype was tested in a 7000-square-meter region of Fukushima, divided into three radiation zones [45]. The Compton camera for industrial use was considered with a ring-shaped NaI(TL) absorber detector, which avoided direct illumination by the source but reduced the solid angle and thus the efficiency [46]. Using a Compton camera system on an unmaned aerial vehicle (UAV) was also developed to characterize the distribution of radioactive materials in highly contaminated areas [47].

According to the applications discussed above, we will mention the significant and practical parameters of the Compton camera in the following sections.

2 Compton Imaging System

Compton imaging is an imaging technique that Compton scattering uses to produce images from a gamma-ray source. Compton imaging systems are also known as Compton cameras. The advantages of Compton imaging over other conventional imaging techniques are that it covers a wide range of energies. This system also makes it possible to construct a 3D image of a fixed object without moving the detector. Compton imaging well eliminates background radiation during scattering processes through energy separation. In the following section, the principles of the Compton imaging system will be explained, and then the effective parameters of these systems will be stated.

2.1 Principles of Compton Camera

The basic design in Compton imaging systems consists of two detectors that are sensitive to the position and energy of the scattered gamma rays, see Fig. 1. The Compton camera principles are as follows: the source emitted photons will scatter from the scatterer detector (Compton scattering); then, the scattered photons will be absorbed in the absorber detector. These two detectors work in coincidence mode to detect photons electronically and without restriction in their entering path. It should be designed to optimize the Compton scattering probability in the prompt gamma energy range while reducing the so-called Doppler broadening effect due to electron binding and motion [48].

The absorber detector finally intends to capture the Compton scattered photons by the photoelectric effect. The Compton scattering angle is the opening angle of the cone, the line joining the two scattered positions is the cone's axis, and the interacted position in the first scatterer is the cone's apex. The intersection of many of these cones indicates the source location [23]. By back-projecting all valid events into an image space through cone surfaces, we can estimate the distribution of gamma-ray sources. The Compton scattering angle θ could be calculated using Eq. (1):

$$\cos(\theta) = 1 - m_0c^2\left(\frac{1}{E_1} - \frac{1}{E_0}\right) \tag{1}$$

Where, E_0 is the energy of the incident gamma-ray, E_1 is the energy of the scattered gamma-ray immediately after the interaction and m_0c^2 is the rest mass energy of the electron.

One of the most important things for a Compton camera is reconstructing the image and getting the exact position of the source. In recent years, different methods and algorithms for image reconstruction have been proposed for Compton cameras. One of the methods used is analytical image reconstruction [49]. The analytical technique aims to find an analytical solution or use operators to help obtain one.

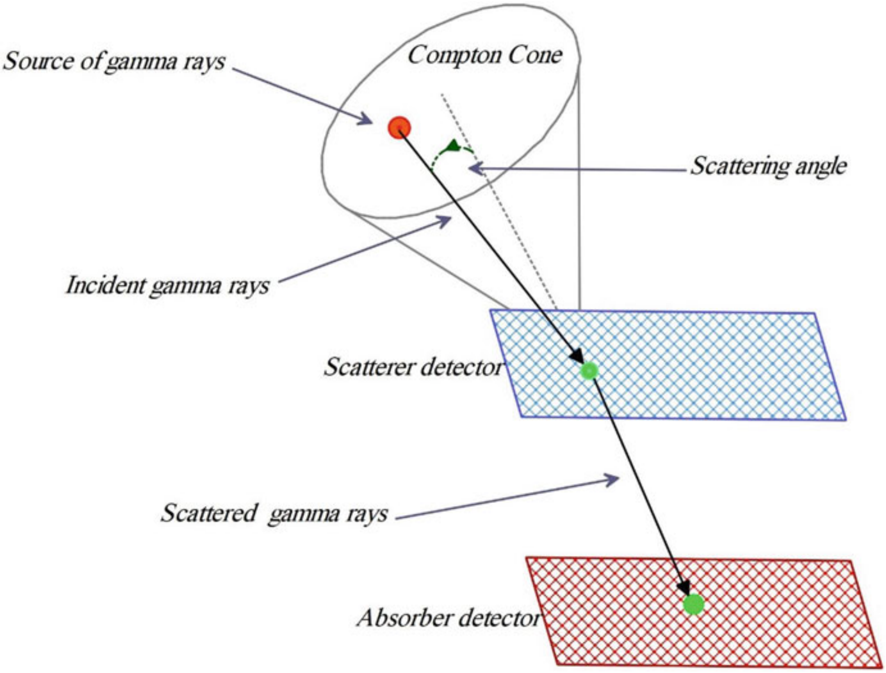

Fig. 1 Basic design in Compton camera

Most of the other methods are based on iterative algorithms for image reconstruction [50]. Deep learning is also being developed to find a way to reconstruct the image of Compton cameras [51].

Four of the most critical parameters in Compton cameras include efficiency, energy resolution, spatial resolution, and angular resolution [52]. In the last four decades of investigations on Compton cameras, researchers used different geometrical designs, different materials for the scatterer and absorber detectors, detectors' dimensions, and the way to reach two-dimensional or three-dimensional output images.

In the next section of this chapter, these parameters will be discussed.

2.2 Effective Parameters on the Performance of Compton Camera

The performance of any medical imaging system is defined by its spatial resolution and the detection sensitivity for a specific particle which for Compton cameras are photons. Because the precision of identifying the photon scatter angle requires tracing the emitted photon's original direction, the conic surface characteristics are defined as a result. The critical factors in defining the expected Compton camera performance are the angular resolution, energy resolution, spatial resolution, and efficiency [53].

The angular resolution defines as the degree of uncertainty in detecting the incident direction of incoming photons [23]. The energy resolution of the scatterer detector, spatial resolution, and geometry of both detectors affect the angular resolution in the Compton camera system [54]. If all of these uncertainties are considered, it could be written as Eq. (2):

$$\tan^2(\Delta\theta_{overall}) = \tan^2(\Delta\theta_1) + \tan^2(\Delta\theta_2) + \tan^2(\Delta\theta_3) + \tan^2(\Delta\theta_4) \tag{2}$$

where $\Delta\theta_1$ is related to energy resolution in scatterer detector, $\Delta\theta_2$ and $\Delta\theta_3$ related to geometry and $\Delta\theta_4$ is related to spatial resolution.

A pulse height distribution characterizes the detector response to a radiation source called the detector response function. The detector's energy resolution is defined as the FWHM of the photopeak divided by the peak centroid [55]. If the energy resolution obtained from the scatterer detector is weak, energy uncertainty will increase, affecting the angular resolution and thus the imaging reconstruction. Equation (1) can be written as Eq. (3) based on the scattered electron energy (E_{re}) for calculation energy resolution uncertainty:

$$\cos\theta = 1 - \left(\frac{E_{re}}{\frac{E_0}{m_0c^2}(E_0 - E_{re})}\right) \tag{3}$$

Moreover, for calculating energy uncertainty, Eq. (3) can be written as Eq. (4):

$$(\Delta\theta_1)^2 = \left(\frac{d\theta}{dE_{re}}\right)^2 (\Delta E_{re})^2 + \left(\frac{d\theta}{dE_0}\right)^2 (\Delta E_0)^2 \tag{4}$$

as the energy of incoming gamma rays is known in nuclear medicine applications, the second part in Eq. (4) is equal to zero; If the differential value $\frac{d\theta}{dE_{re}}$ is taken from Eq. (3), according to Eq. (5):

$$\left(\frac{d\theta}{dE_{re}}\right) = \frac{\left(1 + \left(\frac{E_0}{m_0c^2}\right)(1 - \cos\theta)\right)^2}{E_0\left(\frac{E_0}{m_0c^2}\right)\sin\theta} \tag{5}$$

If set $\alpha = \left(\frac{E_0}{m_0c^2}\right)$ and place Eq. (5) in Eq. (4), finally it can be written as Eq. (6):

$$\Delta\theta_1 = \left(\frac{(1 + \alpha(1 - \cos\theta))^2}{E_0\alpha\sin\theta}\right)\Delta E_{re} \tag{6}$$

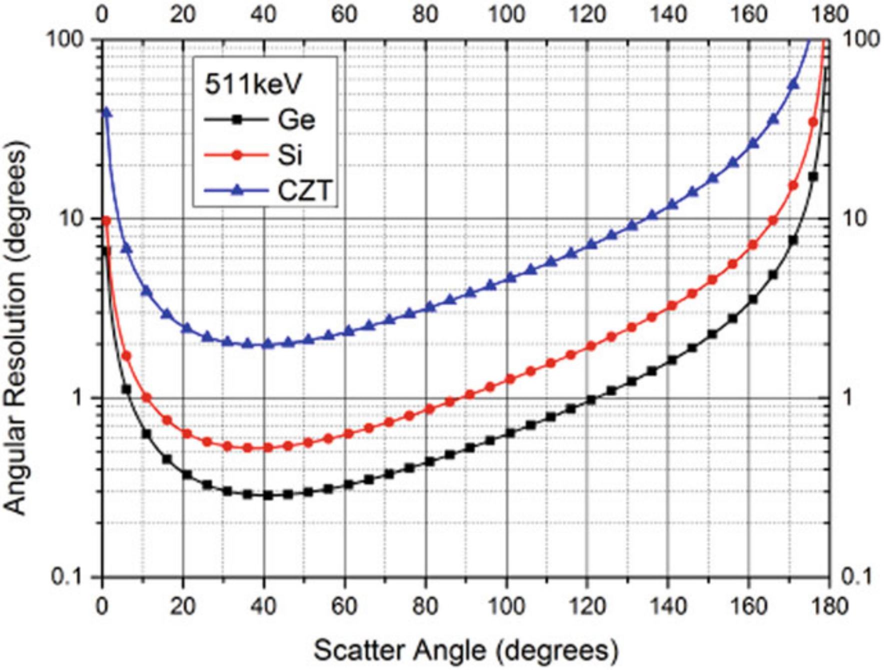

Fig. 2 Angular resolution for Ge, Si, CZT semiconductor materials where the effects of energy resolution shown for a gamma-ray source of 511 keV

ΔE_{re} is the energy measurement uncertainty representing the inherent statistical fluctuations in the number of charge carriers created by each interaction and the electronic noise, defined as Eq. (7):

$$\Delta {E_{re}}^2 = 2.35^2 F w E_{re} + (ELN)^2 \tag{7}$$

In Eq. (7), *F* is the Fano factor, *w* is the ionization energy, and *ELN* is the electronic noise.

The angular uncertainty due to energy contribution is inversely proportional to the gamma-ray energy, as shown by Eq. (6); the higher the energy, the better the angular resolution, making the Compton camera work better at medium to high energies. In addition, the angular resolution improves with the energy resolution of the scatterer detector. In Fig. 2, the semiconductor materials Ge, Si, and CZT for a gamma-ray source of 511 keV were chosen to show energy resolution effects since they are used in most Compton cameras. The energy resolutions of the different materials used were estimated from mathematical models found in the literature [27, 54, 56].

The other parameter that affects the Compton camera angular resolution is Doppler broadening. The scattering angle distribution, known as the Klein-Nishina equation, is based on photons colliding with free and stationary electrons. However, in reality, gamma-ray interacts with moving electrons bound to atoms with momentum around them. Therefore, when the momentum and energy depend on the target electrons become essential (i.e., at low deposited energy or higher atomic numbers), the Klein-Nishina equation does not satisfy scattered electron energy distribution. Thus, instead of a unique value for a certain scattering angle, seen an energy distribution for the scattering photons. In other words, there is a distribution of scattering angles for specific stored energy that distributes around the central angle θ; which means not only a unique value for scattering angle can not be attributed by measuring the stored energy, but also should consider almost a Lorentz distribution around the central angle θ. The higher the photon's energy or, the lower the atomic number, the lower value for FWHM of angular uncertainty would cause. Thus, the Doppler broadening will increase for more large angles.

The degree of the Doppler broadening in a target atom can be calculated from the probability for Compton scattering from an electron in the n$^{\text{th}}$ sub-shell into scattering energy and angle E_A and θ, respectively. The double-differential cross section for Compton scattering that also includes energy dependency and electron momentum is shown as Eq. (8) [57]:

$$\left(\frac{d^2\sigma}{d\Omega dE_A}\right)_n = \frac{r_0^2 m_0}{2E_0}\left(\frac{E_c}{E_0} + \frac{E_0}{E_c} - \sin^2\theta\right)\frac{E_A}{\sqrt{E_0^2 + E_A^2 - 2E_0E_A\cos\theta}}J_n\left(P_z\right) \tag{8}$$

where σ is the Compton cross section, E_c is the energy given by the Compton equation, m_0 is the electron mass, r_0 is the classical electron radius, Ω is spatial angle, and $J_n(P_z)$ is the Compton profile for the n$^{\text{th}}$ sub-shell of the target atom.

The intensity of scattered photons at any scatter energy E_A is proportional to the value of Compton profile at the corresponding (p_z), which is referred to as "electron momentum" and is given by Eq. (9) [48]:

$$p_z = -\frac{E_0 - E_A - E_0E_A\left(1 - \cos\theta\right)/m_0c^2}{\sqrt{E_0^2 + E_A^2 - 2E_0E_A\cos\theta}} \tag{9}$$

where m_0c^2 is the rest mass energy of the electron, and p_z is the projection of the electron's pre-collision momentum on the momentum transfer vector of the gamma-ray.

The angular uncertainty due to the effects of Doppler broadening is given by Eq. (10) [56]:

$$\sigma_\theta = \frac{1}{k_\theta}\left(k_{pz}\sigma_{pz}\right) \tag{10}$$

where

$$k_\theta = \left(\frac{1}{m_0 c^2} - \frac{\overline{p_z}}{m_0 c \sqrt{E_0^2 + \overline{E_A}^2 - 2E_0 \overline{E_A} \cos\theta}} \right) \overline{E_A} E_0 \sin\theta \tag{11}$$

$$k_{pz} = \frac{\sqrt{E_0^2 + \overline{E_A}^2 - 2E_0 \overline{E_A} \cos\theta}}{m_0 c} \tag{12}$$

In Eq. (11), the term k_θ is the contribution of the energy resolution, and in Eq. (12), k_{pz} is the contribution of the Doppler broadening to the angular uncertainty. The parameter σ_{pz} can be estimated by the width of the total Compton profile of the target atom, and the over-bars indicate the mean values of the corresponding variables.

The uncertainty in the number of charge carriers produced by each photon interaction is the statistical noise [58]. This noise makes a physical limit on the energy resolution. Since the number of charged carriers (N) is proportional to the deposited energy, for a Poisson process, then the energy resolution is defined by Eq. (13):

$$E_{res} = \frac{2.35}{\sqrt{N}} \tag{13}$$

which is not a Poisson process and needs the Fano factor to be modified. The noise coming from the electronic setup is called ENC [55].

Detector geometry in the Compton camera plays a vital role because it influences spatial and scattering angle uncertainty. The angular uncertainty due to the geometry contribution is inversely proportional to the square of the distance between the scatterer and absorber detectors [23]. To measure geometry uncertainty, which includes $\Delta\theta_2$, $\Delta\theta_3$, and $\Delta\theta_4$ for spatial uncertainty, consider Eqs. (14) (15) and (16):

$$S\ \tan(\theta + \Delta\theta_2) = \frac{d}{2} + S\ \tan(\theta + \phi) \tag{14}$$

$$S\ \tan(\theta + \Delta\theta_3) = \left(S + \frac{L}{2} \right) \tan\theta \tag{15}$$

$$S\ \tan(\theta + \Delta\theta_4) = S\ \tan\theta + r \tag{16}$$

where S is the distance between scatterer and absorber detectors, d is the scatterer pixel width, L is the scatterer pixel thickness, ϕ is the half-angle subtended by a pixel in the scatterer detector, and r is the FWHM position resolution of the absorber detector [59].

Any radiation detector's efficiency is determined by geometric and intrinsic efficiency. The geometric efficiency is the ratio of photons emitted by the source to valuable signals detected in the camera. The fraction of gamma rays reaching a radiation detector that results in valuable signals is known as the intrinsic efficiency of the detector [55]. The intrinsic Compton camera efficiency is defined as the fraction of photons entering the first detector that undergoes only one Compton scattering and is then photoelectrically absorbed in the second detector and according to Eq. (17) as follows [54]:

$$\varepsilon_{icc} = \frac{1}{\Omega_1} \int\limits_{\text{det 1}} d\upsilon_1 \int\limits_{\text{det 2}} d\upsilon_2 \Delta\Omega_1 \mu_c \left(E_0\right) e^{\left(-\mu_t \left(E_0\right) L_1\right)} \frac{d\sigma}{d\Omega} \left(\theta_{12}\right) \Delta\Omega_2 e^{\left(-\mu_t \left(E_0\right) L_{12}\right)} \mu_p \left(E_1\right) \tag{17}$$

where Ω_1 is the solid angle subtended by the scatterer detector at the source, $\Delta\Omega_1$ is the solid angle for a differential volume element $d\upsilon_1$ in the scatterer detector, Ω_2 is the solid angle subtended by the absorber detector at the interaction position in the scatterer detector, L_1 is the attenuation length in the scatterer detector between the source and $d\upsilon_1$, L_{12} is the attenuation length between the two elements $d\upsilon_1$ and $d\upsilon_2$, μ_c, μ_p, and μ_t are the Compton, photoelectric, and the total linear attenuation coefficients respectively and $\frac{d\sigma}{d\Omega}$ is the Klein-Nishina Compton scattering angular cross-section per electron.

As can be seen from Eq. (17), efficiency depends on incoming photon energy, geometry, system, and the detectors; In fact, the probability of interactions, deposited energy in detectors and the relation between irradiated photons are all stochastic processes; So, the efficiency calculation is more complicated than it seems. The following is an introduction to the GEANT4 Monte Carlo code used to simulate the Compton camera. Then, based on the results obtained in the simulation, the parameters affecting the efficiency of the Compton camera will be examined separately.

3 Sensitivity Analysis of Efficiency in Compton Imaging System

In the present section, the efficiency of a Compton camera was studied based on semiconductor detectors using the GEANT4 simulation toolkit [60]. This tool, performs so well in Monte Carlo processes simulations, especially in medical applications [61]; therefore, in high-energy physics, astrophysics, cosmic rays and particle accelerators, GEANT4 is being used for simulations [62–64].

The effects of various and influential parameters on the efficiency of the Compton camera have been investigated, including source distance to the scatterer detector, the distance between the two detectors, thickness, dimensions, and semiconductor type of the absorber and scatterer detectors, number of scatterer detectors with

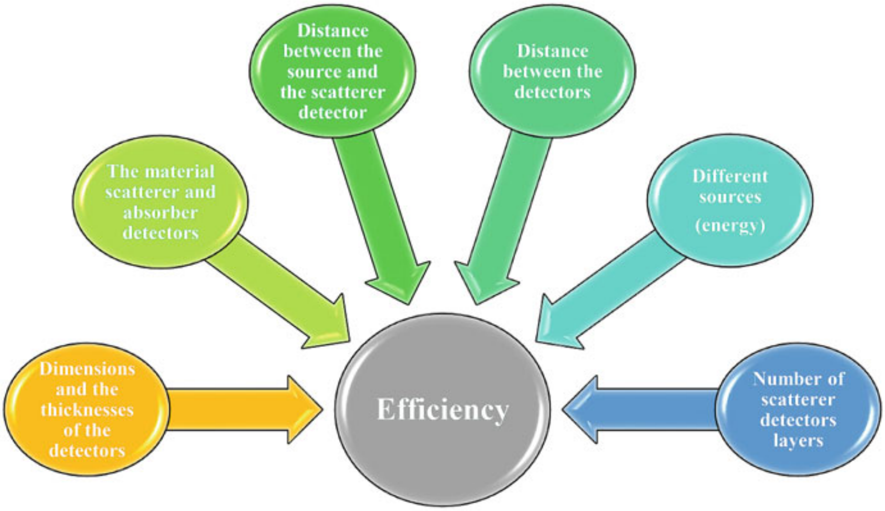
Distance between the source and the scatterer detector
Distance between the detectors
The material scatterer and absorber detectors
Different sources (energy)
Dimensions and the thicknesses of the detectors
Efficiency
Number of scatterer detectors layers

Fig. 3 Effective parameters in the efficiency of the Compton imaging systems

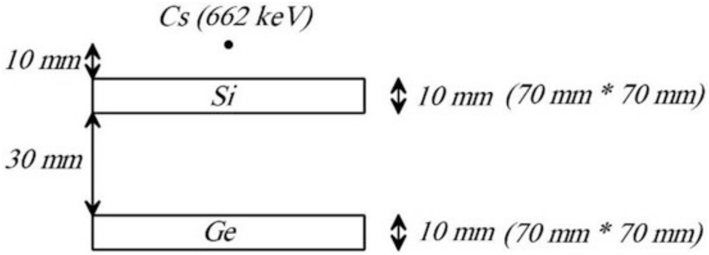

Fig. 4 A sample of a simulation by Compton imaging systems with ^{137}Cs source

different thicknesses, and the energy of the radioisotope, as shown in Fig. 3 [65]. The efficiency is determined by the energy of gamma-ray, system geometry, and detector martial. Interaction probability, energy deposition in both detectors, and photon intervals are random. This study uses GEANT4 to simulate a simple Compton camera pattern using semiconductor scatterer and absorber detectors, as illustrated in Fig. 4, via changing one parameter and keeping the other parameter's constant. The scatterer and absorber detectors' geometry, energy resolution, and spatial resolution (i.e., detector segmentation) are all included in the simulation model. The sensitivity analysis of the Compton imaging system's efficiency to the optimal parameters is investigated in this study. The characteristics of the semiconductor detectors and the different radioisotope sources with their most probable emitting photons used in this simulation are given in Tables 1 and 2, respectively.

Table 1 The features of the semiconductor detectors used in this simulation [66]

Density $\left(\frac{g}{cm^3}\right)$	Pair-Production needed energy (eV)	Energy gap (eV)	Atomic No.	Material
2.33	3.65 (300 K)	1.106 (300 K)	14	Si
5.33	2.96 (77 K)	0.67 (77 K)	32	Ge
6.06	4.43 (300 K)	1.47 (300 K)	48, 52	CdTe
6.04	4.22 (300 K)	2.13 (300 K)	80, 53	HgI_2
5.32	4.51 (300 K)	1.45 (300 K)	21, 33	GaAs
6	4.64 (300 K)	1.57 (300 K)	48, 52, 30	CZT

Table 2 The sources with their most probable emitting photons used in this simulation [66]

Energy (keV)	Source
364.4	^{131}I
412	^{198}Au
511	^{11}C
662	^{137}Cs
835	^{54}Mn
1274	^{22}Na

3.1 Distance Between the Detectors and the Radioisotope Source

In Fig. 5, the efficiency of the Compton camera is evaluated by changing the distance between the radioactive source and the scatterer detector. The range of changes in distance between the source and the detector was from 1 to 75 mm, and the step of each change was 2 mm. According to Fig. 5, the efficiency decreases exponentially as the distance between the scatterer detector and source increases. That is because of having fewer events to determine the location and intensity of the source. As shown in Fig. 5, the effects of the distance between the scatterer and absorber detectors on efficiency were also studied. The distance changes between the two detectors were from 5 to 190 mm, and the step of each change was 5 mm. Figure 5 shows that the more the distance between the two detectors, the more efficiency decreases.

3.2 Geometry of the Detectors

Changes to the dimensions of the scatterer detector plate were made to investigate the effect of geometry on efficiency (Fig. 5). The range of the scatterer detector plate was 5×5 mm^2 to 200×200 mm^2 with a constant thickness and 5×5 mm^2 steps per change. As shown in Fig. 5, the efficiency increases with the dimensions of the scatterer detector plate up to the 80×80 mm^2. Then, it has a saturation value. In the next step, the sensitivity analysis of the efficiency to the dimensions of the absorber detector plate was investigated. The range of the absorber detector

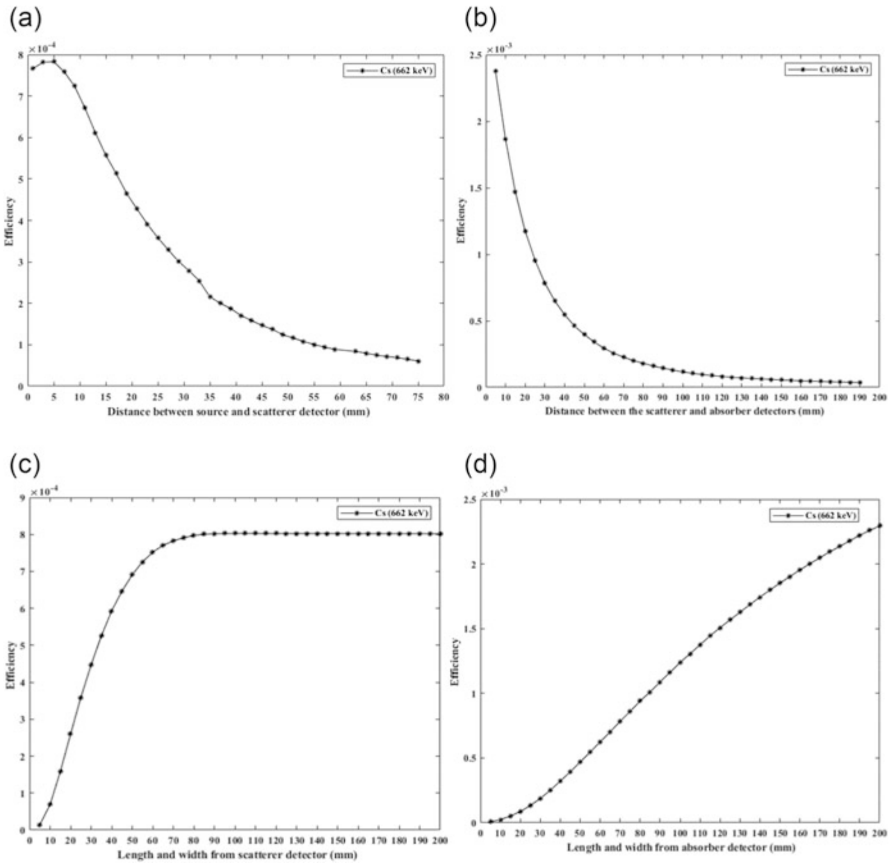

Fig. 5 Efficiency of distance changes between (**a**) the radioactive source and scatterer detector and (**b**) the scatterer detector and the absorber detector. Efficiency of (**c**) Compton camera vs. dimensions of the scatterer detector and (**d**) Compton camera vs. dimensions of the absorber detector. Efficiency of the Compton camera vs. the thickness of the (**e**) scatterer detector and (**f**) absorber detector. (**g**) Efficiency vs. the energy source

plate was 5 × 5 mm^2 to 200 × 200 mm^2 with a constant thickness and 5 × 5 mm^2 steps per change. The efficiency of the absorber detector plate increases with the dimensions of the absorber detector plate, as illustrated in Fig. 5.

In the next step, the thickness of the scatterer detector was changed; while, the other parameters were considered constant. The range of the scatterer detector thickness with the dimensions of the constant detector plate is obtained from 1 to 40 mm, and the steps of each change are 1 mm. According to Fig. 5, the efficiency increases with the increase in thickness of the scatterer detector up to 12 mm thickness. The highest efficiency value belongs to the thicknesses between 12 and 18 mm. Then, it decreases as the thickness of the scatterer detector goes higher than 18 mm. The effects of the thickness of the absorber detector on the Compton camera

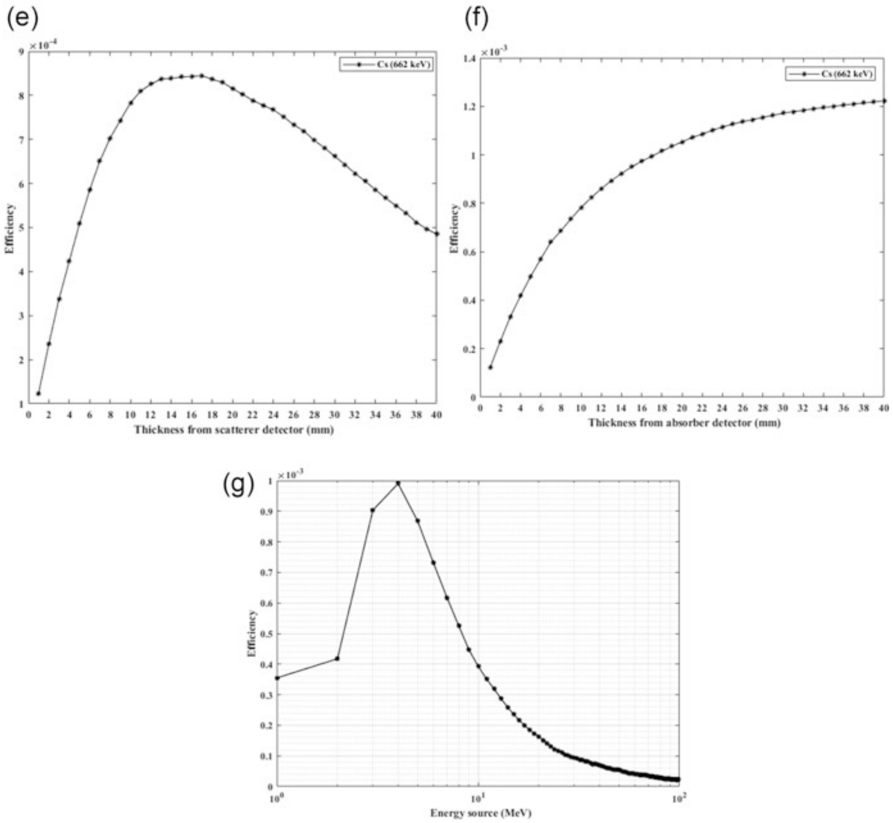

Fig. 5 (continued)

efficiency were also studied. The range of the absorber detector thickness with the dimensions of the constant detector plate was from 1 to 40 mm, and the step of each change was 1 mm. As seen in Fig. 5, the efficiency increases as the thickness of the absorber detector increases, eventually reaching saturation.

3.3 Energy of Gamma-Ray

The simulation was done for several energies in the range of 0.1–10 MeV to investigate the effect of gamma-ray energy on the efficiency of the Compton camera. As shown in Fig. 5, the efficiency of the Compton imaging system has its high values in the energy range between 0.3 and 1.5 MeV. In fact, for this design model, the sources generating gamma rays with this energy range have the highest efficiency values for the Compton camera.

In the continuation of the research, the radioactive sources listed in Table 2 are investigated for the ranges of Fig. 5 that have the highest efficiency. According to Table 2, gamma-ray sources including ^{131}I, ^{198}Au, ^{11}C, ^{137}Cs, ^{54}Mn, ^{22}Na were selected in the present study. The gamma-ray energy, most likely emitted by the sources, was chosen for this study.

In Fig. 6, the study efficiency of the Compton camera was by changing the distance between the radioactive source and the scatterer detector for the sources in Table 2. The range of change for the distance from the source was from 1 to 15 mm, and the step of each change was 2 mm. The maximum efficiency in most parts of the graph is related to ^{11}C. In Fig. 6, for the sources in Table 2, the effects of the distance between the scatterer detector and the absorber detector on efficiency were also studied. The distance change between the two detectors was from 5 to 70 mm, and the step of each change was 5 mm. The maximum efficiency in most parts of the diagram is for ^{11}C and ^{198}Au. As shown in Fig. 6, the effect of geometry on the efficiency parameter changes was made to the dimensions of the scatterer detector plate for Table 2. The range of change was from 70×70 mm^2 to 100×100 mm^2 with each step of 5×5 mm^2. The maximum efficiency in all parts of the graph is related to ^{11}C. Also, as shown in Fig. 6, the sensitivity analysis of the efficiency to the dimensions of the absorber detector plate for the sources in Table 2 was investigated. The range of change was from 20×20 mm^2 to 200×200 mm^2, and the step of each change was 20×20 mm^2. The maximum efficiency in all parts of the graph is ^{11}C and ^{198}Au. In the following studies for the sources in Table 2, the thickness of the scatterer detector was changed. The change range was from 10 to 30 mm, and the step of each change was 2 mm. According to Fig. 6, ^{11}C has the maximum efficiency in all thicknesses. Also, the efficiency study for absorber detector thickness changes in the same range as the maximum scatterer detector thickness was performed. Figure 6 shows the efficiency diagram in terms of absorber thickness changes for sources in Table 2. According to the results in Fig. 6, at all thicknesses, ^{11}C has the maximum efficiency.

3.4 Material Scatterer and Absorber Detectors

In the continuation of the study, the efficiency was evaluated by changing the material of the scatterer detector and keeping the other parameters constant. In Table 3, the efficiency in terms of differences in the material of the semiconductor scatterer detector and the Ge absorber detector for different sources emitting their highest gamma-ray energy is evaluated. As shown in Table 3, the maximum efficiencies in all different materials used for scatterer detectors are ^{11}C and ^{137}Cs.

Also, the efficiency was evaluated by changing the material of the absorber detector and keeping the other parameters constant. As shown in Table 4, the efficiency results in terms of differences in the material of the semiconductor absorber detector and the Si scatterer detector for different sources with their

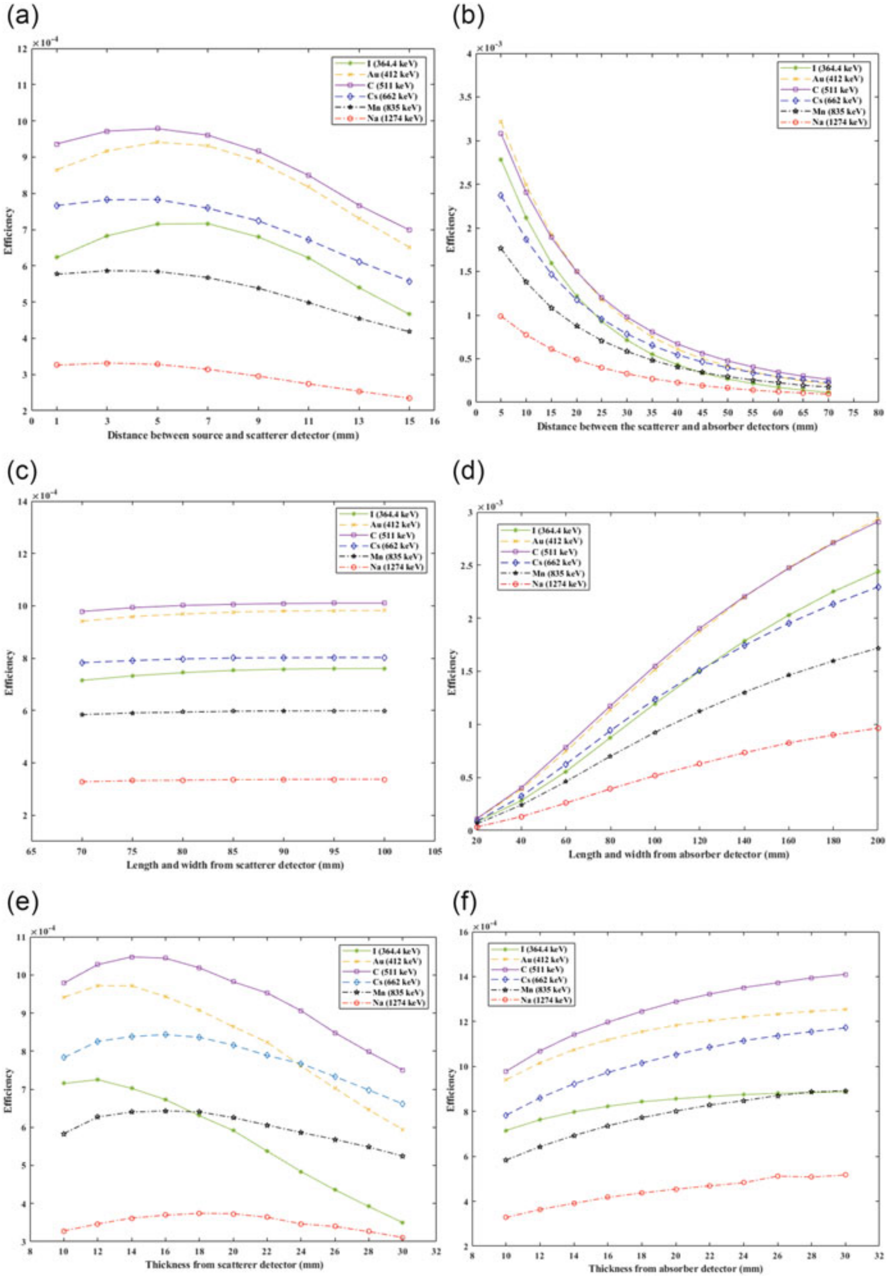

Fig. 6 Efficiency of the Compton camera vs. (**a**) the distance between the radioactive source and scatterer detector, (**b**) the distance between the scatterer detector and the absorber detector, (**c**) dimensions the scatterer detector, (**d**) dimensions the absorber detector, (**e**) the thickness of the scatterer detector and (**f**) the thickness of the absorber detector for different sources

Table 3 Different materials for semiconductor scatterer detector for different sources

			Efficiency ($\times 10^{-4}$)			
Energy (keV)	Si	Ge	CdTe	HgI_2	GaAs	CZT
^{131}I (364.4)	7.151	7.320	3.277	0.875	7.265	4.008
^{198}Au (412)	9.411	10.781	6.028	2.348	10.730	6.838
^{11}C (511)	9.783	12.606	9.109	5.085	12.592	9.789
^{137}Cs (662)	7.829	10.658	9.162	6.270	10.692	9.674
^{54}Mn (835)	5.843	8.324	7.785	5.839	8.349	7.938
^{22}Na (1274)	3.280	4.900	4.807	3.863	4.914	4.884

Table 4 Different materials for semiconductor absorber detector for different sources

			Efficiency ($\times 10^{-4}$)			
Energy (keV)	Si	Ge	CdTe	HgI_2	GaAs	CZT
^{131}I (364.4)	0.219	7.151	21.151	29.440	7.244	18.850
^{198}Au (412)	0.314	9.411	31.485	48.078	9.538	27.478
^{11}C (511)	0.300	9.783	38.364	69.355	9.845	32.602
^{137}Cs (662)	0.244	7.829	33.938	70.060	7.904	28.122
^{54}Mn (835)	0.169	5.843	26.449	58.851	5.927	21.850
^{22}Na (1274)	0.081	3.280	15.439	36.304	3.261	12.557

most probable emitting energy are discussed. As shown in Table 4, the maximum efficiencies in all different materials used for absorber detectors is ^{11}C.

3.5 *Number of Scatterer Detectors*

In the continuation of the investigations, the number of scatterer detector layers was examined by keeping other parameters constant. According to Fig. 5, the best thickness of 17 mm was obtained for Si in this study. For this reason, this thickness was separated into smaller layers, and the efficiency was evaluated for smaller layers; In addition, the efficiency was calculated as before, in this study, multiple scattering as well as in real detectors recorded by coincidence, was not removed. Because Compton scattering interferes with image reconstruction more than once, the scatterer detector layering method reduces the number of Compton scatterings. For example, a scatterer detector is divided into several different layers of the same thickness at a distance of 1 mm, according to Table 5. The total thickness in each division is 17 mm. According to the results, the efficiency is optimal for eight scatterer layers of the same thickness with a distance of 1 mm. In fact, in the number of layers between 14 and 17, the efficiency ratio for single to multiple modes is equal to the same ratio in 8 layers. However, the single efficiency is higher in 8 layers.

Different research groups used Compton cameras for the experimental study to get different results. Energy resolution, efficiency, angular resolution, and spatial

Table 5 Evaluation of efficiency for different number of scattering layers of Si material with total thickness 17 mm with a distance of 1 mm from each other

Number of scatterer detector layers	Efficiency considering multiple Compton scattering in scatterer detector and absorption in absorber detector(10^{-4})	Efficiency considering the single Compton scattering in the scatterer detector and the absorption in the absorber detector(10^{-4})	Single to multiple ratio
1	118.751	8.417	0.070
2	117.035	8.415	0.071
3	115.841	8.576	0.074
4	114.715	8.596	0.074
5	113.713	8.474	0.074
6	112.779	8.502	0.075
7	112.184	8.649	0.077
8	111.294	8.991	0.080
9	110.575	8.540	0.077
10	109.853	8.554	0.077
11	109.593	8.676	0.079
12	109.090	8.681	0.078
13	108.256	8.619	0.079
14	107.722	8.639	0.080
15	107.914	8.712	0.080
16	107.785	8.724	0.080
17	107.083	8.636	0.080

resolution were all studied by each research group [52]. Table 6 summarizes the conclusions of many experimental studies for various Compton cameras worldwide and simulations performed in this research using the GEANT4 tool. According to the results, the difference between efficiency values and experimental research is because of errors in the energy recorded in a detector, the resolution for the coincident of the event used, and the systems used to record the data in the experimental study.

4 Conclusion

Compton cameras can be an excellent alternative to other nuclear imaging systems such as gamma camera and SPECT. They also use electronic collimators instead of mechanical collimators because Compton cameras can detect a wide range of gamma-ray energies. It can be used in applications such as medicine and astrophysics. And also, as mentioned, to design any Compton camera, energy resolution, angular resolution, spatial resolution, and efficiency must be considered.

Table 6 Comparison of the results of different studies for different Compton cameras in the world and simulations in this study

Efficiency in simulation	Efficiency in experimental research	Year	Research group	Energy (keV)	Detector matrials
5.9×10^{-3}	2.6×10^{-3}	1983	University of Southern California	140	HPGe/Na(Tl)
5.5×10^{-3}	2.7×10^{-3}	2008–1998	University of Michigan		Si/Na(Tl)
2.4×10^{-2}	1×10^{-2}	2005	Japan Aerospace Exploration Agency, Japan	360	Si/CdTe
4.1×10^{-5}	1×10^{-5}	2009–2006	Kyoto university		TPG/GSO (ETCC)
6.7×10^{-8}	4.1×10^{-8}	2010	Hanyang university	511	Si/Na(Tl)
3×10^{-4}	1.5×10^{-4}	2001	University of Michigan		CZT
6.3×10^{-5}	3.1×10^{-5}	2011–2004	UCL university	662	HPGe
5.9×10^{-2}	4×10^{-2}	2007	University of Liverpool		HPGe

Another option that can be effective in obtaining the position and intensity of the radiation source in Compton cameras is the algorithm used to reconstruct the images. The better the accuracy and minor error of the algorithm used and the better the intensity of the radioactive source, the better the algorithm. Of course, one of the challenges of the Compton camera, which is less commonly used than other imaging devices, is developing and using an appropriate algorithm. The methods of reconstructing images in the Compton camera can be examined in a separate chapter. In this chapter, only the Compton camera performance parameters were studied.

According to the results in this study, for the distance between the source and the scatterer detector to have good efficiency (for a source with the same number of particles), the source should be in the environment for a longer time. Proximity to a radiation source (especially in medical applications) can be dangerous and damaging. Also, the half-life and activity of the radioactive source should be selected according to the application.

As the distance between the two detectors increases, the efficiency decreases because the beam emitted from the source travels longer to reach the absorber detector. As a result, the probability of other interactions before reaching the absorber detector increases, resulting in fewer events and, consequently, lower efficiencies. The shorter the distance between the detectors, the better the efficiency; however, this is impossible due to the limitations of producing such a low distance between the detectors. The appropriate distance between the detectors must be selected.

According to the results in the research, with increasing the dimensions of the scatterer detector plate, the amount of efficiency increases up to the dimensions of the absorber detector plate. However, a size larger than the absorber detector reaches a degree of saturation. The low efficiency in dimensions more considerable than the dimensions of the absorber detector plate is the recording of almost all the events that the single Compton scattering in the scatterer detector has done and reached the absorber detector. In fact, with a large scatterer detector screen, events that do not reach the absorber detector will increase and will not affect efficiency.

By increasing the dimensions of the absorber detector plate, the amount of efficiency increases almost linearly. The larger the absorber detector plate, the more likely the photons made by a Compton scatter in the scatterer detector will be absorbed, and the efficiency will increase. Considering a large absorber detector, it is not economical but costly if it is more than a scatterer detector.

Moreover, according to the results in this study, with increasing the thickness of the scatterer detector, the efficiency first increases and then reaches the maximum value and then decreases. Because Compton scattering does not occur at low thicknesses and increases at higher thicknesses of multiple Compton scattering, the optimal thickness can be found for any Compton imaging system design. The type of scatterer detector, Compton interaction cross-section, photoelectric interaction cross-section, and radionuclide source energy will significantly determine this optimal thickness.

Also, increasing the thickness of the absorber detector increases efficiency. In fact, as its thickness increases, the photons that make up a Compton scatter in the scatterer detector are more likely to absorb the photoelectric in the absorber detector. It is for sure that very large thicknesses are not economical for the absorber detector because almost all the events necessary for efficiency will be absorbed from a thickness.

Furthermore, suppose this thickness is divided into several smaller layers, the scatterer detector with the same distance as the design studied in 1 mm. In this case, various components are reduced while the efficiency stays essentially unchanged. Of course, if the layers are selected from a smaller thickness, Compton scattering will no longer occur. For this reason, the thickness and number of scattering layers are essential to achieve the optimal design.

The best semiconductor scatterer detector can be “GaAs” and “Ge”. Also, it should be noted that “Ge” detectors can be stored at room temperature, but better performance should be taken to lower temperatures during operation. Therefore, to reduce noise, “Ge” detectors should always be kept at a low temperature, but the “GaAs” detector is known as a semiconductor material that can operate at room temperature. Therefore, the choice of “GaAs” as the scatterer detector in this design is proposed. The best semiconductor absorber detector can be “HgI_2” and “CdTe”. These interpretations show that choosing absorber and scatterer detector material is essential for efficiency to increase the correct number of events.

References

1. Hussein, M. T., Ibrahim, H. F., Morad, E. A., Maamoun, I. K., & Attala, E. M. (2019). A study of single photon emission computed tomography by using Geant4/GATE. *Journal of Nuclear Technology in Applied Science, 7*(1), 1–12.
2. Terzioglu, F., Kuchment, P., Problems, L. K.-I., & undefined. (2018). Compton camera imaging and the cone transform: a brief overview. *Inverse Problems, 34*. iopscience.iop.org
3. Ahmed, A. M., et al. (2020). A validated Geant4 model of a whole-body PET scanner with four-layer DOI detectors. *Physics in Medicine and Biology, 65*(23), 235051.
4. Kim, D., Uenomachi, M., Shimazoe, K., & Takahashi, H. (2021). Evaluation of single scattering correction method in Compton imaging system. *Nuclear Instruments and Methods in Physics Research Section A: Accelerators, Spectrometers, Detectors and Associated Equipment, 1010*, 165568.
5. Fontana, M. *Tests and characterization of gamma cameras for medical applications*.
6. Sakai, M., et al. (2018). In vivo simultaneous imaging with 99mTc and 18F using a Compton camera. *Physics in Medicine and Biology, 63*(20), 205006.
7. Motomura, S., Kanayama, Y., Haba, H., Watanabe, Y., & Enomoto, S. (2008). Multiple molecular simultaneous imaging in a live mouse using semiconductor Compton camera. *Journal of Analytical Atomic Spectrometry, 23*(8), 1089–1092.
8. Kishimoto, A., et al. (2017). First demonstration of multi-color 3-D in vivo imaging using ultra-compact Compton camera. *Scientific Reports, 7*(1), 1–7.
9. Hofstadter, R., & McIntyre, J. A. (1950). Measurement of gamma-ray energies with two crystals in coincidence. *Physics Review, 78*(5), 619.
10. Kalish, Y., & Nardi, E. (1964). A three crystal NaI(Tl) gamma-ray scintillation spectrometer. *Nuclear Instruments and Methods, 26*(C), 329–332.
11. Petersen, L. E., & Howard, R. L. (1961). Gamma-ray astronomy in space in the 50-KEV to 3-MEV region. *IRE Transactions on Nuclear Science, 8*(4), 21–29.
12. Herzo, D., et al. (1975). A large double scatter telescope for gamma rays and neutrons. *Nuclear Instruments and Methods, 123*(3), 583–597.
13. Schönfelder, V., Hirner, A., & Schneider, K. (1973). A telescope for soft gamma ray astronomy. *Nuclear Instruments and Methods, 107*(2), 385–394.
14. McConnell, M. L., et al. (1993). COMPTEL gamma-ray observations of X-ray binaries. *Astronomy and Astrophysics Supplement Series, 183*, 29.05.
15. Bloemen, H., et al. (1994). COMPTEL observations of the Orion complex: Evidence for cosmic-ray induced gamma-ray lines. *Astronomy and Astrophysics, 281*, L5–L8.
16. Schoenfelder, V., et al. (1996). COMPTEL overview: Achievements and expectations. *Astronomy and Astrophysics Supplement Series, 120*, 13–21.
17. Kuiper, L., et al. (2001). The crab pulsar in the 0.75-30 MeV range as seen by CGRO COMPTEL - a coherent high-energy picture from soft X-rays up to high-energy γ-rays. *Astronomy and Astrophysics, 378*(3), 918–935.
18. Iyudin, A. F., et al. (2008). COMPTEL observations of 44Ti gamma-ray line emission from Cas A. *AIP Conf. Proc., 304*(1), 156.
19. Schönfelder, V. (2004). Lessons learnt from COMPTEL for future telescopes. *New Astronomy Reviews, 48*(1–4), 193–198.
20. Boggs, S. E., et al. (2002). The nuclear Compton telescope: A balloon-borne soft γ-ray spectrometer, polarimeter, and imager. *AIP Conf. Proc., 587*(1), 877.
21. Takada, A., et al. (2020). *SMILE-3: Sky survey in MeV gamma-ray using the electron-tracking Compton telescope loaded on balloons* (Vol. 11444, p. 1017–1022).
22. Everett, D., Fleming, J., et al. (1977). Gamma-radiation imaging system based on the Compton effect. *Proceedings of the Institution of Electrical Engineers, 124*, 995. ieeexplore.ieee.org
23. Singh, M., & Doria, D. (1983). An electronically collimated gamma camera for single photon emission computed tomography. Part II: Image reconstruction and preliminary experimental measurements. *Medical Physics, 10*(4), 428–435.

24. Singh, M., & Brechner, R. R. (1990). Experimental test-object study of electronically collimated SPECT. *Journal of Nuclear Medicine, 31*(2), 178.
25. Studen, A., et al. (2004). First coincidences in pre-clinical Compton camera prototype for medical imaging. *Nuclear Instruments and Methods in Physics Research Section A: Accelerators, Spectrometers, Detectors and Associated Equipment, 531*(1–2), 258–264.
26. Llosá, G., et al. (2008). Last results of a first Compton probe demonstrator. *IEEE Transactions on Nuclear Science, 55*(3), 936–941.
27. Çonka-Nurdan, T., et al. (2005). First results on Compton camera coincidences with the silicon drift detector. *IEEE Transactions on Nuclear Science, 52*(5 I), 1381–1385.
28. Motomura, S., Kan, Y., Motomura, S., Kanayama, Y., Haba, H., Watanabe, Y., & Enomoto, S. (2008). Multiple molecular simultaneous imaging in a live mouse using semiconductor Compton camera. *Journal of Analytical Atomic Spectrometry, 23*(8), 1089–1092.
29. Seo, Y. (2019). Quantitative imaging of alpha-emitting therapeutic radiopharmaceuticals. *Nuclear Medicine and Molecular Imaging, 53*(3), 182–188.
30. Nurdan, T. C., Nurdan, K., Brill, A. B., & Walenta, A. H. (2015). Design criteria for a high energy Compton Camera and possible application to targeted cancer therapy. *Journal of Instrumentation, 10*(07), C07018.
31. Omata, A., et al. (2020). Performance demonstration of a hybrid Compton camera with an active pinhole for wide-band X-ray and gamma-ray imaging. *Science Reports, 10*(1), 1–9.
32. Ogane, K., et al. (2021). Simultaneous measurements of single gamma ray of 131I and annihilation radiation of 18F with Compton PET hybrid camera. *Applied Radiation and Isotopes, 176*, 109864.
33. Yoshida, E., et al. (2020). Whole gamma imaging: A new concept of PET combined with Compton imaging. *Physics in Medicine and Biology, 65*(12), 125013.
34. Han, L., Rogers, W. L., Huh, S. S., & Clinthorne, N. (2008). Statistical performance evaluation and comparison of a Compton medical imaging system and a collimated Anger camera for higher energy photon imaging. *Physics in Medicine and Biology, 53*(24), 7029–7045.
35. Zhang, L., Rogers, W. L., & Clinthorne, N. H. (2004). Potential of a Compton camera for high performance scintimammography. *Physics in Medicine and Biology, 49*(4), 617.
36. Fontana, M., Dauvergne, D., Létang, J. M., Ley, J.-L., & Testa, É. (2017). Compton camera study for high efficiency SPECT and benchmark with Anger system. *Physics in Medicine and Biology, 62*(23), 8794.
37. Golnik, C., et al. (2016). Tests of a Compton imaging prototype in a monoenergetic 4.44 MeV photon field—A benchmark setup for prompt gamma-ray imaging devices. *Journal of Instrumentation, 11*(06), P06009.
38. Richard, M. H., et al. (2009). *Design study of a Compton camera for prompt γ imaging during ion beam therapy* (pp. 4172–4175). IEEE Nuclear Science Symposium Conference Record.
39. Aldawood, S., et al. (2017). Development of a Compton camera for prompt-gamma medical imaging. *Radiation Physics and Chemistry, 140*, 190–197.
40. Takeda, S., et al. (2015). A portable Si/CdTe Compton camera and its applications to the visualization of radioactive substances. *Nuclear Instruments and Methods in Physics Research Section A: Accelerators, Spectrometers, Detectors and Associated Equipment, 787*, 207–211.
41. Wahl, C. G., et al. (2015). The Polaris-H imaging spectrometer. *NIMPA, 784*, 377–381.
42. Hmissi, M. Z., et al. (2018, Nov). First images from a CeBr3 /LYSO:Ce temporal imaging portable Compton camera at 1.3 MeV. In *2018 IEEE Nucl. Sci. Symp. Med. Imaging Conf. NSS/MIC 2018 - Proc.*
43. Ziock, K. P. (2018). Principles and applications of gamma-ray imaging for arms control. *Nuclear Instruments and Methods in Physics Research Section A: Accelerators, Spectrometers, Detectors and Associated Equipment, 878*, 191–199.
44. Nishiyama, T., et al. (2014). A novel Compton camera design featuring a rear-panel shield for substantial noise reduction in gamma-ray images. *Journal of Instrumentation, 9*(12), C12031.
45. Sato, Y., et al. (2020). Remote detection of radioactive hotspot using a Compton camera mounted on a moving multi-copter drone above a contaminated area in Fukushima. *Journal of Nuclear Science and Technology, 57*(6), 734–744.

46. Martin, J. B., et al. (1993). A ring Compton scatter camera for imaging medium energy gamma rays. *IEEE Transactions on Nuclear Science, 40*(4), 972–978.
47. Shikaze, Y., & Shimazoe, K. (2021). Improvement of analysis results from the GAGG scintillator Compton camera operated on an unmanned helicopter by selecting stable flight conditions. *Journal of Nuclear Science and Technology, 59*, 1.
48. Ordonez, C. E., Bolozdynya, A., & Chang, W. Doppler broadening of energy spectra in Compton cameras. In *1997 IEEE nuclear science symposium conference record* (Vol. 2, pp. 1361–1365).
49. Basko, R., Zeng, G. L., & Gullberg, G. T. (1997). Analytical reconstruction formula for one-dimensional Compton camera. *IEEE Transactions on Nuclear Science, 44*(3 PART 2), 1342–1346.
50. Ida, T., Motomura, S., Ueda, M., Watanabe, Y., & Enomoto, S. (2018). Accurate modeling of event-by-event backprojection for a germanium semiconductor Compton camera for system response evaluation in the LM-ML-EM image reconstruction method. *Japanese Journal of Applied Physics, 58*(1), 016002.
51. Kroiz, G. C., Barajas, C. A., Gobbert, M. K., & Polf, J. C. (2021). *Exploring deep learning to improve Compton camera based prompt gamma image reconstruction for proton radiotherapy*.
52. Alnaaimi, M. A. (2011, July). *Evaluation of the UCL Compton camera imaging performance*.
53. Phillips, G. W. (1995). Gamma-ray imaging with Compton cameras. *Nuclear Instruments and Methods in Physics Research Section B: Beam Interactions with Materials and Atoms, 99*(1), 674–677.
54. Du, Y. F., He, Z., Knoll, G. F., Wehe, D. K., & Li, W. (2001). Evaluation of a Compton scattering camera using 3-D position sensitive CdZnTe detectors. *Nuclear Instruments and Methods in Physics Research Section A: Accelerators, Spectrometers, Detectors and Associated Equipment, 457*(1–2), 203–211.
55. Knoll, G. F. (1999). *Radiation detection and measurement*. Wiley.
56. Ordonez, C. E., Bolozdynya, A., & Chang, W. (1997). Dependence of angular uncertainties on the energy resolution of Compton cameras. *IEEE Nuclear Science Symposium and Medical Imaging Conference, 2*, 1122–1125.
57. Ribberfors, R. (1975). Relationship of the relativistic Compton cross section to the momentum distribution of bound electron states. *Physical Review B, 12*(6), 2067–2074.
58. Aarsvold, J. N., & Wernick, M. N. (2004). *Emission tomography : The fundamentals of pet and spect*. Elsevier.
59. Singh, M. (1983). An electronically collimated gamma camera for single photon emission computed tomography. Part I: Theoretical considerations and design criteria. *Medical Physics, 10*(4), 421–427.
60. Allison, J., et al. (2006). Geant4 developments and applications. *IEEE Transactions on Nuclear Science, 53*(1), 270–278.
61. Ahmadi Ganjeh, Z., Eslami-Kalantari, M., Ebrahimi Loushab, M., & Mowlavi, A. A. (2021). Calculation of direct DNA damages by a new approach for carbon ions and protons using Geant4-DNA. *Radiation Physics and Chemistry, 179*, 109249.
62. Mori, N. (2021). GGS: A generic Geant4 simulation package for small- and medium-sized particle detection experiments. *Nuclear Instruments and Methods in Physics Research Section A: Accelerators, Spectrometers, Detectors and Associated Equipment, 1002*, 165298.
63. Pak, S., & Cucinotta, F. A. (2021). Comparison between PHITS and GEANT4 simulations of the heavy ion beams at the BEVALAC at LBNL and the booster accelerator at BNL. *Life Sciences in Space Research, 29*, 38–45.
64. Dobynde, M. I., & Guo, J. (2021). Radiation environment at the surface and subsurface of the moon: Model development and validation. *Journal of Geophysical Research, Planets, 126*(11), e2021JE006930.
65. Niknami, M., Hosseini, S. A., & Loushab, M. E. (2021). Sensitivity analysis of the efficiency of Compton camera to the detector parameters using the GEANT4 computer code. *Applied Radiation and Isotopes, 176*, 109883.
66. Tsoulfanidis, N. (2010). *Measurement and detection of radiation*. CRC Press.

Spatial Localization of Radioactive Sources for Homeland Security

Konstantinos Karafasoulis and Aristotelis Kyriakis

1 Introduction

In the new era of homeland security there is a growing concern regarding the possession and the potential use of radiological materials by terrorist groups usually in the form of a radiological dispersion device (RDD), also known as “dirty bomb”. Since the defended areas from such a threat may not have specific entrance and exit points, the problem of how to localize and identify a radioactive source in an open area should be investigated. The detection has to overcome a variety of uncontrollable factors, such as the presence of benign sources, time and space varying background noise, and obstacles that may occlude signal from sources.

In general localization of radioactive sources or hotspots is a major issue for radiological safety of operators in nuclear facilities and in National Security. For this purpose, portable Gamma-Ray Imaging (GRI) systems allow remote localization of radioactive sources from greater distances than conventional rate meters, leading to significant reductions of the dose received by operators.

The difficulty with the operation of a GRI system originates from the γ-ray detection difficulty. Energetic γ-rays interact with matter with low efficiency. As a result large detectors are needed which are made of expensive heavy elements. Another option is to use pixelated array detectors which have a large number of pixels that are rather expensive to be constructed, in contrast to the normal optical wavelength light cameras. Furthermore, gamma rays do not interact with lenses

---

K. Karafasoulis (✉)
Hellenic Army Academy, Attica, Greece

A. Kyriakis
Institute of Nuclear and Particle Physics, National Center for Scientific Research “DEMOKRITOS”, Agia Paraskevi, Greece
e-mail: kyriakis@inp.demokritos.gr

© The Author(s), under exclusive license to Springer Nature Switzerland AG 2023

J. Du, K. (K.) Iniewski (eds.), *Gamma Ray Imaging*,
https://doi.org/10.1007/978-3-031-30666-2_5

and focusing equipment, which results in a limited field of view of the gamma ray detectors.

A way to go around this is to have a mechanical collimation. In this methodology a raster scanning approach is used with a single detector of one pixel that is moving around. Although such a device is relatively inexpensive, the whole process is rather slow. These types of imaging systems are based on a shielded collimated detector. The collimators may have a 2, 4 or 9 degree field of view [1, 2]. An image is produced by raster scanning the sensor head and recreating the gamma image by overlapping the results of each measurement. They have been used extensively in the past. However nowadays are becoming obsolete. A way to improve the localization accuracy of such a system is described in Sect. 2.

A more advanced technique is to use pixelated detector arrays as coded aperture devices. Nowadays, portable coded aperture gamma cameras for industrial applications are undergoing impressive developments and improvements in terms of lightness, usability, response sensitivity, angular resolution, and spectrometric capabilities [3–5]. One of the latest versions of these devices that have been proposed integrates a 1 mm thick CdTe sensor directly bump-bonded to a Timepix chip [6], a tungsten coded-aperture mask, and a mini RGB camera. However, a drawback of the coded aperture imaging approach is its limited field of view (FOV) [7] which is of the order of 60° and was tangled with the panoramic coded aperture gamma camera proposed in [8]. These devices are relatively fast but often expensive due to the pixelated array and are limited by the correct choice of the MURA type mask to detect close or large distance sources.

Another methodology that is commonly used is the Compton Cameras (CC). Compton imaging is a visualization technique that uses the kinematics of Compton scattering for the reconstruction of a gamma radiation source image [9]. A conventional CC is composed of two detector layers. A scatterer (low-Z material) and an absorber (high-Z material) working in time coincidence. The aim is to maximize the probability of Compton scattering in the scatterer and photoelectric absorption of the scattered photon in the absorber. The energy resolution of the scatterer is particularly important to accurately determine the scattering angle and to reduce the effect of Doppler energy broadening, due to the initial momentum of the bound electron [10]. The absorber detector records the energy and position of the scattered gamma. Using the Compton scattering equation, it is possible to determine the scattering angle and estimate possible directions of the original gamma ray as a surface of a cone. By overlapping several such cones from many events the location of the radiation source can be determined. However, in experimental data there is a non-negligible percentage of invalid events that contribute to the background such as partial energy absorption events (recoil electron or scattered photon escapes), incorrectly ordering of interactions and random noise. The CCs have been successfully used for detecting illicit nuclear materials, recovering orphan radioactive sources, and delimiting suspicious radiological contaminated areas. The hardware of CCs is often comprised of a scintillator detector for the absorber and one or several detector layers for the scatterer based on different technologies such as scintillator crystals coupled to compact SiPM/MPPC arrays [11, 12], semiconductor detectors like Si, CdTe or CdZnTe [13, 14]. In general CCs are widely used in the fields of γ-ray astronomy, nuclear medicine, nuclear waste inspection and homeland security. They are effective but expensive devices as well since they are based on pixelated arrays for the readout of both the scatterer and absorber layers. Due to the physics of Compton scattering, they could be inefficient at low photon energies particularly below 300 keV. However, this is mainly the range of interest in national security. This can be improved by selecting appropriate materials for the scatterer and absorber layers. Thus, in principle it is rather difficult to find a material that could cover efficiently both the low and high γ-ray energy spectrum.

2 Radioactive Source Localization Using a Single Sensor and Collimator

In this section the localization of a radioactive source using a single sensor and a collimator will be discussed by adding a simple by quite efficient trick. The basic idea is to increase the localization accuracy of such a device by moving the sensor inside a mechanical collimator. In Fig. 1 this device is hosted in a semi-autonomous rover. The mechanical collimator is made of lead with at least 1 cm thickness. The sensor can move inside the collimator with a piston like mechanism (Fig. 2). The measurements taken using a laboratory low activity ^{152}Eu radioactive source are shown in Fig. 3. It can be seen that the number of counts reaches a maximum when the sensor head (in this case a CTZ sensor) is aligned to the source position. It was proved that a source localization accuracy better than 20° can be achieved when the sensor head was 4 cm deep inside the collimator. Thus, the greater the depth of the sensor inside the collimator the better the localization accuracy is.

3 Radioactive Source Localization Using a Network of CZT Sensors

In this section a sensor network for radioactive source localization will be discussed. The proposed sensor network topology is shown in Fig. 4. The sensor network is consisted of five sensors in a planar cruciform topology. In the following both an analytical and machine learning algorithm will be described capable to localize a stationary radiation source in 3D. The sensor network can be thought as a core module of an easily expandable network topology.

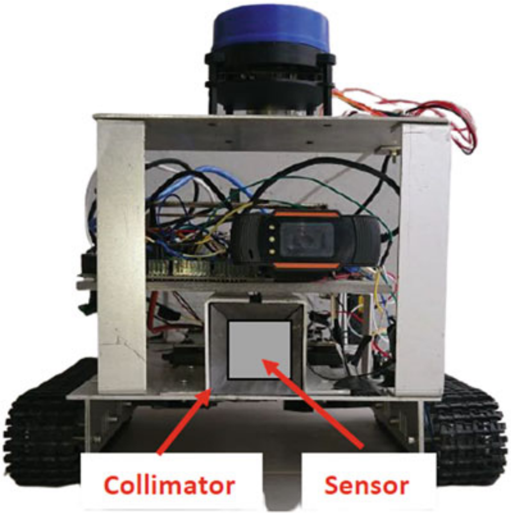

Fig. 1 Semi –autonomous rover equipped with the mechanical collimator and the γ-ray spectroscopic sensor that could move inside the collimator with a piston like mechanism

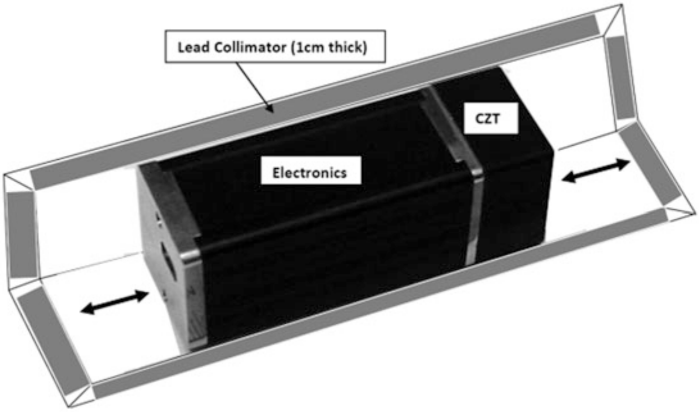

Fig. 2 The CZT spectroscopic γ-ray sensor inside the lead (1 cm thick) collimator. The sensor can move backward and forward using a piston like mechanism

3.1 Analytical Method

A radioactive source is placed in several positions in planes parallel to the plane defined by the five sensors. For each source position, the source spectrum of each sensor has been recorded. Since each source has a unique energy spectrum only the photo-peak counts could be taken for further processing. The analytical source localization algorithm could be explained with the help of Fig. 5.

In the analytical algorithm the only parameters that should be provided are the horizontal inter-sensor distance (S_x) and the vertical inter-sensor distance (S_y). Then the radioactive source position $S(X_r, Y_r, Z_r)$ can be estimated using the photo-peak

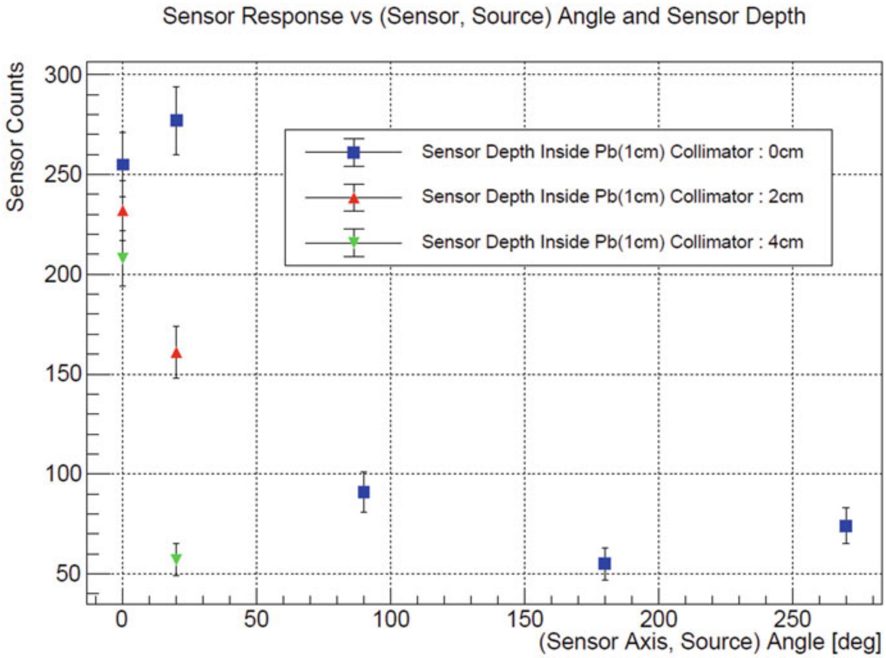

Fig. 3 Performance in source localization of a single CZT γ-ray spectroscopic sensor that could move with a piston like mechanism inside a 1 cm thick lead collimator. The source angle estimation could be better that 20° the case where the sensor depth inside the collimator is great enough

counts (A_i, i = 2,5,7,8,9) recorded by the five spectroscopic sensors and the fact that the number of recorded counts is inversely proportional to the square of the source-sensor distance (R_i, i = 2,5,7,8,9).

Using simple calculus the coordinates $S(X_r, Y_r, Z_r)$ of the radioactive source can be evaluated as follows [15]:

$$X_r = \frac{S_x\left(Q_1^x - Q_2^x\right)}{2\left(Q_1^x + Q_2^x\right) - 4} \tag{1}$$

where:

$$Q_1^x = \frac{R_9^2}{R_8^2} = \frac{A_8}{A_9}, \qquad Q_2^x = \frac{R_7^2}{R_8^2} = \frac{A_8}{A_7}$$

Similarly:

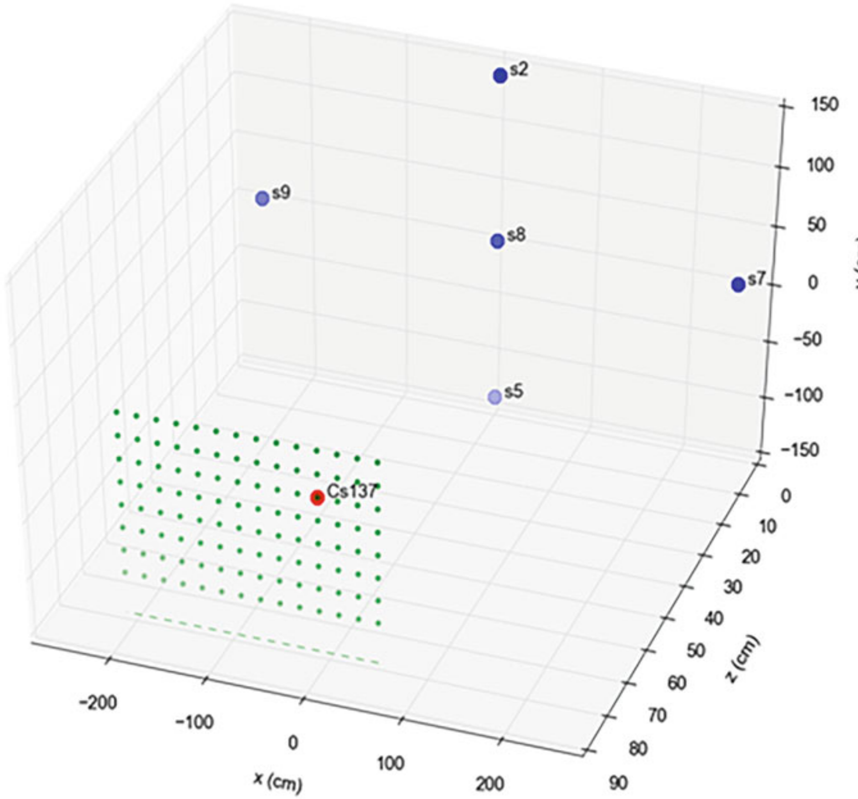

Fig. 4 Schematic of the setup of the five sensors in planar cruciform topology (in blue). The energy response of the sensors is recorded as a radioactive source (in red) is placed in various positions (in green) at planes parallel to the sensor plane

$$Y_r = \frac{S_y\left(Q_1^y - Q_2^y\right)}{2\left(Q_1^y + Q_2^y\right) - 4} \tag{2}$$

where:

$$Q_1^y = \frac{R_2^2}{R_8^2} = \frac{A_8}{A_2}, \qquad Q_2^y = \frac{R_5^2}{R_8^2} = \frac{A_8}{A_5}$$

Finally the depth coordinate (Z_r) can be estimated by the formula:

$$Z_r = \frac{Z_r^x + Z_r^y}{2} \tag{3}$$

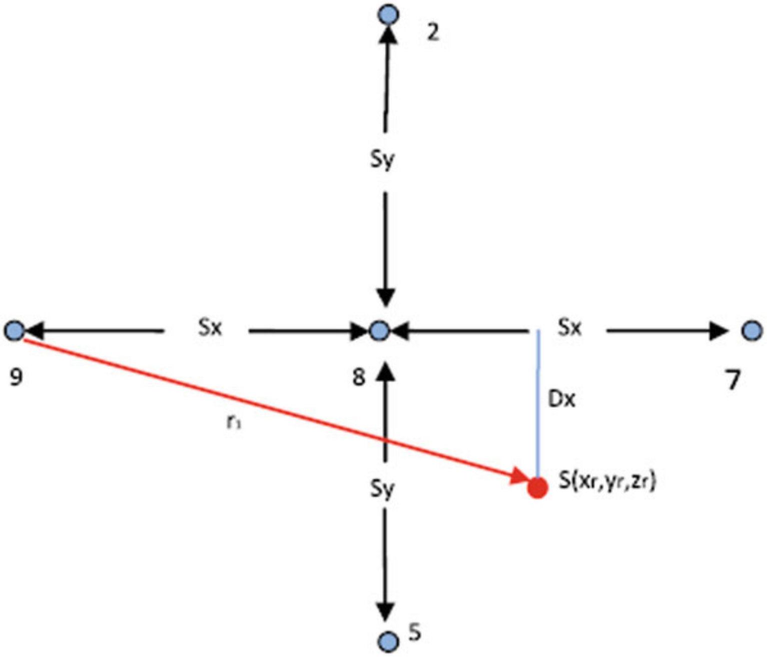

Fig. 5 The schematic explains the analytical method used for the localization of a radioactive source in 3D S(x_r,y_r,z_r). The horizontal inter-sensor distance (S_x) and the vertical inter-sensor distance (S_y) are the only parameters needed by the analytical algorithm

where:

$$Z_r^x = \sqrt{D_y^2 - X_r^2},\quad Z_r^y = \sqrt{D_x^2 - Y_r^2}$$

and $D_x^2 = \frac{2S_xX_r + S_x^2}{Q_1^x - 1} - X_r^2$, $D_y^2 = \frac{2S_yY_r + S_y^2}{Q_1^y - 1} - Y_r^2$.

The analytical method described above can give quite accurate estimation of the horizontal and vertical position of the source. Experimental tests that have been performed using a bare ^{137}Cs source with activity of 7 MBq and exposure time of 3 min gave a spatial position accuracy of less than 15 cm at a distance of 120 cm from the sensor plain within a monitoring volume of 5 m × 2.8 m × 2 m. In the setup the inter-sensor distances were $S_x = 2.5$ m and $S_y = 1.4$ m. The spatial position distributions for the bare source at a distance of 120 cm from the sensor plain can be seen in Fig. 6. The depth of the source can be also estimated using the analytical method but it was proved that this can only be done with a systematic error. This is due to the fact that the analytical method does not take into account the geometrical form factors of the sensors and the radiation attenuation of the medium between the source and the sensors (in general unknown parameter). This leads to an

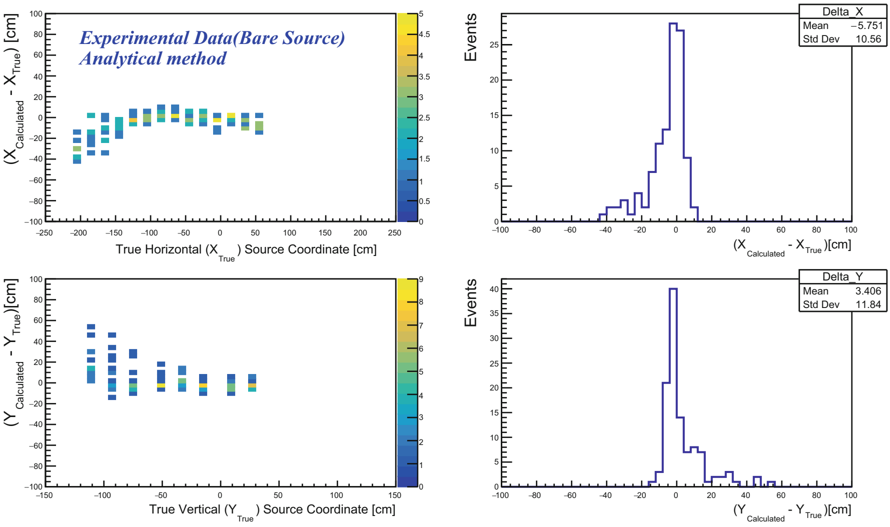

Fig. 6 Horizontal (top) and Vertical (bottom) spatial accuracy distributions calculated using the analytical method for a ^{137}Cs source of 7 MBq located 120 cm away from the sensor plane and for exposure time of 3 min

underestimation of the counts recorded by the sensors. To overcome this problem an approach based on machine learning techniques has been applied and will be described in the next Sect. 3.2.

3.2 Machine Learning Methods

As it was mentioned in the previous Sect. 3.1, the analytical method has some limitations especially in the source depth estimation. The use of fusion algorithms based on machine learning techniques can improve the situation [16]. The most promising algorithms were based on regression Neural Networks (MLP) and Gradient Boosted Decision Trees (BDTG). In general when dialing with machine learning techniques the problem is to find the most appropriate data sets to perform the training of the algorithms. Since a large number of data is needed to train the algorithms the most obvious approach is to use simulated events. This approach has some handicaps since it needs a lot of computational power and a very good simulation of the whole environment of the experimental setup. A second approach is the training of the machine learning algorithms to be done using an enriched set of experimental data (defined as the response of the sensors in different 3D radiation source positions) collected with the sensor network and exploiting the symmetry of the network topology as it was presented in Fig. 4. The initial small set of experimental data points could be increased to a few thousand 3D source position points by utilizing both the symmetry of the network topology and the fact that the response of the sensors is proportional to $Ae^{-\mu R}/R^2$, where A represents the source activity and the sensor efficiency and R is the distance in 3D between each sensor and the radiation source. Finally the factor $e^{-\mu R}$ corresponds to the absorption term. Using the proposed data driven method thousands of data points could be generated and subsequently used for the training of the machine learning algorithms. The benefit of this approach is that without any significant computational cost the effects of both the radiation absorption and scattering can be taken into account, which in other circumstances would require a detailed description of the surrounding materials in order to produce reliable simulated data of the experimental setup. When the effect of the radiation absorption and scattering is not taken into account the source localization especially in the depth direction (source transverse distance from the sensor plain) could be biased or not been able to be estimated at all, especially when dealing with slightly shielded sources.

After the creation of the training data set using the above procedure the following basic steps are implemented:

- The number of events recorded by each sensor is normalized to the recording of the sensor having the maximum number of events during the same time window. By applying this step the method can handle sources with different activities, since the relative sensor response will be the same.
- Machine learning techniques are used to estimate independently the horizontal (X), vertical (Y) and depth (Z) position of the source by taking into account the normalized sensor counts. Extensive tests showed that better results can be obtained by choosing three independent models, one for each space coordinate rather than having one model with two or three coordinates as outputs of the machine learning algorithms.

The above described data driven method has been proven to be quite flexible since it can be applied to localize not only bare but also slightly shielded radioactive sources. For the slightly shielded source, tests were performed using a lead shield of 1 cm width around the bare ^{137}Cs source. A set of weight factors can be produced for each case separately, during the training of the machine learning methods. The source localization accuracy in this case for both bare and shielded source can be seen in Fig. 7. In this figure, the horizontal (top), vertical (middle) and depth (bottom) resolution defined as the RMS of the accuracy (estimated — true coordinate) distribution as a function of the exposure time in seconds are presented. Left (Right) column shows the bare (slightly shielded) source results for a ^{137}Cs source of 7 MBq at various parallel plains of source positions ($Z = 40$ cm, 80 cm, 120 cm) from the sensor plane for both the MLP and the BDTG methods. The analysis showed that a bare source localization resolution of the order of less than 15 cm could be archived in both horizontal and vertical directions after at least of 40 sec of exposure time, whilst the corresponding depth resolution is of the order of less than 20 cm. The resolution gets slightly improved by increasing the exposure time. The two machine learning methods give very similar results. In addition a slightly shielded source can be also localized in 3D with corresponding resolutions

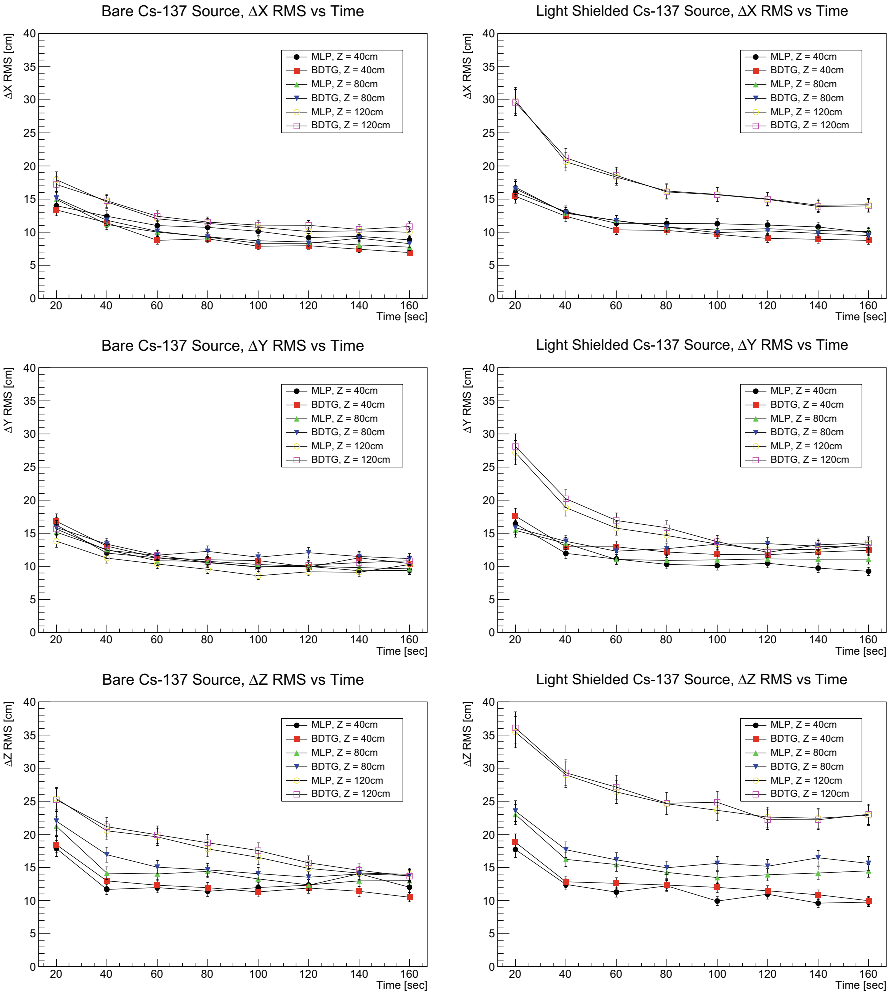

Fig. 7 Horizontal (top), Vertical (middle) and Depth (bottom) spatial accuracy as a function of the exposure time calculated using the machine learning methods for a bare ^{137}Cs source (left) and slight shielded ^{137}Cs source (right) located in various distances away from the sensor plane

of less than 20 cm in both horizontal and vertical directions and 30 cm in depth after at least of 40 sec of exposure time within a monitored volume of 5 m × 2.8 m × 2 m. In the case of the shielded source the mean value of the accuracy distribution is affected by a small bias which reaches the maximum of 15 cm at large values of the depth coordinate. This could be caused by the small number of recorded counts in this region and can be improved by using sensors with larger sensitive volume.

4 Radioactive Source Localization Using a Single Sensor in 360°

To overcome the limitations of the restricted field of view of the Gamma-Ray Imaging systems mentioned in the introduction, in this section a device capable to perform radioactive source localization in 360° using a single scintillator crystal will be discussed. The response of such a device has been studied using simulation. A similar system has also been introduced in [17].

As it can be seen in Fig. 8 the proposed device consists of a 2″ × 3″ NaI cylindrical scintillator. At one endcap of the scintillator cylinder a SiPM array of 12 × 12 cells is placed. The source can be placed around the axis of the scintillator (Y axis) as it is shown in the Fig. 8.

An extended simulation campaign for the proposed device has been performed using the ROOT-based package ANTS2 [18]. Various source types spanning from ^{241}Am to ^{60}Co (i.e. ^{241}Am, ^{57}Co, ^{152}Eu, ^{22}Na, ^{137}Cs and ^{60}Co sources) positioned around the detector in 36 different azimuthal angle positions, with a separation angle of 10° between them. In the simulation the light emitted by the NaI scintillator crystal has been collected by the SiPM array, stored and subsequently analyzed. In Fig. 9 an indicative simulated response of the SiPM array is shown for a ^{57}Co source that emits from an azimuthal angle of 160° (conventionally, source azimuthal angle of 0° is considered as a source emitting from the positive *x-axis*). Similarly in Fig. 10 an indicative simulated response of the SiPM array is shown for a ^{137}Cs source that emits from an azimuthal angle of 270°.

From the figures above it is obvious that the azimuthal direction of the radioactive source can be estimated in 360° around the device. As a first approach a simple analytical algorithm has been used to estimate the source azimuthal direction by analyzing the SiPM response as follows:

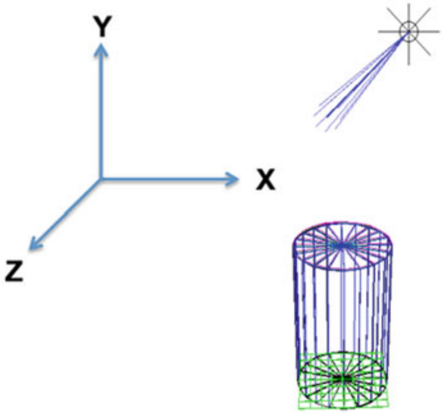

Fig. 8 Simulated Scintillator (Blue-Black line), the SiPM layer (Green line) and the source using the ANTS2 [18] software

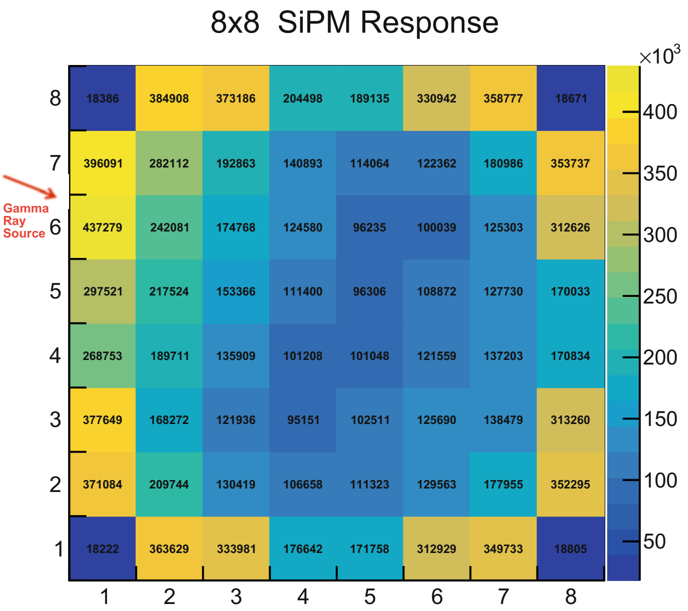

	1	2	3	4	5	6	7	8
8	18386	384908	373186	204498	189135	330942	358777	18671
7	396091	282112	192863	140893	114064	122362	180986	353737
6	437279	242081	174768	124580	96235	100039	125303	312626
5	297521	217524	153366	111400	96306	108872	127730	170033
4	268753	189711	135909	101208	101048	121559	137203	170834
3	377649	168272	121936	95151	102511	125690	138479	313260
2	371084	209744	130419	106658	111323	129563	177955	352295
1	18222	363629	333981	176642	171758	312929	349733	18805

Fig. 9 SiPM indicative response for a ^{57}Co source emitting from an azimuthal angle of 160° (red arrow)

- The centre of gravity (CoG) of each event (response of SiPM array to a γ-ray from the source) is calculated as the weighted sum of each SiPM cell local position multiplied by the deposited number of counts in the corresponding cell and divided by the sum of the recorded counts from all SiPM cells.
- Then a directional vector is formed by taking as the vector starting point the centre of the SiPM array and as the vector ending point the above mentioned CoG point.
- The vectorial sum of the directional vectors is calculated from all the available events.
- Finally, the azimuthal angle of the resultant vector is used as an estimator of the source azimuthal angle.

The advantage of this approach is that the background events that have a uniform distribution response on the SiPM array cancel out each other during the vectorial sum calculation. More advanced machine learning regression techniques could be also applied for improved azimuthal resolution.

In Fig. 11 the difference between the azimuthal angle estimated by the above described algorithm and the true source azimuthal angle is presented for ^{57}Co, ^{137}Cs and ^{60}Co sources. The estimated source azimuthal angle resolution is of the order of 1° in case of low energy sources like the 122 keV ^{57}Co source, while it is of the order of 9° for much higher energy sources like the 1172 keV, 1332 keV ^{60}Co source showing an almost linear behavior.

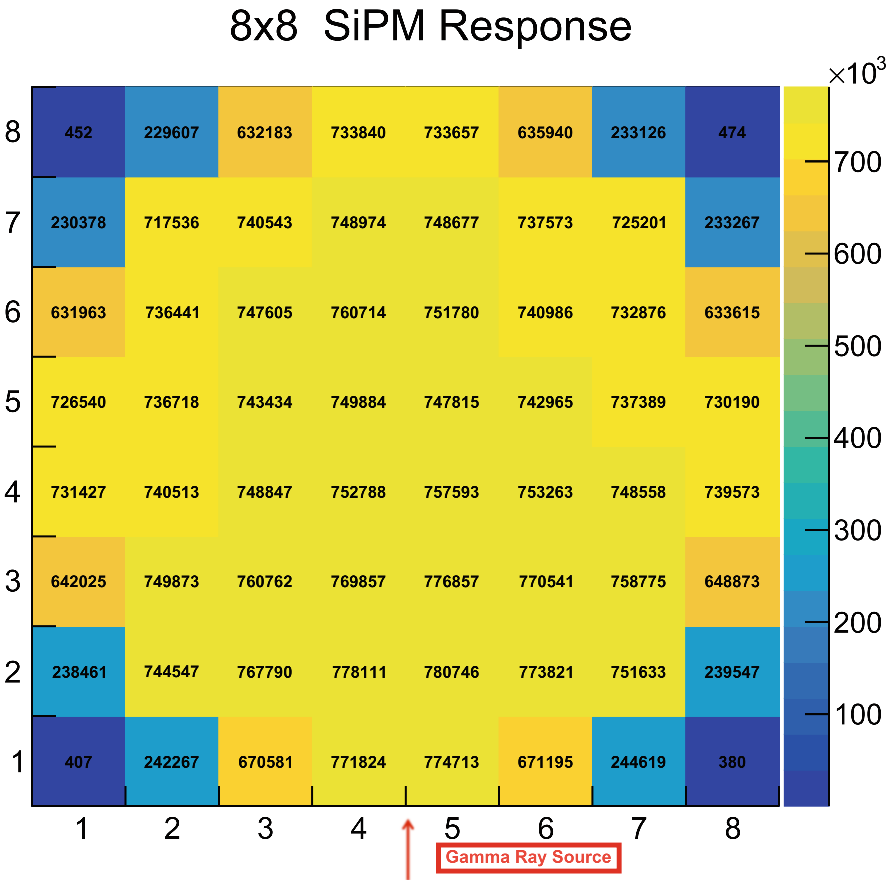

	1	2	3	4	5	6	7	8
8	452	229607	632183	733840	733657	635940	233126	474
7	230378	717536	740543	748974	748677	737573	725201	233267
6	631963	736441	747605	760714	751780	740986	732876	633615
5	726540	736718	743434	749884	747815	742965	737389	730190
4	731427	740513	748847	752788	757593	753263	748558	739573
3	642025	749873	760762	769857	776857	770541	758775	648873
2	238461	744547	767790	778111	780746	773821	751633	239547
1	407	242267	670581	771824	774713	671195	244619	380

Fig. 10 SiPM indicative response for a ^{137}Cs source emitting from an azimuthal angle of 270° (red arrow)

The proposed system can be used to find the direction of sparse sources in 360° without using any moving parts [19]. It is also capable to find the direction of more than one source, provided that they have different emitted γ-ray energy. This can be done by taking into account the recorded energy spectrum. By selecting a specific energy range of known sources the localization algorithm can be applied only for the photo-peak events. Thus, the direction of each individual source can be estimated.

As an example let's suppose three different sources ^{57}Co, ^{137}Cs and ^{60}Co which are located in azimuthal angles of 160°, 270° and 60° respectively. Figure 12 shows the simulated energy spectrum recorded by the system (no NORM is introduced because as explained previously noise events have a uniform distribution in all SiPM cells).

Then, by selecting the energy in the range 100 keV $< E_\gamma <$ 150 keV (corresponding to the photo-peak of the ^{57}Co energy spectrum) the estimated azimuthal

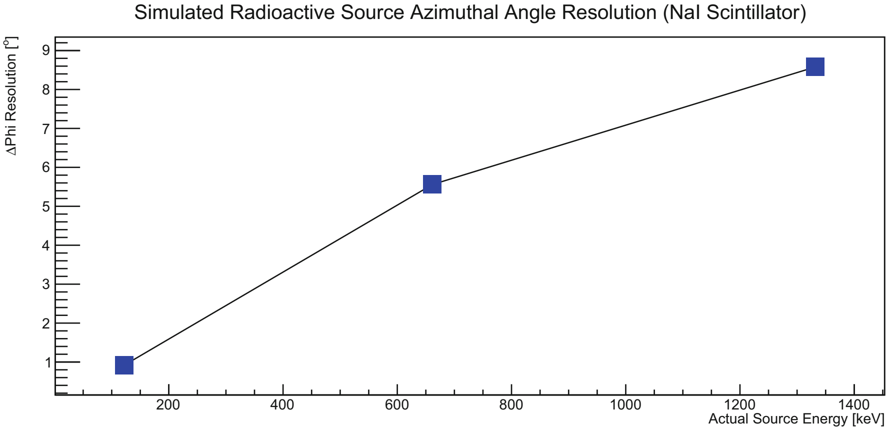

Fig. 11 Difference between the azimuthal angle estimated by the CoG algorithm and the true source azimuthal angle as a function of the source energy for the indicative simulated device

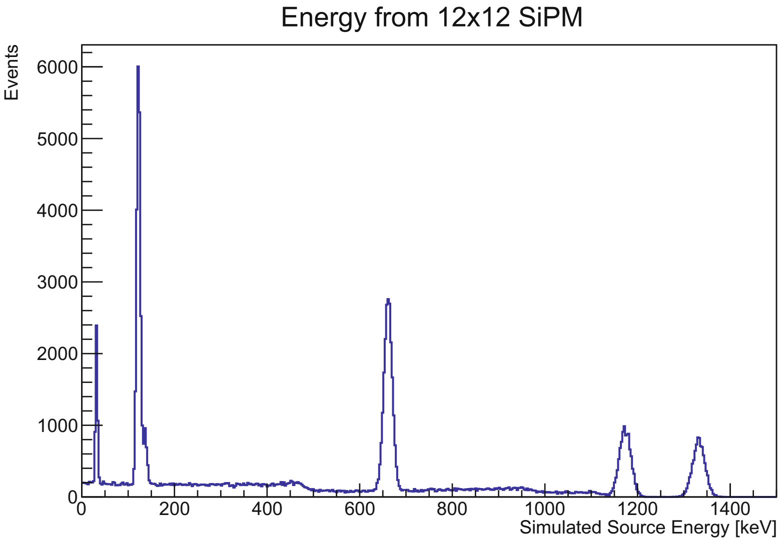

Fig. 12 The simulated energy spectrum by the indicative device while being irradiated simultaneously from three different sources ^{60}Co, ^{57}Co and ^{137}Cs of the same activity located at the same distance away from the device and at azimuthal angles of 60°, 160° and 270° respectively

angle given by the above described CoG algorithm was calculated to be 160.92°. When the energy window was selected to be in the range 640 keV < E_γ < 700 keV (corresponding to the photo-peak of the ^{137}Cs energy spectrum) the estimated azimuthal angle given by the CoG algorithm was calculated to be 272.22°. Finally, when the energy window was selected to be in the range 1100 keV < E_γ < 1400 keV (corresponding to the photo-peak of the ^{60}Co energy spectrum) the estimated azimuthal angle was calculated to be 61.76°. The above estimated source azimuthal angles are very close to their true values.

5 Conclusions

In this chapter various methods for localizing radioactive sources have been discussed. Some ideas to tackle the limited field of view of the Gamma-Ray Imaging (GRI) systems were presented. Firstly in Sect. 2, a system with movable detector head inside a collimator which is placed on a rover can localize radioactive sources with adequate accuracy on the expense of exposure time is described. Secondly in Sect. 3, a modular network of radiation detectors that can cover larger space areas without specific entry or exit points gives very promising radioactive source localization accuracy results. Finally in Sect. 4, a concept for 360° radioactive source localization capable device without moving parts has been analyzed using simulation data. In this device, the localization results showed remarkable accuracy for sources energies spanning for a few tens of keV to the MeV range.

References

1. Hughes, K. A., & Lightfoot, J. A. *RadScan 600 - a portable instrument for the remote imaging of gamma contamination: Its design and use in aiding decommissioning strategy*. 1996 IEEE nuclear science symposium - conference record (Vol. 1, 2 and 3). BNFL Instruments Ltd.
2. RadScan800, https://citeseerx.ist.psu.edu/viewdoc/download?doi=10.1.1.561.3193&rep=rep1&type=pdf
3. Amgarou, et al. (2016). A comprehensive experimental characterization of the iPIX gamma imager. *JINST, 11*, P08012.
4. Dubos, S., et al. (2015). ORIGAMIX, a CdTe-based spectro-imager development for nuclear applications. *Nuclear Instruments and Methods in Physics Research Section A, 787*, 302.
5. Jeong, M., et al. (2018). Scalable gamma-ray camera for wide-area search based on silicon photomultipliers array. *Review of Scientific Instruments, 89*, 033106. https://doi.org/10.1063/1.5016563
6. Llopart, X., et al. (2007). Timepix, a 65k programmable pixel readout chip for arrival time, energy and/or photon counting measurements. *Nuclear Instruments and Methods in Physics Research Section A, 581*(1–2), 485–494. https://doi.org/10.1016/j.nima.2007.08.079
7. Cieślak, M. J., et al. (2016). Coded-aperture imaging systems: Past, present and future development - a review. *Radiation Measurements, 92*, 59.
8. Paradiso, V., et al. (2017). A panoramic coded aperture gamma camera for radioactive hotspots localization. *Journal of Instrumentation, 12*, P11010. https://doi.org/10.1088/1748-0221/12/11/P11010
9. Everet, D. B., et al. (1977). Gamma-radiation imaging system based on the Compton effect. *Proceedings of the IEEE, 124*, 995–1000.
10. Ordonez, C. E., et al. (1997). *Doppler broadening of energy spectra in Compton cameras*. Nuclear Science Symposium, IEEE' Vol. 2 (pp. 1361–1365).
11. Munoz, E., et al. (2017). Performance evaluation of MACACO: A multilayer Compton camera. *Physics in Medicine & Biology, 62*(18), 7321–7341.

12. Zhang, J.-P., et al. (2019). Prototype of an array SiPM-based scintillator Compton camera for radioactive materials detection. *Radiation Detection Technology and Methods, 3*, 17. https://doi.org/10.1007/s41605-019-0095-1
13. Takeda, S., et al. (2015). A portable Si/CdTe Compton camera and its applications to the visualization of radioactive substances. *Nuclear Instruments and Methods in Physics Research Section A, 787*, 207–211.
14. Turecek, D., et al. (2018). Compton camera based on Timepix3 technology. *Journal of Instrumentation, 13*, C11022.
15. Fragkos, G., Karafasoulis, K., Kyriakis, A., & Potiriadis, C. (2020). Localization of radioactive source using a network of small form factor CZT sensors. *Journal of Instrumentation, 15*(04), C04015–C04015. https://doi.org/10.1088/1748-0221/15/04/C04015
16. Kyriakis, A., Karafasoulis, K., & Zampetaki, O. (2022). Radioactive source localization using a data driven MVA method. *Journal of Instrumentation, 17*, C03018. https://doi.org/10.1088/1748-0221/17/03/C03018
17. Buonanno, L., et al. (2020). A directional gamma-ray spectrometer with microcontroller-embedded machine learning. *IEEE Journal on Emerging and Selected Topics in Circuits and Systems, 10*(4), 433–443.
18. Morozov, A., et al. (2016). ANTS2 package: Simulation and experimental data processing for anger camera type detectors. *Journal of Instrumentation, 11*(4), Art. no. P04022.
19. ANSTO - CORIS360. https://www.ansto.gov.au/products-services/detection-imaging/coris360

Concepts for Solid State Detectors in Space-Based Gamma-Ray Astrophysics

Giulio Lucchetta

1 Introduction

Earth's atmosphere is opaque to most electromagnetic radiation, including gamma rays. Therefore, gamma-ray astronomy can only be performed from satellites in space or by balloon flights in the high stratosphere.

Since X-rays canonically indicates the part of electromagnetic radiation with wavelengths λ comprised between 0.01 and 10 nm, the gamma ray energy band conventionally indicates photons with energies higher than $\sim$120 keV (corresponding to $\lambda < 0.01$ nm).[1] However, the separation of these two bands is not so strict in astroparticle physics, and, in many references, the end of the hard X-ray regime overlaps with a small portion of soft gamma rays. Space-based gamma-ray astrophysics extends to an energy around 100 GeV: at these energies, the flux of astrophysical sources is generally too low to allow a significant statistics, given the characteristic satellites' collection areas ($\sim$ m^2) and mission lifetimes ($\sim$5-10 years). At energies above hundred of GeV gamma-ray astronomy becomes the domain of ground based observatories such as Imaging Atmospheric Cherenkov Telescopes (IACT) and Extensive Air Shower (EAS) observatories. In this case, gamma rays are observed indirectly, by detecting the electromagnetic cascades induced by photons in the Earth's atmosphere. An overview of ground-based gamma-ray astrophysics can be found in [22].

---

[1] According to the relation $E = \frac{hc}{\lambda}$, where h is the Plank's constant and c the speed of light.

G. Lucchetta (✉)
Institut de Fisica d'Altes Energies (IFAE), The Barcelona Institute of Science and Technology, Barcelona, Spain
e-mail: glucchetta@ifae.es

© The Author(s), under exclusive license to Springer Nature Switzerland AG 2023

J. Du, K. (K.) Iniewski (eds.), *Gamma Ray Imaging*,
https://doi.org/10.1007/978-3-031-30666-2_6

The detection of gamma rays in space is challenging, due to the penetrating nature of the radiation, requiring the employment of large detector volumes. At the same time, several constraints in mass, power consumption, overall mission budget and telemetry needs to be met. Mechanical and thermal stability are also fundamental requirements: the employed materials need to survive the vibrations and large sustained acceleration generated during the rocket launch, and deal with challenging thermal stresses in orbit. For example in a low-Earth orbit, many times each day, the spacecraft makes a transition from being in full Sun to the cold of deep space. Thermal analysis and control must be considered in vacuum, where radiative transport, rather than conduction or convection, is the principal form of heat transfer. Expendables such as fuel or, if employed, cryogens limit the lifetime of a mission. Finally, and most importantly, detectors and space instrumentation face an intense charged particle environment due to the high flux of cosmic rays, requiring the on-board electronics to be radiation-hardened, in order to minimize failures.

Space-based gamma-ray instrumentation typically uses detectors developed for nuclear and particle physics: the most common choices are based on scintillation or solid-state detectors; additionally, gas detectors has been employed in some applications. The choice of detector technology depends on the energy range of interest, expected levels of signal and background, required energy and spatial resolution, costs and other factors. The instruments are generally complex, as they often comprise multiple sub-systems integrated in a compact geometry. Reliability of long-term operation in space can only be assured by lengthy and expensive testing before launch, while the instrument design and telescope performance are optimized through extensive simulations, which attempt to consider on-orbit conditions as accurately as possible, in order to maximize the scientific return within all the given constraints.

In this chapter, after a small summary of space-based gamma-ray astrophysics history (Sect. 2), some general concepts concerning orbits and background sources for gamma-ray missions are discussed (in Sects. 3 and 4 respectively). The main detection techniques employed in gamma-ray telescopes are deeply discussed in Sect. 5. Finally a glimpse of different detectors used in gamma-ray telescopes is given in Sect. 6; solid state detectors are exhaustively described in Sect. 7: their fundamental role in current operating systems as well as prospects for future proposed mission are highlighted.

2 Brief History of Space-Based Gamma-Ray Astronomy

The dawn of gamma-ray astrophysics dates back in the 1960s, with the launch of the first artificial satellites; the gamma-ray telescope on the OSO-3 satellite (Orbiting Solar Observatory 3, 1967–1969), made of a multilayer scintillation conversion detector and a calorimeter, detected for the first time 621 events attributed to cosmic gamma rays with energies above 50 MeV, with a distribution concentrated along the galactic disk [37]. The next generation of high-energy telescopes, employed tracking detectors, made of spark chambers. Few years after the measurements of OSO-3, the NASA[2] SAS-2 (Small Astronomy Satellite 2, 1972–1973) and the ESA[3] COS-B (Celestial Observation Satellite B, 1975–1982) missions detected the first gamma-ray sources, among which the Crab and Vela pulsars, and the blazar 3C273 [24, 62].

The field has rapidly developed in the next decades. Important milestones have been achieved thanks to the operation of the Compton Gamma-ray Observatory (CGRO, 1991–2000) [38] first, and the current generation of gamma-ray observatories and telescopes: INTEGRAL[4] (2002-) [39], AGILE[5] (2007-) [66] and Fermi-LAT[6] (2008-) [6]. Nowadays, more than 5000 sources have been detected in the GeV domain [1]. Future proposed missions are focused on the exploration of the deeply uncovered MeV regime (see Fig. 1), or to succeed instruments like Fermi-LAT and AGILE after their end of operation.

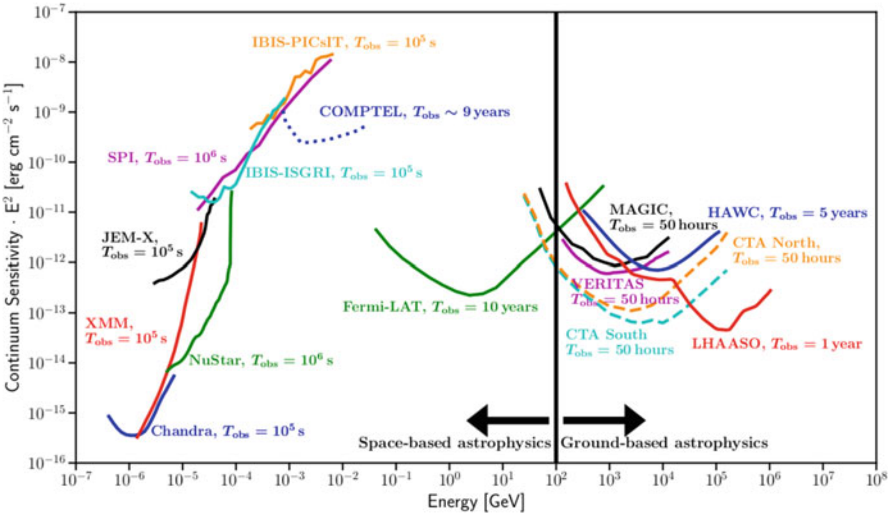

Fig. 1 Continuum sensitivity of different X-ray and gamma-ray instruments, as a function of the energy: past missions are shown in dotted lines, currently operating instruments in solid lines and future planned missions in dashed lines. The sensitivity of a telescope quantify its ability to detect faint sources and is often given as high-level performance parameter: it represents the minimum flux that an astrophysical source need to possess, in order to be detected within a certain observation time and significance (usually $3\,\sigma$ or $5\,\sigma$). The observation time for each telescope reflects the typical operation mode of the instrument itself. The energy of ∼100 GeV marks the transition between space-based gamma-ray astrophysics and ground-based gamma-ray astrophysics. Plot adapted from [44]

---

[2] National Aeronautics and Space Administration.

[3] European Space Agency.

[4] INTErnational Gamma-Ray Astrophysics Laboratory.

[5] Astro-Rivelatore Gamma a Immagini Leggero.

[6] Fermi Large Area Telescope.

3 Orbits for Spaced-Based Gamma-Ray Instruments

The choice of orbit is one of the most important tasks when planning a gamma-ray instrument. The choice is dictated by scientific requirements, like required sky coverage and background level, and by technical constraints as well, such as availability of launchers, costs, and position of ground station to download the acquired data. The most common choice is a low-Earth orbit or LEO. As the name suggests, it is an orbit that is relatively close to Earth's surface, typically at an altitude between 300 and 2000 km (around 1/3 of the Earth's mean radius) and almost circular [4]. The lower limit for the orbit is set by rapid orbital decay caused by the drag of the atmosphere. In practice, most gamma-ray space instruments launched were and are placed between ∼400 and 600 km. At these altitudes the orbital period is ∼95 min and the orbital speed is high, about ∼7.6 km/s. Because of the low orbit, launch costs are also reduced, since smaller and less powerful launchers are needed to reach the flight altitude. A second major advantage of a LEO is that the Earth's magnetic field naturally protects, to some extent, a telescope against the intense charged particles flux generated by cosmic rays or by the Sun. On the other hand, LEOs present some problems and limitations as well. First of all, a satellite in a low-Earth orbit is a moving target for a ground station. Due to the high orbital speed and fast orbit period, the visibility of the satellite by the ground station is limited to ∼10–20 min per orbit. Therefore the acquired data need to be adequately stored on-board and quickly downloaded at the passage over the receiving ground station. Secondly a telescope on a LEO cannot observe all the sky at the same time, being occulted by the Earth itself; the Earth's limb angle at an altitude of 500 km is ∼112° from zenith.

Few telescopes are also launched to high elliptical orbits, spending most of the time outside the Van Allen radiation belts. This is the case, for example, of the X-ray instrument XMM-Newton or the INTEGRAL observatory. These orbits are highly elliptical, with a great difference between the apogee and the perigee: for XMM-Newton the perigee is around 6000 km and the apogee is 115,000 km, while for INTEGRAL the perigee and apogee are respectively ∼3000 km and ∼150,000 km. Despite the higher average background encountered, these orbits offer some advantages like the possibility to observe the entire sky at the same time with longer uninterrupted observations, and more continuous down and upper link with the ground station. Another potentially interesting orbit for a gamma-ray instrument could be an orbit in the Lagrangian point L2, at about 1.5 million kilometres from Earth on the opposite side of the Sun.

Finally, gamma-ray instruments can also fly in stratospheric balloons, at an altitude of ∼30–40 km. Despite the limited observation time of the flight, balloon campaigns offer great opportunities to test prototype instruments and technologies.

4 Background Sources for Space-Based Gamma-Ray Instruments

Gamma-ray telescopes are constantly bombarded by an intense flux of charged particles, photons and neutrons. The number of these background events typically exceeds the signal received from astrophysical sources by order of magnitudes. Cosmic rays are composed for about 80% of free protons, followed by alpha particles (about 15%) and heavier nuclei, while electrons and positrons contribute to about $\sim$1% [54]. The cosmic rays rate changes within the 11-year solar cycle, exhibiting an anti-correlation: since the magnetized solar wind decelerates and partially prevents cosmic rays from reaching the inner solar system, the highest rate is measured for minimum solar activity and viceversa. Moreover, satellites on LEOs are exposed to much lower fluxes than spacecrafts orbiting outside the Van Allen radiation belts, since the Earth's magnetic field offers a natural protection against energetic solar particles and cosmic rays. Due to Earth's magnetic field configurations, the background flux is strongly modulated, depending greatly on the reached latitudes, and so the inclination of the satellite: the effect is maximum on the equator and minimum at the poles. Additionally an increased flux is measured in the so-called *South Atlantic Anomaly* (SAA), a region above South America and the Atlantic Ocean where the inner Van Allen radiation belt comes closer to Earth's surface, dipping down to an altitude of about 200 km. The flux of charged particles is so intense in the SAA that the instrumentation is usually switched off when a telescope passes through this region.

In a low-Earth orbit the interaction of cosmic rays with the atmosphere produces many lower-energy secondary cosmic rays, mainly protons, electrons and positrons. In addition to the charged component also gamma rays are produced by hadronic interactions of protons and alpha particles, or by bremsstrahlung of electrons and positrons. The flux of this photon background component is particularly bright at the Earth's limb, since cosmic rays entering the atmosphere near grazing incidence produce showers whose forward moving gamma rays can penetrate the thin atmosphere layer met.

Another main background component and, at the same time, an important science topic for a gamma-ray instrument comes from photons of both Galactic and extragalactic origin.[7] The extragalactic gamma-ray emission, or EGB for short, is a diffuse and isotropic photon background, due to unresolved sources such as blazars, Seyfert galaxies and star-forming galaxies. Concerning the galactic gamma-ray component, its emission manly consists of unresolved sources from active stars, compact objects and supernova remnants, superimposed on a diffuse continuum radiation from cosmic rays interaction with the interstellar medium.

Finally, the flux of cosmic rays and gamma rays, constantly hitting the spacecraft, activates the satellite materials, producing radioactive isotopes. The decay of these radioactive isotopes into stable elements results in a delayed background component composed of electrons, positrons and gammas. The energy spectrum of this instrumental background component is described by a continuum emission plus several characteristic lines,[8] at energies from keVs to MeVs. The total rate depends strongly on the materials and payload of the spacecraft, and its orbit. A quantitative and extensive study of the different background components here described for a low-Earth orbit can be found in [20].

---

[7] These components are considered as background for observations of gamma-ray sources like pulsars, supernovae and active galactic nuclei because their flux superimposes to the "true" signal aimed to be measured.

4.1 Impact of Background on Space Telescopes

Background events have several detrimental effects on space telescopes. First of all, highly energetic particles and ions constantly hitting the detectors and readout electronics deteriorates their performance, increasing the leakage current and noise, and causing errors such as single-event upset and latch-up. Therefore, space electronics must use radiation-hardened components that are made resistant to damage caused by the ionizing radiation. Secondly the background can trigger the detectors, generating unwanted data superimposed to the faint signal from cosmic sources. Discriminating cosmic gamma rays from all these background sources is the biggest challenge in the design of a successful space telescope. Strategies to reduce the effect of background, include, as mentioned before, the choice of orbit, but also shielding, optimization of the detector geometry and choice of material, and event analysis procedures. Due to the highly penetrating nature of the background radiation, the use of a thick active shield is feasible only at lower energies. The most common approach is to surround the instrument with an anti-coincidence detector; plastic scintillator is the material of choice, because of its high efficiency for detection of charged particles but low probability of absorbing gamma rays. The anti-coincidence shield should be built as hermetic as possible: particles that will go undetected or enter through uncovered parts of the geometry will contribute to the background.

Event analysis can further contribute to separating the signal from background, depending on the energy range and the detection techniques exploited.

5 Detection Techniques for Gamma-Ray Astrophysics

The main interaction mechanisms for X-rays and gamma rays with matter are photoelectric effect, Compton scattering and pair creation; their relative importance depends on the energy of the incoming radiation and the interaction medium (see

---

[8] A particularly strong background line is expected to be, for example, the 511 keV annihilation line, resulting from various $\beta+$ decays.

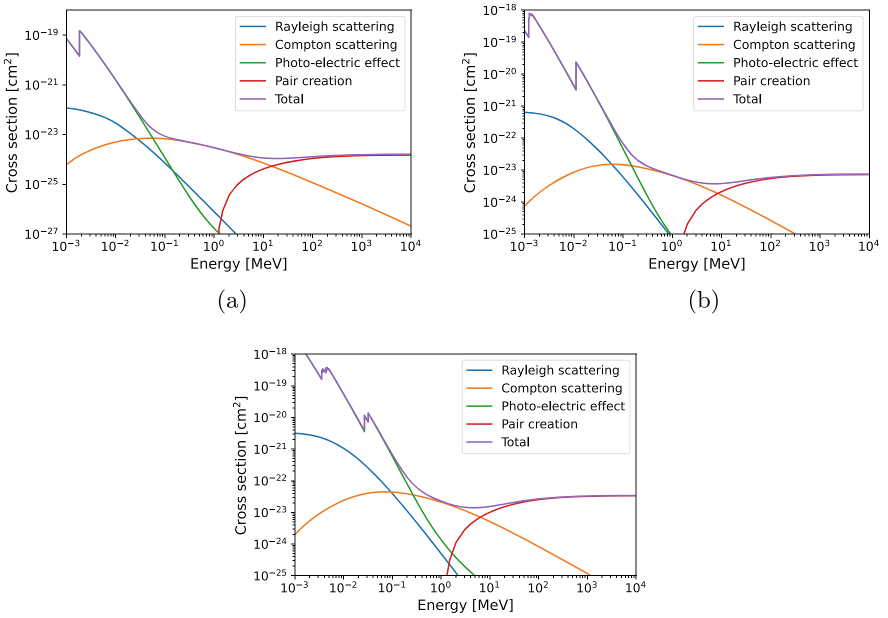

(a)

(b)

(c)

Fig. 2 Cross sections for photon interactions in silicon, germanium and cadmium zinc telluride. For X-rays and gamma rays the three dominating interaction mechanisms are photo-electric effect, Compton scattering and pair creation. Data are taken from the NIST database: https://physics.nist.gov/PhysRefData/Xcom/html/xcom1.html. (**a**) Silicon. (**b**) Germanium. (**c**) Cadmium zinc telluride

Fig. 2). In fact the cross section for all these interaction mechanisms depends on some power n of the atomic number Z of the material, Z^n; in the case of photoelectric absorption $4 < n < 5$, for Compton scattering $n = 1$ and for pair production $n = 2$. For photon energies up to hundreds of keV the photoelectric effect is the dominant interaction process; the photon transfers its total energy to an atom, with the emission of a shell electron (also referred to as photoelectron). In the Compton effect, the photon is scattered elastically off a shell electron; a fraction of the photon's energy and momentum is transferred to the electron. Compton scattering dominates at energies between hundreds keV up to ∼5–10 MeV, for most materials. If the energy of the photon is more than twice that of the electron rest mass (1.022 MeV), the photon can convert in the field of a nucleus into an electron-positron pair. Pair production is the dominant interaction process at energies higher than 10 MeV.

Since the domain of space-based gamma-ray astrophysics extends from hundreds keV to hundreds GeV, different telescope concepts and mode of operation need to be employed in order to cover such extended energy range depending on the main interaction mechanism of photons with matter.

5.1 Collimators

The simplest method to determine the origin of gamma rays, at least at lower energies, is by obscuring part of the field-of-view of the detector through a *collimator* (see Fig. 3a). The collimator generally consists of a high-Z material with an array of narrow holes . All the radiation not co-axial to the collimating holes is completely blocked by the collimator itself, allowing only those photons coming from a precise direction in the sky, to pass and reach the detector plane (the camera) which measures the incoming radiation. The collimator's holes can be shaped as a parallel grid, or in a so-called "lobster eye" configuration, additionally retaining a focusing effect [16]. A collimator is intrinsically capable of imaging spectroscopy, since the directional information of each incoming photon is kept on the detector plane. These telescopes, however, have a very small field-of-view. Therefore, observations of large structures would require re-orientation of the instrument. Another large drawback is that background determination requires off-source pointing, reducing the observation time. Collimators are an effective tool for imaging gamma rays with energies below a few MeVs, since the high penetration power of higher-energy gamma rays typically necessitates a large volume to shield against non-coaxial radiation, making them unsuitable for use in space telescopes.

An example of this kind of technology was the Phoswich Detection System (PDS) on-board the Beppo-SAX satellite (1996–2002) [25]: the instrument consisted of a collimator made of tantalum tubes with hexagonal section, and NaI(Tl)/CsI(Na) phoswich scintillators[9] with a total geometric area of 795 cm^2. The PDS experiment covered the energy band between 15 and 300 keV with a field-of-view of 1.3° FWHM[10] and an energy resolution $\leq$ 15% at 60 keV. Similar in the design was also the Oriented Scintillation Spectrometer Experiment (OSSE) on-board the Compton Gamma Ray Observatory (CGRO, 1991–2000) [30]. OSSE employed 4 identical NaI(Tl)/CsI(Na) phoswich detectors, with a diameter of 33 cm and a thickness of 17.6 cm, and tungsten collimators defining a $3.8° \times 11.4°$ FWHM field-of-view. The telescope covered the range between 50 keV and 10 MeV, with an energy resolution of 7.8% at 662 keV and 3.1% at 6.13 MeV.

5.2 Coded-Masks

Another method to image gamma rays to energies up to $\lesssim$10 MeV, is through *coded-masks* [23]; like collimator systems, a coded-mask camera comprises two elements: the coded-mask itself, and a position-sensitive detector (Fig. 3c). The coded-mask consists of a plate with different areas either transparent or opaque to photons in a

---

[9] Each detector was composed by a 3 mm NaI(Tl) crystal and a 50 mm thick CsI(Na) crystal optically coupled, forming what is known as phoswich (acronym of phosphor sandwich).

[10] Full width at half maximum.

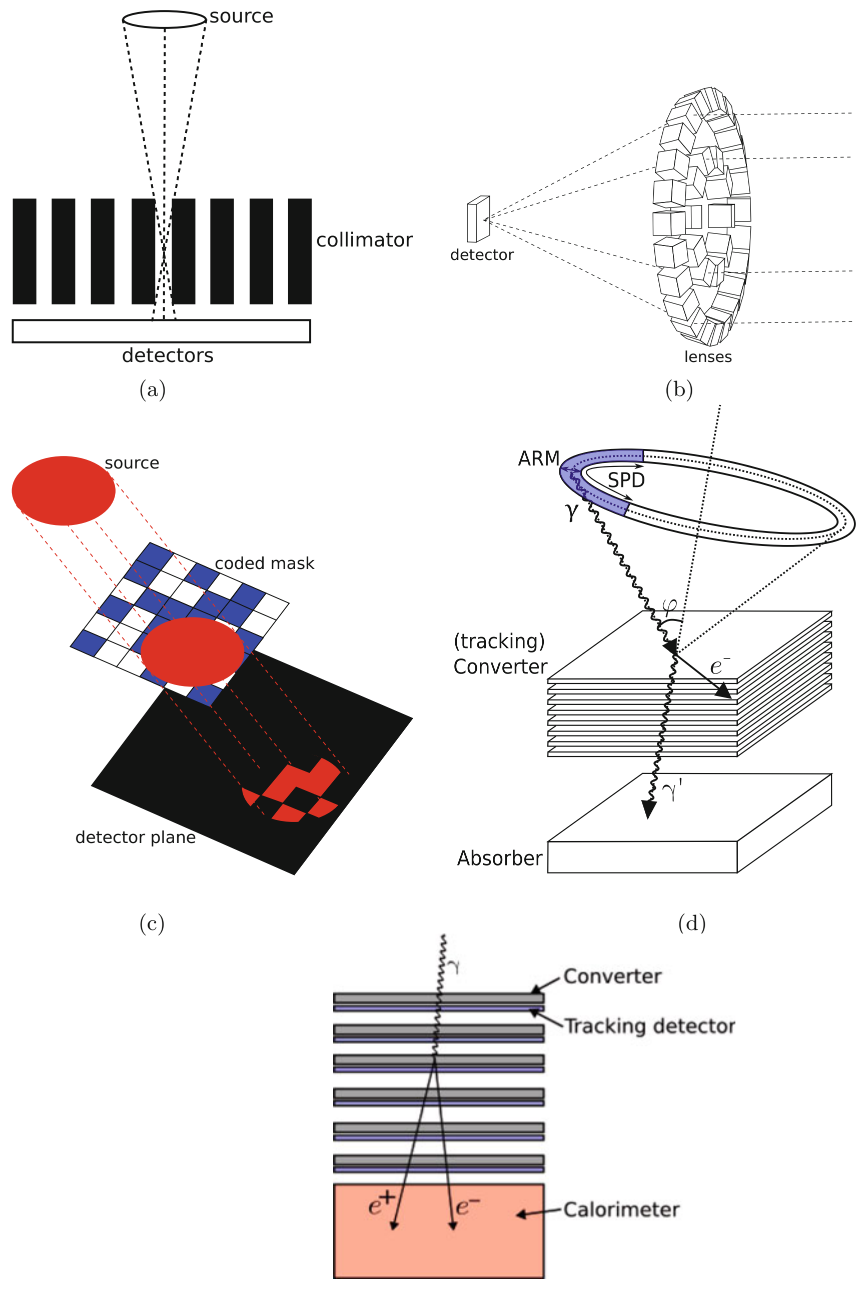

(a) (b) (c) (d) (e)

Fig. 3 Schematic of the main detection techniques and telescopes employed in gamma-ray astrophysics. (**a**) Collimator. (**b**) Laue lens, adapted from [26]. (**c**) Coded-mask, adapted from [18]. (**d**) Compton (tracking) telescope. (**e**) Pair telescope

selected energy range (also called mask elements), distributed in a specific pattern. The detectors, located below the mask, have a spatial resolution similar to the mask element's size. In this way a fraction of the incoming light is blocked by the mask, casting a unique shadow onto the detector surface, while the remaining radiation "illuminate" only certain elements of the camera. Due to the specific pattern of the mask, a different image is created for every source, depending on its direction. Indicating with P the mask pattern used to modulate the flux of the source S, the recorded image I on the detector can be written as the convolution of these two elements, plus a background term B:

$$I = P * S + B\,. \tag{1}$$

The original distribution of the source's photons can be obtained by means of deconvolution.

The resolution of a coded-mask depends on the mask element size, the spatial resolution of the employed detectors and the distance between the mask and the detector plane. For currently operating instruments like Swift-BAT[11] and INTEGRAL-IBIS[12] the angular resolution is around ∼10–20 arcmin. The energy range is limited by the detector range and the transparency of the mask frame (and, therefore, the mask thickness).

The shape of the mask element may be arbitrary, but the most common are rectangular and hexagonal [42]. Concerning the detectors, the most commonly used are scintillators like sodium iodide (NaI) and cesium iodide (CsI), or semiconductor materials such as germanium (Ge) or cadmium-zinc-telluride (CdZnTe). Current telescopes of this type are SPI[13] [70] and IBIS [69] on-board the INTEGRAL observatory (2002-), the CZT Imager (CZTI) [55] on-board *AstroSat* (2015-) and Swift-BAT (2004-) [8]. Moreover, a novel approach combining a Compton imaging telescope (see Sect. 5.4) and a coded-mask has been recently proposed with GECCO[14] [51].

5.3 *Laue and Fresnel Lenses*

Refraction and reflection of high-energy photons onto a focal plane is difficult; focusing gamma rays in the ∼100–1000 keV energy range would be possible with *Laue* [26] or *Fresnel lenses* [60], based on diffraction.

A Laue lens is made of many small high-quality crystals (∼1–2 cm in size) placed on concentric circles. They are oriented in such a way that the crystal planes diffract the radiation towards a common focal point, allowing to collect the signal into a small detector. By concentrating incoming gamma rays from a large collector (the lens), into a small, separated point (the detector), the instrumental background is drastically reduced compared to any other observational method. For each individual crystal gamma rays are diffracted in a transmission configuration, passing through the entire crystal, if the Bragg equation is satisfied:

---

[11] Burst Alert Telescope.

[12] Imager on Board the INTEGRAL Satellite.

[13] SPectrometer on INTEGRAL.

[14] Galactic Explorer with a Coded aperture mask COmpton telescope.

$$2d \sin\theta = n\lambda = n\frac{hc}{E}\,, \tag{2}$$

where d is the spacing between the crystal's atomic planes, θ the diffraction angle and λ the photon's wavelength (related to the energy E via the Planck relation). The response of a Laue lens is strongly energy dependent, with each crystal diffracting only radiation in a small energy band. In order to obtain a lens operating in board energy range many crystals need to be place at different concentric radii: the inner radius diffracts photons at highest energy, while the outer diffracts photons at lowest energy. Laue lenses can reach a great angular resolution below 1 arcmin [26]. This technology has been demonstrated by CLAIRE [72], the only Laue lens instrument that has actually flown up to now, in two balloon campaigns in 2000 and 2001. The instrument employed 659 germanium/silicon mosaic crystals and was design to focus photons with energies ~170 keV onto a cooled Germanium detector with 9 elements, each $15 \times 15 \times 40\,\mathrm{mm}^3$. Missions like MAX [7], GRI [34] and DUAL [73] have been proposed; however no satellite employing Laue lenses have ever flown into space. This is reasonably due to several technical challenges affecting this technology, related to the overall instrument complexity, the need for two satellites to fly in formation due to the long focal length needed (tens to few hundreds of meters), the production of large quantities of good-quality crystals, and the high accuracy required for positioning and alignment of the crystals.

Fresnel lenses for soft gamma-ray astrophysics, based on diffraction from manufactured structures [60], have been discussed only at a conceptual level. Despite the astonishing angular resolution (on the micro-arcseconds level) that such lenses could potentially achieve, major difficulties need to be overcome: a Fresnel lens requires an extremely long focal length ($\sim 10^8$ m) and the bandwidth in which the instrument can operated is narrow because of chromatic aberration.

5.4 Compton Telescopes

In 1923 Arthur Holly Compton firstly showed the elastic scattering of photons and electrons in atomic shells, as primary mechanisms of interaction gamma rays in matter in the energy range from ~100 keV to ~10 MeV [17]. Since the electron's binding energy is typically negligible compared to the energy of the incoming photon, the shell electrons are often considered to be free and non-interacting. In the process the photon transfers part of its energy to the recoiling electron, and is scattered to an angle φ, also referred as *Compton scatter angle*. The relation between the energy and the angle of the scattered photon follows from simple relativistic kinematics:

$$\cos\varphi = 1 - \frac{m_e c^2}{E'_\gamma} + \frac{m_e c^2}{E_\gamma} = 1 - \frac{m_e c^2}{E'_\gamma} + \frac{m_e c^2}{E'_e + E'_\gamma} \,. \tag{3}$$

In Eq. 3, known in literature as *Compton equation* or *Compton formula*, m_e is the electron rest mass, E_γ is the energy of the incident gamma ray, E'_γ is the energy of the scattered gamma ray, and E'_e is the energy of the recoil electron.

Compton telescopes are ideally matched to survey the sky in the MeV energy range: for most materials, the Compton cross section dominates in the energy range from hundreds of keV up to tens of MeV. Moreover Compton telescopes can easily have a large field-of-view, of the order of steradians, enabling excellent sky coverage. However the achievable angular resolution is poorer compared to other methods, $\mathcal{O}(1\,\text{deg})$.

The principle of operation of a Compton telescope is quite straightforward. Let us assume, for simplicity, a telescope made of two detectors planes: soft gamma rays in the MeV energy range undergo Compton scattering in the first detector plane (also referred as the scattering layer or converter); the recoil electron is quickly absorbed and its energy is measured by the detector itself. The scattered photon then deposits the rest of its energy in the second detector layer (also referred as the absorption layer). Assuming, for convenience, that the scattered photon undergoes a single photoelectric absorption in the second detector layer,[15] the direction of the incoming gamma ray can be reconstructed by measuring the energies of the recoil electron and of the scattered photon produced in the Compton process, together with their interaction positions [11, 71]. Specifically, the direction of the incident photon $\vec{e}_\gamma$ is related to the scatter direction $\vec{e}\,'_\gamma$ by:

$$\vec{e}\,'_\gamma \cdot \vec{e}_\gamma = \cos\varphi = 1 - \frac{m_e c^2}{E'_\gamma} + \frac{m_e c^2}{E_\gamma} \,, \tag{4}$$

where the *Compton angle* φ is determined by the Compton formula, through the energies deposited inside the detectors. From Eq. 4, it follows that the direction of the incoming gamma ray $\vec{e}_\gamma$, cannot be determined uniquely, but can only be confined to an annulus on the sky, often referred in literature as the *event circle*.

There are two different uncertainties in determining the origin of gamma rays. The first is the uncertainty in determining $\vec{e}\,'_\gamma$, and is related to the spatial resolution of the detectors. The second is the uncertainty in the measurement of the Compton scatter angle, and is related to the energy resolution of the detectors. The angular resolution of the Compton telescope is determined by the "width" or spreading of the Compton event cycle. The *Angular Resolution Measure* (ARM) for each Compton event is defined as the minimum angular distance between the true source location and each event annulus. The σ (or FWHM) of the ARM distribution is the standard definition of the angular resolution of a Compton telescope. It is related to the uncertainties in the position and energy measurements, plus a fundamental physical limit: in a Compton camera the electron, bound in an atom with an unknown momentum, leads to the so called "Doppler broadening", limiting the angular resolution of the instrument [76].

---

[15] The scattered photon can, alternatively, lose its energy through a series of Compton scatterings and subsequent photo-electric absorption. Even if not explicitly considered here, the treatment of these kind of events is very similar to the one discussed.

When multiple gamma rays from the same source are detected and properly reconstructed, the events circles overlap and intersect each other. Knowing the instrument response function and the background, the original source distribution is obtained from the recorded image by deconvolution.

If the direction of the recoil electron is measured, the direction of each incident gamma ray can be further restricted as a result of momentum conservation: with the detection of the recoil electron track the event circle is reduced to a small segment, defined as the *event arc*. The length of the arc, quantified by the *Scatter Plane Deviation* (or SPD) [77], is a measure of the uncertainty in the electron's recoil direction. The electron's direction can be reconstructed via the implementation of a tracking detector, such as thin silicon layers or a gaseous time-projection chamber. However, multiple scattering inside the tracking material results in a large uncertainty in the direction of the electron track, as described by Molière theory. In fact, electrons traversing a medium are deflected by many small-angle scatters, due to Coulomb interactions with nuclei of the material. The scatter angle distribution can be approximated by a Gaussian. Its width can be written as:

$$\theta_0 = \frac{13.6\,\mathrm{MeV}}{\beta c p} z \sqrt{\frac{x}{X_0}} \left[1 + 0.038 \ln \left(\frac{x z^2}{X_0 \beta^2} \right) \right], \tag{5}$$

where p, βc and z are the momentum, velocity and charge number of the incident particle, X_0 is the radiation length of the material and x is the straight path length of the particle in the material. Again, the source image is reconstructed from the intersection of multiple events. However, in this case, the source position is detectable more easily with fewer photons and with a better discrimination against background.

COMPTEL, on-board CGRO, was the first Compton telescope to fly in the 1990s. The payload was composed of two planes of scintillation detectors, separated by a large distance (1.5 m), allowing time-of-flight measurement. Many Compton telescopes are currently being proposed for the future: these includes ETCC/SMILE [65], Grams [5], COSI [68] and MeVCube [44], the aforementioned GECCO [51], combining a Compton telescope with a coded-mask, and e-ASTROGAM [21] and AMEGO [32, 50], combining a Compton telescope and a pair creation telescope (see next section).

5.5 Pair Telescopes

When the energy of the incoming gamma ray exceeds two times the rest mass of an electron ($E > 1.022\,\mathrm{MeV}$), *pair production* (or *pair creation*) is energetically possible. In pair creation the incoming gamma ray is converted into an electron-positron pair in the electromagnetic field of a nucleus or electron. On a practical level, pair creation telescopes are powerful instruments to survey the gamma-ray sky from energies above tens MeV (since the probability of this interaction remains very low until $\sim 10\,\mathrm{MeV}$, see Fig. 2). The basic design of a pair creation telescope consists of two main detectors: a *tracker*, consisting of position sensitive detectors measuring the tracks of the electron-positron pair created in the pair production process, and a *calorimeter* estimating the energy of the primary photon from the electromagnetic shower developed in the detectors (see Fig. 3e). Spark chambers (see Sect. 6) were originally employed as tracking devices in first pair telescopes like COS-B, and EGRET[16] on-board CGRO. As a consequence of the development of semiconductors devices and technological improvements, silicon strip detectors are now employed in modern-day pair telescopes. In any case, high-Z conversion foils, usually made of tungsten, are combined with the active detectors in order to enhance conversion probability and increase the effective area. Concerning the calorimeter, inorganic scintillation detectors are the technology of choice, due to their high atomic number and density, ensuring good stopping power even at high energies, and due to their low cost and high space technology readiness level[17] as well.

In a pair telescope the origin of the incident photon is reconstructed through a track finding algorithm, which looks for the typical "inverted-V" pattern, produced by the electron and positron pair ionization tracks in the silicon (or gaseous) detector. The angular resolution of the telescope is limited by the position measurement accuracy of the detectors and, especially at lower energies, by multiple scattering (Molière scattering, see Eq. 5). The energy of the gamma ray is inferred from the energy released inside the calorimeter. However a fraction of the initial photon energy is deposited in other detectors (inside the tracker, for example) or passive materials, while for higher-energy gamma rays the electromagnetic shower is not completely absorbed by the calorimeter itself. Therefore, the morphology of the tracks and the shower need to be studied and the missing energy must also be estimated.

Currently operating pair telescope are AGILE (2007-), [66], Fermi-LAT (2008-), [6] and DAMPE (2015-), [15]. Taking the Fermi-LAT as example of the current state of technology of pair telescopes, these instruments achieve a sub-degree angular resolution ($\sim$0.8° at 1 GeV and $<$ 0.2° at $>$ 10 GeV) and a wide field-of-view of $\sim$2.4 sr.

---

[16] Energetic Gamma Ray Experiment Telescope.

[17] The Technology readiness level (TRL) is a scaled used for estimating the maturity of technologies during the different development phases of a program, see https://artes.esa.int/sites/default/files/TRL_Handbook.pdf.

6 Radiation Detectors and Their Applications in Astrophysics

Radiation detectors are separated under three major groups: gas-filled detectors, scintillation detectors (or scintillators), and solid state (or semiconductor) detectors. The interaction of the incoming radiation with the material results in the production of charge carries, either electrons and ions in a gaseous detector or electrons and holes in a semiconductor device, or in the emission of light quanta in the case of a scintillating material, which is then coupled to a photo-sensor. In any case, the produced signal is then processed electronically, to retrieve the desired information. An extensive overview of radiation detectors and their application can be found in [35, 36]. The choice of detector technology depends on many factors, like the energy range of interest, required energy and spatial resolution, expected efficiency, noise level, costs, reliability etc. Additionally, for space operation, particle environment on orbit, and thermal and mechanical stability are other important aspects to take under consideration. Most of the detectors employed in space gamma-ray telescopes are either scintillators or semiconductor detectors, with gas detectors playing only a minimal role.

Gas-filled detectors consist of a sensitive volume of gas between two electrodes. Even if the mode of operation of a gas detector strongly depends on the voltage applied between the electrodes, the basic principle is the same for every gas detector: the gas inside the detector reacts due to passage of the incoming radiation, is ionized, and an electric signal is induced by the drift of electrons and ions towards the electrodes. Spark chambers, made of several conducting layers stacked in a volume filled with a noble gas (most commonly neon or argon), were the track imaging detector of choice in the 1960's. Therefore they were employed in first imaging pair telescope such as SAS-2 (1972–1973) [24] and COS-B (1975–1982) [10]. SAS-2 employed a 32-layer spark chamber, interleaved with thin tungsten plates, 0.03 radiation length-thick, for an active area $\sim$640 cm^2. The telescope measured photons in energy range between 35 and 200 MeV, and operated for about six months, until an electronics failure ended the mission. The gamma-ray telescope on-board COS-B employed a spark chamber as well, with nearly the same size of SAS-2. The main differences with respect SAS-2 were the inclusion of a CsI energy calorimeter, allowing detection on a wider energy range (30 MeV-5 GeV), and a gas replacement system, mitigating the performance degradation and allowing the telescope to operate successfully for more than 6 years. A spark chamber was also chosen with EGRET [31], on-board CGRO (1991–2000), for the next generation of pair telescopes, incorporating the best features of previous instruments. EGRET's tacker consisted of 28 spark chamber modules, with an area of ~6400 cm^2, interleaved with 90 µm thick tantalum foils, acting as converting material. The spark chamber was filled with a gas mixture of neon, argon and ethane; a replenishment system allowed for gas filling of the spark chamber up to four times. After EGRET, gas-filled detectors encountered a hiatus, being replaced by better performing trackers made of microstrip silicon detectors. Nowadays, time projection chambers filled with gas or liquid argon have been proposed for some future MeV Compton telescope, such in the SMILE/ETCC [65] or GRAMS [5] projects.

Scintillation detectors (or scintillators) exploit the luminescence properties of particular elements, when excited by ionizing radiation (i.e. to "scintillate"). The emitted light is converted into electrons via light sensors such as photo-multiplier tubes (PMTs), photodiodes, or silicon photo-multipliers (SiPMs). They also amplify the incoming signal significantly (a gain of $\sim 10^6$ is a typical value), in order to generate a current/voltage pulse that can be processed by the read-out electronics. Scintillators can be produced in large, monolithic volumes in a variety of shapes, and are widely employed in physics due to their low cost and reliability. Additionally, the fast response of scintillators and light sensors, make them the instrument of choice when time resolution is an issue. The disadvantage of scintillation detectors is the generally poorer energy and spatial resolution with respect to other technologies. Scintillators are grouped under two main categories: organic scintillators, and inorganic scintillators. Organic scintillators are made of anthracene, plastics such as polystyrene, or liquids, and are characterised by low atomic number and density. In astrophysics they are usually employed in anti-coincidence system, to veto the in-orbit cosmic ray background. By surrounding the telescope with thin layers of plastic scintillators (thickness ~0.5–1.5 cm), an high efficiency for charged particles detection, but low probability of interaction for gamma rays, is achieved.

On the opposite side, inorganic scintillators exhibit high atomic numbers (Z) and densities (ρ). Combined with the possibility of cover a large area with contained costs, they ensure good stopping power even at high energies. Frequently used inorganic scintillation materials are sodium iodide (NaI, Z=11, 53, $\rho = 3.67\,\mathrm{g/cm^3}$),[18] cesium iodide (CsI, Z=51, 53, $\rho = 4.51\,\mathrm{g/cm^3}$), bismuth germanate ($Bi_4Ge_3O_{12}$, commonly referred to as BGO, Z=83, 32, 8, $\rho = 7.13\,\mathrm{g/cm^3}$), and more recently lanthanum bromide ($LaBr_3$, Z=57, 35, $\rho = 5.29\,\mathrm{g/cm^3}$) and lutetium–yttrium oxyorthosilicate ($Lu_{1.8}Y_{0.2}SiO_5$ or LYSO, Z=71, 39, 16, 8, $\rho = 7.10\,\mathrm{g/cm^3}$). Scintillation detectors have been implemented since the dawn of gamma-ray astrophysics, as the calorimeter detectors in pair creation telescopes, or absorber subsystem in collimators, coded-masks or Compton telescopes. They were employed in telescopes like Beppo-SAX, COS-B, COMPTEL, OSSE and EGRET. Currently, they are employed in the IBIS telescope on-board INTEGRAL (the second plane of the telescope, PICsIT, is composed by CsI detectors covering a sensitive area of 2890 cm^2 [69]) and in the modern generation of pair telescope. The calorimeter of Fermi-LAT is composed of several CsI(Tl) crystals bars read-out by photodiodes, each with a dimension of $326 \times 26.7 \times 19.9$ mm [2, 6]. The crystal are arranged in 16 modules, one per the so called "tower", and each module is composed of 8 layers, each with 12 CsI bars horizontally arranged; each consecutive layer is rotated to 90° with respect to the previous one, forming a so-called "hodoscopic" array. Similar in the design, but smaller in size is the electromagnetic calorimeter of AGILE [40, 66]: it is made of 30 Caesium Iodide bars, each one $15 \times 23 \times 375\,\text{mm}^3$ in size, arranged in two orthogonal planes. Instead the calorimeter on-board DAMPE, consists of 308 BGO crystals arranged in 14 layers (with 22 crystals per layer), covering a geometrical area of $\sim 60 \times 60\,\text{cm}^2$.

---

[18] Here, and in the followings, the atomic number of each element composing the scintillation material is reported, i.e. Z=11 for Na and Z=53 for I.

The last major detector technology used in physics and radiation detection instruments comprises **solid state detectors**. Solid state detectors are composed by a semiconductor material, such as silicon, germanium or cadmium zinc telluride, coupled to a proper read-out system, composed, in most applications, by a charge-sensitive pre-amplifier, one (or more) shaper, and an analog-to-digital converter (ADC), in order to measure and process the produced signal. In semiconductor detector the impact of incoming radiation, depositing a certain amount of energy in the detector volume, results in the motion of electrons from valence band to conduction band, leaving vacancies (called "hole") in the valence band [36, 63]. By the application of an electrical field (around 1000 V/cm), electrons and holes are separated, drifting towards two opposite electrodes (the anode and cathode, respectively). The induced signal, proportional to the deposited energy, is then recorded by the read-out electronics. In this regard the production and drift of electrons and holes in semiconductor detectors can be thought of as the analogue of the electron-ion pairs in gas detectors. Compared to gas and scintillation detectors, semiconductors typically display a better energy resolution. In fact energy resolution is coupled to the statistics of the number of produced charge carriers: the mean energy for production of an electron-hole pair in semiconductor detector is about few electronvolts (3.6 eV in the case of silicon), while for a gas detector the mean energy for production of an electron-ion pair is ~ 30 eV. Instead, for a typical inorganic scintillator around tens thousands photons are produced per MeV.[19] These numbers have to be compared with the $\sim 3 \cdot 10^5$ electron-hole pairs produced in a semiconductor detector. Therefore, semiconductors produce the largest number of charge carries, and so, the lowest statistical fluctuation in the produced signal. Moreover, a multi-electrode layout (strips or pixels) can easily be employed in semiconductor devices, for applications where a fine spatial resolution is required. The drawback is that they are generally more expensive and more difficult to produce and read-out in large volumes. The characteristics and applications of semiconductor detectors in gamma-ray astrophysics are emphasised in great detail in the next section; outstanding operating telescopes are taken as examples, and some prospects on future applications are highlighted.

---

[19] Specifically 43000 ph/MeV are produced in NaI and 52000 ph/MeV in CsI.

7 Solid-State Detectors in Gamma-Ray Astrophysics

As introduced in the previous section, the properties of a semiconductor material are dictated by its band structure and band-gap E_{g}, i.e. the difference between the energy of the lowest conduction band and the energy of the highest valence band. The band-gap should be large enough to guarantee high resistivity and consequently low leakage current, ensuring low noise operation. On the other hand it should be small enough, so the ionisation energy needed to produce an electron-hole pair is not too large. In this way a proper number of electron-hole pairs are created by gamma-ray interactions, and the statistical variation in the number of produced charge carriers is small. The average electron-hole pair creation energy, E_{pair} is around three times the band gap energy [33], since part of the energy is transferred to phonon excitation.

Besides that, other key characteristics are appealing for operation as X-ray and gamma-ray detectors. First of all, a high atomic number Z and density ρ are favourable, in order to enhance efficient radiation interaction. Moreover the drift length for charge carriers should be greater than the detector thickness, in order to ensure a high collection efficiency. The drift length $\lambda_{e,h}$ for electrons and holes, is determined by the carrier mobility μ and the lifetime τ of the material, and the applied electric field E:

$$\lambda_{e,h} = \mu_{e,h}\tau_{e,h}E \,. \tag{6}$$

In a semiconductor charge carrier transport is undermined by impurities and defects in the crystals, acting like trapping centres. The quantity which is often used to describe the charge transport properties of a semiconductor detector is the *charge collection efficiency* (*CCE*) [47], defined as the induced charge Q on an electrode normalized to the total charge $Q_0 = eN_0$ generated in the interaction:

$$CCE = \frac{Q}{eN_0} \,. \tag{7}$$

In the case of a planar detector with uniform electric field, Q is given by the Hecht equation [29]:

$$Q = eN_0\frac{\lambda_e}{L}\left[1 - \exp\left(\frac{x_0 - L}{\lambda_e}\right)\right] + eN_0\frac{\lambda_h}{L}\left[1 - \exp\left(-\frac{x_0}{\lambda_h}\right)\right], \tag{8}$$

where e is the elementary electron charge, N_0 is the number of electron-hole pairs produced by the interaction, L is the detector thickness and x_0 is the interaction location measured from the cathode. Ideally, the CCE should achieve a value close to 1 and as uniform as possible throughout the detector volume.

In reality, it is very difficult to meet all these requirements with a single material or detector, and some aspects need to be compromised in favour of others, depending also on the specific application. Most commonly used semiconductors are silicon

Table 1 Main properties of silicon, germanium, cadmium telluride and cadmium zinc telluride. Electrical properties that depend on the temperature are given here at T = 300 K. Data taken from [64] and [53]

	$\mathbf{Cd_{0.9}Zn_{0.1}Te}$	**CdTe**	**Si**	**Ge**
Atomic number, Z	48, 30, 52	48, 52	14	32
Density, ρ [g/cm^3]	5.78	5.85	2.33	5.33
Band gap, E_g [eV]	1.57	1.44	1.12	0.67
Pair creation energy, E_{pair} [eV]	4.64	4.43	3.62	2.96
Resistivity, ϱ [Ω cm]	$3 \cdot 10^{10}$	10^9	$< 10^4$	50
Fano factor	0.09	0.11	0.12	0.08
Radiation length, X_0 [cm]	1.43	1.44	9.37	2.30
Electron mobility, μ_e [cm^2/V s]	1000	1100	1400	3900
Hole mobility, μ_h [cm^2/V s]	80–120	100	480	1900
Electron lifetime, τ_e [s]	$3 \cdot 10^{-6}$	$3 \cdot 10^{-6}$	$> 10^{-3}$	$> 10^{-3}$
Hole lifetime, τ_h [s]	10^{-6}	$2 \cdot 10^{-6}$	10^{-3}	$2 \cdot 10^{-3}$
$\mu_e \cdot \tau_e$ [cm^2/V]	10^{-3}–10^{-2}	10^{-3}	> 1	> 1
$\mu_h \cdot \tau_h$ [cm^2/V]	10^{-5}–10^{-4}	10^{-4}	~ 1	> 1

(Si) and germanium (Ge). Additionally, compound semiconductors like cadmium telluride (CdTe), cadmium zinc telluride (CdZnTe or CZT), gallium arsenide (GaAs) and mercuric iodide (HgI_2) have gained more and more interest in the last few decades. Among them, cadmium telluride and cadmium zinc telluride have emerged as the most promising materials. The main properties of silicon, germanium, cadmium telluride and cadmium zinc telluride are summarised in Table 1.

7.1 Silicon Detectors

Silicon detectors cannot be easily grown in large volumes with the same purity as germanium. Common thickness for silicon wafers are around 300–500 µm. In order to achieve the high resistivity needed for spectroscopy, it is necessary to introduce dopants that compensate for the existing impurities, and create a region free of charge carriers (the so-called *depletion zone*). Otherwise, the number of electron-hole pairs thermally created, will exceed by order of magnitudes the signals that are wanted to be measured. With the introduction of doping elements from the fifth main group (usually phosphorus), with one more outer electron compared to silicon atoms, an additional donor level near the conduction band is created. On the other side, elements from the third main group (usually boron), have one electron less than silicon, and create an acceptor level close to the valence band. Two "layers" are created: a "n-type" layers, containing a greater number of electrons compared to holes, and one "p-type", with a greater number of holes than electrons. When the positively and negatively doped silicon layers are combined, the so-called pn junction is created: electrons from the n-type migrate across the junction between the two layers to fill the holes in the p-type. When thermal equilibrium is reached a depleted zone of all free charge carriers between both doping regions is formed. This depleted area can be increased by applying a reverse bias voltage and allows silicon detectors to detect the signals produced by particle interaction. Silicon detectors benefit from cooling to reduce leakage current, but at a more modest level than germanium. This can be accomplished by a careful passive cooling design or the use of simple thermoelectric (Peltier) coolers, with temperatures down to $\sim -20\ ^\circ$C.

Small, simple planar p-i-n detectors are often used for X-ray detection up to a few tens of keVs, while in the contest of gamma-ray astrophysics are employed in a single sided (or double sided) strip configuration in tracking systems.

7.1.1 The Tracking System of the Fermi-LAT and AGILE Telescopes

As already mentioned in Sect. 5.5, the main requirement of a tracking system of a pair telescope is to register the passage of electron-positron pairs produced in high-energy photon interactions, generating the distinctive "inverted-V" pattern inside the detectors. In this way the arrival direction of the incident gamma ray can be reconstructed with high precision.

By the time EGRET, the last gamma-ray telescope employing a gas detector as a tracker, had been launched, significant progress concerning particle tracking systems has been made, thanks to the advent and development of solid state detectors. They offered several advantages like lower operating voltages (around $\sim$100 V), better triggering capabilities, and circumvented the limitations due to gas detectors degradation. An excellent spatial resolution could be made by the implementation of a multi-electrode layout. Microstrip silicon detectors represent nowadays the workhorses for pair production gamma-ray telescopes. The first exponent of this new generator of pair production telescopes is represented by the small AGILE satellite, launched in 2007 [66]. About one year later, a second instrument was launched: the Fermi Large Area Telescope (Fermi-LAT), using a similar technology to that of the AGILE, but on a much larger scale [6].

In AGILE the silicon tracker [13] consists of 12 planes, each of them made of two layers of 16 single-sided silicon strip detectors (Fig. 4, left). Each detector has a thickness of 410 μm, a pitch of 242 μm, and an area of $9.5 \times 9.5\,\text{cm}^2$. Therefore, the total active area of the silicon tracker is $38 \times 38\,\text{cm}^2$. The silicon detectors are coupled to low-power ASICs[20] (power consumption $< 400\,\mu\text{W/channel}$) and analogue read-out. The planes of the tracker are interleaved with tungsten layers, 245 μm thick, in order to enhance the conversion probability of high energy photons. The silicon microstrip detector, coupled to the analogue read-out, enables a spatial resolution of the AGILE silicon tracker around 40 μm.

Fermi-LAT is nowadays the most sensitive gamma-ray telescope. The tracking system is modular, made of 16 identical towers in a 4×4 array; each tower has

---

[20] Application-Specific Integrated Circuits.

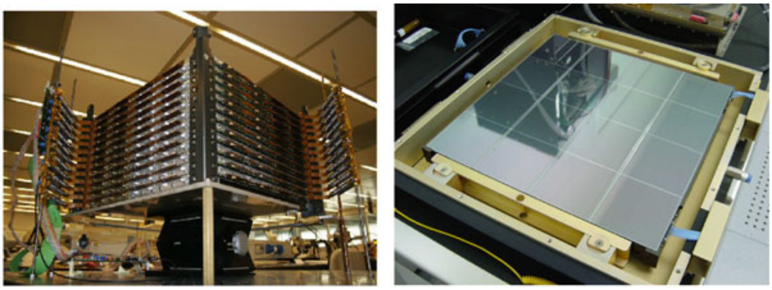

Fig. 4 Left: the AGILE silicon tracker before integration with the rest of the instrument; reproduced from [66]. Right: image of a tacker tray of a single tower as employed in Fermi-LAT; reproduced from [6]

Table 2 Performance of the EGRET, AGILE and Fermi-LAT pair creation telescopes

	EGRET	AGILE	Fermi-LAT
Mass	1380 kg	130 kg	4303 kg
Energy range	20 MeV–30 GeV	30 MeV–50 GeV	$\sim$ 20 MeV to $>$ 300 GeV
Effective area	1500 cm^2	500 cm^2	9000 cm^2
Field-of-view	0.5 sr	2.5 sr	2.4 sr
Angular resolution	5.8° at 100 MeV	4.7° at 100 MeV	3.5° at 100 MeV
	1.3° at 1 GeV	0.7° at 1 GeV	0.6° at 1 GeV

an area of $40 \times 40\,\text{cm}^2$. The tracking detector consists of 18 x-y planes of single-sided silicon strip detectors (Fig. 4, right), coupled to low-power digital read-out ($< 300\,\mu$W/channel). The thickness of the silicon detectors is 400 μm and the pitch between strip is 228 μm. The first 16 layers of the tracker are interleaved with tungsten converter foils. The first 12 foils have a thickness of 0.010 cm (corresponding to 0.03 radiation lengths) while the next 4 foils have a thickness of 0.072 cm (0.18 radiation lengths). In more than 14 years of operation the Fermi-LAT has not experienced any significant hardware failures [3].

The use of precise silicon tracking detectors coupled to conversion foils was the key factor which allows pair creation telescopes to reach their full potential. In Table 2 some of the main performance of AGILE and Fermi-LAT are compared to EGRET's ones.

7.1.2 Future Applications of Silicon Tracking Detectors

Future proposed pair creation telescopes, such as AMEGO [32, 50] and e-ASTROGAM [21], are focused to explore a lower energy range, operating also as Compton telescopes at the same time. They are expected to cover the energy range from few hundreds keV to $\sim$10 GeV improving sensitivity by more one order of magnitudes compared to previous missions. Consequently, the tracker of the e-

ASTROGAM and AMEGO missions needs to fulfill several tasks. First of all, it has to act as a Compton scattering and pair creation converter medium. Secondly, it has to measure the energy and direction of the recoil electrons (in the case of Compton interaction) and secondary electrons and positrons (in the case of pair creation) with great accuracy. Therefore some differences are needed compared to the tracker of Fermi-LAT and AGILE. Extending operation in the lower energy range requires less scattering material in the tracking subsystem, in order to enhance the relatively poor angular resolution of previous instruments at energies below $\sim$100 MeV. As evident from Eq. 5, the performance degradation due to multiple Coulomb scattering is related to the atomic number Z of traversed material; therefore the trackers of e-ASTROGAM and AMEGO does not implement tungsten conversion foils. In order to further improve the angular resolution these instruments foresee double-sided silicon strip detectors (instead of single-sided strips) coupled to analogue low-noise read-out electronics. In AMEGO, the silicon tracker consists of 60 layers of double-sided silicon strip detectors, with a thickness of 500 μm. Every single layer is made of 16 wafers, in a 4×4 array configuration. The area of each wafer is $9.5 \times 9.5\,\mathrm{cm}^2$, and the pitch between strips is 500 μm. The separation between two consecutive layers is 1.0 cm. Very similar in the design is also the tracker of e-ASTROGAM.

An alternative approach for tracking pair production events, investigated, for example by the High Energy cosmic-Radiation Detector (HERD) [27], would be the use of scintillating fibers [57].

7.2 Germanium Detectors

While silicon semiconductor detectors have depletion depths $\lesssim$ 1 mm, germanium can have a depleted, sensitive thickness of several centimeters. Germanium is also characterized by excellent transport properties due to very high mobility-lifetime product for both electrons and holes. However, the small band gap (0.7 eV) results in large thermally generated leakage current, so room-temperature operation is impossible. Low operating temperatures (around liquid nitrogen temperature of 77 K) are therefore mandatory. An energy resolution of $\sim$0.3% FWHM at 662 keV can be achieved with a good germanium detector and optimized electronics, and its density and atomic number are higher compared to silicon ones. For all these reasons, germanium detectors represent the best option for high resolution spectroscopy up to a few MeVs, in the field of nuclear physics and astrophysics.

In first historical applications, germanium detectors could not be produced with sufficient purity to enable proper spectroscopic operation. Crystals were therefore doped with lithium ions (Ge(Li)), in order to produce an intrinsic region in which the electrons and holes would be able to reach the contacts without being trapped and produce a measurable signal. This process became obsolete and high-purity germanium (HPGe) detectors, with very low concentration of impurities, lower than 10^9–10^{10} atoms/cm^3 are now produced. Germanium detectors can be both n-type or p-type, usually with a Li-diffused n+ contact and boron implanted p+ contact. Germanium detectors are mainly produced in two configurations: planar and coaxial (either open-ended or closed-ended configuration). In astrophysics germanium detectors made in coaxial configuration have been implemented, for example, in HEAO-3 [48], in RHESSI [61] and in the SPI spectrometer on-board INTEGRAL [56, 70]. Thick germanium strip detectors are also being developed for Compton telescopes and foreseen as a key payload element in COSI [68].

Operation of germanium detectors in space is challenging due to the necessity of maintaining adequate cooling for long periods of time. In most laboratory measurements, the germanium is cooled through the use of an insulated dewar in which a reservoir of liquid nitrogen is kept in thermal contact with the detector. In order to avoid the necessity of filling the dewar frequently, its capacity is usually about several liters, making its size and weight way greater than those of the detectors itself. The technique could also be used in space operation in principle, but the cryogens have a large mass and limit the mission lifetime. Most of the instruments rely instead on Stirling-cycle mechanical coolers. In this case the cooling system weighs less and guarantees longer operation; however it requires continuous power. Cryocoolers can also be very expensive to qualify for space flight and this should not be underestimated in mission planning.

7.2.1 Application of Germanium Detectors in Space

HEAO-3, the third High Energy Astronomy Observatory, was the first mission employing large germanium detectors in space. HEAO-3 was launched in 1979, and it's Gamma-Ray Spectrometer, composed of 4 coaxial high purity germanium detectors, was operating in the energy range of 0.05–10 MeV. Each detector had a diameter approximately of 54 mm and a length of 45 mm; the bias voltage was around 3000 V. An energy resolution of 3 keV FWHM at 1.46 MeV was achieved at the beginning of operation in space.[21] Cooling of the detectors was achieved thanks to a two-stage solid cryogen cooler: a secondary cryogen at a temperature of 168 K and a primary one reaching a temperature of 91 K.

Germanium detectors with a mechanical cyrocooler were employed in RHESSI (2002–2018), a mission dedicated to the detection of solar photons from 3 keV to 17 MeV and, most importantly, on the SPI spectrometer on-board INTEGRAL (2002-). The SPI instrument is composed of a gamma camera, a two-stage cooling system (a first stage cooling the cryostat housing to 215 K and a second stage cooling the Ge detectors down to 85–90 K), a coded-mask made of tungsten blocks, and a shield made of BGO blocks and plastic scintillators. As it can be seen from Fig. 5, the camera is made of 19 germanium detectors, with a hexagonal shape with a side length of 3.2 cm and an height of 6.94 cm. The total weight of Ge detectors is $\sim$18 kg

---

[21] Since launch a gradual degradation in the energy resolution was observed, due to radiation damage.

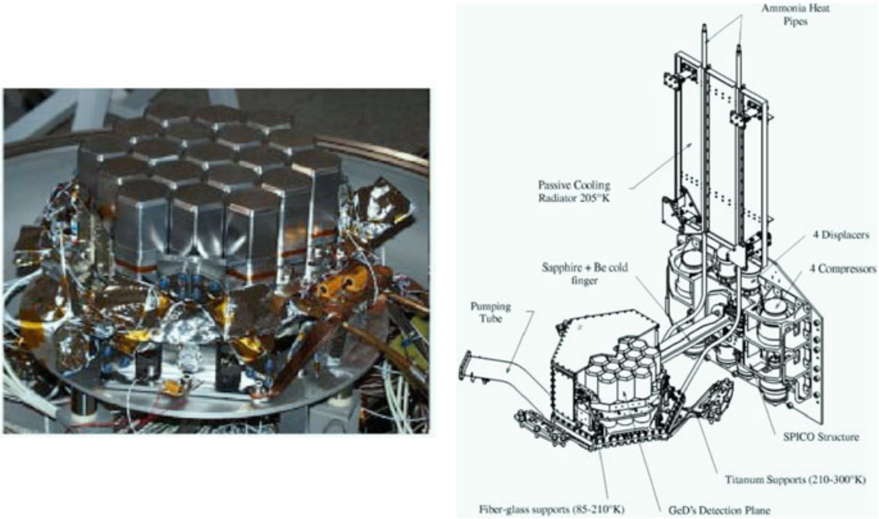
Ammonia Heat Pipes
Passive Cooling Radiator 205°K
4 Displacers
Sapphire + Be cold finger
4 Compressors
Pumping Tube
SPICO Structure
Titanum Supports (210-300°K)
Fiber-glass supports (85-210°K)
GeD's Detection Plane

Fig. 5 Left: image of the SPI germanium camera. Right: schematic of the SPI camera and cooling system. Images reproduced from [70]

(for comparison the mass of the cryostat is 80 kg). The detectors work at a voltage of 4000 V; four of them have ceased to function properly and are now disabled [39]. In order to minimize the effect of radiation damage, the germanium detectors are annealed: the process consists of baking the detectors to ~100° C in order to suppress trapping sites and recover initial performance. This is achieved through four resistors glued on the detectors array support, heating the detectors. Annealing is performed about every 6 months with a duration around 1–2 days. SPI operates in the energy range 20 keV–8 MeV, with a fully coded field-of-view of 16°, and angular resolution of 2.5°, and an energy resolution of 2.5 keV at 1.1 MeV.

The Compton Spectrometer and Imager (COSI) is a compact Compton telescope, designed to survey the gamma-ray sky in the energy range from 200 keV to 5 MeV, and capable to observe 25% of the sky at any time. After two successful balloon flights, COSI has been recently accepted as a small explorer mission (SMEX), with launch foreseen around 2025. The core of the instrument consists of 16 high-purity germanium strip detectors. Each detectors has a volume of $8 \times 8 \times 1.5\ \mathrm{cm}^3$, exploiting 37 orthogonal strips on each side (front and back side of the detector), with a 2 mm strip pitch and a 3 mm guard ring. The detectors operate at voltages ranging from 1000 to 1500 V, and are read-out by custom ASICs. The COSI instrument includes 4 planes; each plane is made by four detectors on a 2×2 array. The detectors have an energy resolution of 0.4% at 662 keV and a 3D spatial resolution of $\lesssim 1$ mm. Therefore, despite the limited size COSI can achieve unprecedented angular and energy resolution in the MeV regime. The germanium strip array is enclosed in a cryostat with a Sunpower mechanical cryocooler. The scientific payload is surrounded by a BGO shield.

7.3 Cadmium Telluride and Cadmium Zinc Telluride Detectors

For a long time, materials alternative to germanium have been proposed, in order to circumvent the complication of cryogenic operation. In compound semiconductor detectors the band-gap is large enough to make cooling unnecessary. Among compound semiconductors cadmium telluride (CdTe) and cadmium zinc telluride (CdZnTe or CZT), have emerged as the most promising materials. Cadmium telluride (CdTe) is a compound II–VI semiconductor material with a cubic zincblende structure, while cadmium zinc telluride $\mathrm{Cd}_{1-\mathrm{x}}\mathrm{Zn}_{\mathrm{x}}\mathrm{Te}$ is a semiconductor crystalline alloy of cadmium telluride and zinc telluride. It can be regarded as a CdTe crystal with a fraction x of Zn atoms substituting Cd atoms. For detector applications Zn concentration is typically in the range $x = 0.1$–0.2 [58]. The addition of this small zinc concentration to the melt ensures an increased band gap and, therefore, a higher bulk resistivity and lower leakage current [14]. Compared to germanium, CdTe and CdZnTe also display a higher atomic number and density. The most significant drawback of CdTe and CdZnTe devices, with respect to silicon and germanium, is the poor transport properties of charge carriers, in particular holes. The lower mobility-lifetime product in CdTe and CdZnTe, results in higher charge trapping and recombination, which prevent the full signal collection and limit spectroscopic performance in thick detectors. In order to optimize performance, detectors are often operated as “single carrier devices”: with particular anode geometry configurations, one attempts to change the charge induction property of the detector making it sensitive only to electron’s movement, being insensitive to the hole contribution. These special electrode configurations include the virtual Frisch grid [19], small pixel arrays or strips [59], the co-planar grid [45, 46] and orthogonal strips [49] geometries.

CdZnTe detectors are attractive for a large variety of applications including nuclear physics, radiation monitoring and medical imaging, X-ray and gamma-ray astronomy, due to the possibility to fabricate compact systems, with good energy resolution and 3D spatial resolution as well. The energy resolution is still slightly worse than the one achieved in germanium detectors, but possibility of room temperature operation drastically simplifies operation in many applications. The spatial resolution on the detector plane is at first order defined by the size of the multi-electrode layout element when employed (strip or pixel),[22] while the depth resolution can be exploited by looking at the variations between the induced signals measured at the cathode and the anode. One of the best results achieved so far in literature have been reported by Zhu and collaborators, from the University of Michigan, [74, 75]. They investigated the performance of a $2.0 \times 2.0 \times 1.5\,\mathrm{cm}$ CdZnTe detector with 11×11 pixels, read-out by low-noise custom designed ASIC. After event analysis and quality cuts they reported an energy resolution of $\sim 0.5\%$

---

[22] Sub-pixels spatial resolution can be achieved in some applications, employing sophisticated read-out electronics and analysis techniques, which allows to compared the signals generated in adiacent pixels.

FWHM at 662 keV, a depth resolution of about 500 μm and a sub-pixel spatial resolution of ∼230 μm on the detector plane.

The capability of CdTe detectors in astrophysical applications has been demonstrated by the IBIS-ISGRI camera on-board the INTEGRAL observatory [41], while CdZnTe detectors are currently employed on Swift-BAT [8], and Astrosat [9], and, on the X-ray energy range, on NuStar [28]. Moreover CdZnTe detector are under consideration for many future proposed missions such as AMEGO [32], GECCO [51, 52] and MeVCube [44].

7.3.1 CdTe and CdZnTe in Space: IBIS, Swift-BAT and AstroSat

The IBIS telescope on-board the INTEGRAL satellite employs two gamma-ray cameras, ISGRI covering the range between 15 keV and 1 MeV, and PICsIT covering the range from 170 keV to 10 MeV. While the PICsIT camera is made by several CsI detectors, ISGRI employed for the first time in the history of gamma-ray astrophysics CdTe detectors. In ISGRI each detector has dimensions of 4 × 4 × 2 mm; 16 detectors (on a 4 × 4 array) are mounted on one side of a multilayer ceramic plate hosting 4 ASICs for the read-out on the opposite side. Two adiacent detectors in the board are separated by a distance of 600 μm. The detectors are biased at 120 V. This ceramic board, called polycell (Fig. 6), is the fundamental element of the camera: the ISGRI camera is formed by 8 independent modules, and each module is formed by 128 polycells distributed on 8 rows of 16 polycells each. Therefore 16384 detectors are employed in total in the camera, for an area around 3600 cm^2. However, the dead zones between detectors and between the camera's modules, restrict the sensitive area to 2621 cm^2. The distance between the ISGRI camera and the coded-mask is 3.2 m, providing an angular resolution of $12'$. The energy resolution $\Delta E/E$ is around 0.03 FWHM.

Cadmium-zinc-telluride telescopes are current employed in two instruments working in the energy range spanning between hard X-ray and soft gamma rays: Swift-BAT (15–150 keV) and the Cadmium Zinc Telluride Imager (CZTI) on-board AstroSat (15–200 keV). They both employ a cadmium-zinc-telluride camera and a coded-mask. In Swift-BAT a detecting area of 5200 cm^2 is covered by 4 × 4 × 2 mm CdZnTe detectors. The coded-mask gives a wide field-of-view of 1.4 sr and an

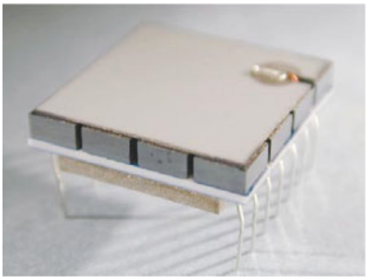

Fig. 6 The ISGRI polycell board, hosting 16 CdTe detectors; reproduced from [41]

angular resolution of 17 arcmin. The CZTI camera consists of 64 detectors, each $\sim 40 \times 40 \times 5$ mm in size with a 16×16 pixel structure; the geometrical area is 976 cm^2. The energy resolution of the detectors is on average 6.5 keV ($\sim$11%) at 60 keV. The telescopes attains an angular resolution of $17'$ and a field-of-view of $4.6° \times 4.6°$.

Due to improvements in technology and crystal growing techniques, cadmium-zinc-telluride detectors foreseen for future proposed missions, will have greater volumes compared to the ones presented in this section, ensuring higher stopping power and allowing to extend the working energy range.

7.3.2 Future Application of CdZnTe Detectors

CdZnTe detectors are currently under investigation for many future missions, most notably proposed Compton telescopes and coded-mask telescopes such as AMEGO [32], GECCO [51] and MeVCube [44].

AMEGO was already introduced in Sect. 7.1.2, as a new concept for a Compton and pair telescope in the MeV–GeV energy range. Even if AMEGO foresees a "conventional" CsI calorimeter for measuring the energy of electrons and positrons produced in pair creation events, the optimization of the instruments in the Compton regime, lead to the proposal of low-energy calorimeter, made of thick bars of cadmium zinc telluride detectors, in a virtual Frisch-grid configuration. As evident from Eq. 4 excellent energy and spatial resolution are mandatory for the development of a good Compton camera. In this regard cadmium zinc telluride detectors offer suitable performance, far superior than scintillation detectors. The objective of the low-energy calorimeter is to measure the scattered photon energy for Compton interaction in the silicon tracker,[23] or to directly measure deposited energies and interaction location for those events only interacting in the calorimeter itself. The low-energy calorimeter surrounds the bottom and partly the sides of the silicon tracker. Each CdZnTe bar, developed at the Brookhaven National Laboratory [12], is $8 \times 8 \times 40$ mm^3 in size and packed in 4×4 arrays; the entire calorimeter is segmented into 4 modules, each consisting of 5×10 of these arrays. Laboratory measurements have shown that the CdZnTe bars, biased at -2.8 kV, enable a sub-mm position resolution in all three dimensions, and a $< 1\%$ energy resolution at 662 keV.

The same detector technology is foreseen for GECCO, a novel concept combining a Compton cadmium-zinc-telluride telescope and a deployable coded aperture mask. The shape of the cadmium-zinc-telluride calorimeter is octagonal with a circumdiameter of $\sim$90 cm. The shape of the coded-aperture mask is octogonal as well, but with a circumdiameter larger than the detector plane, about 150 cm, in order to increase the fully-coded field-of-view. The mask is made of randomly distributed 20 mm thick, 3 mm square tungsten elements. The mask will be deployed at 20 m from the calorimeter. GECCO will operate in the energy range between 100 keV and 10 MeV. The combination of the wide field-of-view and effective area of the Compton telescope, and the extraordinary angular resolution provided by the deployable coded mask, will allow to cover the huge observational gap currently existing between the hard X-ray and soft gamma-ray domain.

---

[23] The silicon tracker also measure the energy of recoil electron.

Cadmium-zinc-telluride detectors are also exploited in the design of MeVCube, a new concept for a Compton telescope based on the CubeSat standard [67]. A CubeSat is a nano-satellite with standardized size and form factor. A single CubeSat unit (1 U) has a volume of $10 \times 10 \times 11.35\,\mathrm{cm}^3$ and a maximum weight of 1.33 kg; more than one unit can be combined together, defining bigger envelopes, e.g. 3 U or 6 U. Initially intended for education purposes, CubeSats have gained increasing interest on commercial companies, government agencies and research centers. In fact, Cubesats provide cheaper and faster ways to demonstrate novel technologies for space application and provide significant scientific results for specific targets of opportunity and selected topics, such as space weather and earth science, or observations of variable stars and transients. MeVCube is a 6 U CubeSat, in which $\sim$2 U would be dedicated to satellite components such as batteries, reaction wheels, attitude control system etc., and $\sim$4 U would be dedicated to the scientific payload. Accordingly, the scientific payload is expected to fit in an estimated volume of $20 \times 20 \times 10\,\mathrm{cm}^3$, and consists of 128 pixelated CdZnTe detectors, arranged in a stack of two layers of 64 detectors. The separation between the two layers is 6 cm. Each CdZnTe detector has a volume of $2.0 \times 2.0 \times 1.5\,\mathrm{cm}^3$ with a 8×8 pixel structure; the pitch between pixels is 2.45 mm. Despite the limited effective area, affected by the CubeSats constraints in size, MeVCube is expected to cover the energy range between 200 keV and 4 MeV, with a field-of-view around 2 sr and a sensitivity comparable to the one achieved by the last generation of larger-scale satellites like COMPTEL and INTEGRAL. First experimental measurements [43] on the custom designed CdZnTe detector, biased at -2500 V and coupled to suitable electronics for space operation, have shown an energy resolution around 3% FWHM at 662 keV and $< 2\%$ at energies above 1 MeV. A 3-D spatial resolution of $\approx$2 mm is achieved. The performance was strongly limited by the parasitic noise generated by large evaluation boards, not perfectly optimised in the set-up, so an improvement can reasonably be expected in future iterations.

8 Conclusions

Starting with the launch of the first satellites in the end of 1960s, gamma-ray astronomy have evolved constantly over the past 60 years, drawing heavily on particle detection instrumentation used in accelerator and nuclear physics. With the exception of first pair tracking telescopes employing gas-filled detectors, most of the instrumentation employed in space gamma-ray telescopes are either based on scintillators or semiconductor detectors. While scintillation detectors are employed where costs and the necessity to cover a large area are driving factors, solid state detectors guarantee far superior spectroscopy performance and spatial resolution. Among solid state detectors silicon, germanium and cadmium zinc telluride are widely exploited in the present generation of gamma-ray telescopes and will play a key role in future instruments currently being proposed.

Acknowledgments IFAE is partially funded by the CERCA program of the Generalitat de Catalunya. The research leading to these results has received funding from the Spanish Ministry of Science and Innovation (PID2020-116075GB-C22/AEI/ 10.13039/501100011033).

References

1. Abdollahi, S., et al. (2020). Fermi large area telescope fourth source catalog. *Astrophysical Journal, Supplement Series, 247*(1), 33. https://doi.org/10.3847/1538-4365/ab6bcb. arXiv: 1902.10045 [astro-ph.HE]
2. Ackermann, M., et al. (2012). The fermi large area telescope on orbit: Event classification, instrument response functions, and calibration. *Astrophysical Journal, Supplement Series, 203*(1), 4. https://doi.org/10.1088/0067-0049/203/1/4. arXiv: 1206.1896 [astro-ph.IM]
3. Ajello, M., et al. (2021). Fermi large area telescope performance after 10 years of operation. *Astrophysical Journal, Supplement Series, 256*(1), 12. https://doi.org/10.3847/1538-4365/ac0ceb. arXiv: 2106.12203 [astro-ph.IM]
4. Allen, C. S., et al. (2018). Chapter 4 - Spaceflight environment. In T. Sgobba et al. (Eds.), *Space Safety and Human Performance* (pp. 87–138). Oxford: Butterworth-Heinemann. ISBN: 978-0-08-101869-9. https://doi.org/10.1016/B978-0-08-101869-9.00004-2
5. Aramaki, T., et al. (2020). Dual MeV gamma-ray and dark matter observatory - GRAMS project. *Astroparticle Physics, 114*, 107–114. https://doi.org/10.1016/j.astropartphys.2019.07.002. arXiv: 1901.03430 [astro-ph.HE]
6. Atwood, W. B., et al. (2009). The large area telescope on the fermi gamma-ray space telescope mission. *Astrophysical Journal, 697*(2), 1071–1102. https://doi.org/10.1088/0004-637X/697/2/1071. arXiv: 0902.1089 [astro-ph.IM]
7. Barrièere, N., et al. (2005). MAX, a Laue diffraction lens for nuclear astrophysics. *Experimental Astronomy, 20*(1–3), 269–278. https://doi.org/10.1007/s10686-006-9058-x
8. Barthelmy, S. D., et al. (2005). The burst alert telescope (BAT) on the SWIFT midex mission. *Space Science Reviews, 120*(3–4), 143–164. https://doi.org/10.1007/s11214-005-5096-3
9. Bhalerao, V., et al. (2017). The cadmium zinc telluride imager on astrosat. *Journal of Astrophysics and Astronomy, 38*(2), 31. https://doi.org/10.1007/s12036-017-9447-8. arXiv: 1608.03408 [astro-ph.IM]
10. Bignami, G. F., et al. (1975). The COS-B experiment for gamma-ray astronomy. *Space Science Instrumentation, 1*, 245–268.
11. Boggs, S. E., & Jean, P. (2000). Event reconstruction in high resolution Compton telescopes. *Astronomy & Astrophysics, Supplement Series, 145*, 311–321. https://doi.org/10.1051/aas:2000107. arXiv: astro-ph/0005250 [astro-ph]
12. Bolotnikov, A. E., et al. (2020). A 4 × 4 array module of position-sensitive virtual Frisch-grid CdZnTe detectors for gamma-ray imaging spectrometers. In *Nuclear Instruments and Methods in Physics Research Section A: Accelerators, Spectrometers, Detectors and Associated Equipment. Symposium on Radiation Measurements and Applications XVII* (vol. 954, p. 161036). ISSN: 0168-9002. https://doi.org/10.1016/j.nima.2018.07.090
13. Bulgarelli, A., et al. (2010). The AGILE silicon tracker: Pre-launch and in-flight configuration. *Nuclear Instruments and Methods in Physics Research A, 614*(2), 213–226. https://doi.org/10.1016/j.nima.2009.12.051

14. Butler, J. F., & Apotovsky, B. (1993). Sub-keV resolution detection with $Cd_{1-x}Zn_xTe$ detectors. In V. J. Orphan (Ed.), *X-Ray Detector Physics and Applications II* (vol. 2009, pp. 121–127). Bellingham: International Society for Optics and Photonics (SPIE). https://doi.org/10.1117/12.164731
15. Chang, J., et al. (2017). The DArk matter particle explorer mission. *Astroparticle Physics, 95*, 6–24. https://doi.org/10.1016/j.astropartphys.2017.08.005. arXiv: 1706.08453 [astro-ph.IM]
16. Cheng, J. (2009). *The Principles of Astronomical Telescope Design*. New York: Springer.
17. Compton, A. H. (1923). A quantum theory of the scattering of x-rays by light elements. *Physical Review, 21*, 483–502. https://doi.org/10.1103/PhysRev.21.483
18. Credits to B.J. Mattson, L3/NASA/Goddard Space Flight Center. Retrieved November 25, 2022 from https://ecuip.lib.uchicago.edu/multiwavelength-astronomy/gamma-ray/tools/07.html
19. Cui, Y., et al. (2009). CZT virtual Frisch-grid detector: Principles and applications. In *2009 IEEE Long Island Systems, Applications and Technology Conference* (pp. 1–5). https://doi.org/10.1109/LISAT.2009.5031559
20. Cumani, P., et al. (2019). Background for a gamma-ray satellite on a low-earth orbit. *Experimental Astronomy, 47*(3), 273–302. https://doi.org/10.1007/s10686-019-09624-0. arXiv: 1902.06944 [astro-ph.IM]
21. De Angelis, A., et al. (2017). The e-ASTROGAM mission. Exploring the extreme universe with gamma rays in the MeV - GeV range. *Experimental Astronomy, 44*(1), 25–82. https://doi.org/10.1007/s10686-017-9533-6. arXiv: 1611.02232 [astro-ph.HE]
22. de Naurois, M., Mazin, D. (2015). Ground-based detectors in veryhigh-energy gamma-ray astronomy. *Comptes Rendus Physique, 16*(6–7), 610–627. https://doi.org/10.1016/j.crhy.2015.08.011. arXiv: 1511.00463 [astro-ph.IM]
23. Fenimore, E. E., & Cannon, T. M. (1978). Coded aperture imaging with uniformly redundant arrays. *Applied Optics, 17*(3), 337–347. https://doi.org/10.1364/AO.17.000337
24. Fichtel, C. E., et al. (1975). High-energy gamma-ray results from the second small astronomy satellite. *The Astrophysical Journal, 198*, 163–182. https://doi.org/10.1086/153590
25. Frontera, F., & von Ballmoos, P. (2010). Laue gamma-ray lenses for space astrophysics: Status and prospects. *X-Ray Optics and Instrumentation, 215375*, 215375. https://doi.org/10.1155/2010/215375. arXiv: 1007.4308 [astro-ph.IM].
26. Frontera, F., et al. (1997). The high energy instrument PDS on-board the BeppoSAX X-ray astronomy satellite. *Astrophysical Journal Supplement Series, 122*, 357–369. https://doi.org/10.1051/aas:1997140
27. Gargano, F. (2022). The high energy cosmic-radiation detection (HERD) facility on board the Chinese space station: Hunting for high-energy cosmic rays. In *Proceedings of Science (PoS) ICRC2021* (p. 026). https://doi.org/10.22323/1.395.0026
28. Harrison, F. A., et al. (2013). The nuclear spectroscopic telescope array (NuSTAR) high-energy x-ray mission. *The Astrophysical Journal, 770*(2), 103. https://doi.org/10.1088/0004-637X/770/2/103. arXiv: 1301.7307 [astro-ph.IM]
29. Hecht, K. (1932). Zum mechanismus des lichtelektrischen primärstromes in isolierenden kristallen. *Zeitschrift fur Physik, 77*(3–4), 235–245. https://doi.org/10.1007/BF01338917
30. Johnson, W. N., et al. (1993). The oriented scintillation spectrometer experiment: Instrument description. *Astrophysical Journal Supplement Series, 86*, 693. https://doi.org/10.1086/191795
31. Kanbach, G., et al. (1989). The project EGRET (energetic gamma-ray experiment telescope) on NASA's gamma-ray observatory GRO. *Space Science Reviews, 49*(1–2), 69–84. https://doi.org/10.1007/BF00173744
32. Kierans, C. A. (2020). AMEGO: Exploring the extreme multi-messenger universe. In J. W. A. den Herder, S. Nikzad, & K. Nakazawa (Eds.), *Space Telescopes and Instrumentation 2020: Ultraviolet to Gamma Ray* (vol. 11444, pp. pp. 528–546). Bellingham: International Society for Optics and Photonics (SPIE). https://doi.org/10.1117/12.2562352
33. Klein, C. A. (1968). Bandgap dependence and related features of radiation ionization energies in semiconductors. *Journal of Applied Physics, 39*(4), 2029–2038. https://doi.org/10.1063/1.1656484

34. Knödlseder, J., et al. (2009). GRI: Focusing on the evolving violent universe. *Experimental Astronomy, 23*(1), 121–138. https://doi.org/10.1007/s10686-008-9119-4. arXiv: 0707.4627 [astro-ph]
35. Knoll, G. F. (2010). *Radiation Detection and Measurement*. New York: Wiley. ISBN: 978-0-470-13148-0
36. Kolanoski, H., & Wermes, N. (2020). *Particle Detectors: Fundamentals and Applications*. Oxford: Oxford University Press. https://cds.cern.ch/record/2721300
37. Kraushaar, W. L., et al. (1972). High-energy cosmic gamma-ray observations from the OSO-3 satellite. *The Astrophysical Journal, 177*, 341. https://doi.org/10.1086/151713
38. Kurfess, J. D., et al. (1997). Overview of the compton observatory instruments. *AIP Conference Proceedings, 410*(1), 509–523. https://doi.org/10.1063/1.54011
39. Kuulkers, E., et al. (2021). INTEGRAL reloaded: Spacecraft, instruments and ground system. *New Astronomy Reviews, 93*, 101629. https://doi.org/10.1016/j.newar.2021.101629
40. Labanti, C., et al. (2009). Design and construction of the Mini-Calorimeter of the AGILE satellite. *Nuclear Instruments and Methods in Physics Research A, 598*(2), 470–479. https://doi.org/10.1016/j.nima.2008.09.021. arXiv: 0810.1842 [astro-ph]
41. Lebrun, F., et al. (2003). ISGRI: The INTEGRAL soft gamma-ray imager. *Astronomy & Astrophysics, 411*, L141–L148. https://doi.org/10.1051/0004-6361:20031367. arXiv: astro-ph/0310362 [astro-ph]
42. Léna, P., et al. (2012). *Observational Astrophysics*. New York: Springer.
43. Lucchetta, G., et al. (2022). Characterization of a CdZnTe detector for a lowpower CubeSat application. *Journal of Instrumentation, 17*(8), P08004. https://doi.org/10.1088/1748-0221/17/08/P08004. arXiv: 2204.00475 [astro-ph.IM]
44. Lucchetta, G., et al. (2022). Introducing the MeVCube concept: A CubeSat for MeV observations. *Journal of Cosmology and Astroparticle Physics, 8*, 013. https://doi.org/10.1088/1475-7516/2022/08/013. arXiv: 2204.01325 [astro-ph.IM]
45. Luke, P. N. (1994). Single-polarity charge sensing in ionization detectors using coplanar electrodes. *Applied Physics Letters, 65*(22), 2884–2886. https://doi.org/10.1063/1.112523
46. Luke, P. N. (1995). Unipolar charge sensing with coplanar electrodes-application to semiconductor detectors. *IEEE Transactions on Nuclear Science, 42*(4), 207–213. https://doi.org/10.1109/23.467848
47. Luke, P. N., & Amman, M. (2007). Room-temperature replacement for ge detectors - Are we there yet? *IEEE Transactions on Nuclear Science, 54*(4), 834–842. https://doi.org/10.1109/TNS.2007.903184
48. Mahoney, W. A., et al. (1980). The HEAO 3 gamma-ray spectrometer. In *Nuclear Instruments and Methods, 178*(2), 363–381. ISSN: 0029-554X. https://doi.org/10.1016/0029-554X(80)90815-0
49. McConnell, M., et al. (2000). Three-dimensional imaging and detection efficiency performance of orthogonal coplanar CZT strip detectors. In: *Proceedings of SPIE - The International Society for Optical Engineering* (vol. 4141). https://doi.org/10.1117/12.407576
50. McEnery, J. et al. (2019). All-sky medium energy gamma-ray observatory: Exploring the extreme multimessenger universe. *Bulletin of the American Astronomical Society, 51*, 245. arXiv: 1907.07558 [astro-ph.IM]
51. Moiseev, A. (2021). New mission concept: Galactic explorer with a coded aperture mask compton telescope (GECCO). In: *Proceedings of 37th International Cosmic Ray Conference — PoS(ICRC2021)* (vol. 395, p. 648). https://doi.org/10.22323/1.395.0648
52. Orlando, E., et al. (2022). Exploring the MeV sky with a combined coded mask and compton telescope: The galactic explorer with a coded aperture mask compton telescope (GECCO). *Journal of Cosmology and Astroparticle Physics, 7*, 036. https://doi.org/10.1088/1475-7516/2022/07/036. arXiv: 2112.07190 [astro-ph.HE]
53. Owens, A., & Peacock, A. (2004). Compound semiconductor radiation detectors. *Nuclear Instruments and Methods in Physics Research Section A: Accelerators, Spectrometers, Detectors and Associated Equipment, 531*(1), 18–37. ISSN: 0168-9002. https://doi.org/10.1016/j.nima.2004.05.071

54. Patrignani, C., et al. (2016). Review of particle physics. *Chinese Physics C, 40*(10), 100001. https://doi.org/10.1088/1674-1137/40/10/100001
55. Rao, A. R., et al. (2017). Cadmium-zinc-telluride imager on-board AstroSat: A multi-faceted hard X-ray instrument. *Current Science, 113*(4), 595. https://doi.org/10.18520/cs/v113/i04/595-598. arXiv: 1710.10773 [astro-ph.IM]
56. Roques, J. P., et al. (2003). SPI/INTEGRAL in-flight performance. *Astronomy & Astrophysics, 411*(1), 91–100. https://doi.org/10.1051/0004-6361:20031501
57. Ruchti, R. C. (1996). The use of scintillating fibers for charged-particle tracking. *Annual Review of Nuclear and Particle Science, 46*(1), 281–319. https://doi.org/10.1146/annurev.nucl.46.1.281
58. Schlesinger, T. E., et al. (2001). Cadmium zinc telluride and its use as a nuclear radiation detector material. *Materials Science and Engineering: R: Reports, 32*(4), 103–189. ISSN: 0927-796X. https://doi.org/10.1016/S0927-796X(01)00027-4
59. Shor, A., Eisen, Y., & Mardor, I. (1999). Optimum spectroscopic performance from CZT γ- and X-ray detectors with pad and strip segmentation. *Nuclear Instruments and Methods in Physics Research A, 428*(1), 182–192. https://doi.org/10.1016/S0168-9002(99)00005-4
60. Skinner, G. K. (2001). Diffractive/refractive optics for high energy astronomy. I. Gamma-ray phase Fresnel lenses. *Astronomy & Astrophysics, 375*, 691–700. https://doi.org/10.1051/0004-6361:20010745
61. Smith, D. M., et al. (2002). The RHESSI spectrometer. *Solar Physics, 210*(1), 33–60. https://doi.org/10.1023/A:1022400716414
62. Swanenburg, B. N., et al. (1981). Second COS-B catalogue of high-energy gammaray sources. *The Astrophysical Journal Letters, 243*, L69–L73. https://doi.org/10.1086/183445
63. Sze, S. M. (2006). *Physics of Semiconductor Devices*. New York: Wiley. https://doi.org/9780470068328
64. Takahashi, T., & Watanabe, S. (2001). Recent progress in CdTe and CdZnTe detectors. *IEEE Transactions on Nuclear Science, 48*(4), 950–959. https://doi.org/10.1109/23.958705
65. Tanimori, T., et al. (2015). An electron-tracking compton telescope for a survey of the deep universe by MeV gamma-rays. *The Astrophysical Journal, 810*(1), 28. https://doi.org/10.1088/0004-637X/810/1/28. arXiv: 1507.03850 [astro-ph.IM]
66. Tavani, M., et al. (2009). The AGILE mission. *Astronomy & Astrophysics, 502*(3), 995–1013. https://doi.org/10.1051/0004-6361/200810527. arXiv: 0807.4254 [astro-ph]
67. The CubeSat Program. (2015). *Cubesat Design Specification, Rev. 13*. Tech. Rep. California Polytechnic State University. Retrieved August 17, 2020, from https://www.cubesat.org/cubesatinfo
68. Tomsick, J., & COSI Collaboration. (2022). The compton spectrometer and imager project for MeV astronomy. In *37th International Cosmic Ray Conference* (p. 652). https://doi.org/10.22323/1.395.0652. arXiv: 2109.10403 [astro-ph.IM]
69. Ubertini, P., et al. (2003). IBIS: The Imager on-board INTEGRAL. *Astronomy & Astrophysics, 411*, 131–139. https://doi.org/10.1051/0004-6361:20031224
70. Vedrenne, G., et al. (2003). SPI: The spectrometer aboard INTEGRAL. *Astronomy & Astrophysics, 411*, L63–L70. https://doi.org/10.1051/0004-6361:20031482
71. von Ballmoos, P., Diehl, R., & Schoenfelder, V. (1989). Imaging the gamma-ray sky with compton telescopes. *Astronomy & Astrophysics, 221*, 396–406.
72. von Ballmoos, P., et al. (2005). CLAIRE: First light for a gamma-ray lens. *Experimental Astronomy, 20*(1–3), 253–267. https://doi.org/10.1007/s10686-006-9071-0.
73. von Ballmoos, P., Takahashi, T., & Boggs, S. E. (2010). A DUAL mission for nuclear astrophysics. *Nuclear Instruments and Methods in Physics Research A, 623*(1), 431–433. https://doi.org/10.1016/j.nima.2010.03.026
74. Zhu, Y., Anderson, S. E., & He, Z. (2011). Sub-pixel position sensing for pixelated, 3-D position sensitive, wide band-gap, semiconductor, gamma-ray detectors. *IEEE Transactions on Nuclear Science, 58*(3), 1400–1409. https://doi.org/10.1109/TNS.2011.2132738
75. Zhu, Y., & He, Z. (2012). Performance of a 2-keV digitizer ASIC for 3-D positionsensitive pixellated semiconductor detectors. In *2012 IEEE Nuclear Science Symposium and Medical*

Imaging Conference Record (NSS/MIC) (pp. 4109–4112). https://doi.org/10.1109/NSSMIC.2012.6551939

76. Zoglauer, A., & Kanbach, G. (2003). Doppler broadening as a lower limit to the angular resolution of next-generation Compton telescopes. In J. E. Truemper & H. D. Tananbaum (Eds.), *X-Ray and Gamma-Ray Telescopes and Instruments for Astronomy* (vol. 4851, pp. 1302–1309). Bellingham: International Society for Optics and Photonics (SPIE). https://doi.org/10.1117/12.461177
77. Zoglauer, A. C. (2005). First light for the next generation of compton and pair telescopes. Ph.D. Thesis. Max Planck Institut für Extraterrestrische Physik. http://hdl.handle.net/11858/00-001M-0000-0011-D84E-B

Radioxenon Detection for Monitoring Subsurface Nuclear Explosion

Harish R. Gadey

1 Introduction

The Comprehensive Nuclear-Test-Ban Treaty (CTBT) was signed in 1996 under the supervision of the United Nations. The treaty aims to ban all nuclear weapon explosions on Earth including atmospheric, surface, subsurface, and underwater explosions [1]. As of early 2022, the treaty had 186 signatory states and 172 of these states had already ratified the treaty [2]. However, it must be mentioned that the treaty is not in force currently because all the required states have not either signed or ratified the treaty. The CTBT and the treaty on the Non-Proliferation of Nuclear-Weapons (NPT) are intended to play an important role in establishing nuclear peace and security in addition to making it inherently difficult to develop and test nuclear weapons. The CTBT requires the establishment of a verification regime under the guidance of the Comprehensive Nuclear-Test-Ban Treaty Organization (CTBTO). To this end, the International Monitoring System (IMS) network was established across the world to detect potential nuclear weapon explosions using infrasound, seismic, hydroacoustic, and radionuclide technologies. The IMS network also assures that signatory states are meeting their treaty obligations of not testing any form of nuclear weapons. A total of 321 monitoring stations are planned across the world, 80 of these IMS stations are radionuclide monitoring stations and 40 of these stations will be retrofitted with noble gas detection systems (Fig. 1) [3]. The noble gas stations detect the concentration of noble gases released from nuclear explosions, reactor operations, medical isotope production facilities, and other potential sources. Employing atmospheric transport models, the measured radionuclide signature can be attributed to a potential region. Using

---

H. R. Gadey (✉)
Pacific Northwest National Laboratory, Richland, WA, USA
e-mail: harish.gadey@pnnl.gov

© The Author(s), under exclusive license to Springer Nature Switzerland AG 2023

J. Du, K. (K.) Iniewski (eds.), *Gamma Ray Imaging*,
https://doi.org/10.1007/978-3-031-30666-2_7

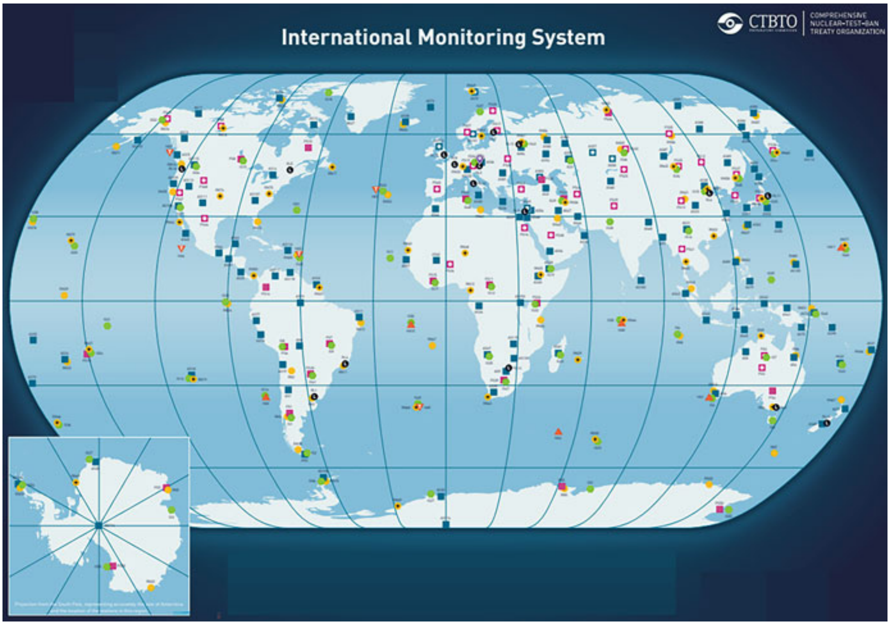
International Monitoring System
CTBTO
COMPREHENSIVE NUCLEAR-TEST-BAN TREATY ORGANIZATION

Fig. 1 Map showing the distribution of IMS stations across the world [5]

conventional technologies such as satellite imaging, identifying nuclear explosions in the Earth's atmosphere, surface, and underwater is relatively straightforward. However, detecting subsurface nuclear explosions is challenging because of the lack of traditional signatures such as the mushroom cloud and the significant elevation of radiation in the vicinity of the explosion. Noble gas detection by IMS stations and application of atmospheric transport models address the specific scenario of subsurface weapon testing [4].

1.1 Role of Xenon in Identifying Subsurface Nuclear Explosions

A large number of radionuclides are produced during a nuclear weapon explosion. Most of these radionuclides are trapped underground when the explosions occur in the subsurface. These explosions do not actively contribute to the event signature. However, xenon isotopes (i.e., ^{131m}Xe, ^{133m}Xe, ^{133}Xe, and ^{135}Xe) play an important role in the identification of subsurface explosions due to the high yield (independent and cumulative) of xenon, the half-lives of the isotopes, their inert chemical nature, and the coincidence decay scheme of xenon isotopes of interest [6]. The importance of each of these characteristics is covered briefly to highlight the significance of xenon to the subsurface weapon detection community.

1.1.1 Inert Chemical Nature

Several of the radionuclides produced in nuclear explosions form chemical bonds under the intense conditions and are unable to escape the blast chamber. However, noble gases, because of their inert nature (stable outer shell configuration), do not easily form chemical bonds and eventually escape the subsurface. Subsequently, once these gases reach the surface, they undergo dilution due to atmospheric transport. Literature has indicated that this venting process is periodic and is dependent on temporal pressure and temperature changes during various parts of the day following a nuclear explosion.

1.1.2 Half Lives

The four radioxenons of interest have half-lives between a few hours and 11 days. The radiological property of half-life plays an important role in subsurface weapon detection because the half-lives of the xenon isotopes of interest are neither too short that they decay below detection limits before reaching the IMS station nor too long, so atmospheric saturation occurs, resulting in limited ability to track temporal changes. Other noble gases such as argon and krypton isotopes also are produced in a nuclear weapon explosion, but challenges related to their decay energies, half-lives, and yield have prevented their application in long range weapon detection.

1.1.3 High Independent and Cumulative Yield

Observing the fission yield curve quickly reveals that xenon isotopes have high independent and cumulative fission yields of over 6%. This large source term aids in the detection of radioxenons even at IMS stations located several thousand kilometers away from the source. Moreover, some radioxenons of interest such as ^{133m}Xe decay into relatively long-lived ^{133}Xe, thereby extending the detection range which potentially would be beneficial for detecting nuclear explosions.

1.1.4 Coincidence Decay Scheme

The xenon isotopes of interest release an electron and a photon simultaneously during their decay; this phenomenon is called coincidence decay. Coincident emissions rarely are observed among background radiation. This enables the detection of very low levels of radioxenon, thus negating traditional electron or photon background signatures. Several radioxenon detection systems developed worldwide employ this coincidence detection feature in detectors with very high sensitivity. It must however be mentioned that high sensitivity systems were developed in the past that only relied on high resolution photon detectors. Table 1 shows the radioxenon emissions of interest.

Table 1 Coincidence emissions from the radioxenon of interest [7]

Isotope		Decay energy (keV)	Branching ratio (%)
^{131m}Xe ($t_{1/2} = 11.93$ days)			
X-Rays	XKα_2	29.46	15.4
	XKα_1	29.78	28.6
	K$'\beta_1$	33.60	10.2
	K$'\beta_2$	34.61	1.85
Conversion electrons		129.4	61
Coincident decays		X-ray and 129 keV e$^-$	56.1
^{133}Xe ($t_{1/2} = 5.35$ days)			
X-Rays	XKα_2	30.62	14.1
	XKα_1	30.97	26.2
	K$'\beta_1$	35.00	9.4
	K$'\beta_2$	36.01	1.7
Gamma rays		80.99	37
Conversion electrons		45	55.1
Betas (max energy)		346	100
Coincident decays		X-ray + 45 keV e$^-$ + 346 keV beta 81 keV gamma + 346 beta	48.9 37.2
^{133m}Xe ($t_{1/2} = 2.19$ days)			
X-Rays	XKα_2	29.46	16.1
	XKα_1	29.78	29.8
	K$'\beta_1$	33.60	10.6
	K$'\beta_2$	34.61	1.9
Conversion electrons		198.7	64
Coincident decays		X-ray and 199 keV e$^-$	58.4
^{135}Xe ($t_{1/2} = 0.38$ days)			
X-Rays	XKα_2	30.62	1.45
	XKα_1	30.97	2.69
	K$'\beta_1$	35.00	0.97
	K$'\beta_2$	36.01	0.185
Gamma rays		249.8 608.2	90 2.9
Conversion electrons		214	5.7
Betas (max energy)		910	100
Coincident decays		X-ray + 214 keV e$^-$ + 910 keV beta 249.8 keV gamma + 910 keV beta	5.7 90

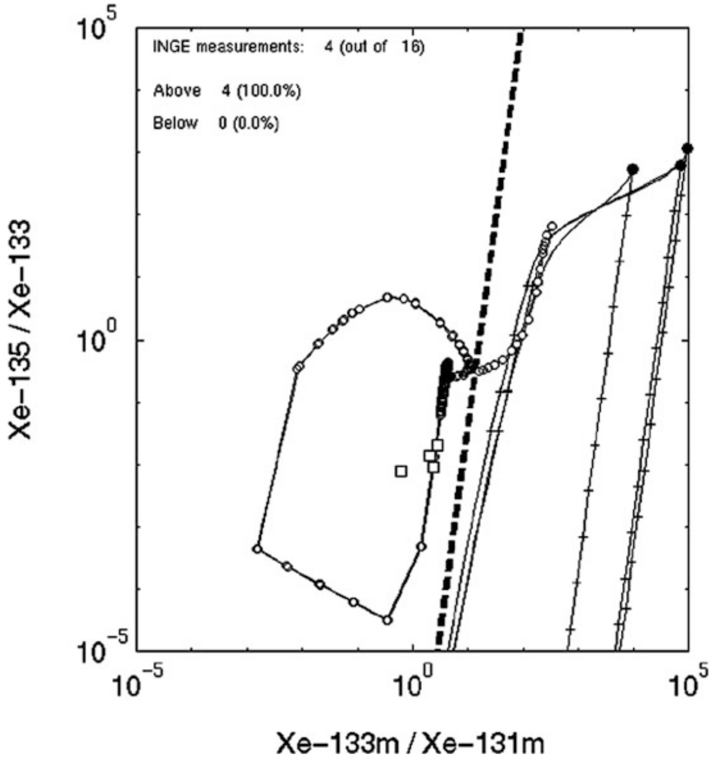

Fig. 2 Plot illustrating the differences between normal reactor operations and nuclear weapon tests. The dashed line is the discriminator between the two potential release sources [9]

1.2 Nuclear Power Plant Operation Versus Nuclear Explosions – The Difference

There are several sources of radioxenon production apart from nuclear weapon explosions (e.g., reactor operations and medical isotope production facilities). Therefore, to identify the source, the ratios of various radioxenon activities are estimated rather than the individual activity of any one radioxenon [8]. For instance, the ratios of ^{135}Xe/^{133}Xe and ^{133m}Xe/^{133}Xe are considerably different for a reactor release as opposed to a nuclear explosion; therefore, the ratios can be used as an effective discrimination metric. Figure 2 shows xenon activity ratios for reactor operations and weapon tests. Releases from a reactor are identified on the left of the dashed discrimination line while releases from nuclear tests are shown on the right. It must be pointed out that ratios for these two releases differ by orders of magnitude, considering the fact that the *x* and *y* axis in Fig. 2 are in log scale. In addition, it must be mentioned that releases from medical isotope production facilities and irradiation of fresh uranium fuel often release signatures that are similar to signatures associated with a nuclear explosion. Therefore, research in recent years has focused on accurately recording the radioxenon background near such sources and developing advanced transport models to accurately predict the source of the release.

1.3 Requirements for IMS Stations

The CTBTO needs IMS stations equipped with noble gas detection to meet performance expectations from a sensitivity and data reporting standpoint [10, 11]. These requirements include:

- Detection of at least a 1 kT nuclear explosion within 14 days with 90% accuracy.
- Counting the sample within 24-hours and reporting data to the International Data Center every day.
- Achieving a minimum detectable concentration (MDC) of under 1 mBq/m^3 for ^{133}Xe.

MDC is a sensitivity metric that was developed to estimate the lowest detectable limit of a noble gas system with a certain accuracy. The concentration of xenon in the atmosphere is estimated to be around 87 parts per billion, this low concentration enables the detection of xenon originating from other sources such as nuclear weapon explosions. The independent ^{133}Xe yield from a 1 kT explosion is about 10^{14}Bq. Typical dilution factors from the source to the average nearest IMS station are between 10^{-14} to 10^{-18}. Considering these two factors, establishing an MDC of about 1 mBq/m^3 makes sure that at least a 1 kT nuclear weapon can be detected by systems deployed in the IMS network. It must also be pointed out that, according to the CTBTO, although the MDC requirements are specified only for ^{133}Xe, in practice the 1mBq/m^3 limit has been extended to all radioxenons of interest. IMS noble gas stations were successful in detecting nuclear weapon explosions and also releases from the Fukushima reactor accident on several occasions [12, 13].

1.4 Minimum Detectable Concentration

The MDC is a quantitative measure dealing with the lowest level at which a detection system can accurately measure radionuclides of interest. The lower the MDC, the more sensitive the detection system. As mentioned previously, the CTBTO requires all detection systems to achieve an MDC under 1 mBq/m^3. The MDC equation considers several factors such as gas processing parameters, detection efficiencies, branching ratios, and the volume of air collected by the system. The general MDC equation used for radioxenon detection systems is presented in Eq. (1) [14].

$$MDC\left(\frac{\mathrm{mBq}}{\mathrm{m}^3 air}\right)=\left[\frac{2.71+4.65\sigma_0}{\varepsilon_\beta\varepsilon_\gamma\beta_{BR}\gamma_{BR}}\right]\left[\frac{\lambda^2}{(1-exp\,(-\lambda T_c))\left(-\lambda T_p\right)(1-exp\,(-\lambda T_A))}\right]\left[\frac{T_C*1000}{V_{air}}\right] \tag{1}$$

where:

$$\sigma_0=\sqrt{BckCnt_{total}+\sigma^2_{BckCnt}+InterferenceCnt+\sigma^2_{InterferenceCnt}+MemoryCnt+\sigma^2_{MemoryCnt}} \tag{2}$$

ε_β: Efficiency for detection of electrons.
ε_γ: Efficiency for detection of photons.
β_{BR}: Branching ratio of β.
γ_{BR}: Branching ratio of γ.
λ: Decay constant of isotope of interest [s^{-1}].
T_c: Collection time of xenon sample [s].
T_p: Processing time of gas [s].
T_A: Counts acquisition time [s].
V_{air}: Collected air volume [m^3].

and:

BckCnt$_{total}$: summation of the total number of background counts observed in the region of interest.
InterferenceCnt: Counts due to interferences from radon daughters and overlapping ~30 keV regions of interest.
MemoryCnt: Counts due to memory effect in the gas cell.

The memory effect is a phenomenon in which the xenon gas sample diffuses through the walls of the plastic scintillator, leading to an elevation in the background radiation level for subsequent measurements. The σ_0 term in Eq. (2) can be simplified if assumptions are made regarding the memory effect and interference counts. For example, when a pure xenon sample is used for testing a prototype detection system, interference from other sources can be ignored. If a detection material with a negligible memory effect is employed in the capacity of a gas cell, the memory effect counts, and the associated error term also can be zero. For prototype detection systems that might not have a dedicated gas processing unit, it is critical to mention the gas processing parameters used in the MDC calculations.

In a situation in which there is more than one decay path of interest, such as the case of ^{133}Xe that emits an 81 keV photon in coincidence with 346 keV beta particle and a 31 keV X-ray in coincidence with a 45 keV conversion electron and a 346 keV beta particle, a weighted average method is employed to calculate the MDC for that radioxenon. This approach is shown in Eq. (3).

$$MDC_{133_{Xe}}\left(\frac{\mathrm{mBq}}{\mathrm{m}^3\ air}\right) = \sqrt{\frac{1}{\left(MDC^{\frac{81\ \mathrm{keV}}{133_{Xe}}}\right)^{-2} + \left(MDC^{\frac{30\ \mathrm{keV}}{133_{Xe}}}\right)^{-2}}} \tag{3}$$

2 Initial Radioxenon Detection Systems and Improvements

In the late 1990s and early 2000s, four nations volunteered to develop noble gas detection systems. The American Automated Radio-xenon Sampler/Analyzer (ARSA), Swedish Automatic Unit for Noble Gas Acquisition (SAUNA), Russian Analyzer for Xenon Radioisotopes (ARIX), and the French Système de Prélèvement Automatique en Ligne Avec l'Analyse du Xénon (SPALAX™) were some of the initial radioxenon systems that were developed. These systems generally include a dedicated gas-processing unit that is responsible for sampling the atmosphere and then isolating the xenon sample. This gas sample is subsequently injected into the gas cell where the xenon sample is counted. It is worth mentioning that these systems generally have complex built-in gas separation and purification systems. However, in this chapter we focus on the radiation detection aspects of these systems.

2.1 *Xenon Counting Strategies*

Most detection systems (i.e., ARSA, SAUNA, and ARIX) rely on either coincidence-based detection or high-resolution gamma spectroscopy for detecting radioxenon (SPALAX™). Coincidence-based detection techniques require two or more detection media to detect electrons and photons. One method to record near-real time coincidence events is using devices like field programmable gate arrays (FPGAs). These electronic devices accept input from two or more channels where the user selects the channels of interest and the acceptable coincidence time window. The coincidence time window (CTW) defines the maximum time between triggers from two or more channels of interest. For example, assume that in a two-channel system, the CTW is set at 500 ns. As soon as one of the channels triggers, the system clock starts, and within 500 ns (i.e., the CTW), if both the channels trigger, the event is classified as a coincidence event; if not, the trigger is considered to be a singles event and is rejected. The second method of identifying coincidence events is using list mode data. In this method, as soon as any channel of interest triggers, the respective pulse data along with the associated timestamps are recorded. No attempts are made to identify coincidence events. After the measurement campaign and data collection is complete, post processing scripts are run to identify and extract coincidence events.

The high-resolution gamma spectroscopy technique employs high purity Germanium detectors (HPGe) for radioxenon detection (i.e., SPALAX™). This technique

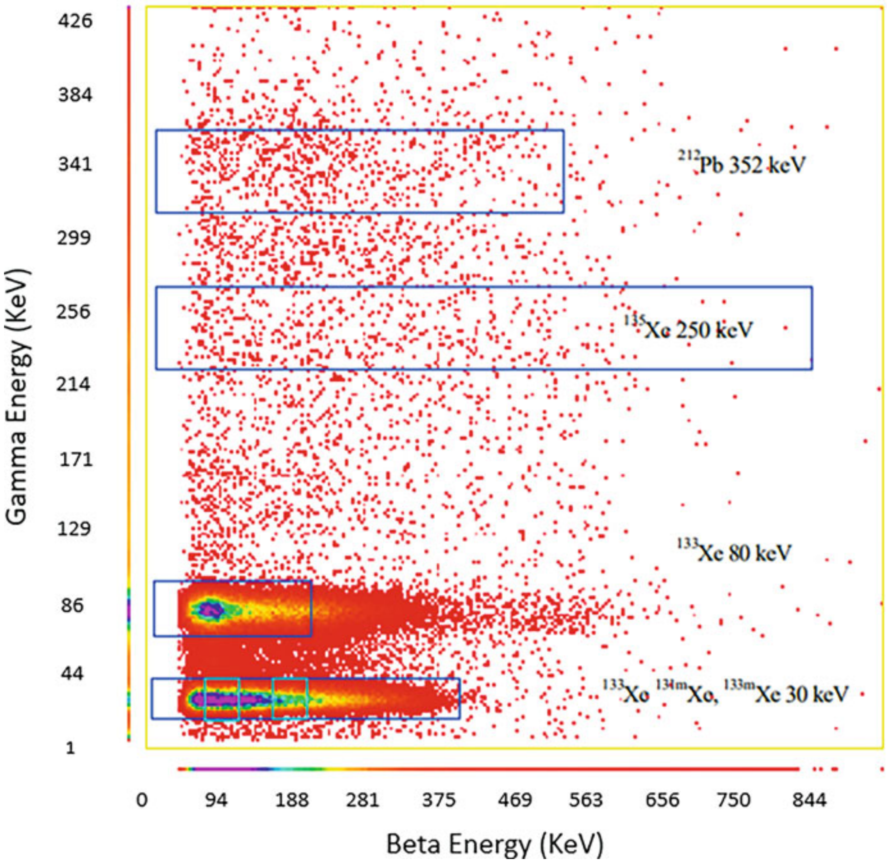

Fig. 3 Regions of interest identified in a two-dimensional coincidence spectrum [15]

only looks for photon emissions, and because of the detector's excellent energy resolution, the photon peaks are finely resolved. Most of the background radiation generally falls outside the regions of interest (ROI) for the photon peaks. An ROI generally is a two or three sigma distribution defined around the peak. The number of counts recorded in these ROIs is used to determine the activity of each radioxenon of interest. The general concept of ROI extends to electron and photon peaks detected in coincidence-based systems as well. It is, however, worth mentioning that recent versions of the SPALAX™ detection system pivoted toward coincidence-based detection. Figure 3 illustrates the concept of regions of interest using a two-dimensional coincidence spectrum obtained from a radioxenon detection system.

2.2 Automated Radio-Xenon Sampler/Analyzer and Xenon International

The ARSA is a coincidence-based detection system designed by Pacific Northwest National Laboratory (PNNL) [16]. In the initial version, photon detection was achieved using NaI detectors, and electrons were detected using plastic scintillators. The plastic detectors also act as a gas cell to hold the gas sample. Optical photon readout from all the scintillators is achieved using photomultiplier tubes. It is worth mentioning that during the development phase of ARSA, PNNL researchers also offered a solution for dealing with ^{222}Rn daughter products. Bi-214 and ^{214}Pb, daughter products of ^{222}Rn emit photons that interfere with ^{133}Xe and ^{135}Xe photon emissions. It must be noted that ^{214}Pb also emits a photon at 352 keV which does not interfere with any radioxenon emissions. It was recommended that prior to xenon measurements, ^{222}Rn be injected into the gas cell and the ratio of counts in the 81, 250, and 352 keV regions be estimated. When radioxenon samples are measured, the counts in the 352 keV region can be used to estimate the number of counts in the 81 and 250 keV ROIs. These counts are subsequently subtracted from the two ROIs to estimate the true counts from xenon isotopes.

Some challenges with the initial ARSA design included the use of the plastic scintillator gas cell which leads to the memory effect. However, it must be mentioned that methods exist to account for memory effect thereby not resulting in an increase in the MDC. The other drawback with this design was the extensive amount of gain matching that was required between various detection media. If one or more photomultiplier tubes (PMT) malfunctioned, there would be a significant effect on the operations of the entire detection system.

Some of these challenges were overcome by the development of a redesigned version of the ARSA coincidence-based detection system [17]. A significant design change was the use of a CsI(Na) detection media rather than NaI. This change in the photon detection medium was supported by an increase in the physical and electron density of CsI(Na) over NaI, thus leading to an increase in the detection efficiency. However, from an energy resolution perspective, NaI provides superior energy resolution compared to CsI(Na) under 100 keV. The next major design change was the introduction of four independent electron and photon detectors. In this design, failure of a single PMT does not affect the performance of the detection system. Other minor improvements include an increase in the solid angle (efficiency) and reductions in the quality control and quality assurance requirements.

The latest radioxenon detection system developed is the Xenon International system [18]. This was developed as part of a collaborative effort between PNNL and Teledyne Brown Engineering. This new design focuses more on the gas-processing systems and employs a NaI detector for photon detection and a plastic detection gas cell for electron detection. Other aspects of the detection system remained similar to the redesigned ARSA detector. The improved design allows xenon sample measurements in quick succession, which also reduces the MDC. The Xenon International system aims to achieve an MDC of under 0.15 mBq/m^3 for ^{131m}Xe, ^{133}Xe, and ^{133m}Xe. An MDC of under 0.5 mBq/m^3 is expected for ^{135}Xe. Other design requirements include two-way communication to be established between the system and the International Data Center at least 95% of the time with an annual downtime of less than 15 days and at most 7 consecutive days.

2.3 Swedish Automatic Unit for Noble Gas Acquisition

The Swedish Defense Research Agency designed and developed the SAUNA coincidence-based detection system [19]. NaI and a plastic scintillator were used for photon and electron detection, respectively. The plastic scintillator also acts as a gas cell. Holes were machined in the NaI detectors to house the plastic scintillators. The gas cell thickness was chosen to maximize the electron detection efficiency while minimizing the attenuation of the 30 keV X-ray photon. Two independent detection systems are used in the SAUNA design, primarily to account for the memory effect observed in the SAUNA system because of the plastic gas cell. A 5 cm (2 inch) thick lead shielding lined with 5 mm of copper is used to shield the system from background radiation and absorb X-ray emissions from the lead shielding. Data acquisition systems such as CAMAC electronics and standard NIM bin modules are used as part of the signal processing chain.

The initial SAUNA system was successful in identifying all radioxenons of interest below the MDC requirements set by the CTBTO. This design however had a few challenges such as memory effect and complex gain matching. Atomic layer deposition was proposed as a potential method to suppress the memory effect [20]. In this method, the interior of the gas cell is coated with a thin layer (a couple hundred nanometers) of Al_2O_3, with the material being slowly deposited in a couple of layers. This layer makes sure there is minimal xenon gas diffusion during counting. A potential challenge with this approach is the reduction in electron detection efficiency because of the Al_2O_3 layer. Efforts also were made to improve gas processing in subsequent designs. Outdated technology, CTBTO requirements set more than two decades ago, significant improvement in radiation detection technologies, advances in gas processing technologies, and improved knowledge of radioxenon background were some of the motivations to develop an advanced design. Improving the overall stability of the system, user friendliness, and maintainability were some of the practical reasons justifying the development of new designs. From a detector performance standpoint, improvements in detection efficiency and increased sampling rate were also achieved in the SAUNA II and SAUNA III systems.

2.4 Analyzer for Xenon Radioisotopes

The ARIX detection system was developed by the Khlopin Radium Institute in the Russian Federation. In the initial version of this design, NaI was used for photon detection while a plastic scintillator was used to detect electrons. It must however be mentioned that only a thin layer of plastic was used on the inside surface of the photon detector, and the thickness of the plastic scintillator was not sufficient to accurately measure the energy deposited by electrons. Events were identified based on electron-gated photon spectroscopy in which only the photon energy is measured, and the thin plastic scintillator signal was only used to detect coincidence events. There is however a significant drawback with this approach. Xe-131m and ^{133m}Xe both emit a 30 keV X-ray in coincidence with conversion electrons. Employing the current design, differentiating the two radionuclide decays is challenging. Variable half-lives between the two radionuclides can be used to estimate the contributions from ^{131m}Xe and ^{133m}Xe. It is worth mentioning that the CTBTO requires data to be reported every 24 hours; however, the variable half-lives method requires about 7–10 days to ascertain the contributions. Therefore, this design cannot effectively differentiate contributions from these two radionuclides while also meeting the requirements of the CTBTO.

To address this shortcoming, the redesigned version of the ARIX detection system used independent electron and photon detection media [21]. The electron and photon spectroscopy were performed using a plastic scintillator and NaI, respectively. Because both the electron and photon energies could be captured in this design, accurate activity measurements of ^{131m}Xe and ^{133m}Xe were feasible.

2.5 Système de Prélèvement Automatique en Ligne Avec l'Analyse du Xénon

The French Atomic Energy Commission (CAE) developed the SPALAX™ detection system. The initial version of this detection system employed only an HPGe detection system; therefore, the detection media were only sensitive to photon emissions. The original SPALAX™ system was able to achieve exceptional energy resolution but suffered from some shortcomings such as the requirement of bulky cooling systems, relatively low detection efficiency because of the use of a low atomic number material (Z), and the detector's increased susceptibility to stray background interactions (compared to coincidence-based systems) in the ROIs defined for the xenon radionuclides of interest (thereby elevating the MDC). To remedy some of these shortcomings, the designers decided to use two independent detection bodies for electron and photon detection. NaI was used in the capacity of a photon detector while Passivated Implanted Planar Silicon (PIPS) was used in the capacity of an electron detector [22]. In this improved version, the PIPSBox, silicon wafers measuring about 0.5 mm are used to detect electrons. Some of the significant advantages of this design include recording only coincidence events (thus improving MCDs), negating the requirement for a dedicated cooling system, and significantly improving photon detection efficiencies. The energy resolution of a PIPSBox is about 7% at a full width at half maximum (FWHM) level of 129 keV, which is significantly better compared to a plastic scintillator (about 23%). The use of a PIPSBox, however, presents the challenge of electron backscatter. Unlike plastics (low Z), the use of a silicon detection media (relatively high Z) results in partial energy deposition and electron backscatter. Therefore, while detecting mono-energetic electron peaks (129 and 159 keV CE), the use of silicon detection media results in a tail representing partial energy deposition. It must be pointed out that algorithms are available to perform the summing operation for energy deposited in the two-silicon media. However, this process only works when the energy deposited by the electron in the two silicon wafers is over the energy threshold. The other significant drawback of this design is the solid angle of the PIPSBox, which is not 4π as in the case of a plastic scintillator gas cell. The next generation of the design was termed as SPALAX-NG. This system employed a PIPSBox for electron detection and a broad energy germanium detector for photon detection [23]. This system could sample about 60 m^3 of air every 8 hours and featured several other improvements on the gas processing end.

Figure 4 illustrates some of the initial radioxenon detectors like the redesigned ARSA, SAUNA, ARIX, and the SPALAX-NG detection systems. Figure 5 shows the two-dimensional coincidence spectra from the ARSA and SAUNA detection systems.

3 Novel Detection Systems and Materials

From the mid-2000s, several groups around the world have been developing radioxenon detectors either using novel detection elements such as CdZnTe (CZT) and stilbene or using variable designs like a phoswich detection system. This section explores a variety of detectors including some new detection concepts and media.

3.1 Gas Based and High-Pressure Scintillation Detectors

In the late 1990s and early 2000s, a few research groups developed gas-based radioxenon detectors. These include the Gas Proportional Scintillation Counter and the Gas Analysis, Separation, and Purification System (GASP) based systems [24, 25]. The Gas Proportional Scintillation Counter employed a multi wire proportional counter and two face-to-face silicon detection media for electron detection. Full widths at half maximum of 1.4 and 25 keV were observed for the 30 keV X-ray and the 45 keV conversion electron, respectively. Because the detection media is gas-based, this system also was exceptional at reducing background counts. However,

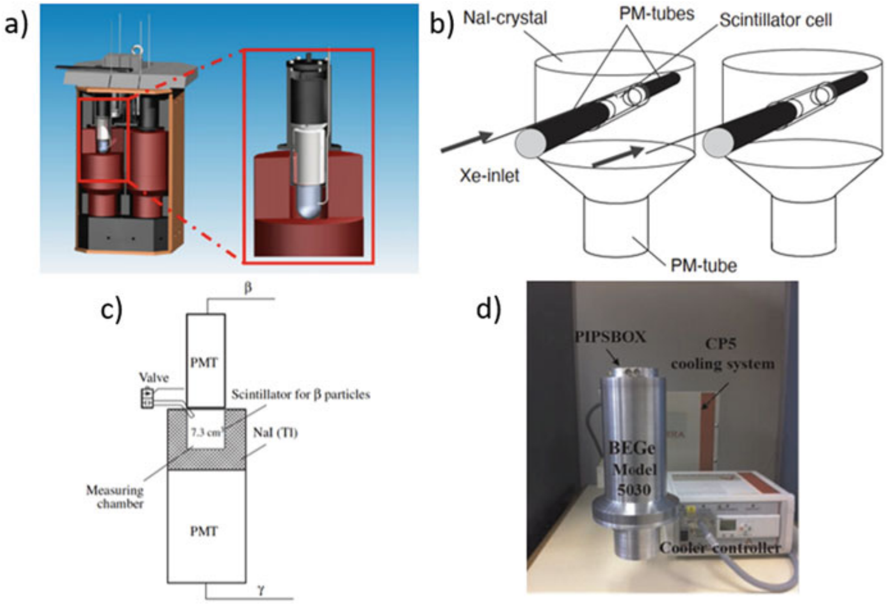

Fig. 4 Various radioxenon detection systems. (**a**) Redesigned ARSA detection system showing a cut section view of the individual electron-photon detection system [17], (**b**) the initial version of the SAUNA detection system [19], (**c**) ARIX detection system employing the electron gated gamma detection technology [21], and (**d**) the SPALAX-NG system showing the PIPSBox and the gamma detection system [23]

in an effort to improve the detection efficiency, especially for ^{133}Xe and ^{135}Xe, it was recommended to switch to inorganic or solid-state detection media. In the Gas Analysis, Separation, and Purification System, flow meters were incorporated to calculate the net counts as a function of the pressure and flow of the gas. This system however presented a challenge of variable electron detection efficiency as a function of pressure. Therefore, at high pressure (1030–2070 kPa), the detection efficiency drastically drops thereby affecting the performance of the system.

3.2 *Phoswich Detectors*

A Phoswich detector is a system that employs multiple scintillation media coupled to a single PMT or a silicon photomultiplier (SiPM) system. Generally, two detection media with dissimilar scintillator properties such as rise time are combined in this configuration. The idea is to deconvolve a single PMT/SiPM pulse into corresponding signals resulting from electron and photon interactions in their respective detection media. Over the years, several phoswich detection systems have

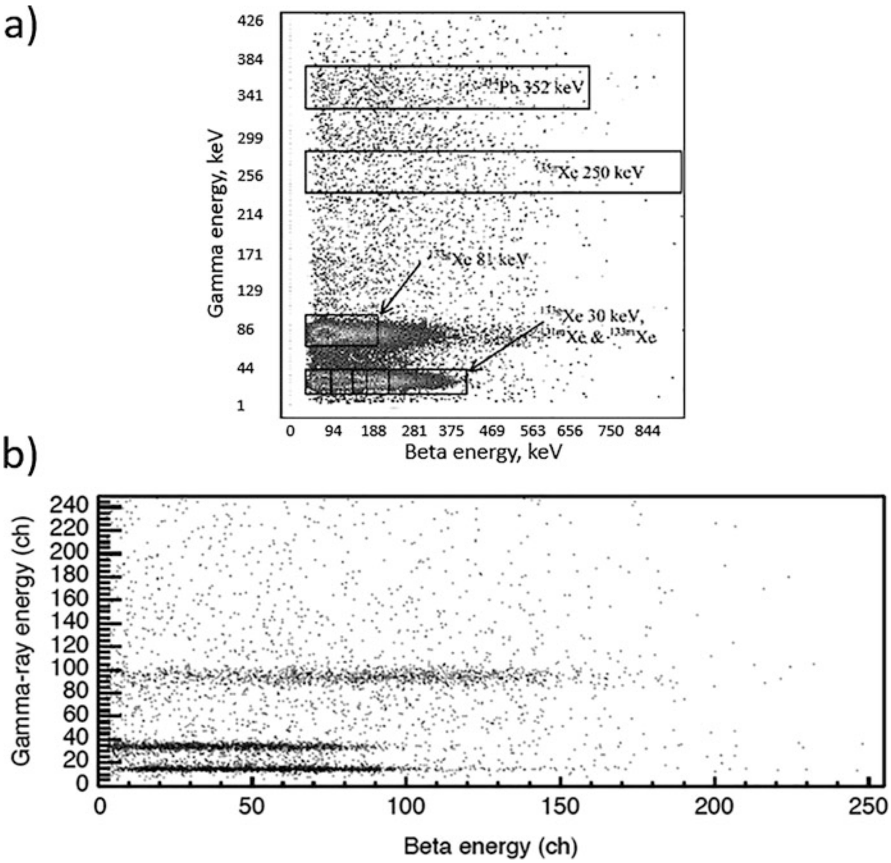

Fig. 5 Coincidence spectra from the (**a**) ARSA [16] and (**b**) SAUNA [19] detection systems

been designed. This section covers a couple of phoswich detection systems that have been developed in the past.

The detection system developed at PNNL employed a cylindrical NaI(Tl) encompassed by CaF_2(Eu) on one end and by the PMT on the other end [26]. The system relied on the variable rise time of the two scintillators to discriminate between the electron and photon signals from CaF_2(Eu) and NaI(Tl), respectively. It however proved to be a challenge in discriminating rise times that fall outside the two predefined regions. It was reported that advancements in discrimination algorithms were required to better discriminate between the various events. A triple-layer phoswich detection system was developed by Oregon State University using NaI(Tl), CaF_2(Eu), and bismuth germanium oxide (BGO) [27]. Custom-designed electronic readout was used for this detection system and initial results indicated that the detection system was successful in detecting electron and photon events at lower energies; however, at higher energies, an increased number of events were rejected or mis-characterized. A second iteration of this design employed CsI(Tl), BGO, and BC-400 plastic scintillators [28]. The concept was to identify electron and photon energy depositions using BC-400 and CsI(Tl), respectively, while BGO was used as a Compton suppression medium to enhance the spectra. A reduction of about 20–25% was observed in the low-energy Compton region with a ^{137}Cs source.

In 2007, a phoswich detection system was proposed that has the capability to detect alpha, beta, and gamma radiation in a mixed field environment using pulse shape discrimination [29]. Several detector configurations including a double phoswich system were proposed in this work while employing ZnS(Ag) for alpha detection, NaI for gamma detection, CaF_2(Eu) or a plastic scintillator for energy dependent electron detection. In this system, CaF_2(Eu) could also be used for low-energy X-ray detection. Liquid scintillation could be used to improve the system sensitivity, thus opening doors for low-level environmental detection.

The phoswich detection system developed by XiA LLC employs a combination of CsI(Tl) and a BC-404 plastic scintillator for radioxenon detection [30]. The 1-inch-diameter plastic cell with a wall thickness of 2 mm was enclosed in an optically coupled 3-inch diameter CsI(Tl) crystal with a height of 3 inch. In 2014, a simulation study was carried out to explore several unconventional gas cell geometries. Based on the study results, a decision was made to explore a planar gas cell fabricated using BC-404 for electron detection and CsI(Tl) for photon detection [31]. Mylar sheets were used on either side of the planar walls to combat the memory effect. Significant improvements in detector weight, size, and memory effect were achieved with this design. Most recently in 2021, a NaI-plastic (BC-404) based phoswich detection system yielded an MDC of under 1 mBq/m^3 for all radioxenons of interest [32].

3.3 Scintillator Systems

This section covers some of the detection systems that rely solely on scintillation technologies to detect radioxenons. These include the Stilbene-NaI, the Iranian Noble Gas Analyzing System for radioxenon measurement, and the Stilbene-SrI_2(Eu) detection systems [33–35]. Stilbene is a hydrocarbon like plastic, but because of its crystalline structure, a two orders of magnitude reduction in the memory effect is generally observed (0.04% vs. 5%). The crystalline structure prohibits the diffusion of xenon gas through the walls of the scintillator.

The stilbene-NaI based detection system was developed by the University of Michigan in collaboration with PNNL. Using the stilbene gas cell also resulted in a slight improvement in the energy resolution of the 129 keV conversion electron compared to plastic scintillators. Stilbene also is capable of exhibiting pulse shape discrimination properties that resulted in an improvement of the MDC by about 1% compared to a traditional plastic cell. It is worth mentioning that an MDC of under 1 mBq/m^3 was obtained for all radioxenons of interest using this design. A memory effect of 0.043% was reported using the stilbene cell.

The Iranian Noble Gas Analyzing System is a detection system that employs NaI for photon detection and a plastic scintillation cell for electron detection. This design is similar to the ARSA, SAUNA, and ARIX coincidence-based detection systems. A minimum detectable activity similar to that obtained by Le Petit and Xie has been reported [22, 36]. The stilbene SrI_2 detection system uses two SrI_2(Eu) bodies for photon detection and the stilbene cell as an electron detector and a gas cell. The two SrI_2(Eu) D-Shaped crystals are positioned adjacent to the stilbene gas cell in an effort to increase the detection efficiency. A horizontal cut on the SrI_2(Eu) crystals enables optical photon collection using the minimum number of SiPM arrays. Custom-made electronics were developed for identifying coincidence events in real-time using an FPGA. An MDC of under 1 mBq/m^3 was obtained for all the radioxenons of interest and a memory effect of 0.069% was reported for this system. The drawback of this design is the requirement of a large CTW because of the slow response time of SrI_2(Eu) compared to other scintillators like lanthanum or cerium bromide.

3.4 Semi-Conductor Systems

Semi-conductor detection systems have been used extensively for the detection of radioxenon. Systems that entirely depend on solid-state detection technologies are covered in this section. Three detection materials are typically used in these detectors, Germanium-based HPGe, CZTs, or silicon-based systems like the PIPS. Some examples of these systems include two PIPSBox-CZT-based designs developed by Czyz et al. [37] and Fan [38], a single detector material system designed using two face-to-face CZT crystals [39], and the prototype 24-element silicon pin diode detector used for radioxenon detection [40].

The Two-Element CZT detection system uses two 1 cm^3 co-planar grid detectors for detecting both electrons and photons. A plastic detector holder was designed, and 3-D printed to act as a gas cell. The use of high Z detection material enables high detection efficiencies for photons to be achieved. On the flip side, because CZT also is being used for electron detection, it has resulted in partial energy deposition and extensive electron backscatter. This feature is especially pronounced for monoenergetic conversion electrons. The photons were detected with an excellent energy resolution but partial electron energy deposition, complex detector electronics, and relatively poor solid angle were some of the challenges. The Two-Element CZT system achieved an MDC under 1 mBq/m^3 for only ^{133}Xe.

Two radioxenon detection systems were developed using the PIPSBox and CZT technology. The initial design developed by Czyz used two 1 cm^3 CZT crystals in conjunction with the PIPSBox [37]. The latest design developed by Fan employed the PIPSBox but used a total of eight CZT crystals, each measuring 1 cm × 1 cm × 0.5 cm [38]. Four CZT crystals were arranged on either side of the PIPSBox. The Two-Element CZT detection system employed near real-time coincidence identification while the Eight-Element CZT detection system collected data in list mode with the respective event timestamp and post-processed the data to identify coincidence events. In both systems, CZT is used for photon detection while the PIPSBox is used as a gas cell and for electron detection. From an electron detection perspective, PIPSBox has excellent energy resolution compared to plastic or stilbene-based systems. This system also has a considerably lower memory effect compared to a plastic based system but a higher memory effect than a stilbene gas cell based system. Because silicon also is relatively high Z compared to plastic or stilbene, some amount of electron backscatter still is observed while using this system. Although digital summing techniques are available when both the silicon wafers trigger within the CTW, this system relies heavily on the fact that the energy deposited in both the silicon wafers is above the energy threshold. Moreover, because the solid angle of the PIPSBox is not near 4π, the electron detection efficiency is low compared to plastic or stilbene-based systems. This also presents a challenge to the digital-summing methodology described previously because there is no certainty that the backscattered electron will definitely interact with the other silicon wafer. Goodwin et al. recently developed a PIPSBox–HPGe detection system that has demonstrated improved discrimination and comparatively less interference compared to the SAUNA II detection system currently used at GBL15, the United Kingdom's CTBT certified laboratory [41].

The 24-element silicon PIN diode detector uses four 25 mm^2 PIN diodes mounted on all six sides to achieve a total detection area of 600 mm^2. A copper housing is used as a detector holder and also the gas cell. A detector response is obtained by digitally summing the signals from all the detectors. This detection system demonstrated excellent energy resolution for the X-rays and conversion electrons. It is worth mentioning that the 129, 159, and 164 keV peaks were all distinctly resolved in the spectrum. Some of the challenges with this detection system is the low interaction cross section at high photon energies because of the low Z of the detection medium. Therefore, from a detection standpoint, the 81 and 250 keV photon peaks from ^{133}Xe and ^{135}Xe will be challenging to observe in a spectrum.

3.5 Scintillator-Semiconductor Systems

Some of the radioxenon detection systems that employ both scintillation and semiconductor technologies are reviewed in this section. The stilbene-CZT and the **C**ZT, an **A**rray of **S**iPMs, and a **P**lastic Scintillator (CASP) detection system were both designed at Oregon State University [42, 43]. Both designs employed a 1 cm^3 co-planar CZT crystal as a photon detector and the stilbene and plastic gas cells were used to detect electrons. The CZT crystal was placed adjacent to the gas cell to achieve the maximum possible photon detection efficiency. Custom electronics were designed to realize a near real-time coincidence identification system for pulse processing. The optical photon readout was achieved using an SiPM array. The stilbene gas cell had a slightly better energy resolution compared to plastic scintillators, and the memory effect observed in stilbene was about two orders of magnitude less compared to traditional plastic scintillators. In sensitivity studies, an MDC under 1 mBq/m^3 was achieved for all radioxenons of interest except ^{135}Xe for both the stilbene-CZT and the CASP detection systems. Although these designs feature a near 4π solid angle for electron detection, the photon detection efficiency is a significant drawback because only a single CZT crystal is used in both designs.

The Mobile Analyzer of Radioactive Gases OuTflows (MARGOT) detection system was designed as part of a collaborative effort between the French CEA and Mirion Technologies [44]. This detection system uses two face-to-face silicon PIN detectors for the detection of electrons. An effort was made to reduce the leakage current in the silicon detectors by realizing each detector with four independent silicon pixels. A NaI(Tl) detector was used on either side of the silicon PIN detectors. This work also studied the implications of increasing the gas pressure inside the system. Increasing the pressure leads to a slight reduction in the detection efficiency and spectral broadening of the conversion electron peaks both of which are detrimental to the MDC. However, it was demonstrated that the benefits of counting a larger gas volume outweigh the shortcomings of reduced detection efficiency and relatively poor energy resolution for conversion electrons.

The PIPS-SrI_2(Eu) detection system was designed as an upgrade to the PIPS-CZT system designed at Oregon State University [45]. In this design, a dedicated preamplifier was used for the PIPSBox in an effort to reduce the noise in the signal. The use of SrI_2(Eu) improved the photon detection efficiency of the system, thereby resulting in obtaining an MDC of under 1 mBq/m^3 for all radioxenons of interest except ^{135}Xe (an MDC of exactly 1 mBq/m^3 was obtained for ^{135}Xe). Challenges with respect to electron backscatter and relatively poor photon detection efficiency compared to systems like ARSA are still some of the challenges with this system. A recently designed plastic–HPGe detection system was an attempt to achieve high electron detection efficiency. A low leakage rate of about 1×10^{-4} PaL/s was calculated for the gas cell. An electron energy resolution of 27% was determined for the 129 keV conversion electron. Sub-atmospheric pressures were maintained inside the gas cell to achieve an electron detection efficiency of 98.8% and 96.6% for the 129 and 346 keV conversion electron and beta particles, respectively. A memory effect of about 3% was reported for the plastic gas cell. The use of a broad energy HPGe detection system makes sure the energy resolution for photons is excellent. From an MDC standpoint, because a single HPGe detection system is used in this work, the photon detection efficiency is likely to be lower compared to other well-type scintillators.

The exploded view of the MARGOT system, the cut-section view of the stilbene-SrI_2(Eu) detector, and the exteriors of the 24-element silicon PIN diode detector are shown in Fig. 6.

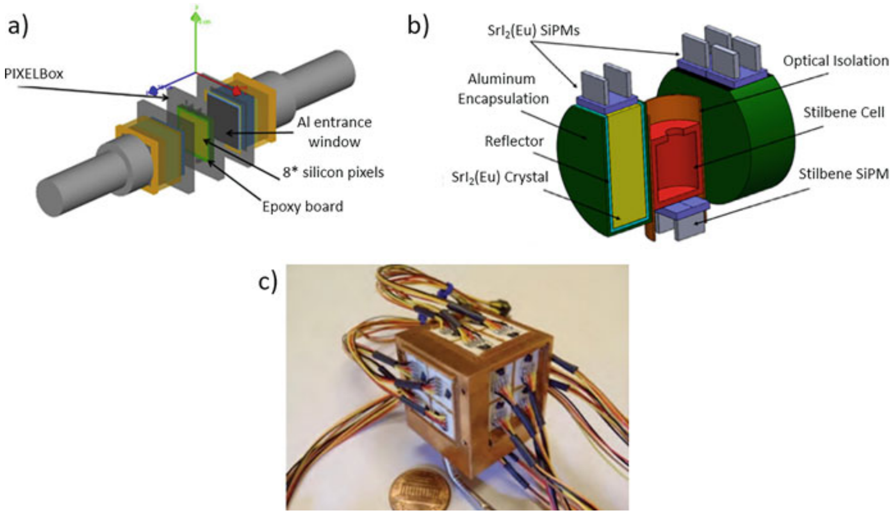

Fig. 6 Detector designs of some novel systems. (**a**) Exploded view of the MARGOT system constructed using Geant4 [44]; (**b**) a SolidWorks cut-section view of the stilbene-SrI$_2$(Eu) detection system [35]; and (**c**) the exterior copper holder of the 24-element silicon PIN diode [40]

4 Discussion and Conclusions

This section provides a high-level overview of various aspects of radioxenon detection systems developed over the past two and half decades. Inferences and conclusions will be drawn based on the expertise of researchers and operational history of some of these systems.

Energy resolution and the MDC of the detection system often go hand in hand. An improvement in energy resolution is theoretically often accompanied by an improvement in the MDC considering all other detection properties are unchanged. This is because some of the ROIs are defined based on the energy resolution of the mono energetic peaks. For electron detection, silicon-based systems offer about two times better energy resolution compared to their organic counterparts. The drawback of silicon-based detectors is often non-4π solid angle, electron backscatter, and the requirement of gain matching. In systems like the PIPSBox, where more than two silicon detection bodies are used, digital energy summing techniques can be used to preserve energy resolution. However, factors such as the energy threshold, solid angle, and electron attenuation often come into play. From a photon detection standpoint, the use of a high-Z, high-density material often is beneficial because it results in an increase in the detection efficiency. Materials such as CZT often have been used in prototype designs; however, the drawback of this practice is that these room-temperature semiconductors face challenges in large-size manufacturing and intricate geometry fabrication such as a well-type design. Therefore, to preserve the solid angle, well-type inorganic detectors can be used even though the energy resolution of these detection materials (CsI, NaI) is often worse compared to CZTs.

As an important parameter, the memory effect is a factor that has been receiving much attention in the past decade. Counts from memory effect can be accounted for in MDC calculations and methods such as atomic layer deposition has been used. New detection materials both in the semiconductor (e.g., PIPS) and organic scintillator (stilbene) families are being explored. It also must be pointed out that using a stilbene cell as opposed to PIPS bypasses the challenges with respect to the solid angle and electron backscatter but results in relatively worse electron energy resolution for conversion electron peaks. Therefore, the tradeoff between energy resolution (PIPS) and detection efficiency (organic gas cells) remains and must be carefully evaluated before designing a system. Demonstrating a near zero memory effect at IMS stations might be beneficial in the long run.

The size of the detection system also plays a role in the overall system performance. A larger detection body implies a higher background rate, which leads to a relatively worse MDC. Although lead shielding is used in an effort to suppress background radiation, high energy particles like muons or other charged particles can traverse through this shielding material and impart energy in the detection media. Sometimes this also leads to a coincidence event being recorded between noise and the high-energy background signal. While using a single instrument (e.g., a data acquisition system) for a system, a high energy interaction also might lead to unintended crosstalk between channels. Therefore, while designing a system aimed at improving MDC, it is often recommended to achieve a near-4π solid angle for detection (for both electrons and photons) while minimizing the detector volume. Table 2 shows the MDCs of various systems for all radioxenons of interest.

Apart from the factors covered, there are other operational and system design aspects for radioxenon detectors that need to be considered. Because most of these systems were designed in the late 1990s and early 2000s, analog electronics were widely used in these designs. It has been noted that analog-based systems generally are from a reliability standpoint more susceptible to environmental conditions such as humidity and temperature than digital electronics. The use of digital systems also helps in reducing the overall size of the detection system. As these systems often are located in remote areas, digital systems might provide dependable data processing, storage, and transmission options. The use of high-resolution detectors for photon detection often uses bulky cooling equipment. As crystal growth technologies evolve, the use of room temperature semiconductor devices might prove to be a logical alternative. Gas processing systems have seen extensive development over the past few years. Integrating technologies such as metal oxide frameworks for selective noble gas capture might help advance the state of the art even further with respect to system sensitivity [49].

The number of detection elements in a system also plays an important role in the performance of the system. Out of the systems covered in this chapter, there are a few detectors that employ more than one element for detecting electrons or photons. Such systems require extensive detector calibration and gain matching to make sure that performance of all the detection bodies is similar. Improper gain

Table 2 MDC of various radioxenon detectors designed around the world

Radioxenon isotope	Xenon International (mBq/m^3) [46]	SAUNA III (mBq/m^3) [47]	SPALAX-NG (mBq/m^3) [21]	MARGOT (mBq/m^3) [48]	24 PIN-Si (mBq/m^3) [40]	PIPSBox-SrI$_2$(Eu) (mBq/m^3) [45]	Stilbene-SrI$_2$(Eu) (mBq/m^3) [35]
^{131m}Xe	0.15	0.246	0.1	0.6	0.72	0.12	0.11
^{133m}Xe	0.15	0.152	0.1	0.6	0.65	0.15	0.13
^{133}Xe	0.15	0.221	0.1	0.9	0.11	0.26	0.20
^{135}Xe	0.5	0.295	0.4	0.9	1.3	1.00	0.73

matching often can lead to spectral broadening that directly impacts the width of the regions of interest and the MDC. For systems like the MARGOT that employ eight silicon detection bodies and two NaI detectors, extensive gain matching was required. Also, employing multiple detection bodies might prove to be a long-term operational challenge.

Finally, we will be covering the choice of material for use in radioxenon detection. Like most systems, some preliminary requirements are high intrinsic and geometric detection efficiency, high energy resolution, low memory effect, relatively compact size, and low electron backscatter. Keeping some of these requirements in mind, if an electron detector were to be chosen, a silicon or an inorganic scintillator would potentially be an ideal choice. Designers must evaluate the pros and cons of high energy resolution as opposed to detection efficiency based on the specific requirements of the system. For a photon detector, generally a high-Z, high-density material is preferred to maximize detection efficiency. CZTs generally fulfill these criteria and also have an energy resolution under 2% for the 662 keV peak. The challenge with CZTs is the non-availability of custom intricate detection geometries that help in improving their solid angle. The leakage current in thick crystals is also of concern for CZTs and any semiconductor system in general for both electron and photon detection. Several new promising solid-state detection materials have been recently discovered such as $TlPbI_3$ and $CsPbBr_3$ that might be used for radioxenon detection when the large size crystal growth technology matures [50, 51]. Moisture uptake with time also is a challenge encountered by hygroscopic scintillators (NaI, CsI). Novel detection materials such as cesium hafnium chloride have been demonstrated to exhibit respectable energy resolution of about 3.3% at 662 keV and maintain a high light yield while also being non-hygroscopic in nature [52]. Materials like this might be used for radioxenon detection in remote and humid areas without extensive encapsulation. In the long run, sensitivity, and performance improvements in radioxenon systems can be achieved with enhancements in selective noble gas capture, crystal growth, and digital pulse processing technologies.

References

1. Comprehensive Nuclear-Test-Ban Treaty Organization. (2022). *Who are we*. https://www.ctbto.org/specials/who-we-are/. Accessed 5 June 2022.
2. Comprehensive Nuclear-Test-Ban Treaty Organization. (2022). *Status of signature and ratification*. https://www.ctbto.org/the-treaty/status-of-signature-and-ratification/. Accessed 5 June 2022.
3. Comprehensive Nuclear-Test-Ban Treaty Organization. (2017). *Four more IMS stations certified in China, 2022*. https://www.ctbto.org/press-centre/highlights/2017/2017-four-more-ims-stations-certified-in-china/. Accessed 5 June 2022.
4. Carrigan, C. R., & Sun, Y. (2014). Detection of noble gas radionuclides from an underground nuclear explosion during a CTBT on-site inspection. *Pure and Applied Geophysics, 171*(3–5), 717–734. https://doi.org/10.1007/s00024-012-0563-8

5. Comprehensive Nuclear-Test-Ban Treaty Organization. (2022). *International Monitoring System*. https://www.ctbto.org/fileadmin/user_upload/IMS_Map/IMS_Map_FRONT_BACK_AUGUST_2021_webfriendly.pdf. Accessed 5 June 2022.
6. Bowyer, T. W., Schlosser, C., Abel, K. H., Auer, M., Hayes, J. C., Heimbigner, T. R., McIntyre, J. I., Panisko, M. E., Reeder, P. L., Satorius, H., Schulze, J., & Weiss, W. (2002). Detection and analysis of xenon isotopes for the comprehensive nuclear-test-ban treaty international monitoring system. *Journal of Environmental Radioactivity, 59*(2), 139–151. https://doi.org/10.1016/S0265-931X(01)00042-X
7. Brookhaven National Laboratory, National Nuclear Data Center. (2021). https://www.nndc.bnl.gov/ensdf/. Accessed 6 June 2022.
8. Kalinowski, M. B., & Tuma, M. P. (2009). Global radioxenon emission inventory based on nuclear power reactor reports. *Journal of Environmental Radioactivity, 100*(1), 58–70. https://doi.org/10.1016/j.jenvrad.2008.10.015
9. Le Petit, G., Armand, P., Brachet, G., Taffary, T., Fontaine, J. P., Achim, P., Blanchard, X., Piwowarczyk, J. C., & Pointurier, F. (2008). Contribution to the development of atmospheric radioxenon monitoring. *Journal of Radioanalytical and Nuclear Chemistry, 276*(2), 391–398. https://doi.org/10.1007/s10967-008-0517-x
10. Sivels, C. B., McIntyre, J. I., Bowyer, T. W., Kalinowski, M. B., & Pozzi, S. A. (2017). A review of the developments of radioxenon detectors for nuclear explosion monitoring. *Journal of Radioanalytical and Nuclear Chemistry, 314*(2), 829–841. https://doi.org/10.1007/s10967-017-5489-2
11. Auer, M., Kumberg, T., Sartorius, H., Wernsperger, B., & Schlosser, C. (2010). Ten years of development of equipment for measurement of atmospheric radioactive xenon for the verification of the CTBT. *Pure and Applied Geophysics, 167*(4–5), 471–486. https://doi.org/10.1007/s00024-009-0027-y
12. Ringbom, A., Elmgren, K., Lindh, K., Peterson, J., Bowyer, T. W., Hayes, J. C., McIntyre, J. I., Panisko, M., & Williams, R. (2009). Measurements of radioxenon in ground level air in South Korea following the claimed nuclear test in North Korea on October 9, 2006. *Journal of Radioanalytical and Nuclear Chemistry, 282*(3), 773–779. https://doi.org/10.1007/s10967-009-0271-8
13. Orr, B., Schöppner, M., Tinker, R., & Plastino, W. (2013). Detection of radioxenon in Darwin, Australia following the Fukushima Dai-ichi nuclear power plant accident. *Journal of Environmental Radioactivity, 126*, 40–44. https://doi.org/10.1016/j.jenvrad.2013.07.002
14. McIntyre, J. I., Bowyer, T. W., & Reeder, P. L. (2006). *Calculation of minimum-detectable-concentration levels of radioxenon isotopes using the PNNL ARSA system*. http://www.osti.gov/servlets/purl/888707-mEmCmY/. Accessed 6 June 2022.
15. Columbia University. (2022). *The DOE automated radioxenon sampler-analyzer (ARSA) beta-gamma coincidence spectrometer data analyzer*. https://www.ldeo.columbia.edu/res/pi/Monitoring/Doc/Srr_2000/6-Radionuclide/06_01.pdf. Accessed 5 June 2022.
16. McIntyre, J. I., Abel, K. H., Bowyer, T. W., Hayes, J. C., Heimbigner, T. R., Panisko, M. E., Reeder, P. L., & Thompson, R. C. (2001). Measurements of ambient radioxenon levels using the automated radioxenon sampler/analyzer (ARSA). *Journal of Radioanalytical and Nuclear Chemistry, 248*, 629–635. https://doi.org/10.1023/A:1010672107749
17. Cooper, M. W., McIntyre, J. I., Bowyer, T. W., Carman, A. J., Hayes, J. C., Heimbigner, T. R., Hubbard, C. W., Lidey, L., Litke, K. E., Morris, S. J., Ripplinger, M. D., Suarez, R., & Thompson, R. (2007). Redesigned β–γ radioxenon detector. *Nuclear Instruments and Methods in Physics Research Section A: Accelerators, Spectrometers, Detectors and Associated Equipment, 579*(1), 426–430. https://doi.org/10.1016/j.nima.2007.04.092
18. Teledyne Brown Engineering. (2022). *Xenon International*. https://www.tbe.com/energy/xenon-international. Accessed 5 June 2022.
19. Ringbom, A., Larson, T., Axelsson, A., Elmgren, K., & Johansson, C. (2003). SAUNA—A system for automatic sampling, processing, and analysis of radioactive xenon. *Nuclear Instruments and Methods in Physics Research Section A: Accelerators, Spectrometers, Detectors and Associated Equipment, 508*(3), 542–553. https://doi.org/10.1016/S0168-9002(03)01657-7

20. Bläckberg, L., Fritioff, T., Mårtensson, L., Nielsen, F., Ringbom, A., Sjöstrand, H., & Klintenberg, M. (2013). Memory effect, resolution, and efficiency measurements of an Al2O3 coated plastic scintillator used for radioxenon detection. *Nuclear Instruments and Methods in Physics Research Section A: Accelerators, Spectrometers, Detectors and Associated Equipment, 714*, 128–135. https://doi.org/10.1016/j.nima.2013.02.045
21. Popov, Y. S., Kazarinov, N. M., Popov, V. Y., Rykov, Y. M., & Skirda, N. V. (2005). Measuring low activities of fission-product xenon isotopes using the β-γ coincidence method. *Instruments and Experimental Techniques, 48*(3), 380–386. https://doi.org/10.1007/s10786-005-0066-2
22. Le Petit, G., Cagniant, A., Morelle, M., Gross, P., Achim, P., Douysset, G., Taffary, T., & Moulin, C. (2013). Innovative concept for a major breakthrough in atmospheric radioactive xenon detection for nuclear explosion monitoring. *Journal of Radioanalytical and Nuclear Chemistry, 298*, 1159–1169. https://doi.org/10.1007/s10967-013-2525-8
23. Le Petit, G., Cagniant, A., Gross, P., Douysset, G., Topin, S., Fontaine, J. P., Taffary, T., & Moulin, C. (2015). Spalax™ new generation: A sensitive and selective noble gas system for nuclear explosion monitoring. *Applied Radiation and Isotopes, 103*, 102–114. https://doi.org/10.1016/j.apradiso.2015.05.019
24. Lopes, J. A. M., Morgado, R. E., & Conde, C. A. N. (2003). A metastable xenon isotope detector for treaty verification. *Nuclear Instruments and Methods in Physics Research Section A: Accelerators, Spectrometers, Detectors and Associated Equipment, 501*(2–3), 623–629. https://doi.org/10.1016/S0168-9002(03)00621-1
25. Schell, W. R., Vives-Batlle, J., Yoon, S. R., & Tobin, M. J. (1999). High-pressure plastic scintillation detector for measuring radiogenic gases in flow systems. *Nuclear Instruments and Methods in Physics Research Section A: Accelerators, Spectrometers, Detectors and Associated Equipment, 421*(3), 591–600. https://doi.org/10.1016/S0168-9002(98)01217-0
26. Ely, J. H., Aalseth, C. E., & McIntyre, J. I. (2005). Novel beta-gamma coincidence measurements using phoswich detectors. *Journal of Radioanalytical and Nuclear Chemistry, 263*(1), 245–250. https://doi.org/10.1007/s10967-005-0044-y
27. Farsoni, A. T., & Hamby, D. M. (2007). A system for simultaneous beta and gamma spectroscopy. *Nuclear Instruments and Methods in Physics Research Section A: Accelerators, Spectrometers, Detectors and Associated Equipment, 578*(3), 528–536. https://doi.org/10.1016/j.nima.2007.06.020
28. Farsoni, A. T., Alemayehu, B., Alhawsawi, A., & Becker, E. M. (2013). A phoswich detector with Compton suppression capability for radioxenon measurements. *IEEE Transactions on Nuclear Science, 60*(1), 456–464. https://doi.org/10.1109/TNS.2012.2226606
29. de Celis, B., de la Fuente, R., Williart, A., & de Celis Alonso, B. (2007). Coincidence measurements in α/β/γ spectrometry with phoswich detectors using digital pulse shape discrimination analysis. *Nuclear Instruments and Methods in Physics Research Section A: Accelerators, Spectrometers, Detectors and Associated Equipment, 580*(1), 206–209. https://doi.org/10.1016/j.nima.2007.05.085
30. Hennig, W., Warburton, W. K., Fallu-Labruyere, A., Sabourov, K., Cooper, M. W., McIntyre, J. I., Gleyzer, A., Bean, M., Korpach, E. P., Ungar, K., Zhang, W., & Mekarski, P. (2009). Development of a phoswich detector system for radioxenon monitoring. *Journal of Radioanalytical and Nuclear Chemistry, 282*(3), 681–685. https://doi.org/10.1007/s10967-009-0181-9
31. Hennig, W., Asztalos, S. J., Warburton, W. K., Fallu-Labruyere, A., Samie, A., & Mekarski, P. (2014). Development of a phoswich detector for radioxenon field measurements. *IEEE Transactions on Nuclear Science, 61*(5), 2778–2785. https://doi.org/10.1109/TNS.2014.2343158
32. Luo, F., Xiang, Y., Gong, J., Ze, R., Yan, Z., Wang, Q., Weng, K., Hao, F., & Zeng, J. (2021). A well-type NaI(Tl)/BC404 phoswich detector for atmospheric radioxenon monitoring. *Nuclear Instruments and Methods in Physics Research Section A: Accelerators, Spectrometers, Detectors and Associated Equipment, 986*, 164715. https://doi.org/10.1016/j.nima.2020.164715
33. Sivels, C. B., McIntyre, J. I., Prinke, A. M., Day, A. R., Lynch, C., Clarke, S. D., & Pozzi, S. A. (2019). Stilbene cell development to improve radioxenon detection. *Nuclear Instruments and Methods in Physics Research Section A: Accelerators, Spectrometers, Detectors and Associated Equipment, 923*, 72–78. https://doi.org/10.1016/j.nima.2019.01.022

34. Doost-Mohammadi, V., Afarideh, H., Etaati, G. R., Safari, M. J., & Rouhi, H. (2016). INGAS: Iranian Noble Gas Analyzing System for radioxenon measurement. *Radiation Physics and Chemistry, 120*, 26–32. https://doi.org/10.1016/j.radphyschem.2015.10.020
35. Gadey, H. R., Farsoni, A. T., & Czyz, S. A. (2022). A stilbene–strontium iodide based radioxenon detection system for monitoring nuclear explosions. *Nuclear Instruments and Methods in Physics Research Section A: Accelerators, Spectrometers, Detectors and Associated Equipment, 1029*, 166427. https://doi.org/10.1016/j.nima.2022.166427
36. Xie, F., Jiang, W., Li, X., He, X., Zhang, J., & Yu, G. (2013). Single channel beta–gamma coincidence system for radioxenon measurement using well-type HPGe and plastic scintillator detectors. *Nuclear Instruments and Methods in Physics Research Section A: Accelerators, Spectrometers, Detectors and Associated Equipment, 729*, 900–904. https://doi.org/10.1016/j.nima.2013.08.070
37. Czyz, S. A., Farsoni, A. T., & Gadey, H. R. (2019). Evaluation of a semiconductor-based atmospheric radioxenon detection system. *Nuclear Instruments and Methods in Physics Research Section A: Accelerators, Spectrometers, Detectors and Associated Equipment, 945*, 162614. https://doi.org/10.1016/j.nima.2019.162614
38. Fan, Y., Ai, X., Wang, S., Li, Q., Wang, Y., Chang, Y., Zhao, Y., Zhang, X., & Jia, H. (2022). A beta–gamma radioxenon detection system using PIPS and CZT-Array. *Nuclear Instruments and Methods in Physics Research Section A: Accelerators, Spectrometers, Detectors and Associated Equipment, 1031*, 166587. https://doi.org/10.1016/j.nima.2022.166587
39. Ranjbar, L., Farsoni, A. T., & Becker, E. M. (2017). 135Xe measurements with a two-element CZT-based radioxenon detector for nuclear explosion monitoring. *Journal of Environmental Radioactivity, 169–170*, 221–228. https://doi.org/10.1016/j.jenvrad.2016.12.003
40. Cox, C. E., Hennig, W., Huber, A. C., Warburton, W. K., Grudberg, P. M., Asztalos, S. J., Tan, H., & Biegalski, S. (2013). A 24-element Silicon PIN diode detector for high resolution radioxenon measurements using simultaneous X-ray and electron spectroscopy. In *2013 IEEE nuclear science symposium and medical imaging conference (2013 NSS/MIC)* (pp. 1–7). IEEE.
41. Goodwin, M. A., Regan, P. H., Bell, S. J., Britton, R., & Davies, A. V. (2022). Enhancing the detection sensitivity of a high-resolution $\beta - \gamma$ coincidence spectrometer. *Journal of Environmental Radioactivity, 250*, 106915. https://doi.org/10.1016/j.jenvrad.2022.106915
42. Gadey, H. R., Farsoni, A. T., Czyz, S. A., & McGee, K. D. (2019). A stilbene – CdZnTe based radioxenon detection system. *Journal of Environmental Radioactivity, 204*, 117–124. https://doi.org/10.1016/j.jenvrad.2019.03.027
43. Czyz, S. A., & Farsoni, A. T. (2017). A radioxenon detection system using CdZnTe, an array of SiPMs, and a plastic scintillator. *Journal of Radioanalytical and Nuclear Chemistry, 313*(1), 131–140. https://doi.org/10.1007/s10967-017-5287-x
44. Thomas, V., Delaune, O., Le Petit, G., & Fontaine, J. P. (2019). The Mobile Analyzer of Radioactive Gases OuTflows (MARGOT): A promising environmental xenon radionuclides detection system. *Applied Radiation and Isotopes, 153*, 108820. https://doi.org/10.1016/j.apradiso.2019.108820
45. Czyz, S. A., Farsoni, A. T., & Gadey, H. R. (2021). A PIPS + SrI2(Eu) detector for atmospheric radioxenon monitoring. *Nuclear Instruments and Methods in Physics Research Section A: Accelerators, Spectrometers, Detectors and Associated Equipment, 1012*, 165619. https://doi.org/10.1016/j.nima.2021.165619
46. Hayes, J. C., Harper, W., Panisko, M., & Cooper, M. W. (2018). *Xenon International Overview*. http://www.osti.gov/servlets/purl/1472068/. Accessed 5 June 2022.
47. Comprehensive Nuclear-Test-Ban Treaty Organization. (2022). https://ctnw.ctbto.org/DMZ/event/3239/posters/F22C0FB597434C9DB3874D8FECF253FB. Accessed 5 June 2022.
48. Thomas, V., Delaune, O., Cagniant, A., Le Petit, G., & Fontaine, J.-P. (2019). Introducing the MARGOT prototype: An ultra-compact and mobile gas detection system for nuclear explosion monitoring. *Applied Radiation and Isotopes, 152*, 91–100. https://doi.org/10.1016/j.apradiso.2019.06.032
49. Banerjee, D., Simon, C. M., Plonka, A. M., Motkuri, R. K., Liu, J., Chen, X., Smit, B., Parise, J. B., Haranczyk, M., & Thallapally, P. K. (2016). Metal–organic framework with optimally

selective xenon adsorption and separation. *Nature Communications, 7*(1), ncomms11831. https://doi.org/10.1038/ncomms11831

50. Hany, I., Yang, G., Phan, Q. V., & Kim, H. J. (2021). Thallium lead iodide (TlPbI3) single crystal inorganic perovskite: Electrical and optical characterization for gamma radiation detection. *Materials Science in Semiconductor Processing, 121*, 105392. https://doi.org/10.1016/j.mssp.2020.105392
51. He, Y., Petryk, M., Liu, Z., Chica, D. G., Hadar, I., Leak, C., Ke, W., Spanopoulos, I., Lin, W., Chung, D. Y., Wessels, B. W., He, Z., & Kanatzidis, M. G. (2021). CsPbBr3 perovskite detectors with 1.4% energy resolution for high-energy γ-rays. *Nature Photonics, 15*(1), 36–42. https://doi.org/10.1038/s41566-020-00727-1
52. Burger, A., Rowe, E., Groza, M., Morales Figueroa, K., Cherepy, N. J., Beck, P. R., Hunter, S., & Payne, S. A. (2015). Cesium hafnium chloride: A high light yield, non-hygroscopic cubic crystal scintillator for gamma spectroscopy. *Applied Physics Letters, 107*(14), 143505. https://doi.org/10.1063/1.4932570

Shield-Free Directional Gamma-Ray Detector Using Small-Angle Compton Scattering

Yoshiharu Kitayama

1 Introduction

Ten years have passed since the Great East Japan Earthquake of March 11, 2011, and the Fukushima Daiichi Nuclear Power Station (FDNPS) accident. As the FDNPS is being decommissioned, decontamination of the surrounding areas is progressing. People are gradually returning to areas considered difficult to live in 10 years ago.

At the FDNPS, many workers are currently working daily on decommissioning. In certain areas, especially inside the buildings, there are places where people cannot work for long periods due to high air dose rates. There are also hot spots, i.e., areas where radioactive materials have accumulated, and the dose rates are locally high. Remote visualization of the distribution of radioactive materials in such spaces will prevent workers from inadvertently approaching hot spots and increasing their radiation exposure, thus improving their safety. Therefore, an attempt has been made to determine the distribution of radioactive materials in the workplace in advance by using a gamma-ray imager.

Gamma-ray imaging is used in a variety of fields, including medicine, nuclear security, and space observation. Recently, it is also commonly used to understand the situation on and off FDNPS sites [1–4]. Typical gamma-ray imagers can be broadly classified as Compton or pinhole cameras.

Compton cameras are small and light because they do not require any shielding. Therefore, attempts have been made to remotely visualize the distribution of radioactive materials by mounting Compton cameras on small robots or unmanned aerial vehicles [5, 6]. It is also possible to mount a Compton camera on a drone to image a vast area [7, 8]. In the case of the FDNPS site, there is a strong demand to

---

Y. Kitayama (✉)
Remote System and Sensing Technology Division, Collaborative Laboratories for Advanced Decommissioning Science, Japan Atomic Energy Agency, Tomioka, Fukushima, Japan
e-mail: kitayama.yoshiharu@jaea.go.jp

© The Author(s), under exclusive license to Springer Nature Switzerland AG 2023

J. Du, K. (K.) Iniewski (eds.), *Gamma Ray Imaging*,
https://doi.org/10.1007/978-3-031-30666-2_8

quantitatively estimate the radioactivity of hot spots. However, there are difficulties in the use of Compton cameras in the quantitative evaluation of spatially distributed radioactive materials.

A pinhole camera can perform quantitative evaluation of radioactive materials in their field of view (FOV) by simultaneously acquiring the distance to the measurement target while performing gamma-ray imaging. Gamma-ray imaging and quantitative evaluation of radioactivity using a pinhole camera have been conducted on the operating floor of FDNPS Unit 2 [9]. However, a pinhole camera requires heavy shielding, such as lead or tungsten, and the total weight of the device is several tens of kilograms. It is unrealistic to mount them on small robots or drones. Therefore, pinhole cameras are powerful for fixed-point measurements but unsuitable for applications such as remote gamma-ray imaging of workplaces.

Coded aperture cameras, another type of gamma cameras, are also attracting attention. In a coded aperture, a mask with a mixture of apertures and shields is placed in front of a position-sensitive pixel detector, and the source position is estimated from the shadow projected onto the pixel detector [10]. Coded apertures are also being used in decommissioning operations [11].

An example of research on a quantitative, compact gamma-ray imager for use at the Fukushima Daiichi Nuclear Power Plant is the Virtual Pinhole Camera (VPC) [12], which combines the characteristics of a pinhole camera and a Compton camera and has been proven to be valid by experiment. I have proposed a new gamma-ray imager with a different approach. The Gamma-ray imager using small-angle scattering (GISAS) is a new gamma-ray imager that combines the key features of a Compton camera (small and light) and a pinhole camera (quantitative evaluation ability) [13]. Similar to a Compton camera, GISAS uses Compton scattering dynamics to estimate the incident direction of gamma rays and does not require any shielding. Unlike a Compton camera, GISAS estimates the incident direction of gamma rays for each event by using only ultra-small-angle scattering events that can be considered almost straight. This feature is similar to that of a pinhole camera, and GISAS is expected to be able to perform quantitative evaluations using the same method as that used by a pinhole camera.

GISAS consists of multiple shield-free directional gamma-ray detectors, which are its fundamental technical element and can detect ultra-small-angle Compton scattering. In this study, a feasibility study is conducted on shield-free directional gamma-ray detectors via simulations and experiments.

2 Principles of Existing Gamma-Ray Imagers and GISAS

2.1 Principles of Compton and Pinhole Cameras

As the name suggests, a Compton camera is a gamma-ray imager that uses Compton scattering to estimate the incident direction of a gamma-ray. Compton scattering is

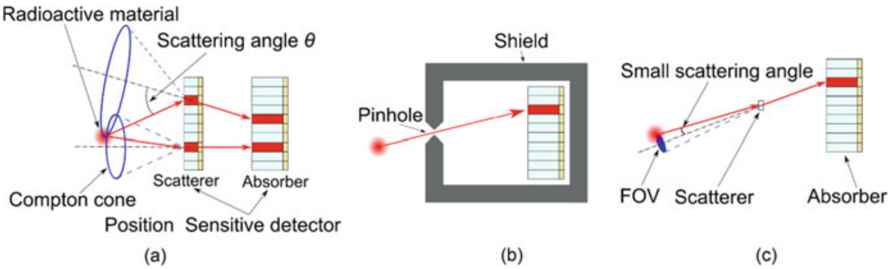

Fig. 1 Schematic diagrams of the gamma-ray imager: (**a**) Compton camera, (**b**) Pinhole camera, and (**c**) GISAS

one of the major interactions that occur between gamma rays and electrons in a material. Through Compton scattering, the gamma ray transfers part of their energy to the electron. This electron is called recoil electron. Given the energy of recoil electron $E_{e'}$ and energy of scattered gamma ray $E_{\gamma'}$, the scattering angle θ can be written as

$$\cos\theta = 1 + m_e c^2 \left(\frac{1}{E_{\gamma'} + E_{e'}} - \frac{1}{E_{\gamma'}} \right), \tag{1}$$

where m_e is the electron's mass, and c is the speed of light. In other words, by measuring the energy of the recoil electron $E_{e'}$ and the energy of the scattered gamma ray $E_{\gamma'}$, we can determine the scattering angle θ of the gamma ray.

A Compton camera consists of a scatterer detector and an absorber detector, which are both position-sensitive, as shown in Fig. 1a. Incident gamma rays are Compton scattered by the scatterer and then photoelectrically absorbed by the absorber. The scattering angle θ of the incident gamma-ray can be calculated from Eq. (1) by measuring $E_{e'}$ and $E_{\gamma'}$ at the scatterer and the absorber, respectively. Therefore, the incident direction of gamma rays can be estimated to be in the shape of a cone with an apex angle of 2θ; the central axis is the line connecting the detection positions of the scatterer and the absorber. This cone is called the Compton cone. A gamma-ray source can be considered to exist at the intersection of multiple Compton cones. In this way, a Compton camera can statistically estimate the direction of a gamma-ray source by acquiring many events.

A pinhole camera is based on the same principle as that of the old visible-light camera except that a position-sensitive detector replaces the photo film of the latter camera. As shown in Fig. 1b, the position-sensitive detector is placed inside a box made of a heavy material (such as lead or tungsten), which serves as a shield against gamma rays. The box has a small pinhole, which lets in gamma rays. The position-sensitive detector absorbs gamma rays entering the box through the pinholes. The gamma-ray source is presumed to be located along the straight line connecting the pinhole and the detected position.

2.2 Principle of GISAS

Since a Compton camera uses Compton scattering to estimate the direction of the radioactive source, it does not require any shielding, and the total weight can be reduced to a few kilograms. However, quantitative estimation of spatially distributed radiation sources is complicated because the incident direction is not uniquely determined by one event. A pinhole camera can estimate the incident direction of gamma rays for each event. Therefore, with prior knowledge about the relationship of the count rate, the radioactive material's activity, and distance to the radioactive material, the radioactive material's activity in the FOV can be estimated. The drawback is that the device weighs several tens of kilograms due to its need for shielding.

Therefore, GISAS was proposed as a gamma-ray imager that combines the features of a Compton camera, which does not require shielding due to its use of Compton scattering, and a pinhole camera, which can estimate the incident direction of gamma rays for each event. As shown in Fig. 1c, GISAS consists of a scatterer detector and an absorber detector. Using the same principle as that of a Compton camera, GISAS estimates the incident direction of gamma rays by measuring the recoil electron's energy $E_{e'}$ and the scattered gamma-ray's energy $E_{\gamma'}$. Therefore, no shielding is required, and the weight can be reduced. GISAS differs from a Compton camera in that GISAS counts only ultra-small-angle Compton scattering events, which can be regarded as almost straight, as valid events. Therefore, GISAS is expected to estimate the incident direction of gamma rays for each event and be as capable of quantitative evaluation of radioactivity as a pinhole camera.

3 Principle of Shield-Free Directional Gamma-Ray Detector

A pair of a scatterer and an absorber pixel of GISAS acts as a shield-free directional gamma-ray detector. This pair is similar to the relationship between the pinhole and the position-sensitive detector's pixel in a pinhole camera. With each shield-free directional gamma-ray detector counting only ultra-small-angle scattering events as valid events, GISAS performs imaging similarly to a pinhole camera. This section explains the principle of shield-free directional gamma-ray detectors, which are the main topic of this research. A shield-free directional gamma-ray detector aims to have a directivity of 15°, i.e., ±7.5°, in front of the detector. This directivity corresponds to a spatial resolution of about 80 cm at a distance of 3 m ahead of the directional detector. Inside the FDNPS buildings, 662 keV gamma rays from ^{137}Cs and their scattering components are dominant. In this study, the feasibility of the imaging of 662 keV gamma rays was investigated.

First, the relationship between the FOV and the directivity of a shield-free directional gamma-ray detector is explained here. The scatterer of the directional detector selects only ultra-small-angle scattering events, which can be considered

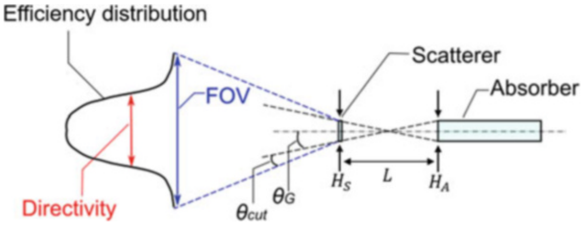

Fig. 2 Schematic diagram of the shield-free directional gamma-ray detector

almost straight. The maximum scattering angle selected by the scatterer is called θ_{cut}. If a simple model is used (the size of the detector is negligible), the FOV of the directional detector is $\pm\theta_{cut}$ on the detector axis. Therefore, if θ_{cut} is set to 7.5°, then the desired directional detector can be made. However, as shown in Fig. 2, the angle θ_G, which is determined by the detector's geometry, also has a significant effect on FOV in reality. The angle θ_G is determined by the size of the gamma-ray incident surface of the scatterer H_S, the size of the incident surface of the absorber H_A, and the distance between the scatterer and the absorber L. θ_G is larger when H_S and H_L are larger and L is smaller. In addition, a distribution of detection efficiency is deemed to exist within the FOV. In other words, the FOV and directivity have a different meaning. Therefore, as shown in Fig. 2, the directivity of the shield-free directional gamma-ray detector is defined as the area within the FOV with a certain level of detection efficiency.

The principle of the angle selection is described here. The scatterer has an energy window of E_{Smin} to E_{Smax}. Here, the maximum energy threshold E_{Smax} of the scatterer is determined from the $E_{e'}$ value corresponding to θ_{cut} and the scatterer's energy resolution. The minimum energy threshold of the scatterer E_{Smin} is determined by the background noise of the scatterer and should be set to a value slightly larger than the noise level. Since E_{Smin} determines the minimum detectable scattering angle, it should be as small as possible. If the detected energy of the scatterer satisfies the energy window condition, the scatterer will determine an event below the scattering angle θ_{cut} to have been detected, and a trigger signal will be produced. The absorber also has the minimum energy threshold E_{Amin} and the maximum energy threshold E_{Amax}; these thresholds ensure selecting only photoelectrically absorbed events by the absorber. The center value of the energy window of the absorber is 662 keV, and the absorber's energy resolution determines its width. If the absorber detects events that satisfy the energy window condition, between the times the trigger signal is generated and the coincidence time τ lapses, these events will be considered events caused by the same gamma-ray and will be counted as valid events. In other words, events that satisfy the energy window conditions set for the scatterer and the absorber are deemed caused by an ultra-small-angle Compton scattering event if they occur within a short enough time τ such that they can be considered to have occurred simultaneously.

Here, the technical conditions required for the scatterer and the absorber are described. The scatterer must be able to detect energies of a few kiloelectron volts with high accuracy. Because, if a 662 keV gamma-ray is Compton scattered with a scattering angle of 7.5°, then $E_{e'}$ is about 7.3 keV. In other words, in the design of a shield-free directional gamma-ray detector with $\theta_{cut} = 7.5°$ for a 662 keV gamma-ray, a value of a few kiloelectron volts is set as E_{Smax}. Since general gamma-ray detection techniques target an energy range of several tens of kiloelectron volts to several megaelectron volts, it is difficult to detect energies of several kiloelectron volts with high accuracy. Therefore, a silicon drift detector (SDD) was used as scatterer detector; SDDs are commonly used in soft X-ray (0.1–100 keV X-rays) detection. An SDD is a small, cooled silicon detector with a unique electrode configuration [14, 15]; it has an extremely high energy resolution of about 130 eV (Full width at half maximum: FWHM) at 5.9 keV gamma rays emitted by ^{55}Fe. In addition, Si is an advantageous scatterer because of its small atomic number, which means that Compton scattering is more likely to occur than photoelectric absorption.

In this chapter we present a study, where a GAGG(Ce) scintillator was used as the absorber. The absorber's density should be high because it is essential for absorbing gamma rays efficiently. GAGG(Ce) scintillators have a high density of 6.63 g/cm^3 and a relatively fast decay time of 90 ns. They also have a high light yield and good energy resolution. The photodetector is a SiPM, which is much smaller than a photomultiplier tube, can be driven by a low voltage, and is operated by a simple signal readout circuit. The SiPM is a photodetector that has recently been very popular in gamma-ray detection [16].

4 Feasibility Study by Simulation

4.1 Selection of Scattering Angle Using Detected Energy Information

As described above, energies of several kiloelectron volts ($E_{e'}$) should be detected with high accuracy to detect ultra-small-angle scattering. Therefore, an energy window of E_{Smin} to E_{Smax} is set for an SDD with a high energy resolution, and only events with a target scattering angle of θ_{cut} or less are selected by energy information.

However, there are over θ_{cut} events, even in cases where the detected energy of the scatterer is less than E_{Smax}. There are two main reasons why scattering events above θ_{cut} are mixed with events where the detected energy of the scatterer is less than E_{Smax}. The first reason is that recoil electrons generated by large-angle scattering deposit only a part of their energy and escape from the scatterer. For example, when a 662 keV gamma-ray is scattered at 70°, the recoil electron energy $E_{e'}$ becomes about 300 keV. A recoil electron with energy of 300 keV will move several hundred micrometers from the scattering position before stopping in Si. However, the Si thickness of a typical SDD is several hundred to one thousand micrometers. Therefore, depending on the scattering position, an event may occur where recoil electrons generated by large-angle scattering deposit energy less than E_{Smax} to the scatterer and then escape from the scatterer. In this case, false recognition will occur. The second is fluctuation of the detected energy due to the energy resolution of the detector. Due to the statistical fluctuations of generated carriers or electronic noise, the detected energy fluctuates, even for the same energy particles. As a result, there is a possibility of detecting energies below E_{Smax} for scattering events above θ_{cut}. In this case, false recognition will also occur.

A simulation was conducted to understand the effects of these factors and confirm whether angle selection is possible based on the detected energy information. The simulations were performed using Geant4 [17], a Monte Carlo simulation toolkit. Gamma rays were irradiated to the scatterer, and the relationship between the Compton scattering angle and the actual deposited energy was investigated. From the simulation result, the accuracy of selecting scattering events below θ_{cut} using energy information was examined.

The simulation conditions are described below. The scatterer was a circular Si with a gamma-ray incident area of 25 mm^2, and the simulations were performed for three Si thicknesses: 300, 500, and 1000 μm. The energy resolution of the scatterer was set to FWHM 123 eV at 5.9 keV. In the subsequent simulations, this value was used as the energy resolution of the scatterer. The scatterer was irradiated vertically with 662 keV gamma rays. When the incident gamma rays caused Compton scattering in the scatterer, the scattering angle and the amount of deposited energy were recorded as list data.

Figure 3a shows the result of the list data for the Si thickness of 1000 μm. The figure shows many events that are concentrated to form a single curve. This curve is consistent with the relationship between θ and $E_{e'}$, which was theoretically predicted from Eq. (1). Most of the events are distributed around the curve, with a width close to the energy resolution. In addition, there is a widely distributed component in the low-energy region. This component is due to the escape electrons, which deposited a part of their energy to the scatterer and then escaped from it.

According to the data in Fig. 3a, only the events where the $E_{e'}$ detected in the scatterer is in the range of E_{Smin} : 0.1 keV, E_{Smax} : 7.3 keV are selected, and the histogram is shown in Fig. 3b. The range E_{Smin} : 0.1 keV, E_{Smax} : 7.3 keV corresponds to $E_{e'}$ values at scattering angles of about 0.9 and 7.5°, respectively. In Fig. 3b, the peak is seen at a scattering angle of under 10°. The presence of this peak indicates that the targeted small-angle scattering is selectively detected. By contrast, large-angle scattering events of over 10° are distributed over a wide range of angles. These components are due to escape electrons. The cumulative sum of the histogram shows that the peak of the small-angle scattering event accounts for about half of the total events, and the other half is the escape electron component of over 10°. The effect of escape electrons is more substantial for thinner Si. The large-angle scattering component accounts for 64% and 75% of the scattering at the Si thicknesses of 500 and 300 μm, respectively. These results indicate that the energy window of the scatterer alone is strongly affected by the escape electrons.

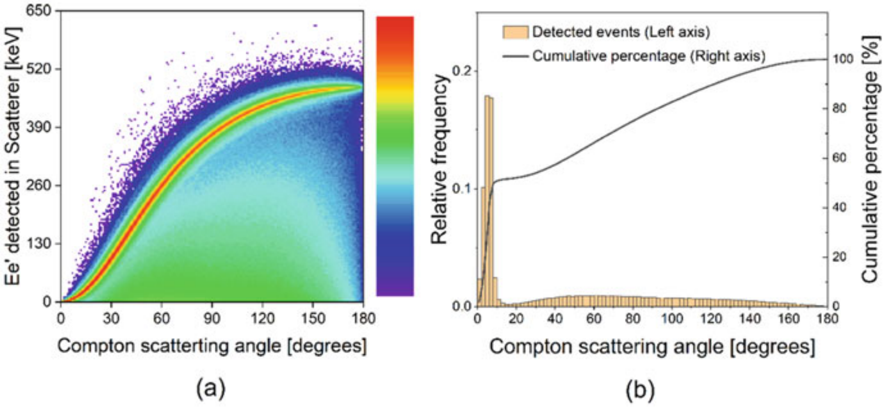

Fig. 3 Simulation result of angle selection: (**a**) The relationship between $E_{e'}$ detected in the scatterer and Compton scattering angle, (**b**) Histogram of the number of events per scattering angle at E_{Smin} : 0.1 keV, E_{Smax} : 7.3 keV

The absorber also has an energy window, from E_{Amin} to E_{Amax}, for selecting only the events that are photoelectrically absorbed. Only the events that satisfy the energy window conditions of the scatterer and the absorber are counted as valid events. In other words, events where the $E_{e'}$ ($E_{\gamma'}$) detected in the scatterer (absorber) satisfies the energy window of the scatterer (absorber) are deemed valid events. Therefore, it was confirmed to what extent the effect of the escaping electrons can be reduced by setting an energy window condition for the absorber in the results of Fig. 3b. The energy window for the absorber was set to 662 ± 56 keV, i.e., E_{Amin} : 606 keV, E_{Amax} : 718 keV; 56 keV is the typical FWHM of a GAGG(Ce) scintillator at 662 keV [18]. As a result, the ratio of events of over 10° to the valid events was reduced to about 2%. These results indicate that it is possible to reduce the effect of escape electrons and select only small-angle scattering events by setting energy windows for both the scatterer and the absorber.

Let θ_{cut} be an angle where 90% of the events counted as valid events are less than θ_{cut}. In the abovementioned example for the Si thickness of 1000 μm, the calculated θ_{cut} was 7.3°. θ_{cut} was calculated under different E_{Smax} conditions to investigate how E_{Smax} affect θ_{cut}. About the simulation results for the Si thicknesses of 300, 500, and 1000 μm, the changes in θ_{cut} when E_{Smax} was set to 1.2, 2.1, 3.2, 4.7, 6.3, and 8.2 keV were calculated and are summarized in Table 1. Each E_{Smax} corresponds to $E_{e'}$ scattering angles of 3°, 4°, 5°, 6°, 7°, and 8°. As shown in Table 1, even when the Si thickness changes from 300 to 1000 μm, the maximum change in θ_{cut} remains about 10%. Therefore, the thickness of Si in the SDD does not have a significant effect on θ_{cut}. By contrast, θ_{cut} can be adjusted significantly by changing E_{Smax}.

Table 1 The relationship between Si thickness, E_{Smax}, and θ_{cut}

		Si thickness		
		300 μm	500 μm	1000 μm
E_{Smax}	1.2 keV	3.8°	3.5°	3.4°
	2.1 keV	4.5°	4.4°	4.3°
	3.2 keV	5.4°	5.3°	5.2°
	4.7 keV	6.4°	6.2°	5.9°
	6.3 keV	7.2°	7.1°	6.9°
	8.2 keV	8.0°	7.9°	7.7°

4.2 Relationship Between θ_G, θ_{cut}, and Directivity

As mentioned in chapter “Cascade Gamma Emission Coincidence Tomography”, θ_G, which is determined by the detector’s geometry, affects the directivity. θ_G changes with the size of the gamma-ray incident surface (H_S and H_A) and the distance between a scatterer and an absorber (L). The larger the θ_G and θ_{cut} values, the wider the FOV and directivity. The relationship between θ_{cut}, θ_G, and directivity was investigated by simulation using Geant4.

A shield-free directional gamma-ray detector consisting of a scatterer and an absorber was constructed using Geant4. The directional detector was irradiated with 662 keV gamma rays from the front of the detector at different incident angles, and the magnitudes of the energies detected by the scatterer and the absorber were recorded as list data. The events satisfying the conditions of the scatterer’s and absorber’s energy windows were selected from the list data as valid events. Given the number of valid events, intrinsic efficiency ε_{int} is defined as

$$\varepsilon_{int} = \frac{Number\ of\ valid\ events}{Number\ of\ gamma\ rays\ incidents\ on\ the\ scatterer},$$

and the ε_{int} values for each incident angles were compared.

The simulation conditions are described here. The scatterer is a circular Si with a thickness of 1000 μm and a gamma-ray incident area of 25 mm^2. The H_S shown in Fig. 2 is 5.6 mm. The absorber is a 5 × 5 × 30 mm^3 GAGG. H_A is 5.6 mm. Three L values, namely, 50, 100, and 150 mm, were simulated to confirm the change in directivity due to the difference in θ_G. These L values corresponded to θ_G: 6.0°, 3.0°, and 2.0°. Gamma rays were irradiated while changing the incident angle from 0° to 20° at 2° increments. Here, the incident angle of 0° was defined as the front of the detector. To confirm the change in directivity due to the difference in θ_{cut}, the directivity for E_{Smax} values of 1.2, 2.1, 3.2, 4.6, 6.3, and 8.2 keV was calculated. These E_{Smax} values corresponded to θ_{cut}: 3.4°, 4.3°, 5.2°, 6.0°, 6.9°, and 7.7°, respectively. In other words, for the directional detectors with three different geometries, namely, θ_G : 6.0 ° , 3.0°, and, 2.0°, the directivity was calculated for θ_{cut}: 3.4°, 4.3°, 5.2°, 6.0°, 6.9°, and 7.7°.

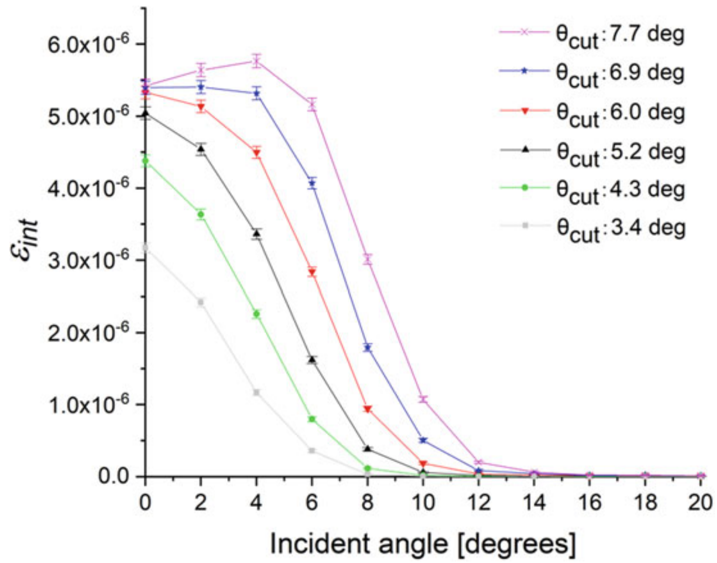

Fig. 4 ε_{int} distribution at θ_G : 6.0°

Table 2 Relationship between θ_{cut}, θ_G, and *Directivity*

		θ_G		
		6.1°	3.0°	2.0°
θ_{cut}	3.4°	**±5.1°**	**±3.9°**	**±4.0°**
	4.3°	**±5.5°**	**±4.8°**	**±5.1°**
	5.2°	**±6.1°**	**±5.6°**	**±5.7°**
	6.0°	**±7.1°**	**±6.5°**	**±6.5°**
	6.9°	±7.7°	**±7.4°**	**±7.3°**
	7.7°	±8.5°	±8.0°	±7.9°

The simulation results are shown below. Figure 4 shows the ε_{int} distribution at θ_G : 6.0°. As θ_{cut} increases, the overall ε_{int} increases, and the FOV widens. However, the ε_{int} at the incident angle of 0° does not exceed 5.4×10^{-6}, even when θ_{cut} is increased. This is because the detector's geometry limits the maximum ε_{int}. For example, when the incident angle is 0°, even if θ_{cut} is larger than θ_G, events with scattering angles greater than θ_G will not be incident to the absorber due to the geometry. Therefore, under the condition of θ_G : 6.0°, ε_{int} will be saturated at $\theta_{cut} \geq 6.0°$.

The cumulative percentage was obtained for the area of the ε_{int} distribution, and the directivity was defined as the angle when the cumulative percentage reached 90%. The relationship between θ_{cut}, θ_G, and the calculated directivity is shown in Table 2. According to the table, the directivity expands as θ_{cut} is increased for detectors with the same θ_G. For detectors with the same θ_{cut}, the directivity tends to increase as θ_G is decreased, but it is not a significant change. For example, between θ_G : 3.0° and θ_G : 2.0°, the directivity hardly changes while L is lengthened 1.5

times (from 100 to 150 mm). The target value of directivity, namely, ±7.5°, could be achieved under the conditions shown in bold letters in Table 2.

5 Simple Experiments with Prototype Shield-Free Directional Gamma-Ray Detector

Based on the simulation results, a shield-free directional gamma-ray detector was fabricated. A simple performance evaluation was performed with a ^{137}Cs radioactive source. The performance evaluation was also simulated by Geant4, and the results were compared.

First, an overview of the fabricated shield-free directional gamma-ray detector is described here. Figure 5 shows an overview of the fabricated directional detector. A SDD (thickness: 1000 μm, diameter: 5.6 mm), manufactured by Amptek [19], was used as the scatterer detector. The SDD signal was preamplified and then sent to Amptek's X123 digital pulse processing module. X123 can set a scatterer's energy window. A 5 × 5 × 30 mm^3 GAGG(Ce) scintillator and a SiPM (S1360-6025CS) manufactured by Hamamatsu Photonics were used as the absorber detector. The

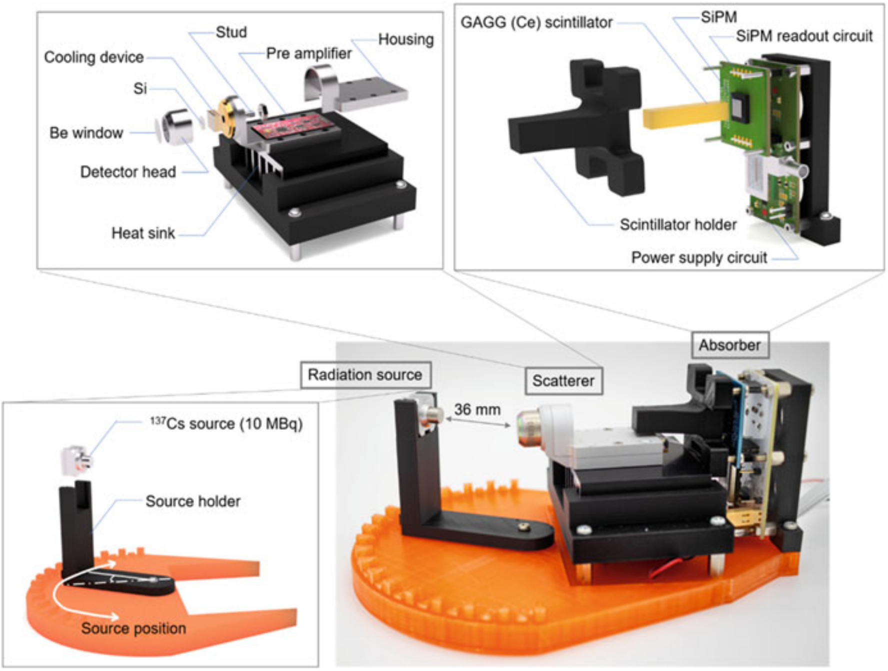

Fig. 5 Fabricated shield-free directional gamma-ray detector

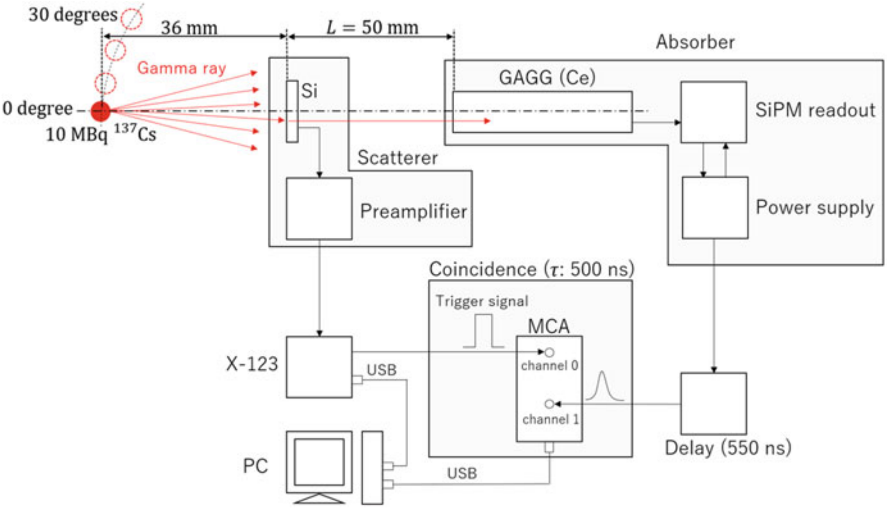

Fig. 6 Schematic diagram of experimental setup setup

distance between the scatterer and the absorber was 50 mm, i.e., H_S : 5.6 mm, H_A : 5.0 mm, L : 50 mm, θ_G : 6.0°.

Next, the experimental setup is described here. The experimental scheme is shown in Fig. 6. A 10 MBq ±20% ^{137}Cs check source was used as the gamma-ray source. The distance between the scatterer and the source was set to 36 mm. The position of the source was changed from 0° to 30°, and the rate of valid events for each position was recorded. The energy window of the scatterer was set to E_{Smin} : 0.4 keV, E_{Smax} : 4.7 keV, and the energy window of the absorber was set to E_{Amin} : 640 keV, E_{Amax} : 684 keV, i.e., 662 ± 22 keV, where 44 keV was the FWHM at 662 keV of a GAGG(Ce) of this experimental setup. In the experiment, E_{Smin} was set to 0.4 keV due to the electronic noise of the SDD. Whenever a detected event satisfied the energy window of the scatterer, X123 outputted a digital pulse as a trigger signal. The trigger signal was sent to channel 0 of a multichannel analyzer (MCA), CAEN N6781. The absorber signal was also sent to channel 1 of the MCA after a delay of 550 ns. If an event that satisfied the energy window of the absorber was detected at channel 1 during a coincidence time of 500 ns after the trigger signal was sent to the MCA, then it was counted as a valid event.

The simulation conditions are described here. A directional detector with the geometry of the fabricated directional detector was constructed in Geant4. The scatterer was a circular Si with a gamma-ray incident area of 25 mm^2 and a thickness of 1000 μm, and the absorber was a 5 × 5 × 30 mm^3 GAGG. The distance between the scatterer and the absorber was 50 mm, and their energy windows were set to E_{Smin} : 0.4 keV, E_{Smax} : 4.7 keV and E_{Amin} : 640 keV, E_{Amax} : 684 keV, respectively. The ^{137}Cs source was a cylindrical volume source with a diameter of 5.5 mm and a height of 3 mm. The distance between the scatterer and the source was set to

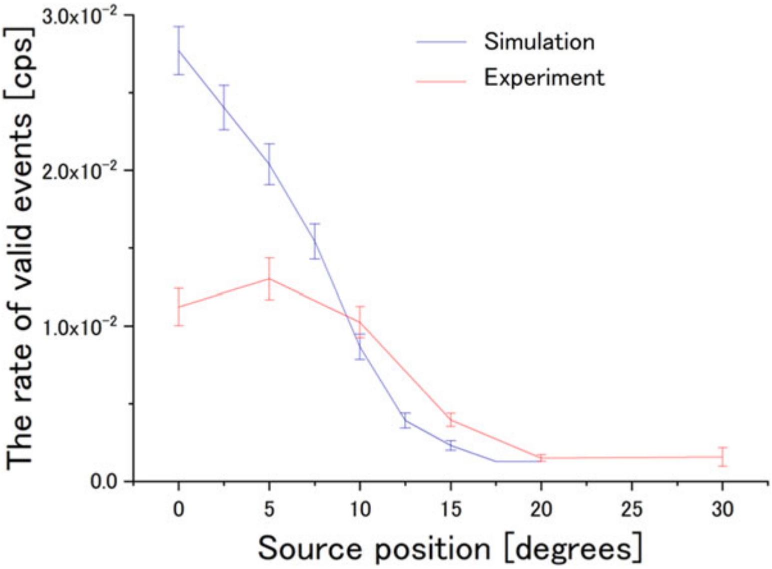

Fig. 7 Result of experiment and simulation

36 mm. The rate of valid events was calculated by converting the measurement time based on the number of gamma rays incident to the scatterer, the source intensity (10 MBq), and the distance to the source (36 mm). The baseline calculated based on the experimental results was added to the rate of valid events.

As seen in Fig. 7, both the simulation and experimental results show a tendency for the rate of valid events to be high near the center and almost drop to the baseline level around 20°. The reason for the broad distribution compared with that in Fig. 4 is that the distance between the volume source and the scatterer was too short to obtain a parallel beam. Although the simulated rate of valid events in front of the detector tended to be estimated higher than the experiment result, the results show the feasibility of determining the directionality by detecting small-angle Compton scattering.

In the region from 0° to 10°, the experimental results show a lower rate of valid events than the simulation. One possible cause is the effect of shielding by structures that were not considered in the simulation. For example, as shown in Fig. 5, the SDD was composed of a cooling module, a fixing bolt, and a housing. These components were not considered in the simulation due to the complexity of the structure. Furthermore, the simulation did not consider pile-ups and the counting off of events outside the coincidence window. These factors also increase the rate of valid events in the simulation.

6 Conclusion

The feasibility of shield-free directional gamma-ray detectors, which are the basic technology of the new gamma-ray imager GISAS, was verified by simulations and experiments and has been presented in this chapter. A shield-free directional gamma-ray detector consists of a scatterer and an absorber, and detects only ultra-small-angle scattering by setting appropriate energy windows. Since the energy of scattered electrons generated by small-angle scattering is only a few kiloelectron volts (much smaller than the energy range of conventional gamma-ray detection techniques), an SDD was used as the scatterer. A GAGG scintillator was used as the absorber. In the simulation, a 25 mm^2, 1000 μm thick SDD and a $5 \times 5 \times 30$ mm^3 GAGG scintillator were placed 50 mm apart, and their energy windows were set to E_{Smin} : 0.1 keV, E_{Smax} : 4.7 keV and E_{Amin} : 606 keV, E_{Amax} : 718 keV, respectively. The simulation result indicated that a directivity of about $\pm 7.1°$ was obtained in the condition.

Based on the simulation results, a prototype shield-free directional gamma-ray detector was fabricated, and a simple experiment was conducted. A 10 MBq ^{137}Cs check source was placed in front of the detector, and the rate of valid events was measured while changing the source position. The findings confirmed that the directivity was centered on the front of the detector. Compared with the results of the simulations on a similar system, the trend was consistent, although the rate of valid events near the front of the detector was underestimated than the simulation result. This result indicates the feasibility of a directional gamma-ray detector that does not have shielding and detects small-angle Compton scattering by using an SDD as a scatterer. Since this study aimed to investigate the feasibility of the idea, a commercial SDD was used as the scatterer. Since it was not a custom-made detector, the structures were placed behind the Si. These structures are disadvantageous in terms of detection efficiency. The readout circuit and other circuits that were fabricated were also simple ones. In order to conduct more accurate experiments, these circuits need to be improved. Since this study has shown the feasibility of directional detectors using small-angle scattering, more accurate directional detectors will be fabricated to realize GISAS in the future works.

Acknowledgement This work was financially supported by the JAEA Fund for Exploratory Researches (Houga fund).

References

1. Takeda, S., Harayama, A., Ichinohe, Y., et al. (2015). A portable Si/CdTe Compton camera and its applications to the visualization of radioactive substances. *Nuclear Instruments and Methods in Physics Research Section A, 787*, 207–211. https://doi.org/10.1016/j.nima.2014.11.119
2. Tomono, D., Mizumoto, T., Takada, A., et al. (2017). First on-site true gamma-ray imaging-spectroscopy of contamination near Fukushima plant. *Scientific Reports, 7*. https://doi.org/10.1038/srep41972

3. Vetter, K., Barnowski, R., Heafner, A., et al. (2018). Gamma-ray imaging for nuclear security and safety: Toward 3-D gamma-ray vision. *Nuclear Instruments and Methods in Physics Research Section A, 878*, 159–168. https://doi.org/10.1016/j.nima.2017.08.040
4. Vetter, K., Barnowski, R., Cates, J. W., et al. (2019). Advances in nuclear radiation sensing: Enabling 3-D gamma-ray vision. *Sensors, 19*(11). https://doi.org/10.3390/s19112541
5. Sato, Y., Tanifuji, Y., Terasaka, Y., et al. (2018). Radiation imaging using a compact Compton camera inside the Fukushima Daiichi Nuclear Power Station building. *Journal of Nuclear Science and Technology, 56*, 801–808. https://doi.org/10.1080/00223131.2019.1581111
6. Jiang, J., Shimazoe, K., Nakamura, Y., et al. (2016). A prototype of aerial radiation monitoring system using an unmanned helicopter mountaing a GAGG scintillator Compton camera. *Journal of Nuclear Science and Technology, 53*, 1067–1075. https://doi.org/10.1080/00223131.2015.1089796
7. Mochizuki, S., Kataoka, J., Tagawa, L., et al. (2017). First demonstration of aerial gamma-ray imaging using drone for prompt radiation survey in Fukushima. *Journal of Instrumentation, 12*, P11014. https://doi.org/10.1088/1748-0221/12/11/P11014
8. Sato, Y., Ozawa, S., Terasaka, Y., et al. (2018). Remote radiation imaging system using a compact gamma-ray imager mounted on a multicopter drone. *Journal of Nuclear Science and Technology, 55*, 90–96. https://doi.org/10.1080/00223131.2017.1383211
9. Nuclear Regulation Authority, Conference Material. (2021). https://www.nsr.go.jp/data/000306609.pdf. Japanese.
10. Caroli, E., Stephen, J. B., Di Cocco, G., et al. (1987). Coded aperture imaging in X- and gamma-ray astronomy. *Space Science Reviews, 45*, 349–403.
11. Carrel, F., Khalil, R. A., Colas, S., et al. (2011). GAMPIX: A new gamma imaging system for radiological safety and homeland security purpose. In *IEEE nuclear science symposium conference record* (pp. 4739–4744). https://doi.org/10.1109/NSSMIC.2011.6154706
12. Nogami, M., Hitomi, K., Torii, T., et al. (2019). *Development of thallium bromide gamma-ray detectors for intense radiation field.* IEEE NSS & MIC 2019 RTSD Poster Session, R-04-410. https://www.eventclass.org/contxt_ieee2019/online-program/session?s=R-04#e2330
13. Kitayama, Y., Terasaka, Y., Sato, Y., et al. (2021). Simulation study of a shield-free directional gamma-ray detector using small-angle Compton scattering. *Journal of Nuclear Engineering and Radiation Science, NERS-20-1088*. https://doi.org/10.1115/1.4048902
14. Gatti, E., & Rehak, P. (1984). Semiconductor drift chamber – An application of a novel charge transport scheme. *Nuclear Instruments and Methods in Physics Research Section A, 225*, 608.
15. Lechner, P., Fiorini, C., Hartmann, R., et al. (2001). Silicon drift detectors for high count rate X-ray spectroscopy at room temperature. *Nuclear Instruments and Methods in Physics Research Section A, 458*, 281. https://doi.org/10.1016/S0168-9002(00)00872-X
16. Kataoka, J., Kishimoto, A., Fujita, T., et al. (2015). Recent progress of MPPC-based scintillation detectors in high precision X-ray and gamma-ray imaging. *Nuclear Instruments and Methods in Physics Research Section A*, 248–254. https://doi.org/10.1016/j.nima.2014.11.004
17. Agostinelli, S., Allison, J., Amako, K., et al. (2003). Geant4 – A simulation toolkit. *Nuclear Instruments and Methods in Physics Research Section A, 506*, 250–303. https://doi.org/10.1016/S0168-9002(03)01368-8
18. C&A Corporation, data sheet. https://www.c-and-a.jp/assets/img/products/101210514_GAGG.pdf
19. AMPTEK INC, data sheet. https://www.amptek.com/-/media/ametekamptek/documents/products/pa210-pa230-specs-sept-2017.pdf?la=en&revision=d5330b8b-c653-444f-9d35-1014176ffac1

Materials for Gamma Radiation Sensors

Paul M. Johns

1 Introduction

Matter all over the Earth is continuously absorbing radiation. An average sized human may absorb thousands of gamma rays from terrestrial and cosmic sources of radiation every second of their adult life. Some microorganisms can naturally respond to radiation or radioactive elements; however, humans are not as lucky, and in turn need sensors to provide knowledge on the presence of radiation. Despite the prevalence of radiation absorption in all materials, detecting that radiation is a challenging feat. It becomes even more challenging when sources of radiation with activities equivalent-to or lower than background levels are the target for detection or identification.

Significant consideration of materials science goes into making a sensor capable of detecting radiation. The distinction between a material simply absorbing radiation to detecting radiation comes from how it converts energy deposited from radiation into signals that can be translated into useful information about the interaction. Individual gamma radiation interactions impart relatively small amounts of energy into matter, and thus sensor materials with sensitive and precise properties are necessary detect the signatures. Signals on these orders are not trivial to detect. To give an example, if 100,000 electron-hole pairs are produced in the ionization of a semiconductor from a gamma ray, the resulting charge will only be on the order of pico- to femto-Coulombs. Likewise, if 30,000 optical photons are produced

---

Material adapted from: Johns, P. (2022). Radiation Detection Materials Introduction. In *Advanced Materials for Radiation Detection*. Springer, Cham. https://doi.org/10.1007/978-3-030-76461-6_1.

P. M. Johns (✉)
Pacific Northwest National Laboratory, Richland, WA, USA
e-mail: paul.johns@pnnl.gov

© The Author(s), under exclusive license to Springer Nature Switzerland AG 2023

J. Du, K. (K.) Iniewski (eds.), *Gamma Ray Imaging*,
https://doi.org/10.1007/978-3-031-30666-2_9

from ionization in a scintillator the resulting signal on a photocathode will need to undergo several stages of gain before useful information from the interaction can be extracted. Materials must therefore be designed so that signals can be extracted without being overwhelmed by noise – placing electrodes and measuring induced charge on a piece on concrete, for instance, will not yield a useful radiation sensor. For a material to be a good radiation sensor, the physical and electronic properties it exhibits must be intrinsically and extrinsically optimized to produce highly resolved signals from interactions.

Selecting a good material is just the beginning of making a useful sensor for detecting, identifying, or otherwise quantifying radiation. The spectral signatures from radiation in a sensor must be stable over the duration of a measurement or series of measurements, and the algorithms in place on a detector must be able to correctly work no matter the environment that the detector is operating in. The methods commonly implemented for keeping a detector energy-aligned are often simple in concept but difficult to implement in field conditions where temperatures and radiation backgrounds are not constant. Most frontline users of radiation detectors are not experts trained in the science of radiation interactions or spectral analysis. It is therefore crucial that the results from radiation detection instruments come from robust hardware and versatile algorithms that can deliver true positive results with high accuracy.

This chapter provides an overview on the factors that go into developing radiation detectors. Discussion is separated into the material science concepts behind selecting compounds and growing sensors optimized for radiation detection, and separately, detector design and engineering concepts that make robust for field operations are reviewed. Modern algorithms applied to radiation detection are also discussed.

2 Producing Radiation Detectors

There remain many standing challenges in the field of radiation detection science [1]. Many, if not all, of these challenges could be resolved by surging capital investments into radiation detector research and development. In reality, radiation sensors will only be used if they are cost-balanced solutions to a mission need. Laboratory instrumentation, homeland security efforts, commercial power plant monitoring, and medical applications each have a different vision of a “perfect” radiation detection system. A common gap seen in each of these applications is that the state of the art is often limited by the lack of a sensor with ideal properties being available on a large enough scale and low enough cost. Radiation sensor R&D thus operates around a process flow of developing better candidate materials, growing them into larger sensors, and finding ways to manufacture those sensors at low production costs.

Many new materials with properties that exceed conventionally employed radiation sensors are continuously discovered (see Tables 1 and 2 later in this chapter for

Table 1 Scintillator materials with light output greater than NaI(Tl) and those with historic significance

Material	Reference	Luminosity[a] (≤photons/MeV)	Emission peak[b] (nm)	Energy resolution (% FWHM at 662 keV)
$C_{14}H_{O}$ (Anthracene)	[2]	17,000	400–450	n.r.
$BaBr_{1.7}I_{0.3}$(Eu)	[3]	112,000	414	n.r.
$BaBr_2$(Eu)	[3, 4]	58,000	408–414	6.9
BaBrCl(Eu)	[3, 5]	59,500	405	4.3
BaBrI(Eu)	[3, 6–8]	97,000	413	3.4
$BaCl_2$(Eu)	[4, 9]	52,000	406	3.5
BaFI(Eu)	[3]	55,000	405	8.5
$Bi_4Ge_3O_{12}$	[10–12]	10,600	510	9.1
CaF_2(Eu)	[13–15]	25,000	435	6.1
CaI_2(Eu)	[16, 17]	110,000	470	5.2
$CeBr_3$	[18, 19]	68,000	371	3.6
$CsBa_2I_5$(Eu)	[6, 8, 20]	102,000	430	2.3
Cs_4CaI_6(Eu)	[21]	51,800	474	3.6
$Cs_3Cu_2I_5$(Tl)	[22]	87,000	450	3.4
Cs_4EuBr_6	[23]	78,000	455	4.3
Cs_4EuI_6	[23]	53,000	465	5.0
Cs_2HfCl_6	[24, 25]	54,000	400	2.8
$Cs_2LiLaBr_6$(Ce)	[26]	60,000	410	2.9
$Cs_2LiLaCl_6$(Ce)	[26]	35,000	400	3.4
Cs_2LiYCl_6(Ce)	[26]	20,000	490	3.9
$Cs_2NaGdBr_6$(Ce)	[27]	48,000	418	3.3
$Cs_2NaLaBr_6$(Ce)	[28]	46,000	415	3.9
$Cs_2NaYBr_3I_3$(Ce)	[29]	43,000	350–465	3.3
$Cs_2NaLaBr_3I_3$(Ce)	[29]	58,000	350–460	2.9
Cs_4SrI_6(Eu)	[21]	62,300	474	3.3
CsI(Tl)	[10, 11]	61,000	540	5.6
$CsSrI_3$(Eu)	[30]	65,000	446–457	5.9
GdI_3(Ce)	[26, 31]	89,000	563	8.7
Gd_2O_2S(Tb)				
K_2BaI_4(Eu)	[32]	63,000	448	2.9
$K_2Ba_2I_5$(Eu)	[32]	90,000	444	2.4
K_2LaCl_5(Ce)	[33, 34]	30,000	340–380	5.0
K_2LaI_5(Ce)	[33]	55,000	400–440	4.5
$KCaI_3$(Eu)	[35]	72,000	465	3.0
KSr_2Br_5(Eu)	[36]	75,000	427	3.5
KSr_2I_5(Eu)	[37]	94,000	452	2.4
LaBr3(Pr)	[38]	74,500	490–730	3.2
$LaBr_3$(Ce)	[12, 39, 40]	63,000	380	2.6

(continued)

Table 1 (continued)

Material	Reference	Luminosity[a] (≤photons/MeV)	Emission peak[b] (nm)	Energy resolution (% FWHM at 662 keV)
$LaBr_3$(Ce, Sr)	[41]	78,000	n.r.	2.0
$LiCa_2I_5$(Eu)	[42]	90,000	472	5.6
$LiGdCl_4$(Ce)	[43]	64,600	345–365	n.r.
$LiSr_2I_5$	[42]	60,000	417–493	3.5
LuI_3(Ce)	[44, 45]	115,000	522	3.3
NaI(Tl)	[46]	38,000	415	7.1
Rb_2AgBr_3	[47]	25,600	480	n.r.
$RbGd_2Br_7$(Ce)	[48]	55,000	420	3.8
SrI_2(Eu)	[49, 50]	120,000	435	2.6
Tl_2GdCl_5(Ce)	[51]	53,000	389	5.0
$TlGd_2Cl_7$(Ce)	[52]	49,700	350–550	6.0
Tl_2LaCl_5(Ce)	[53, 54]	82,000	383	3.3
$TlSr_2I_5$(Eu)	[55]	70,000	463	4.2
Tl_2ZrCl_6	[56, 57]	50,800	450–470	4.3
$TlSr_2I_5$(Eu)	[55]	70,000	463	4.2
YI_3(Ce)	[26, 31]	98,600	549	9.3
ZnS(Ag)	[58]	50,000	450	n.r.
ZnSe(O)	[59]	71,500	595	7.4

References to each material are provided along with reported luminosity, peak emission wavelength, and the energy resolution at 662 keV

[a] Peak reported emission, or integrated over all fluorescence components when applicable

[b] Average emission wavelength at room temperature. Emission wavelength can shift with varying activator dopant concentration and temperature

examples). Why then does the industry not more fervently pursue and adopt these new materials? The answer comes down largely to the cost and effort associated with optimizing yield in crystal growth. NaI(Tl) has been the staple of handheld radiation detection and identification systems for decades because it comes from cheap precursor materials and is relatively easy to grow into large single crystals. If a warehouse of NaI(Tl) sensors can be acquired for the same cost as small batch of low yield sensors with better properties, the cost benefit favors sticking with the conventional sensor material. In the following paragraphs the general process is described for producing a new sensor from starting material to packaged product. Exceptions to some steps or processes for producing specific materials are expected; however, the efforts and costs associated with manufacturing most sensor materials are hard to avoid.

For a new sensor material to be a serious contender for widescale use in radiation detectors it must be cheap to produce, and able to be produced in large volumes. Excluding R&D labor, sensor production costs are determined by the capital needed to acquire high purity precursor materials, and effort needed to grow the crystal.

Table 2 Electronic properties of candidate RTSD materials as reported in literature

Material	Reference	Band gap (eV)	Resistivity (Ω-cm)	$(\mu\tau)_e$ (cm^2/V)	Spectroscopic response?	Pair creation energy
CdTe	[60, 61]	1.44	$1\cdot10^{9}$	$1–2\cdot10^{-2}$	Yes	4.43
CdZnTe	[62, 63]	1.57	$10^{9}–10^{10}$	$7.5\cdot10^{-3}$	Yes	4.64
HgI_2	[64]	2.15	$1\cdot10^{13}$	$3\cdot10^{-4}$	Yes	4.20
TlBr	[65, 66]	2.68	$1\cdot10^{10}$	$3\cdot10^{-3}$	Yes	6.50
CdMnTe	[67–70]	1.61	$3\cdot10^{10}$	$7\cdot10^{-3}$	Yes	2.12
CdSe	[71, 72]	1.73	$1\cdot10^{12}$	$6.3\cdot10^{-5}$	Yes	5.50
CdZnSe	[73]	2.00	$2\cdot10^{10}$	$1\cdot10^{-4}$	No	6.00
CdTeSe	[74, 75]	1.47	$5\cdot10^{9}$	$4\cdot10^{-3}$	Yes	(4.56)
GaAs	[76]	1.42	$1\cdot10^{8}$	$8\cdot10^{-5}$	Yes	4.20
GaSb	[77]	0.72	n.r.	$3\cdot10^{-5}$	Yes	(2.51)
GaSe	[78–80]	2.03	$10^{8}–10^{10}$	$3.7\cdot10^{-5}$	Yes	4.49
GaTe	[80]	1.66	$1\cdot10^{9}$	n.r.	No	(5.08)
GaN	[81]	3.40	$1\cdot10^{11}$	$1\cdot10^{-4}$	No	10.2
GaP	[81]	2.26	$1\cdot10^{9}$	$1\cdot10^{-5}$	No	7.00
InP	[82]	1.34	$1\cdot10^{9}$	$5\cdot10^{-6}$	Yes	4.20
AlSb	[83]	1.65	$1\cdot10^{8}$	$1.2\cdot10^{-4}$	No	4.71
$TlHgInS_3$	[84]	1.74	$4\cdot10^{9}$	$3.6\cdot10^{-4}$	No	(5.30)
$Cs_2Hg_6S_7$	[85, 86]	1.63	$6\cdot10^{7}$	$1.7\cdot10^{-3}$	Yes	(4.99)
$CsHgInS_3$	[87]	2.30	$9\cdot10^{10}$	$3.6\cdot10^{-5}$	No	(6.83)
$TlGaSe_2$	[88]	1.93	$1\cdot10^{9}$	$6\cdot10^{-5}$	No	(5.82)
$AgGaSe_2$	[89]	1.70	$1\cdot10^{11}$	$6.0\cdot10^{-6}$	No	(5.19)
$TlInSe_2$	[90–92]	1.10	$10^{6}–10^{7}$	$1\cdot10^{-2}$	No	3.60
$LiInSe_2$	[93, 94]	2.85	$1\cdot10^{11}$	$3.0\cdot10^{-6}$	No	(8.33)
$LiGaSe_2$	[95]	2.80	$1\cdot10^{8}$	n.r.	No	(8.19)
$CsCdInSe_3$	[96]	2.40	$4\cdot10^{9}$	$1.2\cdot10^{-5}$	No	(7.10)
Tl_3AsSe_3	[97]	n.r.	$10^{6}–10^{7}$	n.r.	No	n.r.
$Cs_2Hg_3Se_4$	[98]	2.1	$1.1\cdot10^{9}$	$8.0\cdot10^{-4}$	No	(6.28)
$Pb_2P_2Se_6$	[99, 100]	1.88	$5\cdot10^{11}$	$3.1\cdot10^{-4}$	Yes	(5.68)
$Cu_2I_2Se_6$	[101]	1.95	10^{12}	n.r.	No	(5.87)
$CsCdInTe_3$	[96]	1.78	$2\cdot10^{8}$	$1.1\cdot10^{-4}$	No	(5.06)
$Cs_2Cd_3Te_4$	[98]	2.5	$1\cdot10^{6}$	$1.1\cdot10^{-4}$	No	(7.38)
PbI_2	[64]	2.32	$1\cdot10^{13}$	$1\cdot10^{-5}$	Yes	4.90
InI	[102, 103]	2.00	$1\cdot10^{11}$	$7\cdot10^{-5}$	Yes	(6.01)
SbI_3	[104]	2.20	$1\cdot10^{10}$	n.r.	No	(6.56)
BiI_3	[105, 106]	1.67	$10^{8}–10^{11}$	$1\cdot10^{-4}$	Yes	5.80
β-$Hg_3S_2Cl_2$	[107]	2.56	$1\cdot10^{10}$	$1.4\cdot10^{-4}$	No	(7.54)
$CsPbBr_3$	[108–110]	2.25	$10^{9}–10^{11}$	$8.0\cdot10^{-3}$	Yes	(6.69)
$Hg_3Se_2Br_2$	[111]	2.22	$1\cdot10^{11}$	$1.4\cdot10^{-4}$	Yes	(6.56)
SbSeI	[112]	1.70	$1\cdot10^{8}$	$4.4\cdot10^{-4}$	No	(5.19)
Tl_4CdI_6	[113]	2.80	$2\cdot10^{10}$	$6.1\cdot10^{-4}$	Yes	(8.19)

(continued)

Table 2 (continued)

Material	Reference	Band gap (eV)	Resistivity (Ω-cm)	$(\mu\tau)_e$ (cm^2/V)	Spectroscopic response?	Pair creation energy
Tl_6SI_4	[114]	2.04	$1{\cdot}10^{10}$	$2.1{\cdot}10^{-3}$	Yes	(6.12)
Tl_6SeI_4	[115]	1.86	$4{\cdot}10^{12}$	$7.0{\cdot}10^{-3}$	Yes	(5.63)
Tl_4HgI_6	[97]	n.r.	10^{11}–10^{12}	$8.0{\cdot}10^{-4}$	Yes	n.r.
$TlSn_2I_5$	[116]	2.14	$4{\cdot}10^{10}$	$1.1{\cdot}10^{-3}$	No	(6.39)
$Hg_3S_2I_2$	[117]	2.25	$2{\cdot}10^{11}$	$1.6{\cdot}10^{-6}$	No	(6.69)
$Hg_3Se_2I_2$	[117]	2.12	$1.2{\cdot}10^{12}$	$1.0{\cdot}10^{-5}$	Yes	(6.34)
$Hg_3Te_2I_2$	[117]	1.93	$3.5{\cdot}10^{12}$	$3.3{\cdot}10^{-6}$	No	(5.82)
$Rb_3Bi_2I_9$	[118]	1.93	$3.2{\cdot}10^{11}$	$1.7{\cdot}10^{-6}$	No	(5.82)
$Rb_3Sb_2I_9$	[118]	2.03	$8.5{\cdot}10^{10}$	$4.5{\cdot}10^{-6}$	No	(6.09)
$Cs_3Bi_2I_9$	[118]	2.06	$9.4{\cdot}10^{12}$	$5.4{\cdot}10^{-5}$	No	(6.17)
$Cs_3Sb_2I_9$	[118]	1.89	$5.2{\cdot}10^{11}$	$1.1{\cdot}10^{-5}$	No	(5.71)
$CdGeAs_2$	[119]	0.9–1.0	10^{7}–10^{9}	n.r.	No	(3.30)
LiZnAs	[120, 121]	1.51	10^{6}–10^{11}	n.r.	No	(4.67)
LiZnP	[120, 122]	2.04	10^{6}–10^{11}	n.r.	Yes	(6.12)
4H-SiC	[81, 123]	3.27	$2{\cdot}10^{12}$	$4{\cdot}10^{-4}$	Yes	7.78
Diamond	[124, 125]	5.47	$5{\cdot}10^{14}$	$2.7{\cdot}10^{-7}$	No	13.0
PbO	[126]	2.80	$1{\cdot}10^{13}$	$1{\cdot}10^{-8}$	No	(8.19)
ZnO	[127]	3.30	$3{\cdot}10^{13}$	10^{-6}–10^{-4}	No	(8.37)
$MAPbI_3$	[128–130]	1.54	10^{8}–10^{9}	$1.0{\cdot}10^{-2}$	Yes	(4.75)
$FAPbI_3$	[128, 131–133]	1.43	10^{6}–10^{9}	$1.8{\cdot}10^{-2}$	Yes	(4.40)
$FACsPb(BrI)_3$	[132]	1.52	10^{8}–10^{9}	$1.2{\cdot}10^{-1}$	Yes	(4.69)
$MAPb(BrI)_3$	[128]	n.r.	n.r.	$1.0{\cdot}10^{-5}$	Yes	n.r.
$MAPbBr_3$	[134, 135]	2.3	$1.7{\cdot}10^{7}$	$1.2{\cdot}10^{-2}$	No	(6.83)
$MAPbBr_3$:Cl	[136]	2.3	$3.6{\cdot}10^{9}$	$1.2{\cdot}10^{-2}$	Yes	(6.83)

Value references taken from Owens [137] along with sources given in column 2. Table is a reproduction of the property table provided in Ref. [138] with new data provided on compounds that have emerged since the original publication

Costs of precursor materials are proportional to the abundance and access of a chemical compound, or more generally, its elements. Many compounds with promising properties and performance are hamstrung by being composed of rare and expensive transition metals and lanthanide elements. While niche applications will always exist for higher performing yet more expensive sensors to fill, widescale use in the small field of radiation detection will only be achievable if a sensor is derived from abundant precursor sources. In addition to a precursor being cost effective, a stable supply chain is needed for scaling to large production volumes, which can often be a hinderance toward the acquisition of rare and expensive compounds.

Pure precursors are necessary because performance-driving properties are closely linked to impurity element concentrations in most radiation sensor materials. Impurities can also hinder the growth of large single crystals by affecting thermodynamic properties of the melt or promoting unwanted nucleation if present in high enough concentrations. Several techniques can be employed to improve the purity of precursors before crystal growth. For materials with low vapor pressures, and vapor pressure differences between the compound and its impurities, physical vapor redeposition techniques can be effective in reducing impurity concentrations [139]. More commonly, zone refining techniques are used to drive impurities, which often have different solubilities than their host matrix, out of a bulk material [140]. In both methods, furnace components, fill gasses, and surfaces in contact with precursors must likewise be sourced such that impurities are not diffused into the material being refined. These purification steps, while necessary for producing high quality precursors for crystal growth, are a significant source of added time, energy, and cost to sensor production.

With a sufficiently pure amount of precursor material, efforts can be made to grow a single crystal gamma radiation sensor. A majority of spectroscopic semiconductor and scintillator radiation sensors are inorganic compounds grown into single crystals. Hundreds of comprehensive literary resources cover the concepts and challenges associated with crystal growth. In summary, it is very difficult to grow a large (>5 cm^3) single crystal without first expending significant effort and trial-and-error to perfect growth conditions. Each specific material requires growth conditions that are optimized to its thermodynamic properties, and precise management of many parameters during growth that are difficult to control: temperature gradient across a boule, solidification speed, solid-liquid interface shape, stress and strain at the solid-liquid interface, prevention of secondary phase nucleation, and many other factors [141]. Microscopic defects that can be present within single crystal phases must also be minimized so that signals generated in radiation interactions are not quenched within the crystal. At many steps along the growth process, material characterization may be necessary to ensure properties expected by a sensor are being achieved. Single crystals with large yields are more easily grown at lower temperatures, from congruently melting compounds (the simpler the phase diagram, the better), or from compounds that can be grown via solution. These ideal growth concepts are the recommendation rather than the requirement, though costs scale with effort. Sensors composed of compounds that require high temperatures or pressures, have issues with secondary phase formations, or otherwise require difficult growth conditions are not uncommon, and there are many examples of commercially successful materials with such problems. Despite successes seen in growing challenging materials, there is a clear correlation between widespread use in instrumentation and ease of sensor production.

Finally with a single crystal in hand, among the last remaining costs to expend in producing radiation sensors are fabricating, packaging, and accounting for other practical factors such as hygroscopicity, mechanical durability, and stability against environmental aging effects. These final production steps are vastly different depending on whether the sensor is a semiconductor or a scintillator. For both, the first step when a single crystal boule is removed from its growth ampoule is to cut and polish the single crystal into the form factor that the sensor is to take in an instrument. Specialized precision machining and polishing instruments are used to prepare crystal surfaces without introducing optical defects or surface damage that can lead to shunt currents. For semiconductors, anode and cathode metals are then deposited on the surfaces of the crystal, while scintillators have optical coupling applied to the surface that contacts a photocathode. The crystals can then be packaged as sensors into environment-protective enclosures. Many sensor materials are hygroscopic or highly sensitive to oxidation, thus protection against environmental conditions, particularly humidity and oxygen, are necessary to extend the longevity of most sensors. Enclosures must also be light-tight to shield semiconductors from photocurrent effects and scintillator enclosures from noise.

The steps and processes outlined above are just those to consider when manufacturing a sensor. When a sensor is to then to be integrated into a radiation detection system, numerous other components need to be designed and incorporated into a detection system. Supply chain factors around microelectronics availability must also be accounted for (detector manufacturing has not been immune to the global supply chain issues of the early 2020's). Finally, for a radiation detection system to be useful to an end user, the on-board algorithms must be reliable at interpreting the signals produced from radiation interactions into useful output. Discussion is next provided on the physics behind converting radiation signatures into output in a sensor, and examples of common materials used in detection systems.

3 Scintillator Gamma-Ray Sensor Materials

The majority of commercially available detection and identification technologies are based on scintillating compounds, which come in many forms from inorganic crystals to organic plastics. Scintillators are key in radiation detection applications where large area coverage is necessary. The distance that light can travel unimpeded in a scintillator is much greater than a charge can drift in a comparably sized semiconductor. Extremely large volume ($\geq$100,000 cm^3) detection systems can therefore be economical when built with scintillators that scale well with size. Developing new scintillator materials that emit light on a very fast time scale (*i.e.* ps to ns), exhibit no phosphorescence, and feature high scintillation yields (>100,000 ph./MeV) continues to make scintillator research a thriving field within radiation detection science.

Scintillator radiation detectors are referred to as indirect energy converters. A number of energy conversion mechanisms, and subsequent stages where energy loss occurs, take place before signals from interactions are produced. After energy from a gamma ray is transferred into a scintillator, at least five energy transfer or conversion mechanisms take place before a signal is produced at the output of the photodetector [10, 142]:

1. Conversion of primary ionized electron(s) energy into secondary ionized electron-hole pairs in the lattice.

2. Efficiency of ionized electrons or holes entering scintillator centers (intrinsic or activator trap states) in the lattice.
3. Quantum efficiency of the scintillation center undergoing a radiative transition and producing a scintillation photon.
4. Collection efficiency of the scintillation photon being absorbed at the photodetector vs. being reabsorbed in the lattice.
5. The quantum efficiency of which scintillation light is converted to a photoelectron at the photodetector.
6. (For photomultiplier tubes) The efficiency of the photocathode ejecting a photoelectron that is collected on the first dynode amplification stage.

Considering how many stages are present in this conversion process, the fact that advanced scintillator materials can produce spectra with resolution as low as 2% is quite remarkable. Much of the ongoing R&D on scintillators focuses on reducing loss in these conversion processes. In addition, scintillator material engineering is most often applied to produce better light output, foster faster timing response, and tailor emission wavelengths to overlap with the absorption spectra of photodetectors.

Many intrinsic properties impact the utility of scintillators in radiation detectors. First, a high light yield (photons/MeV) is necessary for the best spectral resolution limits. Luminosity in a material can be intrinsic or, more commonly, enabled by "activator" dopants. Enhancements to light yield via optical center activators are possible when lattice sites are available and suitable for the valence state of the engineered dopant. The two most common activators, Eu^{2+} and Ce^{3+}, need lattice sites that can host the 3+ or 2+ valence state to enable scintillation [143]. Optical properties are then needed to provide complete transparency to light at the wavelength(s) at which scintillation photons are emitted. A large mean free path for emitted scintillation light is enabled by a minimizing mechanism for photon reabsorption and providing a refractive index that allows perfect reflection on non-photodetector surfaces. Finally, a fast decay of trapped charges from optical centers in the band gap is necessary to reduce dead time and pulse pileup. At a minimum, scintillators target a pulse width within 10 μs for sensor applications.

Figure 1 presents an overview of the periodic table showing element selection considerations, based primarily upon the criteria presented by Cherepy et al. [16] and Derenzo et al. [144]. Elements in Fig. 1 that are unshaded are those that can be applied in scintillator design with the potential to grow useful compounds. Elements that are radioactive, have insufficiently low band gaps, do not form into compounds, do not grow easily, or are optically absorptive are not strong contenders for scintillator materials [16]. Factors such as toxicity and price are also important, but do not rule out promising sensor materials.

Perhaps the most pervasive of materials seen in handheld detection and identification systems is NaI, a halide scintillator typically doped with ppm-levels of Tl to enhance its light output. Since its first application as a particle counter in the 1940s, NaI(Tl) has become a prevalent sensor material in the nuclear industry, and is often the performance benchmark against which emerging sensor materials are compared

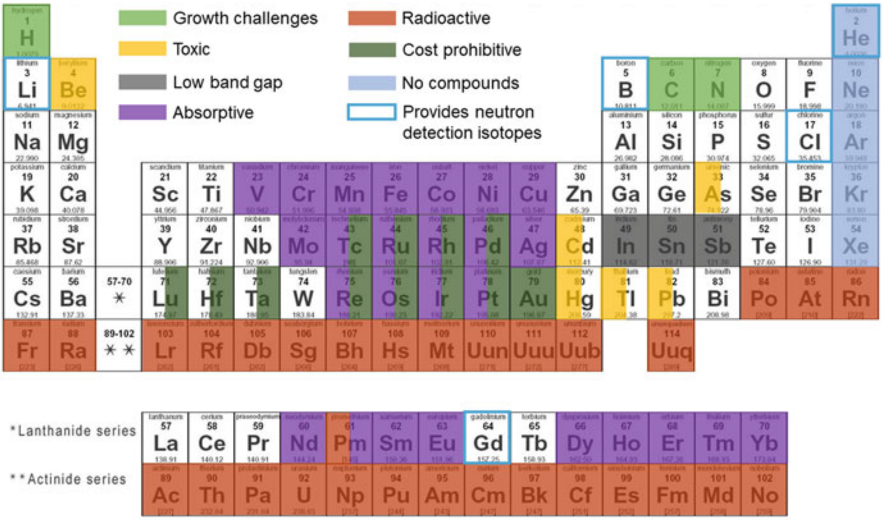

Fig. 1 Periodic table mapping of the elements investigated for scintillating materials, based on the criteria in Cherepy et al. [16] and Derenzo et al. [144]. Compounds that present challenges that inhibit use in scintillating materials are highlighted. Elements that, when enriched, are incorporated into scintillators to enable neutron detection are also highlighted

[145, 146]. With a typical resolution of 7–10% at 662 keV, NaI(Tl) sensors provide the radioisotope detection capability in a majority of handheld detectors used in laboratory, environmental monitoring, and homeland security applications [46]. NaI(Tl) is neither impressive performance-wise, as dozens of other scintillators have better light emission and resolution, nor is it particularly robust, as it is notably hygroscopic and prone to fractures or cracking when mechanically or thermally shocked. Despite these drawbacks, NaI(Tl) is inexpensive, relatively easy to grow in large volumes, and has a scintillation emission spectrum that couples well to bialkali PMTs and Si-based photodiodes. Other commercially available and deployed radiation detectors based on scintillation technology include $LaBr_3$, CsI(Tl), $Bi_4Ge_3O_{12}$ (BGO), and plastic scintillators such as polyvinyltoluene (PVT) and polystyrene (PS) [46, 147].

Comprehensive review articles on emerging scintillator materials over the last decade have been provided by Dorenbos [148], Nikl et al. [149], Martin et al. [150], Dujardin et al. [151], Zhou et al. [152], and Hajagos et al. [153], and the book by Korzhik [154]. An online database comprised of hundreds of scintillators and their properties has also been developed by Derenzo et al. and is hosted at scintillator.lbl.gov [155]. Some key scintillator materials drawn from the forementioned reviews and databases are reported with their key properties in Table 1. The presented compounds have greater reported luminosity than NaI(TI) or are historically significant in radiation detection. Luminosity, energy resolution at 662 keV, and emission wavelength are reported. It should be noted that timing

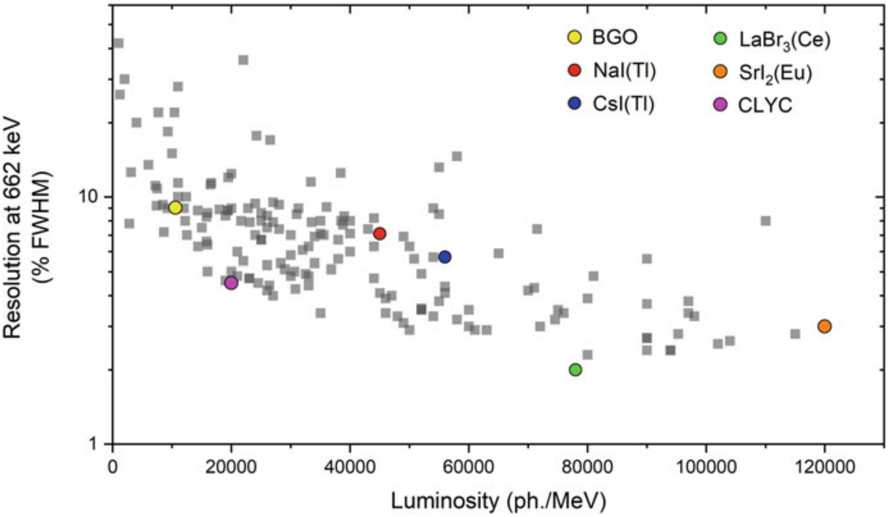

Fig. 2 Luminosity plotted against the reported resolution of compounds from Table 1. Data shows the minimum reported resolution trends lower as the luminosity increases

response is an equally important property; however, due to wide variations seen across literature on emerging compounds, it is excluded from the table. It is also worth noting that light yield is often extracted by comparison to commercial scintillators such as BGO or NaI(Tl); these methods are prone to error based on the specific performance of the reference sensor.

Figure 2 presents light output (in ph./MeV) against the minimum resolution reported by scintillating compounds in the LBNL database [155]. As expected, the average resolution improves (lower % value) as light output increases up to the range of ~80,000 ph./MeV. Above this point, reported light output continues to improve; however, the minimum reported resolution does not trend as anticipated. These results suggest that there remains room for significant improvements in the minimum achievable resolution in scintillating radiation sensors. In his review, Dorenbos poses that resolution of 1.5% is theoretically achievable in advanced scintillating materials with light output beyond 100,000 ph./MeV if high quantum efficiency overlap can be achieved between emission wavelength and photodetector absorption [148]. Figure 3 provides a comparison of spectra collected among the commercially available scintillator materials NaI(Tl), CsI(Tl), and $LaBr_3$(Ce), to emerging scintillator compounds with high resolution such as SrI_2(Eu), KBa_2I_5, and $CsBa_2I_5$(Eu).

A number of solid-state neutron-detecting scintillators based on ^{6}Li have seen focused development over the past decade to reduce dependence on ^{3}He in times of market shortages. Recently, scintillating compounds with the elpasolite crystal structure generated significant interest as dual gamma and neutron detection sensors [157]. Isotopes with high neutron absorption cross sections, typically ^{6}Li, or ^{157}Gd,

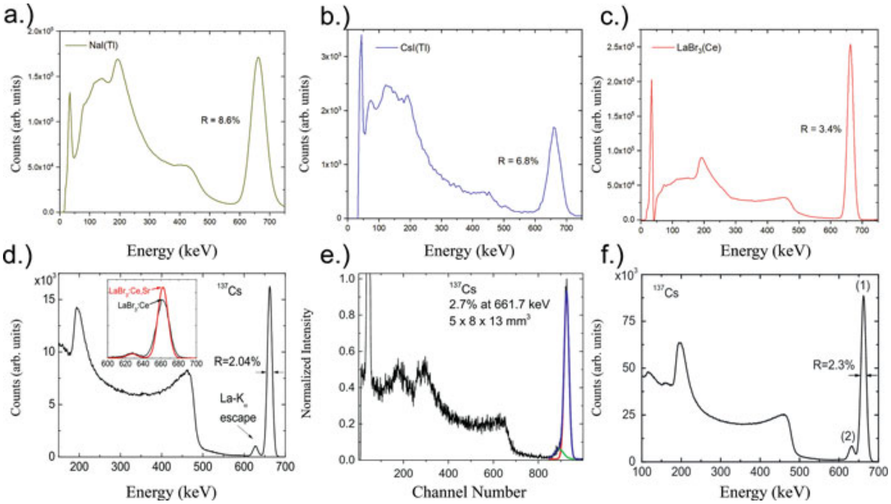

Fig. 3 Comparison of the spectral response to ^{137}Cs among commercially available (top row) and emerging high-performance scintillator materials (bottom row). Spectra from ^{137}Cs are presented as measured by (**a**) NaI(Tl) (commercial spectrometer, 2″ × 2″ sensor), (**b**) CsI(Tl) (commercial spectrometer, 0.5″ × 2″ sensor), (**c**) $LaBr_3$(Ce) (commercial spectrometer, 1.5″ × 1.5″ sensor), (**d**) $LaBr_3$(Ce,Sr). (From Ref. [156]), (**e**) KBa_2I_5. (From Ref. [32]), and (**f**) $CsBa_2I_5$(Eu). (From Ref. [20]). Images reused used with permissions

are integrated into scintillators where pulse shape discrimination methods are then employed to determine if interaction origins come from gamma or neutron radiation [158]. The most prevalent inorganic scintillator with dual gamma and neutron detection capabilities is the elpasolite material $Cs_2{}^6LiYCl_6$(Ce), known as CLYC. Personal radiation detectors comprised of small ~5 cm^3 CLYC crystals have recently entered the market [159]. Apart from CLYC, other dual gamma and neutron detecting scintillators include the Ce-doped elpasolites such as $Cs_2{}^6LiLaCl_6$ (CLLC), $Cs_2{}^6LiLaBr_6$ (CLLB), and $Cs_2{}^6LiYBr_6$ (CLYB). Commercially available neutron detectors have also recently emerged based on pulse shape discrimination in common halides such, as NaI(Tl), doped with high neutron interacting isotopes [160]. When NaI(Tl) is co-doped with ^{6}Li, “NaIL” sensors have been shown to have comparable neutron detection efficiency to CLYC without sacrificing much reduction in light yield or resolution [161, 162].

To overcome the size scaling difficulties associated with crystal growth, the largest sensors utilized in radiation detectors are not crystalline materials but amorphous plastics, and are typically produced by casting or extrusion methods [163]. Plastic compounds used for radiation detection are comprised of a polymer matrix base, typically polyvinyltoluene (PVT) or polystyrene (PS), in which soluble flour compounds are added to promote the generation of light upon radiation interaction. Due to the low wavelengths of emission typically seen in plastic scintillators, additional soluble wavelength-shifting compounds can be added to vary the emission wavelength (typically as a redshift) to wavelengths more easily absorbed by a photodetector [164]. The most widely implemented plastic scintillator is PVT, which serves as the sensor component of radiation portal monitoring (RPM) systems deployed at borders across the world. Economical and large scale PVT formulations have relatively low light output of ~6500 ph./MeV and do not produce spectra with discernable photopeaks due to the low Z_{eff} of the compound [165]. Despite this, PVT can be produced in large volumes that make it particularly attractive for large volume detection applications. For context, a typical RPM system can contain ~100,000 cm^3 of PVT sensor volume. Apart from low spectroscopic quality, a key drawback in PVT is the tendency for moisture-induced defects, known as “fogging”, to reduce the opacity of the material over years of thermal cycling in operational environments [166, 167].

4 Semiconductor Gamma-Ray Sensor Materials

The second major class of gamma-ray sensors, semiconductor detectors, are direct energy converters that innately produce higher resolution signals than scintillators. A large number of electron/hole pairs are generated when gamma rays ionize the atoms within semiconductors. This provides good resolution in photopeaks within the resulting gamma-ray spectra, and enables them to identify and characterize sources at farther standoff distances and shorter measurement times than equivalently sized scintillators. Additionally, unlike scintillators, there are not a large number of resolution-reducing conversion processes necessary to produce the signals that make up a spectrum. The resolution of a semiconductor instead depends on the Poisson statistics behind the generation of e^-/h^+ pairs, material properties intrinsic to the sensor, and the manner in which electronics shape the signal [46].

One of the drawbacks in semiconducting sensor materials is that they are highly sensitive to atomic-scale phenomena that quench charges generated in radiation interactions. A good response to radiation in a semiconductor therefore depends on defect tolerant crystal structures, thermodynamically stable lattices, chemical and structural stability, and, most importantly, electronic properties that enable stable charge generation and collection across operating temperatures. High material purity is more important in semiconductor sensors than in scintillators; impurity concentrations of just a few billion atoms per cubic centimeter can significantly impact the charge transport of electrons and holes. As ionized charge carriers drift through the lattice after a gamma-ray interaction, they can become trapped at electronic states within the band gap that arise from the presence of defects or impurities. Optimization of material properties at the atomic scale is therefore crucial for most semiconductor sensors. For a semiconducting compound to perform well as a radiation sensor it must also exhibit electronic properties that enable the detection of ionization-induced charges on the order of fC to pC. The properties that enable this are determined by the electronic structure and the band gap of the compound: high resistivity (at least 10^8 Ω-cm), electron-hole pair creation energies that approach the value of the band gap, and charge carrier mobilities and lifetimes that enable optimum charge collection efficiency (mobility-lifetime product of at least 10^{-5} cm^2/V-s). Schlesinger et al. lay out at least six key properties for semiconductors to be capable radiation detectors [168]:

1. Adequate electron density to support high stopping power and interaction rates between sensor matter and gamma radiation.
2. A band gap in the "sweet spot" that is low enough to promote a high number of electron-hole ionization pairs upon interactions, but not also large enough to ensure high resistivity and low leakage current.
3. High intrinsic mobility-lifetime product, such that the charge carrier drift length is far larger than the detector thickness.
4. Single crystal phases with low impurity concentrations and few intrinsic lattice defects or trap states.
5. Compatibility with electrode metals such that space charge buildup and polarization effects are eliminated.
6. High surface resistivity to prevent shunt current across detector surfaces and ensure electric field lines are not perturbed at surfaces.

Similar to scintillators, Se, Br, Te, and I are commonly selected as the high-Z anions and are paired with elements that produce to semiconducting characteristics when bonded. Like Fig. 1, in Fig. 4 the elements commonly selected (and avoided) for semiconductor gamma-ray sensors are presented. The main considerations in semiconductor element selection are pairs of anions and cations that provide compounds with band gaps suitable for sensor application, which is typically limited to between 1.5 and 2.5 eV. Many of the same critera for scintillator element selection apply to semiconductors. Elements that are radioactive, have insufficiently high or low band gaps, do not form into compounds, or do not grow easily. Of note, few lanthanide elements have been shown to be incorporated into feasible semiconducting materials.

The most obvious contenders for semiconducting gamma-ray sensors are the most utilized semiconducting materials worldwide: Si and Ge. Si is one of the most ubiquitous and developed materials in the modern world and is found in nearly every electronic device worldwide. The attractiveness of using Si as a radiation sensor comes from its excellent electronic transport properties, such as its 3.62 eV pair creation energy, electron mobility of 1350 cm^2/V-s, and hole mobility of 480 cm^2/V-s at 300 K [46]. Unfortunately, Si is prevented from serving viably in most gamma radiation detectors due to its moderately low stopping power, and the high leakage currents that stem from its 1.12 eV band gap at room temperature. Si therefore is most often used in X-ray detection systems, and typically operates at cryogenic temperatures to increase its band gap and resistivity. Germanium, which has a greater atomic number and density, has instead arisen as one of the most widely used sensors in laboratory gamma-ray detection applications. Reducing impurity concentrations to the order of 10^{10} atoms/cm^3 and cooling the crystal with liquid nitrogen enables Ge detectors to serve as the world's highest resolution semiconductor sensor for gamma-ray spectrometers. Currently,

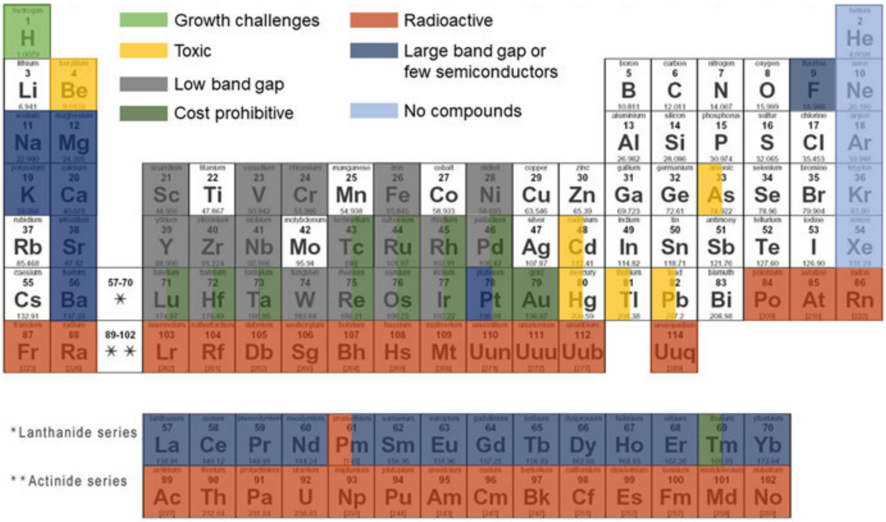

Fig. 4 Periodic table mapping the elements frequently incorporated into semiconductor materials. Compounds that present challenges that inhibit use in semiconducting materials are highlighted

high purity germanium (HPGe) detectors are the industry performance benchmark for spectroscopy due HPGe's ability to produce spectra with photopeak resolution below 0.8% over a large range of energies [169].

Due to their intrinsically low 0.67 eV room temperature band gap, the Ge crystals in HPGe spectrometers must be cooled to liquid nitrogen temperature (~80 K) in order to operate as a gamma-ray sensor. Without sufficient cooling, thermal phonons in the Ge create too high of an electron density in the conduction bands to distinguish signal from noise. Cooling HPGe spectrometers most often requires liquid nitrogen reservoirs or electromechanical coolers that add weight and power draw to detectors. Because of this, many semiconductors with larger band gaps have come under investigation as candidate materials for room temperature semiconductor detectors (RTSDs).

RTSDs remain a R&D focus in detection science because they can generate theoretically higher resolution spectra than comparably sized scintillators at ambient operating temperatures. Many semiconductors with sufficient band gaps have come under investigation as candidate materials for radiation sensors. Despite the number of requirements for materials to serve effectively as RTSD sensors, new promising compounds are frequently discovered. Within the last decade, review articles on RTSD sensor materials have been written by McGregor [170], Owens [137], Luke [171], Sellin [172], Zaletin [81], and Johns [138], as well as the books by Owens [64], Awadalla [173], and Iniewski [174].

The highest technology-readiness level RTSD compounds are currently CdZnTe (CZT), TlBr, and HgI_2. Among these, CdTe and CdZnTe (CZT) are the forefront RTSD sensor materials and currently are the only RTSD compounds found widely

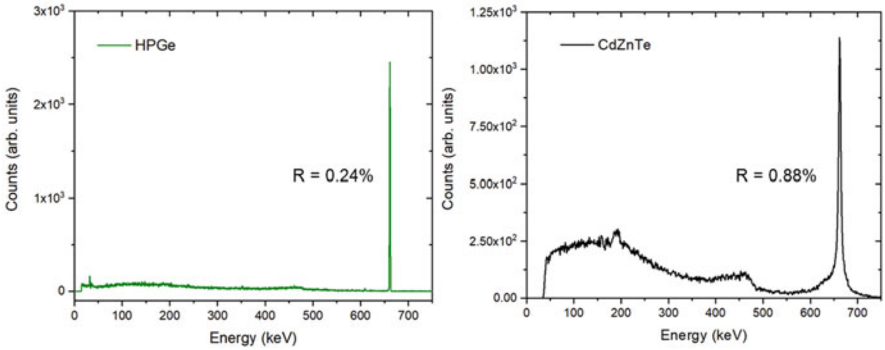

Fig. 5 Examples of sub-1% spectral resolution at 662 keV achieved from commercial HPGe and CZT sensors

among commercial detection systems. CZT in particular is the performance benchmark RTSD compound against which emerging sensor materials are compared. CZT is CdTe alloyed with <15% Zn to increase the band gap and prevent polarization effects from occurring after long periods under bias [175]. CZT features a band gap around 1.57 eV (for 10% Zn-doped), is the industry standard RSTD material [176]. With modern charge sensing and depth of interaction correction techniques, it is possible for CZT to exhibit photopeak resolution well below 1% at 662 keV [177–179]. Figure 5 provides a comparison between HPGE and CZT spectra obtained from commercially available spectrometers.

TlBr and HgI$_2$ are other sensors materials widely seen in RTSDs. TlBr has density is among the highest of RTSD candidates at 7.56 g/cm^3, and its band gap of 2.56 eV maximizes resistivity at the cost of a slightly higher pair creation energy. One of the historical drawbacks of TlBr is polarization that leads to the degeneration of electronic performance after extended periods under bias [180]; however, by engineering the crystals with Tl contacts, this issue has been solved [181]. Today, both pixelated [182] and capacitive Frisch grid detectors [183] have demonstrated resolution <1% at 662 keV. Likewise, HgI$_2$ has been honed into a quality RTSD gamma-ray sensor. HgI$_2$ originally proved challenging due to the hole ($\mu\tau$) product lagging orders of magnitude behind that of electrons. Modern techniques that allow spectra to be reconstructed from single charge carrier interactions have demonstrated remarkable resolution in HgI$_2$. Resolution of 1.55% at 662 keV has been demonstrated from collecting charge from pixelated anode electrodes and performing depth correction on interaction signals [184].

CZT, HgI$_2$, and TlBr each experience a problem common to RTSD sensors: transport characteristics of one charge carrier (electron or hole) are dominant relative to the other. Equation (1) shows how induced charge, Q_{induced}, is generated on an electrode after radiation interaction in a semiconductor. Change in weighing potential, Ψ, experienced by electrons and holes with individual charge q, induces charge on the anode and cathode as carriers travel from the interaction position

(x_1) to the anode (x_A) or cathode (x_C). When a single carrier is unable to transit effectively through the semiconductor, the induced charge on the electrode is reduced proportional to the weighing potential change not experienced by the electron or hole.

$$Q_{induced} = \underbrace{q\,[\psi\,(x_1) - \psi\,(x_C)]}_{holes} - \underbrace{\{-q\,[\psi\,(x_A) - \psi\,(x_1)]\}}_{electrons}, \qquad (1)$$

To compensate for charge collection loss effects, single polarity charge sensing techniques are commonly used to improve resolution in RTSD spectrometers. These techniques incorporate an electrode design that allows the majority charge carrier to experience a change in its weighing potential much greater than the minority charge carrier. The most common single polarity charge sensing techniques are pixel electrode grids and Frisch collars [185, 186]. That enable the majority carrier to experience the most change in weighing potential. Application of these techniques create weighing potential distributions where nearly all the induced charge is due to the majority carrier, thereby improving overall spectral resolution.

5 Perovskites

Over at least the last half-decade, interest in a particular class of materials for radiation detection has expanded significantly. These materials, perovskites, are already the focus of several review articles that summarize their promising properties for both scintillator and semiconductor radiation detectors [187–190]. Perovskites are materials with the structure ABX_3 where ‘A’ is an anion, ‘C’ is a cation, and ‘X’ is another anion that bonds to ‘A’ and ‘B’. These materials primarily come in two flavors as all-inorganic or organic-inorganic hybrid materials. The draw toward perovskite-based compounds comes from the ease of their growth routes and the excellent charge transport properties that they can exhibit as semiconductor radiation sensors. Rather than expending the time and energy needed to produce single crystals in a furnace, perovskites can be grown in a fraction of the time through crystallization in solution. A review of the perovskite solution crystallization methods, often which occur from room temperature to 100 °C, is provided by Jung et al. [191].

Many organic-inorganic hybrids and halide perovskites have recently gained attention from their impressive performance as thin film photovoltaics and have seen interest and development as X-ray detectors. Toward gamma radiation detection applications, many research groups have made efforts to transition these materials from thin films to thicker bulk crystals needed for absorbing higher energy photons. Perovskite material development within the last few years has culminated in several compounds that have produced promising responses to radiation as both indirect (scintillation) and direct (semiconductor) applications. Zhou et al., Liu et al., and references therein summarize to date a majority of the scintillating

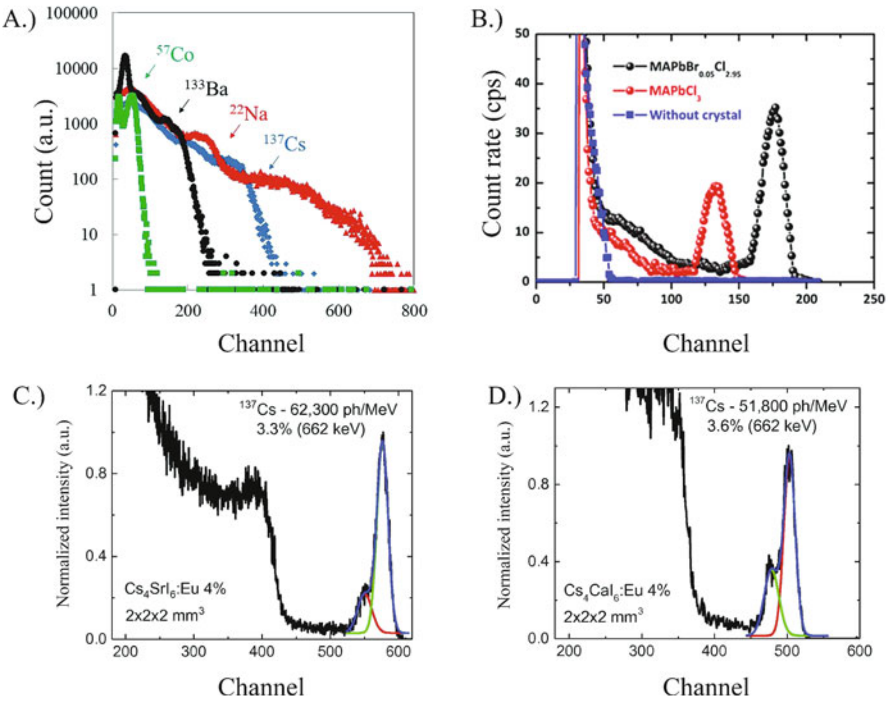

Fig. 6 Scintillator perovskite materials: (**a**) Spectra from a number of sources measured by $(C_6H_5C_2H_4NH_3)_2PbBr_4$ [193], (**b**) ^{137}Cs spectra measured from MAPbBrxCl3-x [194], (**c**) ^{137}Cs measured by Cs_4SrI_6, and (**d**) ^{137}Cs measured by Cs_4CaI_6 [21]. Images reused used with permissions

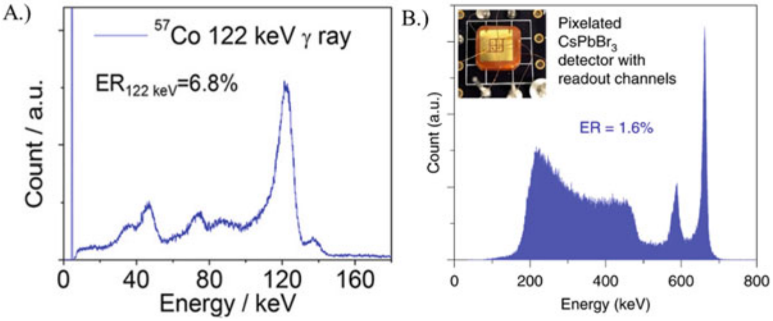

Fig. 7 Semiconductor perovskite materials: (**a**) ^{57}Co spectra from an organic-inorganic hybrid $CH_3NH_3PbI_3$ sample [130], and (**b**) depth-corrected ^{137}Cs spectra from an all-inorganic $CsPbBr_3$ perovskite [196]. Images reused used with permissions

and semiconducting perovskite compounds [152, 192]. Figures 6 and 7 showcase some spectra obtained from perovskite-based compounds as both scintillators and semiconductors.

6 Conclusions

Throughout the radiation detection industry, significant R&D and engineering effort continues to focus on identifying new materials with better properties for radiation detection, then scaling those materials so they can be produced into sensors with large physical sizes. Identifying new compounds with better intrinsic properties for radiation detectors, and then growing those materials to scales with good extrinsic properties requires significant investment. As new sensors continuously emerge with better properties than existing sensors, manufacturers can be understandably reluctant to take on the significant costs it takes to build or rebuild a production chain around a new material. There is significant risk and effort involved in pursuing new materials with improved performance figures of merit over established sensors and the technologies built around them.

Several compounds show tremendous promise as radiation detectors that have improved light yields, charge transport properties, and overall better detection response than conventionally used sensors. Many of these materials also show promise not only in their detection properties, but also in their scalability and potential for low-cost manufacturing. It is likely that within the next decade, some of these emerging materials, particularly perovskites, will begin to see adoption into commercial radiation detectors.

References

1. Johns, P. (2022). Radiation detection materials introduction. In K. Iniewski (Ed.), *Advanced materials for radiation detection* (pp. 1–31). Springer International Publishing.
2. Galunov, N., Tarasenko, O., & Tarasov, V. (2013). Determination of the light yield of organic scintillators. *Functional Materials*.
3. Gundiah, G., et al. (2011). Structure and scintillation of Eu2+-activated solid solutions in the BaBr2–BaI2 system. *Nuclear Instruments and Methods in Physics Research Section A: Accelerators, Spectrometers, Detectors and Associated Equipment, 652*(1), 234–237.
4. Yan, Z., et al. (2014). Eu2+-activated BaCl2, BaBr2 and BaI2 scintillators revisited. *Nuclear Instruments and Methods in Physics Research Section A: Accelerators, Spectrometers, Detectors and Associated Equipment, 735*, 83–87.
5. Yan, Z., Shalapska, T., & Bourret, E. D. (2016). Czochralski growth of the mixed halides BaBrCl and BaBrCl:Eu. *Journal of Crystal Growth, 435*, 42–45.
6. Bizarri, G., et al. (2011). Scintillation and optical properties of BaBrI:Eu^{2+} and $CsBa_2I_5$:Eu^{2+}. *IEEE Transactions on Nuclear Science, 58*(6), 3403–3410.
7. Bourret-Courchesne, E. D., et al. (2010). BaBrI:Eu2+, a new bright scintillator. *Nuclear Instruments and Methods in Physics Research Section A: Accelerators, Spectrometers, Detectors and Associated Equipment, 613*(1), 95–97.
8. Shirwadkar, U., et al. (2013). Promising alkaline earth halide scintillators for gamma-ray spectroscopy. *IEEE Transactions on Nuclear Science, 60*(2), 1011–1015.
9. Yan, Z., Bizarri, G., & Bourret-Courchesne, E. (2013). Scintillation properties of improved 5% Eu2+-doped BaCl2 single crystal for X-ray and γ-ray detection. *Nuclear Instruments and Methods in Physics Research Section A: Accelerators, Spectrometers, Detectors and Associated Equipment, 698*, 7–10.

10. Moszynski, M., et al. (1997). Absolute light output of scintillators. *IEEE Transactions on Nuclear Science, 44*(3), 1052–1061.
11. Sakai, E. (1987). Recent measurements on scintillator-photodetector systems. *IEEE Transactions on Nuclear Science, 34*(1), 418–422.
12. Haas, J. T. M. D., & Dorenbos, P. (2008). Advances in yield calibration of scintillators. *IEEE Transactions on Nuclear Science, 55*(3), 1086–1092.
13. Michail, C., et al. (2019). Absolute luminescence efficiency of europium-doped calcium fluoride (CaF2:Eu) single crystals under X-ray excitation. *Crystals, 9*(5), 234.
14. Holl, I., Lorenz, E., & Mageras, G. (1988). A measurement of the light yield of common inorganic scintillators. *IEEE Transactions on Nuclear Science, 35*(1), 105–109.
15. Plettner, C., et al. (2013). CaF2(Eu): an "old" scintillator revisited. *Journal of Instrumentation, 8*(06), P06010.
16. Cherepy, N. J., et al. (2009). Scintillators with potential to supersede lanthanum bromide. *IEEE Transactions on Nuclear Science, 56*(3), 873–880.
17. Hofstadter, R., O'Dell, E., & Schmidt, C. (1964). CaI2 and CaI2 (Eu) scintillation crystals. *Review of Scientific Instruments, 35*(2), 246–247.
18. Shah, K. S., et al. (2005). CeBr/sub 3/scintillators for gamma-ray spectroscopy. *IEEE Transactions on Nuclear Science, 52*(6), 3157–3159.
19. Quarati, F., et al. (2013). Scintillation and detection characteristics of high-sensitivity CeBr3 gamma-ray spectrometers. *Nuclear Instruments and Methods in Physics Research Section A: Accelerators, Spectrometers, Detectors and Associated Equipment, 729*, 596–604.
20. Alekhin, M. S., et al. (2014). Optical and scintillation properties of CsBa2I5:Eu2+. *Journal of Luminescence, 145*, 723–728.
21. Stand, L., et al. (2018). Crystal growth and scintillation properties of Eu2+ doped Cs4CaI6 and Cs4SrI6. *Journal of Crystal Growth, 486*, 162–168.
22. Cheng, S., Nikl, M., Beitlerova, A., Kucerkova, R., Du, X., Niu, G., et al. (2021). Ultrabright and highly efficient all-inorganic zero-dimensional perovskite scintillators. *Advanced Optical Materials, 9*(13), 2100460.
23. Wu, Y., et al. (2018). Zero-dimensional Cs 4 EuX 6 (X= Br, I) all-inorganic perovskite single crystals for gamma-ray spectroscopy. *Journal of Materials Chemistry C, 6*(25), 6647–6655.
24. Burger, A., et al. (2015). Cesium hafnium chloride: A high light yield, non-hygroscopic cubic crystal scintillator for gamma spectroscopy. *Applied Physics Letters, 107*(14), 143505.
25. Ariesanti, E., et al. (2020). Improved growth and scintillation properties of intrinsic, non-hygroscopic scintillator Cs2HfCl6. *Journal of Luminescence, 217*, 116784.
26. Glodo, J., et al. (2011). Selected properties of Cs_2LiYCl_6, $Cs_2LiLaCl_6$, and $Cs_2LiLaBr_6$ scintillators. *IEEE Transactions on Nuclear Science, 58*(1), 333–338.
27. Samulon, E. C., et al. (2014). Luminescence and scintillation properties of Ce3+-activated Cs2NaGdCl6, Cs3GdCl6, Cs2NaGdBr6 and Cs3GdBr6. *Journal of Luminescence, 153*, 64–72.
28. Gundiah, G., et al. (2014). Structure and scintillation properties of Ce3+-activated Cs2NaLaCl6, Cs3LaCl6, Cs2NaLaBr6, Cs3LaBr6, Cs2NaLaI6 and Cs3LaI6. *Journal of Luminescence, 149*, 374–384.
29. Wei, H., et al. (2014). Two new cerium-doped mixed-anion elpasolite scintillators: Cs2NaYBr3I3 and Cs2NaLaBr3I3. *Optical Materials, 38*, 154–160.
30. Yang, K., M. Zhuravleva, and C.L. Melcher, Crystal growth and characterization of CsSr1–xEux I3 high light yield scintillators Physica Status Solidi (RRL)–Rapid Research Letters, 2011. 5(1): p. 43–45.
31. van Loef, E. V., et al. (2008). Crystal growth and characterization of rare earth iodides for scintillation detection. *Journal of Crystal Growth, 310*(7), 2090–2093.
32. Stand, L., et al. (2016). Scintillation properties of Eu2+-doped KBa2I5 and K2BaI4. *Journal of Luminescence, 169*, 301–307.
33. van Loef, E. V. D., et al. (2005). Scintillation properties of K2LaX5:Ce3+ (X=Cl, Br, I). *Nuclear Instruments and Methods in Physics Research Section A: Accelerators, Spectrometers, Detectors and Associated Equipment, 537*(1), 232–236.

34. van't Spijker, J. C., et al. (1999). Scintillation and luminescence properties of Ce3+ doped K2LaCl5. *Journal of Luminescence, 85*(1), 1–10.
35. Lindsey, A. C., et al. (2015). Crystal growth and characterization of europium doped KCaI3, a high light yield scintillator. *Optical Materials, 48*, 1–6.
36. Stand, L., et al. (2015). Crystal growth and scintillation properties of potassium strontium bromide. *Optical Materials, 46*, 59–63.
37. Stand, L., et al. (2013). Potassium strontium iodide: A new high light yield scintillator with 2.4% energy resolution. In *2013 IEEE nuclear science symposium and medical imaging conference (2013 NSS/MIC)*.
38. Glodo, J., et al. (2005). LaBr/sub 3/:Pr/sup 3+/ – a new red-emitting scintillator. In *IEEE nuclear science symposium conference record, 2005*.
39. Menge, P. R., et al. (2007). Performance of large lanthanum bromide scintillators. *Nuclear Instruments and Methods in Physics Research Section A: Accelerators, Spectrometers, Detectors and Associated Equipment, 579*(1), 6–10.
40. Rozsa, C. M., Menge, P. R., & Mayhugh, M. R. (2019). *Scintillation products technical note lanthanum bromide scintillators performance summary*, 0419.
41. Alekhin, M. S., et al. (2013). Improvement of γ-ray energy resolution of LaBr3: Ce3+ scintillation detectors by Sr2+ and Ca2+ co-doping. *Applied Physics Letters, 102*(16), 161915.
42. Soundara-Pandian, L., et al. (2016). Lithium alkaline halides—Next generation of dual mode scintillators. *IEEE Transactions on Nuclear Science, 63*(2), 490–496.
43. Porter-Chapman, Y. D., et al. (2009). Scintillation and luminescence properties of undoped and cerium-doped $LiGdCl_4$ and $NaGdCl_4$. *IEEE Transactions on Nuclear Science, 56*(3), 881–886.
44. Glodo, J., et al. (2008). Mixed lutetium iodide compounds. *IEEE Transactions on Nuclear Science, 55*(3), 1496–1500.
45. Birowosuto, M. D., et al. (2006). High-light-output scintillator for photodiode readout: LuI_3: Ce^{3+}. *Journal of Applied Physics, 99*(12), 123520.
46. Knoll, G. F. (2010). *Radiation detection and measurement*. Wiley.
47. Zhang, M., Wang, X., Yang, B., Zhu, J., Niu, G., Wu, H., et al. (2021). Metal halide scintillators with fast and self-absorption-free defect-bound excitonic radioluminescence for dynamic X-Ray Imaging. *Advanced Functional Materials, 31*(9), 2007921.
48. Dorenbos, P., et al. (1997). Scintillation properties of RbGd2Br7 : Ce3+ crystals; fast, efficient, and high density scintillators. *Nuclear Instruments and Methods in Physics Research Section B: Beam Interactions with Materials and Atoms, 132*(4), 728–731.
49. Rowe, E., et al. (2013). A new lanthanide activator for iodide based scintillators*:* Yb^{2+}. *IEEE Transactions on Nuclear Science, 60*(2), 1057–1060.
50. van Loef, E. V., et al. (2009). Crystal growth and scintillation properties of strontium iodide scintillators. *IEEE Transactions on Nuclear Science, 56*(3), 869–872.
51. Khan, A., et al. (2018). Ce3+-activated Tl2GdCl5: Novel halide scintillator for X-ray and γ-ray detection. *Journal of Alloys and Compounds, 741*, 878–882.
52. Khan, A., et al. (2018). Scintillation properties of TlGd2Cl7 (Ce3+) single crystal. *IEEE Transactions on Nuclear Science, 65*(8), 2152–2156.
53. Hawrami, R., et al. (2017). Tl2LaCl5:Ce, high performance scintillator for gamma-ray detectors. *Nuclear Instruments and Methods in Physics Research Section A: Accelerators, Spectrometers, Detectors and Associated Equipment, 869*, 107–109.
54. Khan, A., et al. (2020). Crystal growth and Ce3+ concentration optimization in Tl2LaCl5: An excellent scintillator for the radiation detection. *Journal of Alloys and Compounds, 827*, 154366.
55. Kim, H. J., et al. (2018). Scintillation performance of the TlSr2I5 (Eu2+) single crystal. *Optical Materials, 82*, 7–10.
56. Fujimoto, Y., et al. (2018). New intrinsic scintillator with large effective atomic number: Tl2HfCl6 and Tl2ZrCl6 crystals for X-ray and gamma-ray detections. *Sensors and Materials, 30*(7), 1577–1583.

57. Phan, Q. V., et al. (2018). Tl2ZrCl6 crystal: Efficient scintillator for X- and γ-ray spectroscopies. *Journal of Alloys and Compounds, 766*, 326–330.
58. Yehuda-Zada, Y., et al. (2018). Optimization of 6LiF:ZnS(Ag) scintillator light yield using GEANT4. *Nuclear Instruments and Methods in Physics Research Section A: Accelerators, Spectrometers, Detectors and Associated Equipment, 892*, 59–69.
59. Kim, Y. K., et al. (2007). Properties of semiconductor scintillator ZnSe:O. *Nuclear Instruments and Methods in Physics Research Section A: Accelerators, Spectrometers, Detectors and Associated Equipment, 580*(1), 258–261.
60. Takahashi, T., & Watanabe, S. (2001). Recent progress in CdTe and CdZnTe detectors. *IEEE Transactions on Nuclear Science, 48*(4), 950–959.
61. Amman, M., et al. (2009). Evaluation of THM-grown CdZnTe material for large-volume gamma-ray detector applications. *IEEE Transactions on Nuclear Science, 56*(3), 795–799.
62. Szeles, C., et al. (2006). *Fabrication of high performance CdZnTe quasi-hemispherical gamma-ray CAPture™ plus detectors*.
63. Szeles, C., et al. (2004). Development of the high-pressure electro-dynamic gradient crystal-growth technology for semi-insulating CdZnTe growth for radiation detector applications. *Journal of Electronic Materials, 33*(6), 742–751.
64. Owens, A. (2012). *Compound semiconductor radiation detectors*. Taylor & Francis.
65. Hitomi, K., et al. (2011). Recent development of TlBr gamma-ray detectors. *IEEE Transactions on Nuclear Science, 58*(4), 1987–1991.
66. Kim, H., et al. (2009). Developing larger TlBr detectors–Detector performance. *IEEE Transactions on Nuclear Science, 56*(3), 819–823.
67. Wu, W., et al. (2016). Traveling heater method growth and characterization of CdMnTe crystals for radiation detectors. *Physica Status Solidi (c), 13*, 408–412.
68. Kochanowskab, D., Witkowska-Baranb, M., & Jamesa, R. (2008). *CdMnTe in X-ray and gamma-ray detection: Potential applications*.
69. Rafiei, R., et al. (2013). High-purity CdMnTe radiation detectors: A high-resolution spectroscopic evaluation. *IEEE Transactions on Nuclear Science, 60*(2), 1450–1456.
70. Kim, K. H., et al. (2015). Spectroscopic properties of large-volume virtual Frisch-grid CdMnTe detectors. *Journal of the Korean Physical Society, 66*(11), 1761–1765.
71. Burger, A., Shilo, I., & Schieber, M. (1983). Cadmium selenide: A promising novel room temperature radiation detector. *IEEE Transactions on Nuclear Science, 30*(1), 368–370.
72. Roth, M. (1989). Advantages and limitations of cadmium selenide room temperature gamma ray detectors. *Nuclear Instruments and Methods in Physics Research Section A: Accelerators, Spectrometers, Detectors and Associated Equipment, 283*(2), 291–298.
73. Kishore, V., et al. (2005). Structural and electrical measurements of CdZnSe composite. *Bulletin of Materials Science, 28*(5), 431–436.
74. Roy, U. N., et al. (2014). Growth of CdTexSe1−x from a Te-rich solution for applications in radiation detection. *Journal of Crystal Growth, 386*, 43–46.
75. Roy, U., et al. (2013). Growth and characterization of CdTeSe for room-temperature radiation detector applications. In *SPIE optical engineering + applications*. International Society for Optics and Photonics.
76. Sze, S. M., & Ng, K. K. (2006). *Physics of semiconductor devices*. Wiley.
77. Bor-Chau, J., et al. (2016). Characterization of GaSb photodiode for gamma-ray detection. *Applied Physics Express, 9*(8), 086401.
78. Manfredotti, C., Murri, R., & Vasanelli, L. (1974). GaSe as nuclear particle detector. *Nuclear Instruments and Methods, 115*(2), 349–353.
79. Nakatani, H., et al. (1989). GaSe nuclear particle detectors. *Nuclear Instruments and Methods in Physics Research Section A: Accelerators, Spectrometers, Detectors and Associated Equipment, 283*(2), 303–309.
80. Mandal, K.C., et al. GaSe and GaTe anisotropic layered semiconductors for radiation detectors. 2007.
81. Zaletin, V. M., & Varvaritsa, V. P. (2011). Wide-bandgap compound semiconductors for X- or gamma-ray detectors. *Russian MicroElectronics, 40*(8), 543–552.

82. Zdansky, K., et al. (2006). Evaluation of semiinsulating annealed InP:Ta for radiation detectors. *IEEE Transactions on Nuclear Science, 53*(6), 3956–3961.
83. Yee, J. H., Swierkowski, S. P., & Sherohman, J. W. (1977). ALSB as a high-energy photon detector. *IEEE Transactions on Nuclear Science, 24*(4), 1962–1967.
84. Li, H., et al. (2015). TlHgInS3: An indirect-band-gap semiconductor with X-ray photoconductivity response. *Chemistry of Materials, 27*(15), 5417–5424.
85. Li, H., et al. (2012). Crystal growth and characterization of the X-ray and γ-ray detector material Cs2Hg6S7. *Crystal Growth & Design, 12*(6), 3250–3256.
86. Li, H., et al. (2014). Investigation of semi-insulating Cs2Hg6S7 and Cs2Hg6-xCdxS7 alloy for hard radiation detection. *Crystal Growth & Design, 14*(11), 5949–5956.
87. Li, H., et al. (2012). CsHgInS3: A new quaternary semiconductor for γ-ray detection. *Chemistry of Materials, 24*(22), 4434–4441.
88. Johnsen, S., et al. (2011). Thallium chalcogenide-based wide-band-gap semiconductors: TlGaSe2 for radiation detectors. *Chemistry of Materials, 23*(12), 3120–3128.
89. Roy, U. N., et al. (2004). *Crystal growth, characterization, and fabrication of AgGaSe2 crystals as novel material for room-temperature radiation detectors*.
90. Alekseev, I. V. (2008). A neutron semiconductor detector based on TlInSe2. *Instruments and Experimental Techniques, 51*(3), 331–335.
91. Kilday, D. G., et al. (1987). Electronic structure of the “chain” chalcogenide $\mathrm{TlInSe_2}$. *Physical Review B, 35*(2), 660–663.
92. Alekseev, I. (1993). Application of TlInSe2 crystals for the detection of hard radiation. *Inorganic Materials, 28*(12), 1961–1964.
93. Tupitsyn, E., et al. (2012). Single crystal of LiInSe2 semiconductor for neutron detector. *Applied Physics Letters, 101*(20), 202101.
94. Bell, Z. W., et al. (2015). Neutron detection with LiInSe2. In *SPIE optical engineering+ applications*. International Society for Optics and Photonics.
95. Stowe, A. C., et al. (2013). Crystal growth in LiGaSe2 for semiconductor radiation detection applications. *Journal of Crystal Growth, 379*, 111–114.
96. Li, H., et al. (2013). CsCdInQ3 (Q = Se, Te): New photoconductive compounds as potential materials for hard radiation detection. *Chemistry of Materials, 25*(10), 2089–2099.
97. Kahler, D., et al. (2011). Performance of novel materials for radiation detection: Tl3AsSe3, TlGaSe2, and Tl4HgI6. *Nuclear Instruments and Methods in Physics Research Section A: Accelerators, Spectrometers, Detectors and Associated Equipment, 652*(1), 183–185.
98. Androulakis, J., et al. (2011). Dimensional reduction: A design tool for new radiation detection materials. *Advanced Materials, 23*(36), 4163–4167.
99. Wang, P. L., et al. (2015). Hard radiation detection from the selenophosphate Pb2P2Se6. *Advanced Functional Materials, 25*(30), 4874–4881.
100. Wang, P. L., et al. (2016). Refined synthesis and crystal growth of Pb2P2Se6 for hard radiation detectors. *Crystal Growth & Design, 16*, 5100–5109.
101. Lin, W., et al. (2018). Cu2I2Se6: A Metal–inorganic framework wide-bandgap semiconductor for photon detection at room temperature. *Journal of the American Chemical Society, 140*(5), 1894–1899.
102. Squillante, M. R., et al. (1992). InI nuclear radiation detectors. In *Nuclear science symposium and medical imaging conference, 1992. Conference record of the 1992*. IEEE.
103. Onodera, T., Hitomi, K., & Shoji, T. (2006). Fabrication of indium iodide X- and gamma-ray detectors. *IEEE Transactions on Nuclear Science, 53*(5), 3055–3059.
104. Onodera, T., Baba, K., & Hitomi, K. (2018). Evaluation of antimony tri-iodide crystals for radiation detectors. *Science and Technology of Nuclear Installations, 2018*, 1–7.
105. Podraza, N. J., et al. (2013). Band gap and structure of single crystal BiI3: Resolving discrepancies in literature. *Journal of Applied Physics, 114*(3).
106. Saito, T., et al. (2016). BiI3 single crystal for room-temperature gamma ray detectors. *Nuclear Instruments and Methods in Physics Research Section A: Accelerators, Spectrometers, Detectors and Associated Equipment, 806*, 395–400.

107. Wibowo, A. C., et al. (2016). An unusual crystal growth method of the chalcohalide semiconductor, β-Hg3S2Cl2: A new candidate for hard radiation detection. *Crystal Growth & Design*.
108. Stoumpos, C. C., et al. (2013). Crystal growth of the perovskite semiconductor CsPbBr3: A new material for high-energy radiation detection. *Crystal Growth & Design, 13*(7), 2722–2727.
109. He, Y., et al. (2018). High spectral resolution of gamma-rays at room temperature by perovskite CsPbBr3 single crystals. *Nature Communications, 9*(1), 1609.
110. He, Y., et al. (2021). CsPbBr 3 perovskite detectors with 1.4% energy resolution for high-energy γ-rays. *Nature Photonics, 15*(1), 36–42.
111. Li, H., et al. (2016). Mercury chalcohalide semiconductor Hg3Se2Br2 for hard radiation detection. *Crystal Growth & Design, 16*(11), 6446–6453.
112. Wibowo, A. C., et al. (2013). Photoconductivity in the chalcohalide semiconductor, SbSeI: A new candidate for hard radiation detection. *Inorganic Chemistry, 52*(12), 7045–7050.
113. Wang, S., et al. (2014). Crystal growth of Tl4CdI6: A wide band gap semiconductor for hard radiation detection. *Crystal Growth & Design, 14*(5), 2401–2410.
114. Nguyen, S. L., et al. (2013). Photoconductivity in Tl6SI4: A novel semiconductor for hard radiation detection. *Chemistry of Materials, 25*(14), 2868–2877.
115. Johnsen, S., et al. (2011). Thallium chalcohalides for X-ray and γ-ray detection. *Journal of the American Chemical Society, 133*(26), 10030–10033.
116. Lin, W., et al. (2017). TlSn2I5, a robust halide antiperovskite semiconductor for γ-ray detection at room temperature. *ACS Photonics, 4*(7), 1805–1813.
117. He, Y., et al. (2017). Defect antiperovskite compounds Hg3Q2I2 (Q = S, Se, and Te) for room-temperature hard radiation detection. *Journal of the American Chemical Society, 139*(23), 7939–7951.
118. McCall, K. M., et al. (2018). α-Particle detection and charge transport characteristics in the A3M2I9 defect perovskites (A= Cs, Rb; M= Bi, Sb). *ACS Photonics, 5*(9), 3748–3762.
119. Johnson, B. R., et al. (2008). *FY07 annual report: Amorphous semiconductors for gamma radiation detection (ASGRAD)*. Pacific Northwest National Laboratory.
120. Montag, B. W., et al. (2016). Device fabrication, characterization, and thermal neutron detection response of LiZnP and LiZnAs semiconductor devices. *Nuclear Instruments and Methods in Physics Research Section A: Accelerators, Spectrometers, Detectors and Associated Equipment, 836*, 30–36.
121. Kuriyama, K., Kato, T., & Kawada, K. (1994). Optical band gap of the filled tetrahedral semiconductor LiZnAs. *Physical Review B, 49*(16), 11452–11455.
122. Kuriyama, K., & Katoh, T. (1988). Optical band gap of the filled tetrahedral semiconductor LiZnP. *Physical Review B, 37*(12), 7140.
123. Nava, F., et al. (2008). Silicon carbide and its use as a radiation detector material. *Measurement Science and Technology, 19*(10), 102001.
124. Friedl, M. (1999). *Diamond detectors for ionizing radiation*. Austrian Academy of Sciences.
125. Conte, G., et al. (2004). Temporal response of CVD diamond detectors to modulated low energy X-ray beams. *Physica Status Solidi (a), 201*(2), 249–252.
126. Willig, W. R. (1972). Large bandgap mercury and lead compounds for nuclear particle detection. *Nuclear Instruments and Methods, 101*(1), 23–24.
127. Zhao, X., Chen, L., He, Y., Liu, J., Peng, W., Huang, Z., et al. (2016). Nanosecond X-ray detector based on high resistivity ZnO single crystal semiconductor. *Applied Physics Letters, 108*(17), 171103.
128. Yakunin, S., et al. (2016). Detection of gamma photons using solution-grown single crystals of hybrid lead halide perovskites. *Nature Photonics., 10*(9), 585–589. Advance online publications.
129. Mettan, X., et al. (2015). Tuning of the thermoelectric figure of merit of CH3NH3MI3 (M=Pb, Sn) photovoltaic perovskites. *The Journal of Physical Chemistry C, 119*(21), 11506–11510.

130. He, Y., et al. (2018). Resolving the energy of γ-ray photons with MAPbI3 single crystals. *ACS Photonics, 5*(10), 4132–4138.
131. Han, Q., et al. (2016). Single crystal formamidinium lead iodide (FAPbI3): Insight into the structural, optical, and electrical properties. *Advanced Materials, 28*(11), 2253–2258.
132. Nazarenko, O., et al. (2017). Single crystals of caesium formamidinium lead halide perovskites: Solution growth and gamma dosimetry. *NPG Asia Materials, 9*, e373.
133. Liu, X., et al. (2021). Solution-grown formamidinium hybrid perovskite (FAPbBr3) single crystals for α-particle and γ-ray detection at room temperature. *ACS Applied Materials & Interfaces, 13*(13), 15383–15390.
134. Wei, H., et al. (2016). Sensitive X-ray detectors made of methylammonium lead tribromide perovskite single crystals. *Nature Photonics, 10*(5), 333–339.
135. Ryu, S., et al. (2014). Voltage output of efficient perovskite solar cells with high open-circuit voltage and fill factor. *Energy & Environmental Science, 7*(8), 2614–2618.
136. Wei, H., et al. (2017). Dopant compensation in alloyed CH3NH3PbBr3−xClx perovskite single crystals for gamma-ray spectroscopy. *Nature Materials, 16*(8), 826.
137. Owens, A., & Peacock, A. (2004). Compound semiconductor radiation detectors. *Nuclear Instruments and Methods in Physics Research Section A: Accelerators, Spectrometers, Detectors and Associated Equipment, 531*(1), 18–37.
138. Johns, P. M., & Nino, J. C. (2019). Room temperature semiconductor detectors for nuclear security. *Journal of Applied Physics, 126*(4), 040902.
139. Mattox, D. M. (2002). Physical vapor deposition (PVD) processes. *Metal Finishing, 100*, 394–408.
140. Zhang, X., Friedrich, S., & Friedrich, B. (2018). Production of high purity metals: A review on zone refining process. *Journal of Crystallization Process and Technology, 8*(01), 33.
141. Dhanaraj, G., et al. (2010). *Springer handbook of crystal growth*. Springer Science & Business Media.
142. Lempicki, A., Wojtowicz, A. J., & Berman, E. (1993). Fundamental limits of scintillator performance. *Nuclear Instruments and Methods in Physics Research Section A: Accelerators, Spectrometers, Detectors and Associated Equipment, 333*(2), 304–311.
143. Bliss, M., & Stave, J. A. (2012). *Final report on actinide glass scintillators for fast neutron detection*. Pacific Northwest National Lab. (PNNL).
144. Derenzo, S. E., et al. (2008). Design and implementation of a facility for discovering new scintillator materials. *IEEE Transactions on Nuclear Science, 55*(3), 1458–1463.
145. Hofstadter, R. (1949). The detection of gamma-rays with thallium-activated sodium iodide crystals. *Physical Review, 75*(5), 796.
146. Hofstadter, R. (1948). Alkali halide scintillation counters. *Physical Review, 74*(1), 100–101.
147. Siciliano, E. R., et al. (2005). Comparison of PVT and NaI(Tl) scintillators for vehicle portal monitor applications. *Nuclear Instruments and Methods in Physics Research Section A: Accelerators, Spectrometers, Detectors and Associated Equipment, 550*(3), 647–674.
148. Dorenbos, P. (2019). (INVITED) The quest for high resolution γ-ray scintillators. *Optical Materials: X, 1*, 100021.
149. Nikl, M., et al. (2013). Development of LuAG-based scintillator crystals–A review. *Progress in Crystal Growth and Characterization of Materials, 59*(2), 47–72.
150. Martin, T., Koch, A., & Nikl, M. (2017). Scintillator materials for x-ray detectors and beam monitors. *MRS Bulletin, 42*(6), 451–457.
151. Dujardin, C., et al. (2018). Needs, trends, and advances in inorganic scintillators. *IEEE Transactions on Nuclear Science, 65*(8), 1977–1997.
152. Zhou, Y., et al. (2021). Metal halide perovskites for X-ray imaging scintillators and detectors. *ACS Energy Letters, 6*(2), 739–768.
153. Hajagos, T. J., et al. (2018). High-Z sensitized plastic scintillators: A review. *Advanced Materials, 30*(27), 1706956.
154. Korzhik, M., & Gektin, A. (2017). *Engineering of scintillation materials and radiation technologies*. Springer.

155. Stephen Derenzo, M. B., Weber, M., & Brennan, K. (2021, November 22). *Scintillation properties*. 2019 [cited 2021 March 1]. Available from: http://scintillator.lbl.gov/
156. Alekhin, M. S., et al. (2013). Improvement of LaBr3: 5% Ce scintillation properties by Li+, Na+, Mg2+, Ca2+, Sr2+, and Ba2+ co-doping. *Journal of Applied Physics, 113*(22), 224904.
157. Glodo, J., et al. (2012). Pulse shape discrimination with selected elpasolite crystals. *IEEE Transactions on Nuclear Science, 59*(5), 2328–2333.
158. Roush, M. L., Wilson, M. A., & Hornyak, W. F. (1964). Pulse shape discrimination. *Nuclear Instruments and Methods, 31*(1), 112–124.
159. Thermo scientific RadEye SPRD-GN personal radiation detector. (2017). Thermo Fisher Scientific.
160. Brubaker, E., Dibble, D., & Yang, P. (2011). Thermal neutron detection using alkali halide scintillators with 6Li and pulse shape discrimination. In *2011 IEEE nuclear science symposium conference record*.
161. Yang, K., Menge, P. R., & Ouspenski, V. (2017). Li co-doped NaI:Tl (NaIL)—A large volume neutron-gamma scintillator with exceptional pulse shape discrimination. *IEEE Transactions on Nuclear Science, 64*(8), 2406–2413.
162. Caifeng, L., et al. (2020). Particle discrimination and fast neutron response for a NaIL:Tl and a NaI:Tl scintillator detector. *Nuclear Instruments and Methods in Physics Research Section A: Accelerators, Spectrometers, Detectors and Associated Equipment, 978*, 164372.
163. Pla-Dalmau, A., Bross, A. D., & Mellott, K. L. (2001). Low-cost extruded plastic scintillator. *Nuclear Instruments and Methods in Physics Research Section A: Accelerators, Spectrometers, Detectors and Associated Equipment, 466*(3), 482–491.
164. Wieczorek, A. (2017). Development of novel plastic scintillators based on polyvinyltoluene for the hybrid J-PET/MR tomograph. *arXiv preprint arXiv:1710.08136*.
165. Crystals, S.-G. (Ed.). (2018). *BC-400,BC-404,BC-408,BC-412,BC-416 premium plastic scintillators*.
166. Rose, P. B., et al. (2020). Onset of fogging and degradation in polyvinyl toluene-based scintillators. *IEEE Transactions on Nuclear Science, 67*(7), 1765–1771.
167. Lance, M. J., et al. (2020). Nature of moisture-induced fogging defects in scintillator plastic. *Nuclear Instruments and Methods in Physics Research Section A: Accelerators, Spectrometers, Detectors and Associated Equipment, 954*, 161806.
168. Schlesinger, T. E., et al. (2001). Cadmium zinc telluride and its use as a nuclear radiation detector material. *Materials Science and Engineering: R: Reports, 32*(4), 103–189.
169. Ortec, G. (2009).*Series coaxial HPGe detector product configuration guide*. AM Technology (Ed.).
170. McGregor, D. S., & Hermon, H. (1997). Room-temperature compound semiconductor radiation detectors. *Nuclear Instruments and Methods in Physics Research Section A: Accelerators, Spectrometers, Detectors and Associated Equipment, 395*, 101.
171. Luke, P. N., & Amman, M. (2007). Room-temperature replacement for Ge detectors – Are we there yet? *IEEE Transactions on Nuclear Science, 54*(4), 834–842.
172. Sellin, P. J., & Vaitkus, J. (2006). New materials for radiation hard semiconductor detectors. *Nuclear Instruments and Methods in Physics Research Section A: Accelerators, Spectrometers, Detectors and Associated Equipment, 557*(2), 479–489.
173. Awadalla, S. (2015). *Solid-state radiation detectors: Technology and applications*. CRC Press.
174. Iniewski, K. (2010). *Semiconductor radiation detection systems*. CRC Press.
175. Butler, J., Lingren, C., & Doty, F. (1992). Cd1−xZnxTe gamma ray detectors. *IEEE Transactions on Nuclear Science, 39*(4), 605–609.
176. Del Sordo, S., et al. (2009). Progress in the development of CdTe and CdZnTe semiconductor radiation detectors for astrophysical and medical applications. *Sensors, 9*(5), 3491–3526.
177. Zhang, Q., et al. (2013). Progress in the development of CdZnTe unipolar detectors for different anode geometries and data corrections. *Sensors, 13*(2), 2447–2474.

178. Bolotnikov, A. E., et al. (2016). Use of high-granularity CdZnTe pixelated detectors to correct response non-uniformities caused by defects in crystals. *Nuclear Instruments and Methods in Physics Research Section A: Accelerators, Spectrometers, Detectors and Associated Equipment, 805*, 41–54.
179. Streicher, M., et al. (2014). A portable 2 × 2 digital 3D CZT imaging spectrometer system. In *2014 IEEE nuclear science symposium and medical imaging conference (NSS/MIC).*
180. Hitomi, K., et al. (2009). Polarization phenomena in TlBr detectors. *IEEE Transactions on Nuclear Science, 56*(4), 1859–1862.
181. Hitomi, K., Shoji, T., & Niizeki, Y. (2008). A method for suppressing polarization phenomena in TlBr detectors. *Nuclear Instruments and Methods in Physics Research Section A: Accelerators, Spectrometers, Detectors and Associated Equipment, 585*(1–2), 102–104.
182. Kim, H., et al. (2011). Continued development of thallium bromide and related compounds for gamma-ray spectrometers. *Nuclear Instruments and Methods in Physics Research Section A: Accelerators, Spectrometers, Detectors and Associated Equipment, 629*(1), 192–196.
183. Hitomi, K., et al. (2013). TlBr capacitive Frisch grid detectors. *IEEE Transactions on Nuclear Science, 60*(2), 1156–1161.
184. Baciak, J. E., & He, Z. (2003). Comparison of 5 and 10 mm thick HgI2 pixelated γ-ray spectrometers. *Nuclear Instruments and Methods in Physics Research Section A: Accelerators, Spectrometers, Detectors and Associated Equipment, 505*(1–2), 191–194.
185. Barrett, H. H., Eskin, J. D., & Barber, H. B. (1995). Charge transport in arrays of semiconductor gamma-ray detectors. *Physical Review Letters, 75*(1), 156–159.
186. McNeil, W. J., et al. (2004). Single-charge-carrier-type sensing with an insulated Frisch ring CdZnTe semiconductor radiation detector. *Applied Physics Letters, 84*(11), 1988–1990.
187. Wei, H., & Huang, J. (2019). Halide lead perovskites for ionizing radiation detection. *Nature Communications, 10*(1), 1–12.
188. Li, F., Yang, T., & Zheng, R. (2022). Radiation detection technologies enabled by halide perovskite single crystals. In *Advanced materials for radiation detection* (pp. 97–118). Springer.
189. Basiricò, L., Ciavatti, A., & Fraboni, B. (2021). Solution-grown organic and perovskite X-Ray detectors: A new paradigm for the direct detection of ionizing radiation. *Advanced Materials Technologies, 6*(1), 2000475.
190. Moseley, O. D., Doherty, T. A., Parmee, R., Anaya, M., & Stranks, S. D. (2021). Halide perovskites scintillators: Unique promise and current limitations. *Journal of Materials Chemistry C, 9*(35), 11588–11604.
191. Jung, M., et al. (2019). Perovskite precursor solution chemistry: From fundamentals to photovoltaic applications. *Chemical Society Reviews, 48*(7), 2011–2038.
192. Liu, F., et al. (2022). Recent progress in halide perovskite radiation detectors for gamma-ray spectroscopy. *ACS Energy Letters, 7*(3), 1066–1085.
193. Xu, Q., et al. (2020). A solution-processed zero-dimensional all-inorganic perovskite scintillator for high resolution gamma-ray spectroscopy detection. *Nanoscale, 12*(17), 9727–9732.
194. Kawano, N., et al. (2017). Scintillating organic–inorganic layered perovskite-type compounds and the gamma-ray detection capabilities. *Scientific Reports, 7*(1), 1–8.
195. Xu, Q., et al. (2019). Bulk organic–inorganic methylammonium lead halide perovskite single crystals for indirect gamma ray detection. *ACS Applied Materials & Interfaces, 11*(50), 47485–47490.
196. He, Y., et al. (2021). CsPbBr3 perovskite detectors with 1.4% energy resolution for high-energy γ-rays. *Nature Photonics, 15*(1), 36–42.

Metascintillators for Ultra-Fast Gamma Detectors

Georgios Konstantinou

1 Introduction

1.1 Time-of-Flight

While the demand for positron emission tomography (PET) examinations is increasing [1], the techno-economical, engineering and physical limitations of the process are restricting the offer of new devices. For this reason, PET instrumentation and image reconstruction developments are very active fields in the last years, offering new solutions in both hardware and software. These have resulted in significant improvements in system effective sensitivity [2, 3]. On a clinical level, improved effective sensitivity is translated to shorter examination time, lower radiotracer dose, and general boost of the image quality as measured through the signal-to-noise ratio (SNR).

Improving the timing of the detectors, for instance by developing gamma detectors based on faster scintillators, increases the effective sensitivity [4]. This is due to the possibility of adding time-of-flight (TOF) information on each event characterization. TOF corresponds to the time photons need from the electron-positron annihilation event until they reach the detector. TOF adds longitudinal information to the traditional line of response (LOR), allowing more precise localization of the spatial origin of the coincidence gamma pair. In particular, the time difference (Δt) between the two recorded timestamps of a coincidence pair corresponds to a Δx distance according to Eq. (1) [5]:

G. Konstantinou (✉)
CTO Multiwave Metacrystal S.A., Geneva, Switzerland

International Visiting Researcher, Instituto de Instrumentación para Imagen Molecular (I3M), Centro Mixto CSIC—Universitat Politècnica de València, Valencia, Spain
e-mail: georgios@metacrystal.ch

© The Author(s), under exclusive license to Springer Nature Switzerland AG 2023

J. Du, K. (K.) Iniewski (eds.), *Gamma Ray Imaging*,
https://doi.org/10.1007/978-3-031-30666-2_10

$$\Delta t = \frac{2\Delta x}{c} \tag{1}$$

where c is the speed of light in vacuum. Having access to TOF information reduces the effective number of resolution elements, thus improving the statistical properties of the PET image and leading to a better SNR for the same amount of gamma captures and acquisition time, as quantified in Eq. (2):

$$\frac{SNR_{TOF}}{SNR_{PET}} = \sqrt{\frac{D}{\Delta x}} = \sqrt{\frac{2D}{c\Delta t}} \tag{2}$$

where D is the diameter of the object to be imaged. Coincidence timing resolution (CTR) in the range of 200 ps FWHM, the current state of the art for commercial designs set by the Siemens Biograph Vision [6], leads to 3 cm position uncertainty in the longitudinal direction. In this case, in a human brain with 20 cm diameter, the TOF SNR improvement is close to a factor 2.5. A CTR of 10 ps leads to 1.5 mm TOF information, corresponding to an improvement of 11.5. This spatial TOF resolution approaches the physical limit of positron range [7] and is similar to the standard voxel dimensions of existing scanners. This might allow for virtually reconstruction-less acquisitions and a quantum leap in effective sensitivity [8], leading to an important reduction of radiotracer dose and examination duration. With such coincidence timing and corresponding sensitivity improvement, PET technology gains an unprecedented advantage in the fields of molecular imaging and theranostics [9].

1.2 PET Detectors

The standard gamma detector block in a PET scanner includes some conversions to bring the information of gamma detection to a digital format. The first conversion is based on the physical process of scintillation. This is the characteristic property of particular materials able of capturing an incoming high energy gamma-ray and release part of its energy in a shower of lower energy optical photons. These scintillation photons are consequently detected by photosensors such as silicon photomultipliers (SiPMs), capable of producing a measurable electric signal. This signal is then digitized, allowing the registration of the main characteristics of the optical shower, such as the time of arrival and number of collected optical photons.

In sum, the timing resolution of the detector corresponds to the certainty on the value of a measured timestamp and is calculated through the statistical characteristics of a significant population of gamma detections. It is a combination of the timing resolutions of all the aforementioned conversions. For TOF to be included in these detectors, all conversions have to be made in a time-critical manner. Today, very fast SiPMs [10] can be read out by sub-10 ps time-to-digital converters (TDCs) [11]. These advances have a high technological readiness level, meaning that they can soon be deployable in an industrial scale. As such, the bottleneck in the quest for ultra-fast gamma detectors is the physical process of scintillation, which depends significantly on the type of scintillator.

1.3 Scintillation

Scintillation is the process in which a material converts the energy of an incident particle (UV, X-ray or γ-ray) into a number of photons of much lower energy, in the visible or near-visible range, which can be easily detected with current photomultipliers, photodiodes or avalanche photodiodes [12]. Two main categories of such materials exist, namely organic and inorganic, with distinct conversion mechanisms. Nevertheless, any material containing luminescent centers which are activated by the incoming ionization radiation is a scintillator. The time function of optical photon production through this multi-step process is accurately modeled through the bi-exponential model shown in Eq. (3), where E is the gamma energy, LY_{scint} the light yield and τ_{rise} and τ_{decay} correspond to rise and decay times, respectively [13].

$$f_{scint}(t) = \frac{E \times LY_{scint}}{\tau_{decay} - \tau_{rise}} \left(e^{\frac{-t}{\tau_{decay}}} - e^{\frac{-t}{\tau_{rise}}} \right) \tag{3}$$

1.4 Scintillators

Due to its advantageous optical photon generation kinetics, lutetium-ytrium oxide (LYSO) has replaced bismuth germanium oxide (BGO) as the industry standard since its creation. They are both inorganic scintillators, LYSO and BGO. Due to their high effective atomic number (high-Z) and density, which results in a high photoelectric cross-section and stopping power for the 511 keV annihilation photons, they are well suited for PET. In the bi-exponential model of Eq. (3), LYSO exhibits a very rapid response with a rising exponential of 74 ps and a decay one of around 40 ns, as well as a robust light production of about 32,000 per MeV and no self-absorption for the emission wavelengths. All of these elements enhance the LYSO-based detectors' timing capabilities [14]. There are still many scintillation materials available that could be used for TOF PET [8]. Barium Fluoride (BaF_2), another compound in the inorganic realm, has the ability to emit light using a variety of scintillation mechanisms, which results in a more complicated photon emission equation [15]. Through cross-luminescence, its quick decay component, which only lasts 600–800 ps, it generates around 1800 optical photons per MeV in the VUV range. Although this material has longer attenuation length than LYSO, it can provide better timing. It should be noted that scintillator costs are influenced by the expenses of their commercial distribution and manufacturing processes. As a result, LYSO is substantially more expensive as a raw material than other scintillators like BGO and BaF_2.

As mentioned earlier, scintillators include more materials, even beyond the realm of inorganic crystals. In particular, plastic scintillators, produced commercially by various companies in patented designs provide fast kinetics with sufficient light yield [16]. As an example, Eljen's EJ232 produces 8400 optical photons with a 350 ps rise and 1.4 ns decay times, respectively. Such components are not more broadly used for the TOF PET application due to their low density and corresponding low stopping power. In spite of that, a whole-body PET design exclusively based on plastic scintillators has been developed [17]. This design compensates its low detection efficiency with an accurate TOF resolution of 266 ps, and a very long axial field-of-view (FoV). Plastic scintillators are generally easier to produce and machine, coming thus with a reduced cost.

Other materials that are hopeful for TOF applications in PET correspond to compounds that have a particular structure on the nano-scale. Such are quantum dots and nano-platelets such as Cadmium Selenide (CdSe). Similarly, modern developments of perovskite scintillators could lead to improved scintillating characteristics, even though these compounds are still in the research phase and often require particular conditions such as very low temperature [18].

A straight-forward way to improve stopping power of a detector exists and corresponds to using thicker scintillators. However, in that case, there are more possible paths for a photon to travel before reaching the photon detector and important depth-of-interaction dependency of timing, leading to increased time variance of detection [19]. This uncertainty is detrimental for fast timing on picosecond scale. This is clearly demonstrated by the estimation of the statistical lower bound, calculated through the Cramér-Rao method [20]. This statistical measure corresponds to the number of photons that have to be detected within a given time in order to provide enough information for specifying the time of a scintillation event. In short, the trade-off between detector material, elementary detector size and timing resolution seems to be unbreakable with conventional scintillator solutions. In this chapter, we introduce the novel concept of metascintillators, which intends to address this trade-off.

1.5 Definition of Metascintillators

"Meta" is an ancient Greek word that entered scientific nomenclature through Latin as "beyond", "with" or "after" [21]. With this in mind, metamaterials as a term was introduced in material science by the physicist Victor Veselago in 1968 for the particular application of materials with negative refraction index [22]. Since then, this definition has been broadened to include any synthetic composite material that has a structure that causes it to have characteristics that are unusual for natural materials [23]. In the context of scintillators, the composite topologies of scintillating and light-guiding materials arranged to produce a synergistic effect at some stage of the scintillation process, from gamma absorption to light detection, and combining thus the advantageous physical characteristics of their constituent parts, could be thus referred to as meta-scintillators [24]. The work being done in this regard aims to provide the groundwork for future advancements that could eventually result in TOF PET with adequate gamma detection efficiency and a timing resolution of 10 ps in the next years [25].

Photoelectric absorption and Compton scattering are the two primary electromagnetic interaction mechanisms that are important for PET instrumentation. A recoil electron is created at the start of the gamma interaction in both scenarios. Along its entire route, the recoil electron interacts with the scintillator, losing energy through a dE/dx process that creates electrons and holes; these can either directly excite the luminescent centers or join together to form so-called excitons. The excitons can be confined by luminescent centers or impurities or can combine directly in a radiative manner. The intrinsic properties of the scintillating medium, particularly its density, determine the recoil electron's travel range. The recoil electron range for dense inorganic scintillators is up to around 400 μm.

Having various scintillators share the energy of a gamma interaction is one technique to combine their advantageous traits. In theory, there is no mechanism that would constrain the recoil electron to a specific medium. This means that various scintillating materials can share the optical photon production associated with a single interaction annihilation gamma, if they are placed close together. Therefore, it is conceivable to build a geometrical topology that brings fast optical photon emitters, providing significant initial photon density, close enough to use a high-Z material and benefit from its stopping power. Precisely this combination of a high-Z host and a rapid emitter design forms the first generation of composite heterostructures. The materials are sliced into laminas with thicknesses below the recoil electron range and are positioned in geometrically periodic alternating positions (Fig. 1).

Fig. 1 First-generation metascintillator conceptual design, demonstrating the process of energy being leaked into the fast material for gamma interactions taking place in the dense, high-Z material through the simulated range of the recoil electron

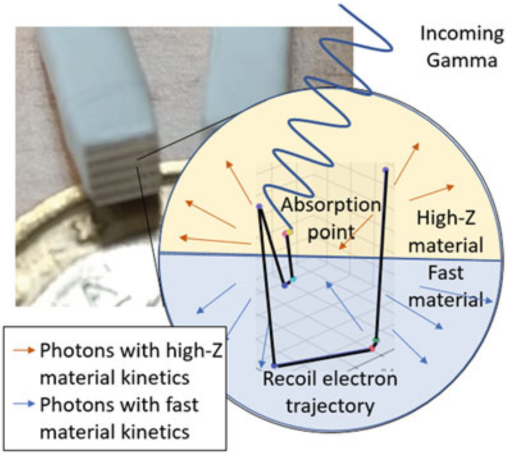
Incoming Gamma
Absorption point
High-Z material
Fast material
Recoil electron trajectory
Photons with high-Z material kinetics
Photons with fast material kinetics

It has to be noted that the topology of a Shashlik calorimeter [26] bears some similarity to the metascintillators, to such extent that it can be considered a predecessor. Those are structures where a heavy non-scintillating material such as lead, is placed in close proximity to plastic scintillators, taking advantage of the same synergistic mechanism of recoil electron gradual energy loss. However, the significant difference is that by using two scintillating materials, instead of a heavy non scintillating one, the energy resolution, a significant aspect in the PET application, can potentially remain as good as the worse of the two materials.

2 Metascintillators: Review of State of the Art

2.1 First Generation Heterostructure Metascintillators

Proof-of-concept findings for this straightforward strategy have been tested and published in [27]. In this publication, tests with both LYSO and BGO for their high-Z and the BC-422 plastic (Saint Gobain, France) as fast emitter are presented. Timing features of this plastic are comparable to those of the EJ232. Eight pairs of 3 × 3 × 0.25 mm^3 BC-422 and 3 × 3 × 0.2 mm^3 dense hosts were combined to create a so-called metapixel, which had a final size of 3 × 3 × 3.6 mm^3 (Fig. 2, left). The majority of interactions had some energy leaking out of the pixel, as would be expected for a pixel of such a small size and with such a high proportion of light material (Fig. 2, center). The remaining interactions, however, showed a specific proportion of events that were shared by the two materials, offering the first proof-of-concept for metascintillators.

Given that the light yields for BGO and BC-422 are comparable, measuring the pulse amplitude and the integral of the first 200 ps allows one to determine the degree of energy sharing. This is shown in Fig. 2, right, as a continuous form of

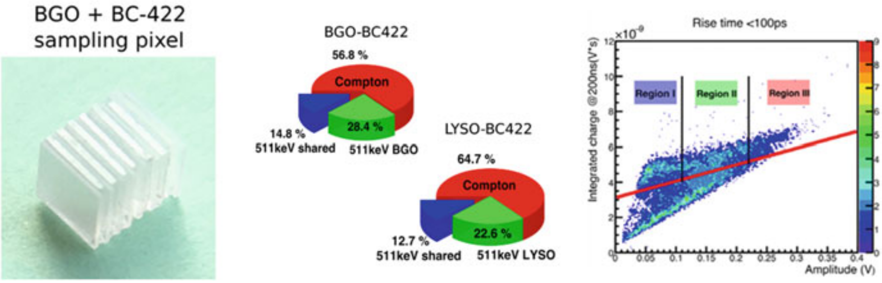

Fig. 2 (Left) Picture of a BGO-BC422 metascintillator pixel; (center) BGO-BC422 and LYSO-BC422 interaction percentages; and (right) event distribution in a plot of 200 ns integral over maximum pulse amplitude. For events with faster rise time, occurring due to event energy sharing. (Figures taken from Ref. [24])

energy sharing that ranges from interactions that are exclusively BGO-based, which make up the majority, to a lesser number of interactions that mostly involve the plastic scintillator. The type of sharing is crucial since it is important to understand which scintillation process generated the photons in order to accurately detect the timing of such a meta-structure. By doing so, the timing reconstruction algorithm will be able to more precisely predict the scintillation event beginning, thereby enhancing the CTR, in addition to taking into account information from other sources, such as time-walk [28].

Such knowledge is used in [27] to compute the timing of various locations' energy sharing. The detector time resolution of BGO events is 120 ps FWHM, whereas the resolution of events with a higher proportion of the fast emitter is as low as 40 ps FWHM. The first instance of energy sharing was demonstrated via this proof-of-concept, nonetheless with a very small pixel. The final specifications of metascintillators can be greatly influenced by pixel dimensions, material combinations, slab surface treatment, and light collection.

The first generation of metascintillators is being studied extensively with the purpose of developing commercially deployable solutions, with primary application in TOF PET [29–31]. In these works, the main concern is using crystals of sizes that ensure sufficient stopping power to be complemented by the added TOF sensitivity from including a fast scintillator. While BGO and BC422 or EJ232 are the main target at this stage, as the commercially relevant purpose here is to achieve CTR values similar to LYSO, other combinations are also tried. In particular, BaF_2 is considered as a potential fast emitter with some stopping power that doesn't compromise the general sensitivity of the detector. As described in [30], this can be achieved through different orientations of the scintillating components relative to the impinging gammas, different ratio of slow and fast materials and different detector lengths. In [31], with the application of timewalk correction, a combination of BGO with EJ232 at a ratio of 3:1 achieves 204 ps CTR, with an ultrafast subset of ~10% of the fastest events below 100 ps, while the combination of BGO with BaF_2 at a ratio of 1:1 achieves 241 ps CTR, with the ultrafast subset of ~10% of the fastest events at 108 ps.

The addition of various novel elements, including nanocrystals, can enhance this scheme even further. For this reason, we consider the first generation of metascintillators to be heralded with these works, corresponding to scintillating heterostructures that are composed of materials that are also used standalone in commonly deployed detectors.

2.2 Nanocrystal Based Metascintillators

To improve their timing qualities, metascintillators can use any scintillating method. Because of quantum confinement, nanocrystals in particular demonstrate exceptionally fast scintillation characteristics if their size is less than the exciton's Bohr radius (10 nm). When made as nanoplatelets, which confine the excitons to one direction

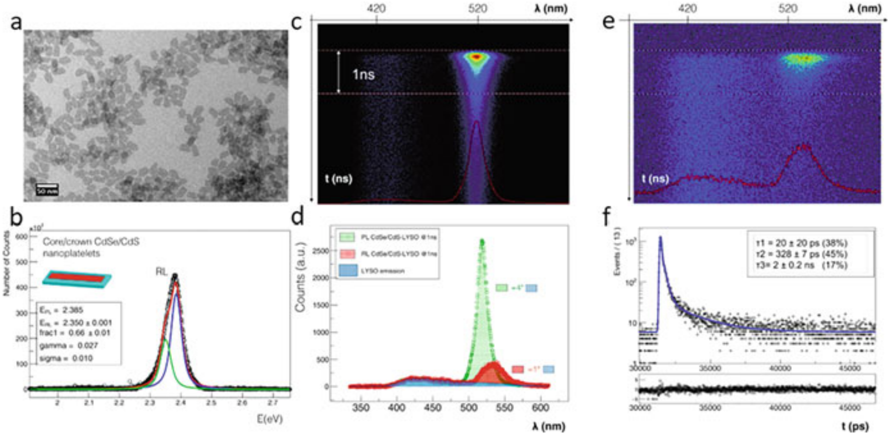

Fig. 3 (**a**) Microscope image of CdSe nanoplatelets in polysterene; (**b**) emitted photon wavelength distribution for compounds with different crown densities. (**c**) Photoluminescence and (**e**) radioluminescence time-resolved spectra of a CdSe/CdS drop-casted film deposited on a LYSO:Ce substrate as readout by a Hamamatsu streak camera; (**d**) comparison of photoluminescence (green), radioluminescence (red) and LYSO emission (blue) wavelengths, integrated over the first nanosecond; and (**f**) time-resolved CdSe/CdS core-crown radioluminescence integrated from 200–800 nm as measured with a hybrid PMT in time correlated single photon counting mode. (Figures taken from Ref. [26])

only and enable even quicker multi-exciton recombinations, CdSe nanocrystals stand out for their unmatched timing performance and other benefits [32]. They were one of the earliest direct band-gap semiconductor nanocrystals to be investigated for use in ultrafast timing detector applications. Potential candidates for a new generation of metascintillators, its red-shifted radioluminescence signal exhibits fast (20 ps) photon production and a sub-nanosecond pulse duration. However, due to inherent flaws such as strong self-absorption and the requirement of organic ligands for surface passivation and control of the luminescence and spatial distribution of nanoplatelets, their implementation as radiation detectors is extremely problematic, especially when considered for industrial application.

In a metascintillator configuration, CdSe nanoplatelets have been examined [27], with a high-Z material (LYSO) serving as the dense host and supplying the high detection efficiency, as well light guiding. Fast photons are then produced by the excitons after they pass through the nanoplatelets. Specifically, drop-casted films made of CdSe/CdS core/crown nanoplatelets (Fig. 3a) embedded in polystyrene as a host matrix were investigated. In the first instance, an X-ray induced radioluminescence experiment used a streak camera (Hamamatsu Photonics, Japan) to evaluate the combination of produced light and its timing features (see Fig. 3b). The function of this method is that a sample's light output is read out within a range of wavelengths with picosecond sampling, after being exposed to an X-ray. This gives researchers a previously unattainable grasp of the physical process and light production. The metastructure's spectrum time-resolved characterization shows how CdSe/CdS light is gathered in the first few hundred picoseconds following the start of the event. The timing properties of core/crown nanoplatelets drop-cast on LYSO are quite desirable, and this correlates to an incredibly quick, practically prompt, form of emission.

Due to several factors, such as among others CdSe casing, concentration, and arrangement within the metascintillator, optimal CdSe application in a metacrystal heterostructure still has to be thoroughly explored. However, they are a strong candidate for the next generation of metascintillator-based detectors due to the powerful and ultra-fast pulse at a wavelength within the parameters of most current SiPMs. In this context, nano-elements such as these require at least a second optical or scintillating material to function. In the same time, they are not yet ready for industrial application. As such, these compounds do not belong to the first generation described before, but introduce a second generation of metascintillators that is currently being researched, which corresponds to metascintillator structures with materials developed exclusively for heterostructure application and in consideration of its characteristics.

2.3 Metamaterial Aspect of Metascintillators

The unique property of electromagnetic metamaterials is often obtained by the constructive and destructive interference of incoming light after being scattered by a large number of periodic structurations. The wave model of light as well as the Maxwell equations, as opposed to the particle model of photons, provide a more accurate representation of interactions as constituents' sizes approach dimensions of the same order of magnitude as the light wavelength. Unusual characteristics can be found under these circumstances, as quantum effects play a prominent role; these include perfect anti-reflection at all angles, control over propagation direction and negative refractive index [33].

These optical phenomena could be able to address a number of inherent issues in scintillation sub-optimal light generation, propagation, and extraction. The degradation of time resolution on light detection is mostly caused by the isotropic nature of scintillation light and the high refractive index of the majority of scintillators. Effective light collection increases the statistical likelihood that fast photons will be detected, while light directionality lowers the variance of optical routes, improving single-detector temporal resolution even further. Such procedures lie under the purview of nano-photonics and nano-manufacturing, hence enhancing the multidisciplinary aspect of metascintillator research. Developed photonic crystal slabs are thin layers of dielectric that have had their permittivity or permeability periodically changed in order to produce desired light scattering effects.

Prior research put a lot of emphasis on increasing light extraction efficiency [34]. Total internal reflection (TIR), which is the primary optical transmission mechanism, is made possible by the high refractive index of crystal scintillators in their emission spectrum. As a result, there is a low likelihood that photons will

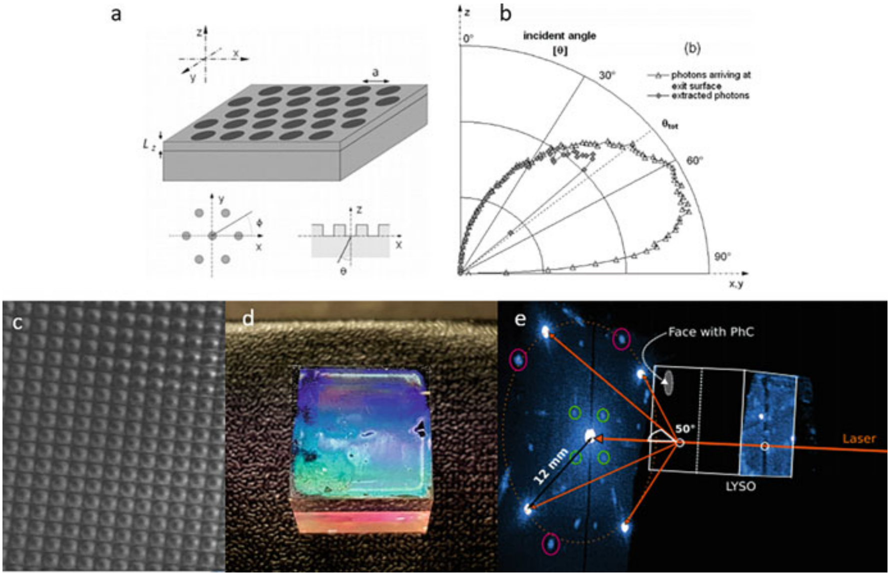

Fig. 4 Initial photonic crystal slab approaches: precise shape and arrangement of the nanostructured slab (**a**), increases the photon extraction efficiency beyond geometrical expectations (**b**). (Figures taken from Ref. [28]). (**c**) microscopic image of the patterned polymer on the read out face of a sample; and (**d**) patterned sample with pattern facing up, showing diffraction colors. (Figure taken from Ref. [30]); and (**e**) experiment performed on the crystal depicted in (**d**): A green laser is used to simulate light, traveling inside the crystal and interacting with the PhC slab from the inside. Diffraction orders are generated at an angle dependent on the periodicity of the pattern. The image is shown in false color to increase contrast. (Figure taken from Ref. [29])

enter the extraction side of the scintillator, where a photosensor is positioned, at an angle that permits direct extraction, and a sizeable portion of photons—up to 90% in the case of BGO—will be reflected back. The bulk of unextracted photons continue to move across the optical medium, which impairs timing resolution and increases the likelihood that they will be absorbed. This work showed that it is possible to adjust the pattern and enhance the light extraction by inserting one layer of photonic crystal slab between the scintillation crystal and the photon detector (Fig. 8). Simulations with a straightforward periodic pattern revealed that photons would be extracted directly for a substantially wider range of incoming angles. The event signal-to-noise ratio, energy resolution, and single-detector timing resolution may all be enhanced by avoiding TIR.

This method was further researched using a laser-based experiment [35], in which a green laser is directed onto the extraction surface of a LYSO crystal that has a photonic slab laid on top of it (Fig. 4). This experiment simulates scintillation light and shows that depending on the properties of the photonic crystal slab pattern, diffraction orders are formed at higher angles than permitted by the Snell law. The development and testing of a set of scintillators that had a photonic crystal slab added to their read-out side is shown in the same figure [36]. A single detector was used in the initial experiment, which used Cs-137's 662 keV gamma radiation. Most importantly, coincidence studies were conducted using a dedicated setup. This experiment provided a proof-of-concept for more study and development in this area by showing a considerable improvement in both CTR (up to 57%) and light yield (up to 144%) (Fig. 4).

In order to improve the effectiveness of the scintillator detector, the metastructure can therefore incorporate layers that shift the direction of light in a non-classical manner, introducing a metamaterial component to the notion of metascintillators. Nevertheless, energy sharing in metascintillators occurs from a different process than those effecting light propagation in metamaterials, hence the concept is not based on metamaterial behavior. Given the technology readiness level of such approaches, as well as the fact that these as well require functioning in tandem with some scintillating material, we consider them to also belong to the second generation of metascintillators.

2.4 Metascintillator Signal Analysis

One of the main concerns in the discussion on metascintillator applicability in commercial TOF-PET is the complication added by the addition of at least a second scintillating mechanism in the stack, with the addition of another stochasticity per event in the form of energy sharing. Indeed, Eq. (3), corresponding to the scintillation photon production time-series upon gamma absorption is now presented as the system (4), where indices fe correspond to the fast emitter, hz to the high-Z material and E_{abs} is the absorbed energy of interaction [31]:

$$f_{metascint}(t) = \frac{E_{fe} \times LY_{fe}}{\tau_{fed} - \tau_{fer}} \left(e^{\frac{-t}{\tau_{fed}}} - e^{\frac{-t}{\tau_{fer}}} \right) + \frac{E_{hz} \times LY_{hz}}{\tau_{hzd} - \tau_{hzr}} \left(e^{\frac{-t}{\tau_{hzd}}} - e^{\frac{-t}{\tau_{hzr}}} \right) \tag{4a}$$

$$E_{fe} + E_{hz} = E_{abs} \tag{4b}$$

The amount of produced photons, or effective light yield ($LY_{effective}$), is dependent on the ratio between E_{fe} and E_{hz}, according to Eq. (5):

$$LY_{effective} = \frac{E_{hz} \times LY_{hz} + E_{fe} \times LY_{fe}}{E_{hz} + E_{fe}} = \frac{LY_{hz} + \frac{E_{fe}}{E_{hz}} \times LY_{fe}}{1 + \frac{E_{fe}}{E_{hz}}} \tag{5}$$

This means that the standard approach of integrating the pulse over an integral window significantly larger than the decay coefficient, which in the single scintillator readout provides a surrogate for the energy of interaction through the light yield,

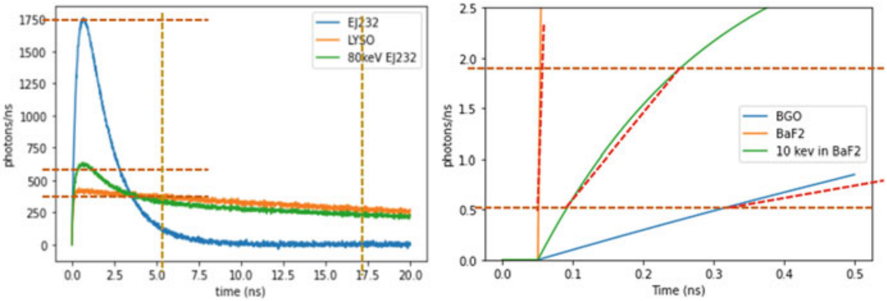

Fig. 5 (Left) The simulation of a LYSO/EJ232 metascintillator pulse, demonstrating the variability caused by the extent of energy sharing, of different features such as maximum value (brown dashed line) and integral with different integration windows (yellow dashed line); and (right) zooming in the first half nanosecond, we observe similar variability for the rising slope of a BGO/BaF_2 metascintillator, again as a reference to the energy sharing

in metascintillators is not sufficient. Instead, to calculate the absorbed energy, two energy surrogates are required. If we consider the pulse in Fig. 5, left, we see that an energy surrogate does not need be the standard integral of the full pulse; in contrast, any two measurements of any integration window integral, maximum voltage, rising slope or other pulse features can be used. With any two measurements, a system including the contributions of the independent scintillators can be solved, leading to calculation of energy of interaction and energy sharing. The choice of the best features depends on the metascintillator materials and their photon-emitting characteristics, but also on the specificities of the read-out.

With the precise determination of energy sharing and interaction energy, it is possible to reconstruct a more accurate interaction energy spectrum [36]. In this example, a BGO-BaF_2 metapixel with original energy resolution at 511 keV around 28%, uses energy sharing information to correct it down to 22%, close to the energy resolution of BGO (18%) and BaF_2 (21%), in the same electronics. If the light yield of the materials is too different, such as for instance in the case of LYSO (~35,000 photons per MeV) and EJ232 (8400 photons per MeV), this process is more complicated and prone to error. In contrast, if the light yield of the materials is very close, no energy correction is necessary.

Another application of energy sharing is related to optimizing the estimation of gamma ray arrival, which can then significantly improve the detector's CTR. Given that the events with more photons released through the fast emitter mechanism have a prompter response (Fig. 5, right), the addition of a time-walk correction, which can improve the time response of metascintillators most significantly can only be performed with precise understanding of energy sharing [31]. For the BGO-EJ232 metascintillator presented here, the original measurement of 280.1 ps is improved down to 204.7 ps. In this light, the data throughput can be expected to double, limiting the use of metascintillators for system level development. In reality, nevertheless, most modern ASIC-based readouts include at least two pulse energy surrogates [37, 38], while the approach of double window integration can be performed in a single channel. Regardless of system level developments, the main notion of energy sharing is one that is relevant in any metascintillator context, in existing or future materials and designs.

3 Future Perspectives

3.1 Metascintillator System Level Application

The choice of materials for subsequent testing should be influenced by the dependence of metascintillator energy sharing on geometrical properties, as well as the light guiding capabilities of the respective materials. This process starts with the simulation [39] of the recoil electron trajectory, and the estimation of the energy sharing distribution for different materials and dimensions [40]. This task is commonly performed with the use of GEANT4 or the relevant GATE software for Monte Carlo simulations [41]. For slab thicknesses ranging from 50 to 300 μm, two alternative arrangements of slabs aligned in parallel or perpendicular to the gamma trajectory have been taken into consideration (Fig. 6a). Compared to the energy deposited in the fast emitter material, this likelihood follows a distribution with a positively skewed normal character, as depicted in Fig. 6b. Although the basic form of sharing is the same, variations in material and geometry somewhat change this shape's average, deviation and skew.

The effect of having a metascintillator with reduced stopping power due to the fast material is estimated through Monte Carlo simulations of a given TOF PET architecture, such as for instance a brain PET (Fig. 6c) [42]. To compensate for the reduced stopping power of metascintillator, a longer crystal is used, to match the sensitivity of state of the art scanners (Fig. 6d). The simulation considers a metascintillator array composed of pixels; such arrays are already constructed industrially (Fig. 6e).

A potentially disruptive metascintillator architecture is the semi-monolithic metascintillator approach. This approach intends to convey the advantages of semi-monolithic readouts, where a crystal is read-out by several photodetectors allowing precise estimation of the depth-of-interaction [43], with the supreme timing of pixelated designs. As demonstrated in Fig. 6f, a design where the fast emitter is matched 1-to-1 to distinct photomultipliers, while the high-Z material is arranged in the semi-monolithic manner, simplifies the construction of metascintillators when compared to pixelated designs. On top of that, simulation has demonstrated that there is no effect to the timing resolution, while knowledge of the DOI allows improvement of the timing characteristics of this design [44]. The interplay between CTR, DOI and energy sharing is estimated through an iterative process to improve all specifications of the detector. With the application of neural networks on raw data, the elemental detector of this stack is a $3 \times 3 \times 3$ mm^3 cube, allowing for

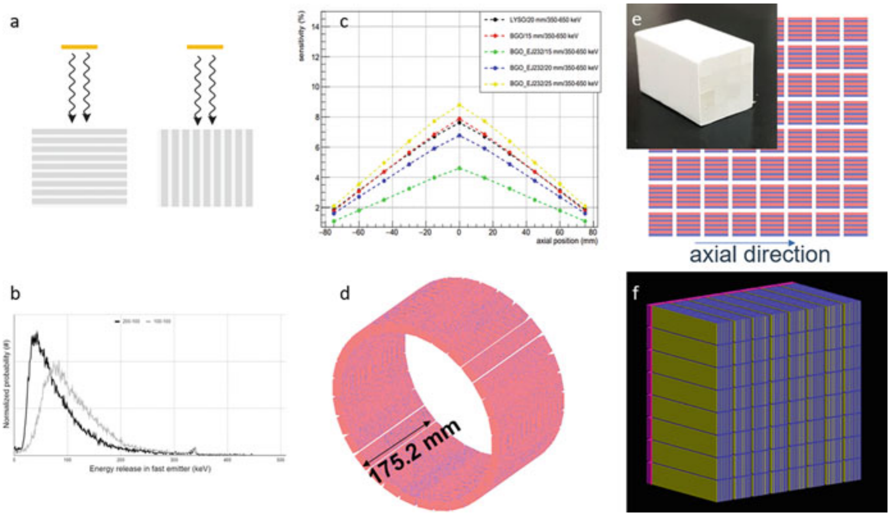

Fig. 6 (**a**) Possible orientations of metascintillator slabs compared to the direction of incoming gammas; (**b**) simulated energy sharing distribution for two LYSO/EJ232 geometrical scenarios, with 100/200 μm thicknesses(black line) and 100/100 μm (gray line); (**c**) sensitivity curve for different metascintillator and reference scenarios, for a brain PET design (**d**) furnished with metascintillator pixels (**e**); and (**f**) simulation model of a semi-monolithic metascintillator detector head. Notice how the high-Z material (blue) is distributed over 8 SiPM, in contrast to the fast emitter (yellow) which is matched to a single SiPM to retain pixel level timing. (Figure **a** taken from Ref. [40], **b** from Ref. [24], **c**–**e** from Ref. [42], and **f** from Ref. [43])

significant improvement of effective sensitivity, also through the reduction of voxel size in reconstruction.

3.2 *Cherenkov-Based Timing*

The method described above for evaluating scintillation-based detectors with variable timing resolution is applicable to all detector types where timing varies for each event. This is the case for detectors that characterize individual events in terms of timing based on the presence of Cherenkov photons. Cherenkov-based detectors produce photons at the picosecond scale following ionization [45], in contrast to metascintillators that use fast emitters for quicker photon production.

Depending on the material's refractive index, Cherenkov light emits primarily in the deep blue-VUV region of the spectrum. As the intensity of this emission is minimal, producing at most a few tens of photons, it is challenging to characterize its energy or position. Timing characterization is still conceivable, though. In fact, as a function of the quantity of photons detected, the short emission duration of

Cerenkov photons (approximately 10 ps) permits extremely accurate time resolution values for a portion of the recorded events.

There have already been suggestions for hybrid Cherenkov-Scintillation detectors [46]. Additionally, there are three ways in which Cherenkov detection relates to the metascintillators. Similar to metascintillators, the stochastic change of the quantity of created and detected Cerenkov photons produces a distribution of time resolution for the events recorded [47]. Furthermore, metascintillators themselves, made of different materials with different refractive indices, can be created to produce Cherenkov with specific properties, leading to improved temporal characterization. Last but not least, the close proximity of materials with different optical properties in the metascintillator case allows for improved Cherenkov extraction from scintillators such as the BGO, that are good producers of Cherenkov photons but suffer from internal absorption, through BaF_2 or organic scintillators [48].

3.3 New Materials

The highly fast scintillation kinetics of ZnO:Ga nanocrystals, with decay time components ranging from 40 to 350 ps, render them interesting for the metascintillator application. Various methods for integrating them in polystyrene host films have been explored. Hot pressing has been employed to create ZnO:Ga by combining the powder with polystyrene pellets and pressing the mixture at temperatures between 100 and 200 °C [49], leading to a loading factor of up to 10% weight in transparent films. The loading factor is important since hosts such as polystyrene and polyvinyl toluene are non-scintillating substances with very low stopping powers, in contrast to the nanocrystals themselves.

Halide perovskites stand out among a wide range of nanoscintillators for metascintillator integration because of their special characteristics [50]. When bromide vacancies in $CsPbBr_3$ are filled with methylammonium, for example, mixed organic-inorganic perovskites also offer intriguing perspectives in terms of luminescence characteristics and surface passivation [51]. This increases the materials' quantum yield, radiation hardness, and high temperature stability. Two approaches have been used for $CsPbBr_3$. Firstly, the $CsPbBr_3$ nanocrystals were added to a solution with polystyrene, after the polystyrene pellets had been dissolved in toluene [52]. By slowly evaporating toluene at room temperature, transparent films with weight loadings of 1%, 5%, and 10% have been produced. Another attempt corresponds to directly assessing the potential of perovskite nanocrystals as quick photon producers in metascintillators. In this context, layers of $CsPbBr_3$ nanocrystals were directly deposited on GAGG:Ce plates using two alternative spin-coating techniques (Fig. 7, left).

The confinement of electrons and holes in multiple quantum wells with GaN/InGaN heterostructures, where they can radiatively recombine with a very high quantum efficiency, is another way to generate prompt photons in nanostructured systems (Fig. 7, center and right). A paradigm shift for PET applications, these are

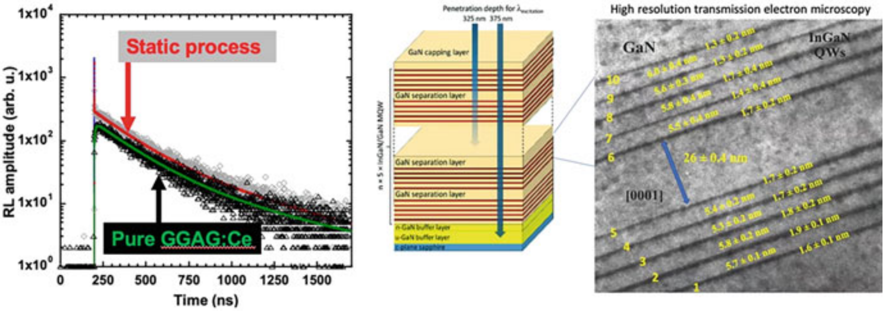

Fig. 7 (Left) Demonstration of the effect of adding a $CsPbBr_3$ layer on GGAG:Ce scintillator, as observed on the accumulation of pulses; notice the ultra-fast component at the beginning of the pulse, as well as the afterglow throughout the duration; (center) conceptual design and (right) high resolution microscopic image of a GaN/InGaN heterostructure. (Figures taken from Ref. [54])

measured to reach a light yield of 100,000 photons per MeV. Realizing a sufficient overall thickness for multiple quantum well systems is a significant technological problem. Up to 100 layers with a total thickness of 2 µm have been successfully deposited according to the state of the art on sapphire substrates [53].

These and more similar materials are developed and analyzed by several groups, as they can provide scintillating characteristics to improve detector timing resolution. Such can allow the second generation of metascintillators described before, to reach industrial applicability, with sufficient stopping power and an effective time resolution below 50 ps.

3.4 Light-Guiding with Photonic Crystal Slabs

The photonic crystal elements presented earlier correspond to designs intended to facilitate the extraction of photons to the photodetector. However, the vast capabilities of new designs in Photonic crystal slabs (PhC) can be applied to support streamlining the transport of light over the length of the scintillator [54]. As the character of scintillator light, with isotropic directionality, random phase and polarization and variable wavelength provides significant challenges to photonic crystal slab design, only initial efforts have been performed in this direction. Electromagnetic simulations demonstrate that a leaky mode approach can guide part of the produced scintillation light (Fig. 8), reducing in this way the optical path but also the optical modes of propagation within the crystal, leading to improved timing resolution.

What is even more interesting is designing PhC slabs made of scintillating material, such as nanoplatelets. In that case, the fast scintillator will be designed in such way that the light will be directly led towards extraction, providing capabilities of design such as inherent DOI encoding. A design of the sort would practically be

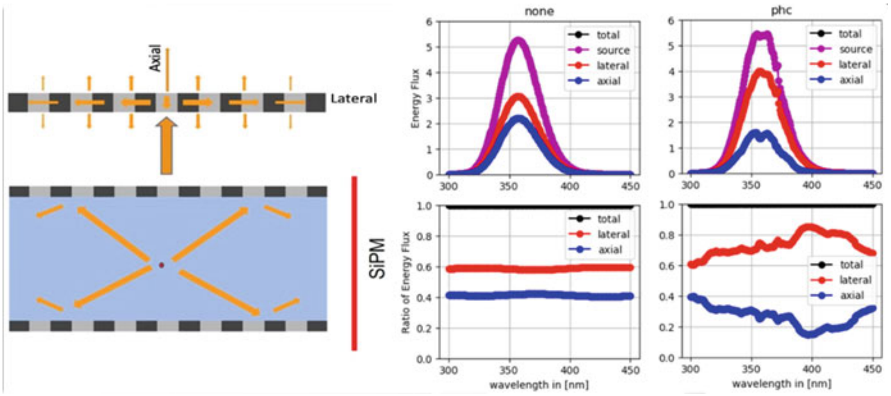

Fig. 8 (Left) Mechanism of leaky mode propagation on a designed photonic crystal slab, deposited on the surface of a LYSO crystal; and distribution of energy flux between a lateral and axial direction without (center) and (right) with a leaky mode favoring photonic crystal slab. (Images taken from Ref. [54])

a constructed opto-physical circuit with light wavelength or distribution-encoded information, in what will herald the third generation of metascintillators. Such characteristics, along with fast emission with photons confined in narrow optical paths around the PhC, will further improve the timing capabilities of such metascintillators with a potential within range of the target of 10 ps.

3.5 Other Future Developments

The application of machine learning and neural networks has shown recently significant results, interleaving timing and spatial information. The metascintillator signal has the increased complexity as well as including the stochastic quantity of energy sharing, another key factor affecting the timing resolution. Applying neural networks for improvements in energy resolution or custom time-walk corrections could further improve the timing, spatial and DOI behavior of metascintillator structures.

Another objective is to bring down the price of all of the aforementioned paradigms through concept popularization and cooperation with system-level PET and scintillator development firms. The field of metascintillators may also benefit from the use of cutting-edge materials and techniques, such as sub-surface laser engraving processing [55], which could enhance timeliness and lower costs.

The creation of a new set of PET image reconstruction techniques based on the accurate calculation of energy sharing and ensuing variable event timing is the ultimate goal of metascintillators. An initial strategy can simply classify events based on their energy content into timing groups and utilize those to establish an exact number of resolution elements, increasing the TOF related sensitivity in the process. The size of the organ or subject being studied may directly influence how the events are binned, extracting the most information possible from timing variations. Another intriguing idea is to use a quick collection of events to direct reconstruction using new mathematical techniques like compressed sensing [56] or sparse matrix analysis [57].

4 Conclusions

The quest for cutting-edge timing resolution in scintillation detectors is a multidisciplinary one that involves many different scientific and technological disciplines. Through integration of novel science and technology, metascintillators aim to break the technological deadlock caused by the trade-off between optical photon production and detection efficiency. The metascintillator technique can be the cornerstone of next designs that could potentially achieve the 10 ps CTR that the 10 ps challenge [58] is aiming for, by using innovative materials, architectures, and read-out configurations. In order to improve scientific output and afterwards offer technology solutions to the critically significant medical concerns connected to PET applicability, the work is conducted in an atmosphere of openness and cooperation for the advancement of research and public health.

While there seems to be an added element of complexity in merging two different materials in a metascintillator heterostructure, the added effect of a synergistic gain can lead to significant improvements in timing, without deterioration of energy resolution and sensitivity of the detector. BGO-based 1st generation metascintillators have managed to replicate the behavior of state of the art LYSO crystals, with a significantly reduced cost of materials. Better understanding of the nature of energy sharing, and manipulation of the geometrical characteristics of metascintillators can lead to further improvements without added cost in material or complexity. Simulation is the most important tool in this quest, and it is possible that novel architectures, extending from the existing slab-sandwich geometry, could lead to better statistical characteristics of energy sharing.

Further to the developed and tested 1st generation, different groups work for the research and development of 2nd generation metascintillators, implementing novel ultra-fast materials in heterostructures, or including photonic elements for better extraction and transportation of photons to the photodetector. A combination of the aforementioned can lead to the 3rd generation of metascintillators, a new paradigm of scintillation detector with potential to reach the goal of 10 ps coincidence timing resolution with enough stopping power to be applicable in medical scenarios.

The dominance of LYSO has been stretching for more than 20 years now, and even though active research has been ongoing in the material direction, with significant interest from both the high energy physics and the medical community, no better material has been found yet. In the same time, electronics and photodetectors keep improving, making the scintillator the bottleneck for the development of detectors below 50 ps timing resolution. Unless new physics and new concepts, such as the ones described in this book, manage to produce system-level deployable gamma detectors in the next few years, it is expected that the metascintillator paradigm will be the one to integrate all the modern developments in various fields. This will lead these communities to better detecting capabilities, into new research and better healthcare, improving the standing of all humanity in relation to the inwards and outwards mysteries of the universe.

Acknowledgements The author would like to thank Pr. Paul Lecoq (CERN, Geneva), Dr. Antonio Gonzalez (instituto de instrumentación para imagen molecular – I3M, Valencia) and Dr. Daniel Bonifacio (IPEN/CNEN, Sao Paolo) for proof-reading and recommendations.

References

1. Healthcare resource statistics – technical resources and medical technology. Availability of technical resources in hospitals. *Eurostat*. Retrieved 19.08.2020.
2. Bailey, D. L., Meikle, S. R., & Jones, T. (1997). Effective sensitivity in 3D PET: The impact of detector dead time on 3D system performance. *IEEE Transactions on Nuclear Science, 44*(3), 1180–1185.
3. Cherry, S. R., Jones, T., Karp, J. S., Qi, J., Moses, W. W., & Badawi, R. D. (2018). Total-body PET: Maximizing sensitivity to create new opportunities for clinical research and patient care. *Journal of Nuclear Medicine, 59*(1), 3–12.
4. Surti, S. (2015). Update on time-of-flight PET imaging. *Journal of Nuclear Medicine, 56*(1), 98–105.
5. Budinger, T. F. (1983). Time-of-flight positron emission tomography: Status relative to conventional PET. *Journal of Nuclear Medicine, 24*(1), 73–78.
6. van Sluis, J., et al. (2019). Performance characteristics of the digital biograph vision PET/CT system. *Journal of Nuclear Medicine, 60*(7), 1031–1036.
7. Del Guerra, A., Belcari, N., & Bisogni, M. (2016). Positron emission tomography: Its 65 years. *Rivista del Nuovo Cimento, 39*(4), 155–223.
8. Lecoq, P., Morel, C., Prior, J. O., Visvikis, D., Gundacker, S., Auffray, E., et al. (2020). Roadmap toward the 10 ps time-of-flight PET challenge. *Physics in Medicine & Biology, 65*(21), 21RM01.
9. Shiri, I., Abdollahi, H., Atashzar, M. R., Rahmim, A., & Zaidi, H. (2020). A theranostic approach based on radiolabeled antiviral drugs, antibodies and CRISPR-associated proteins for early detection and treatment of SARS-CoV-2 disease. *Nuclear Medicine Communications*, 837–840.
10. Betancourt, C., Dätwyler, A., Owen, P., Puig, A., & Serra, N. (2020). SiPM single photon time resolution measured via bi-luminescence. *Nuclear Instruments and Methods in Physics Research Section A: Accelerators, Spectrometers, Detectors and Associated Equipment, 958*, 162851.
11. Nolet, F., Roy, N., Carrier, S., Bouchard, J., Fontaine, R., Charlebois, S. A., & Pratte, J. F. (2020). 22 μW, 5.1 ps LSB, 5.5 ps RMS jitter Vernier time-to-digital converter in CMOS 65 nm for single photon avalanche diode array. *Electronics Letters, 56*(9), 424–426.
12. Lecoq, P., Gektin, A., & Korzhik, M. (2017). Scintillation and inorganic scintillators. In *Inorganic scintillators for detector systems. Particle acceleration and detection*. Springer.
13. Choong, W. S. (2009). The timing resolution of scintillation-detector systems: Monte Carlo analysis. *Physics in Medicine & Biology, 54*(21), 6495–6513.

14. Pepin, C. M., Bérard, P., Perrot, A. L., Pépin, C., Houde, D., Lecomte, R., et al. (2004). Properties of LYSO and recent LSO scintillators for phoswich PET detectors. *IEEE Transactions on Nuclear Science, 51*(3), 789–795.
15. Zhu, R. Y. (2019, January). Ultrafast and radiation hard inorganic scintillators for future HEP experiments. *Journal of Physics: Conference Series, 1162*(1), 012022. IOP Publishing.
16. Wen, X., & Hayward, J. P. (2020). Time resolution measurements of EJ-232Q with single and dual-sided readouts. *IEEE Transactions on Nuclear Science, 67*, 2081–2088.
17. Moskal, P., Rundel, O., Alfs, D., Bednarski, T., Białas, P., Czerwiński, E., et al. (2016). Time resolution of the plastic scintillator strips with matrix photomultiplier readout for J-PET tomograph. *Physics in Medicine & Biology, 61*(5), 2025–2047.
18. Mykhaylyk, V. B., Kraus, H., & Saliba, M. (2019). Bright and fast scintillation of organolead perovskite MAPbBr 3 at low temperatures. *Materials Horizons, 6*(8), 1740–1747.
19. Cates, J. W., & Levin, C. S. (2016). Advances in coincidence time resolution for PET. *Physics in Medicine & Biology, 61*(6), 2255–2264.
20. Seifert, S., van Dam, H. T., & Schaart, D. R. (2012). The lower bound on the timing resolution of scintillation detectors. *Physics in Medicine & Biology, 57*(7), 1797–1814.
21. https://www.oxfordlearnersdictionaries.com/definition/english/meta_2. Retrieved 29.08.2022.
22. Kshetrimayum, R. S. (2004). A brief intro to metamaterials. *IEEE Potentials, 23*(5), 44–46.
23. https://www.lexico.com/definition/metamaterial. Retrieved 19.08.2020.
24. Konstantinou, G., Lecoq, P., Benlloch, J. M., & Gonzalez, A. J. (2022, January). Metascintillators for ultrafast gamma detectors: A review of current state and future perspectives. *IEEE Transactions on Radiation and Plasma Medical Sciences, 6*(1), 5–15. https://doi.org/10.1109/TRPMS.2021.3069624
25. Lecoq, P. (2017). Pushing the limits in time-of-flight PET imaging. *IEEE Transactions on Radiation and Plasma Medical Sciences, 1*, 473–485.
26. Badier, J., Busson, P., Charlot, C., Dobrzynski, L., Tanaka, R., Bordalo, P., et al. (1994). Shashlik calorimeter beam-test results. *Nuclear Instruments and Methods in Physics Research Section A: Accelerators, Spectrometers, Detectors and Associated Equipment, 348*(1), 74–86.
27. Turtos, R. M., Gundacker, S., Auffray, E., & Lecoq, P. (2019). Towards a metamaterial approach for fast timing in PET: Experimental proof-of-concept. *Physics in Medicine & Biology, 64*(18), 185018.
28. Gundacker, S., Turtos, R. M., Kratochwil, N., Pots, R. H., Paganoni, M., Lecoq, P., & Auffray, E. (2020). Experimental time resolution limits of modern SiPMs and TOF-PET detectors exploring different scintillators and Cherenkov emission. *Physics in Medicine & Biology, 65*(2), 025001.
29. Pagano, F., Kratochwil, N., Salomoni, M., Pizzichemi, M., Paganoni, M., & Auffray, E. (2022). Advances in heterostructured scintillators: Toward a new generation of detectors for TOF-PET. *Physics in Medicine & Biology, 67*, 135010.
30. Lecoq, P., Konstantinou, G., Latella, R., Moliner, L., Nuyts, J., Zhang, L., et al. (2022). Metascintillators: New results for TOF-PET applications. *IEEE Transactions on Radiation and Plasma Medical Sciences, 6*(5), 510–516.
31. Konstantinou, G., Latella, R., Moliner, L., Zhang, L., Benlloch, J. M., Gonzalez, A. J., & Lecoq, P. (2021). Metascintillator pulse feature and shape analysis to detect photoelectric interactions and energy sharing. In *2021 IEEE nuclear science symposium and medical imaging conference (NSS/MIC)* (pp. 1–4). IEEE.
32. Turtos, R. M., Gundacker, S., Omelkov, S., et al. (2019). On the use of CdSe scintillating nanoplatelets as time taggers for high-energy gamma detection. *npj 2D Materials and Applications, 3*, 37. https://doi.org/10.1038/s41699-019-0120-8
33. Lecoq, P. (2008). Metamaterials for novel X- or g-ray detector designs. In *2008 IEEE nuclear science symposium conference record, N07-1* (pp. 680–684).
34. Kronberger, M., Auffray, E., & Lecoq, P. R. (2010). Improving light extraction from heavy inorganic scintillators by photonic crystals. *IEEE Transactions on Nuclear Science, 57*(5), 2475–2482. Salomoni, M., Pots, R., Auffray, E., & Lecoq, P. (2018). Enhancing light extraction of inorganic scintillators using photonic crystals. *Crystals, 8*(2), 78.

35. Salomoni, M., Pots, R., Lecoq, P., Auffray, E., Gundacker, S., Paganoni, M., et al. (2018). Photonic crystal slabs applied to inorganic scintillators. *IEEE Transactions on Nuclear Science, 65*(8), 2191–2195.
36. Konstantinou, G., Latella, R., Moliner, L., Zhang, L., Benlloch, J. M., Gonzalez, A. J., & Lecoq, P. (2023). A proof-of-concept of cross-luminescent metascintillators. *Physics in Medicine & Biology, 68*(2), 025018.
37. Binder, T., Kang, H. G., Nitta, M., Schneider, F., Yamaya, T., Parodi, K., et al. (2021). Performance evaluation of a staggered three-layer DOI PET detector using a 1 mm LYSO pitch with PETsys TOFPET2 ASIC: Comparison of HAMAMATSU and KETEK SiPMs. *Physics in Medicine & Biology, 66*(12), 125016.
38. Gómez, S., Alozy, J., Campbell, M., Fernandez-Tenllado, J. M., Manera, R., Mauricio, J., et al. (2022). FastIC: A fast integrated circuit for the readout of high performance detectors. *Journal of Instrumentation, 17*(05), C05027.
39. Loignon-Houle, F., Charlebois, S. A., Fontaine, R., & Lecomte, R. (2022). Monte Carlo simulations of energy, time and spatial evolution of primary electrons generated by 511 keV photons in various scintillators. *Nuclear Instruments and Methods in Physics Research Section A: Accelerators, Spectrometers, Detectors and Associated Equipment, 1030*, 166449.
40. Konstantinou, G., Barrio, J., Moliner, L., Cañizares, G., Cucarella, N., Benlloch, J. M., Lecoq, P., & Gonzalez, A. J. (2021). A novel metascintillator approach for ultra-fast timing in positron emission tomography. In *2020 IEEE nuclear science symposium and medical imaging conference (NSS/MIC)* (pp. 1–4). IEEE.
41. Jan, S., et al. (2004). GATE: A simulation toolkit for PET and SPECT. *Physics in Medicine and Biology, 49*, 4543–4561.
42. Bonifacio, D. A. B., Benlloch, J. M., Konstantinou, G., Latella, R., Murata, H. M., Gonzalez, A. J., & Lecoq, P. (2022). GATE simulation of a brain-dedicated PET system using metascintillators for optimized ToF capability. In *2022 IEEE nuclear science symposium and medical imaging conference (NSS/MIC)* (pp. 1–4). IEEE.
43. Barrio, J., Cucarella, N., Freire, M., Lamprou, E., Aguilar, S., Valladares, C., et al. (2020, October). PET detector based on a semi-monolithic crystal with DOI and TOF capabilities. In *2020 IEEE nuclear science symposium and medical imaging conference (NSS/MIC)* (pp. 1–3). IEEE.
44. Zhang, L., Konstantinou, G., Latella, R., Gonzalez, A. J., & Lecoq, P. (2022). Simulation and analysis of semi-monolithic meta-scintillators, combining accurate DOI and TOF. In *2022 IEEE nuclear science symposium and medical imaging conference (NSS/MIC)* (pp. 1–4). IEEE.
45. Caravaca, J., Descamps, F. B., Land, B. J., Yeh, M., & Gann, G. O. (2017). Cherenkov and scintillation light separation in organic liquid scintillators. *The European Physical Journal C, 77*(12), 1–7.
46. Brunner, S. E., & Schaart, D. R. (2017). BGO as a hybrid scintillator/Cherenkov radiator for cost-effective time-of-flight PET. *Physics in Medicine & Biology, 62*(11), 4421–4439.
47. Efthimiou, N., Kratochwil, N., Gundacker, S., Polesel, A., Salomoni, M., Auffray, E., & Pizzichemi, M. (2020). TOF-PET image reconstruction with multiple timing kernels applied on Cherenkov radiation in BGO. *IEEE Transactions on Radiation and Plasma Medical Sciences, 5*, 703–711.
48. Latella, R., Gonzalez, A. J., Benlloch, J. M., Lecoq, P., & Konstantinou, G. (2022). Exploiting Cherenkov radiation with BGO-based metascintillators. *IEEE Transactions on Radiation and Plasma Medical Sciences* (submitted).
49. Burešová, H., et al. (2016). Preparation and luminescence properties of ZnO:Ga. *Optics Express, 24*, 15289. https://doi.org/10.1364/OE.24.015289
50. Tomanova, K., et al. (2019, January). On the structure, synthesis and characterization of ultrafast blue-emitting $CsPbBr_3$ nanoplatelets. *APL Materials*. https://doi.org/10.1063/1.5079300. American Institute of Physics.

51. Rodà, C., Zafallon, M., et al. (2021). Understanding thermal and a-thermal trapping processes in lead halide perovskites towards effective radiation detection schemes. *Advanced Functional Materials, 31*(43), 2104879. https://doi.org/10.1002/adfm.2104879
52. Děcká, K., et al. (2022). Timing performance of lead halide perovskite nanoscintillators embedded in a polystyrene matrix. *Journal of Materials Chemistry C, 10*(35), 12836–12843.
53. Hubacek, T., et al. (2019). Advancement toward ultra-thick and bright InGaN/GaN structures with a high number of QWs. *CrystEngComm, 21*, 356.
54. Lecoq, P., Gonzalez, A. J., Auffray, E., Konstantinou, G., Nuyts, J., Prior, J., Turtos, R., & Varela, R. J. (2022). Fast timing in medical imaging. *IEEE Transactions on Radiation and Plasma Medical Sciences* (submitted).
55. Konstantinou, G., Chil, R., Desco, M., & Vaquero, J. J. (2017). Subsurface laser engraving techniques for scintillator crystals: Methods, applications, and advantages. *IEEE Transactions on Radiation and Plasma Medical Sciences, 1*(5), 377–384.
56. Zhou, J., & Qi, J. (2011). Fast and efficient fully 3D PET image reconstruction using sparse system matrix factorization with GPU acceleration. *Physics in Medicine & Biology, 56*(20), 6739–6757.
57. Malczewski, K. (2013, September). PET image reconstruction using compressed sensing. In *2013 Signal processing: Algorithms, architectures, arrangements, and applications (SPA)* (pp. 176–181). IEEE.
58. Lecoq, P., Morel, C., & Prior, J. https://the10ps-challenge.org

Metal-Loaded Plastic Scintillators Toward Gamma Spectroscopy Applications

Yunyun Li and Yuntao Wu

1 Introduction

Scintillators, as the core element for nuclear radiation detector, have been widely used in applications such as medical imaging, homeland security, and industrial nondestructive inspection [1–4]. The scalability of scintillation materials to large volume is particularly demanded for radiation portal monitors in the field of homeland security [5–7]. Current used portal monitoring materials are dominated by plastic scintillators and NaI:Tl single crystal scintillators. Plastic scintillators are emerging as a highly promising class of materials due to their low cost (<1 $/cm^3), robustness, and ease of fabrication in large volumes [8–10]. In principle, efficient photoelectric effect is a prerequisite for gamma spectroscopy detection applications. And the photoelectric effect probability (P_{pe}) is estimated by rule of thumb proportional to a power of effective atomic number (Z_{eff}), roughly between ${Z_{eff}}^4$ and ${Z_{eff}}^5$. Thus, Z_{eff} has a decisive impact on the probability of photoelectron production. Thus, plastic scintillators toward high-energy gamma spectroscopy are limited by their low stopping power due to low effective atomic number (Z_{eff} ~ 4–5) [11]. Hence, for primary screening of weak radioactive sources, large-sized plastic scintillators were utilized as gross counting detector materials [12]. In practice, once the portal monitors alarm, further secondary screening with handheld radioisotope identification detectors based on scintillation crystals, such as NaI:Tl and $\mathrm{LaBr_3}$:Ce, is inevitably needed [13].

Detection materials capable of countering and identifying radiological sources in a single mode could enhance the screening efficiency [14]. Nonetheless, the widely deployment of single crystal scintillators are constrained by high use cost

---

Y. Li (✉) · Y. Wu
Shanghai Institute of Ceramics, Chinese Academy of Sciences, Shanghai, China
e-mail: liyunyun@mail.sic.ac.cn; ytwu@mail.sic.ac.cn

© The Author(s), under exclusive license to Springer Nature Switzerland AG 2023

J. Du, K. (K.) Iniewski (eds.), *Gamma Ray Imaging*,
https://doi.org/10.1007/978-3-031-30666-2_11

and challenges in large-sized crystal production [15]. Thus, the need for affordable, stable and scalable plastic scintillators offering gamma spectroscopy has aroused extensive research interests. Continuous attempts aiming at developing plastic scintillators capable of gamma spectroscopy via the incorporation of organometallics to enhance the photoelectric effect by increasing Z_{eff} have been proven to be an effective approach [16]. There are several significant limitations that preclude toward gamma-ray spectroscopy. Since plastic scintillators are mainly composed of carbon and hydrogen, the limited solubility of large polarized organometallics in polymer matrix is the first major roadblock to be solved [17, 18]. In addition, the incorporation of organometallics is often detrimental to scintillation light yield due to heavy-atom quenching effect [19, 20]. Nonetheless, substantial progresses had been made to develop organometallic-loaded plastic scintillators possessing gamma spectroscopic capability. We will herein review recent studies on organometallic-loaded plastic scintillators, such as bismuth, lead, and tin-based compounds.

2 Bismuth-Loaded Plastic Scintillators

Bismuth (Bi) is the heaviest non-radioactive element with low toxicity. Introduction of bismuth to plastic scintillators dramatically improved sensitivity to gamma radiation, and can provide distinct photopeaks for practical gamma spectroscopy. Thus, the development of organobismuth-loaded plastics has received extensive attention [21–27].

As shown in Fig. 1a, Cherepy *et al.* developed $BiPh_3$-loaded plastics based on polyvinylcarbazole (PVK) polymer [24]. The maximum loading of $BiPh_3$ is 40 wt%, resulting in a high Z_{eff} of 26. It has a light yield of 12,000 photons/MeV and an energy resolution of 9.0% at 662 keV. When iridium compound (FIrpic) replaced the standard organic fluor diphenylanthracene (DPA) toward triplet-harvesting, the light yield and energy resolution can be improved to 30,000 photons/MeV and 6.8% at 662 keV, respectively. Nonetheless, several drawbacks still need to be addressed, such as the high cost of PVK and a slow response time of 1.2 μs. Subsequently, Cherepy *et al.* developed a promising alternative of bismuth compound, bismuth tripivalate ($Bi(OPiv)_3$), with high solubility in non-polar polyvinyl toluene (PVT)-based polymer matrix [26]. The existence of tripivalate group provides excellent solubility in the non-polar polymer matrix, offering the loading content as high as 29 wt% Bi element (70 wt% $Bi(OPiv)_3$) without degrading transparency. As shown in Fig. 1b, an energy resolution of 15% at 662 keV and a light yield of 5000 photons/MeV can be realized in a plastic sample containing 15 wt% $Bi(OPiv)_3$. The partially resolved photopeak includes a strong escape peak from ^{209}Bi Kα X-ray.

Recently, scale-up of above-mentioned Bi-loaded plastic with a higher Bi-loading content (20 wt% $Bi(OPiv)_3$) with a size of 16 in.^{3} has been achieved [27]. It exhibits a moderate energy resolution of 22% at 662 keV (Fig. 2a). These Bi-loaded plastics can be applied for use in the existing radiation portals, and detect radiation

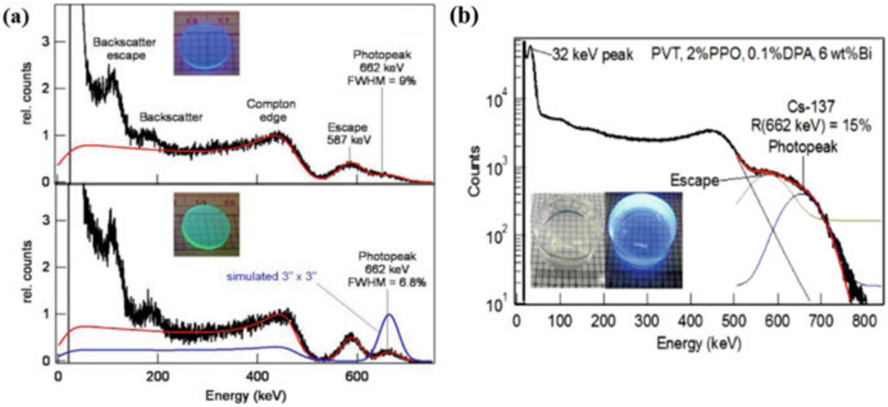

Fig. 1 (**a**) Pulse height spectrum obtained with $BiPh_3$-loaded plastic scintillator under ^{137}Cs source [24]. DPA was used as the standard blue-emitting organic fluors (top). FIrpic was used as the green-emitting fluors for triplet-harvesting (bottom). The inset photos show the sample used, illuminated by a UV lamp. (**b**) Pulse-height spectrum with ^{137}Cs, acquired with a 2 in.^{3} 15 wt% $Bi(OPiv)_3$-loaded plastic scintillator based on PVT matrix [26]

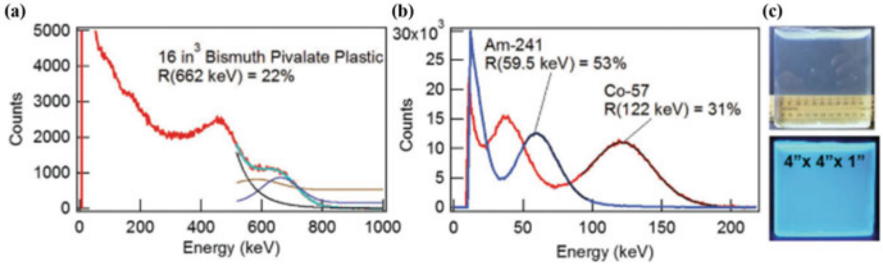

Fig. 2 (**a**) Pulse height spectrum obtained with 20 wt% $Bi(OPiv)_3$-loaded (8 wt% Bi) plastic scintillator under ^{137}Cs source [27]. (**b**) Pulse height spectrum obtained with 20 wt% $Bi(OPiv)_3$-loaded (8 wt% Bi) plastic scintillator under ^{241}Am and ^{57}Co sources [27]. (**c**) The photo of 16 in.^{3} 20 wt% $Bi(OPiv)_3$-loaded plastic scintillator, shown under daylight and UV excitation [27]

photons in the 30–200 keV range, as depicted in Fig. 2b. Well-resolved photopeaks can be observed in the gamma spectra of these plastic scintillators under ^{241}Am and ^{57}Co gamma sources irradiation.

3 Lead-Loaded Plastic Scintillators

Lead (Pb), as a non-radioactive heavy element except bismuth, is still of great scientific and practical interest. Organolead compounds, as the earliest organometallics to be studied in plastic scintillators for the detection of gamma rays, can be dated back to 1965 [28]. Lead loading markedly increased their low

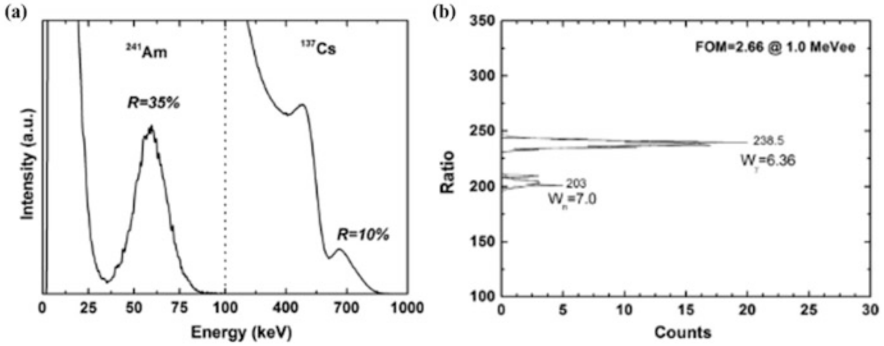

Fig. 3 (**a**) Pulse height spectra obtained with the lead-loaded plastic scintillator under ^{241}Am (60 keV) and ^{137}Cs (662 keV) sources [33]. (**b**) Pulse shape discrimination (PSD) Figure of Merit (FOM) of the lead-loaded plastic scintillator [33]

energy photon detection efficiencies, however, photopeaks toward gamma rays were absent for *p*-triphenyllead styrene, triphenyl-4-ethylphenyllead, or triphenyl-2,4-dimethylphenyllead loaded plastic scintillators. It can be attributed to the quenching effect of organolead. Hereafter, significant efforts has been made to develop organolead-loaded plastic scintillators [29–33]. For instance, the use of dicarboxylic lead (Pb(MMA)$_2$) was reported by Matthieu Hamel [32]. However, the incorporation of Pb leads to a serious luminescence quenching, causing a low light yield of 200 photons/MeV. Subsequently, a novel plastic scintillator loaded with organolead was reported by E. van Loef [33]. Under X-ray excitation, the spectrum of lead-loaded plastic scintillator consists of a broad emission band between 350 and 600 nm, peaking at 450 nm. Figure 3a shows the pulse height spectra of this novel plastic scintillator under ^{241}Am and ^{137}Cs gamma sources irradiation. It can achieve a light yield of 9000 photons/MeV and an energy resolution of 10% at 662 keV. In addition, n and γ-ray pulse shape discrimination capability with a Figure of Merit (FoM) of 2.66 was obtained (as shown in Fig. 3b).

4 Tin-Loaded Plastic Scintillators

Tin (Sn) is also a highly potential element to increase the Z_{eff} of plastic scintillators. Sandler and Tsou initially reported that *p*-triphenyl-4-ethylphenyltin and copolymerized *p*-phenyltinstyrene loaded plastic scintillators were able to resolve photopeaks in pulse height spectra [18, 28]. It also pointed out that the scintillation efficiency is approximately independent of whether the organometallic is loaded by physical mixing means or by copolymerization. Moreover, the scintillation efficiency can be improved by the use of a more efficient fluor [18, 28]. Thus, organotin compounds were identified as a suitable choice to increase gamma-ray sensitivity due to sufficient effective atomic number. In addition, there are

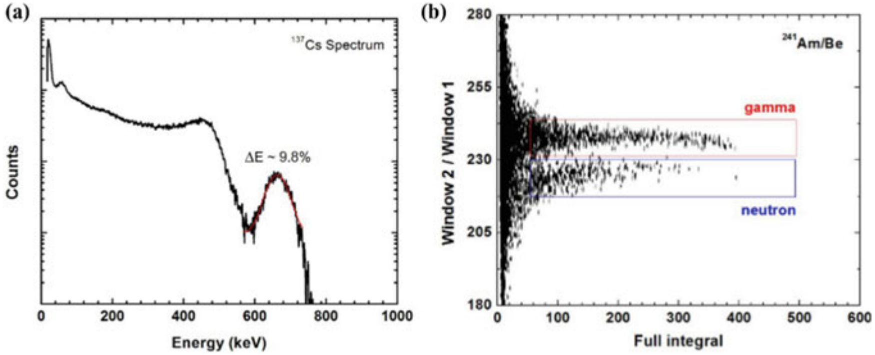

Fig. 4 (**a**) Pulse height spectrum obtained with a 1 in. diameter plastic scintillator sample made with magic tin under 662 keV gamma-ray excitation [36]. (**b**) PSD scatter plot of the 1 in. diameter plastic scintillator made with magic tin obtained with a ^{241}Am/Be source

many kinds of organotin compounds as promising candidates in terms of chemical compatibility, high solubility, and commercial availability [34].

In 2000, G. I. Britvich *et al.* fabricated 17 wt% tin tetraphenyl ($SnPh_4$)-loaded plastic scintillator with polystyrene (PS) as matrix [31]. However, the Sn loading is only 2.4 wt%, resulting in limited improvement of gamma sensitivity. Patrick L. Feng *et al.* prepared a series of polystyrene (PS)-based plastic scintillators loaded with organotin compounds, and studied the effect of distance-dependent quenching (DDQ) on gamma spectroscopy [35]. It proves that DDQ is related to radiative energy transfer from host matrix to fluorophore and non-radiative heavy atom quenching. The radiative energy transfer, also known as Foster Resonant Energy Transfer (FRET), is dominated when the separation distance is more than 5 Å but less than 20 Å. Based on that, various tin-containing compounds with steric distances within 10 Å were investigated. In the case of tributyltin methacrylate ($Bu_3Sn(MA)$), it possessed a favorable steric distance of 6.54 Å and a co-polymerized methacrylate ligand group. The maximum tin loading content can be 15 wt%. Its energy resolution at 662 keV can reach 10.9%. In 2016, Edgar V. van Loef *et al.* designed and synthesized a new organotin compound (magic tin) [36]. They successfully prepared a 1 in. diameter PS-based plastic scintillator containing 50 wt% so-called "magic tin", and achieved a light yield of 7000 photons/MeV and an energy resolution of 9.8% at 662 keV (Fig. 4a). This is the best ever energy resolution obtained (at 662 keV) with a plastic scintillator. It also exhibits good neutron-gamma PSD with a FoM of 1.3 at 2.5 MeV cut-off energy (Fig. 4b). Subsequently, the Radiation Monitoring Devices, Inc. achieved the commercialization of these "magic tin"-loaded plastic scintillators [37]. They typically have a superior energy resolution of 10% at 662 keV and a high light yield of 10,000 photons/MeV. They could be regarded as low-cost, practical neutron and gamma scintillators.

These impressive results motivate us to develop novel organotin-loaded plastic scintillators for gamma-ray spectroscopy applications. Very recently, we reported

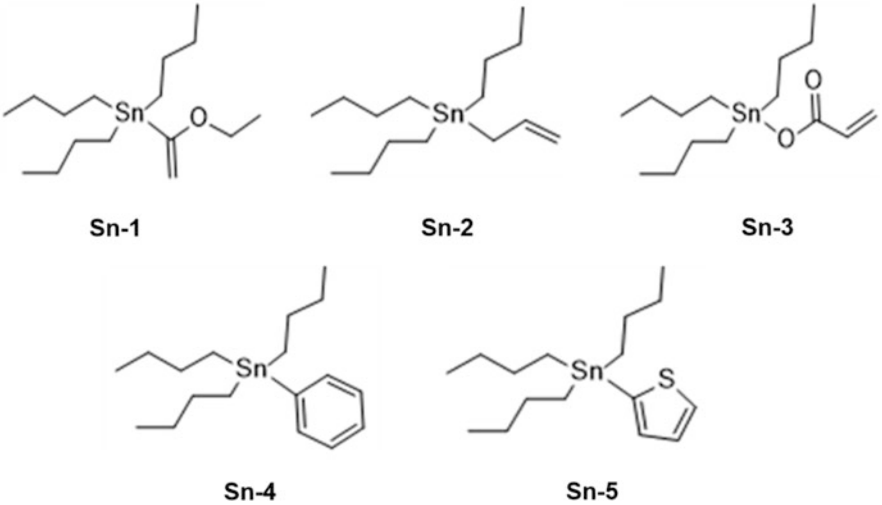

Fig. 5 Molecular structures of organotin compounds, including tributyl(1-ethoxyvinyl)tin (Sn-1), allyltributyltin (Sn-2), tributyltin acrylate (Sn-3), tributylphenyltin (Sn-4), and 2-(tributylstannyl)thiophene (Sn-5)

Table 1 Properties of 20 wt% organotin compounds loaded plastic scintillators

Materials	Sn-1	Sn-2	Sn-3	Sn-4	Sn-5
Organotin loading (wt%)	20	20	20	20	20
Sn (wt%)	6.59	7.17	6.57	6.47	6.36
Z_{eff}	18.8	19.3	18.8	18.7	18.7
Light yield (photons/MeV)[a]	7100	5100	5500	6700	7000
Energy resolution at 662 keV (%)	11.7	13.8	18.1	13.8	13.3

[a] Light yield compared with EJ-200 with the same size as reference

polyvinyl toluene (PVT)-based plastic scintillators highly loaded with five different kinds of organotin compounds (as shown in Fig. 5) [38]. In this work, a protocol of increasing solubility by using liquid organotin compounds as additives was reported, which makes it much easier to dissolve the dopant into matrix in any ratio. These newly developed Sn-loaded plastic scintillators demonstrate the capability of gamma spectroscopy detection with fast decay characteristics.

The physical and scintillation properties of plastic scintillators loaded with 20 wt% of five organotin compounds were summarized in Table 1. The maximum organotin loading ratio of 33 wt% (10.8 wt% Sn) was achieved in the tributyl(1-ethoxyvinyl) tin (Sn-1). The PVT plastic scintillator containing 20 wt% Sn-1 exhibits the optimal performance, providing gamma-ray spectroscopy with a light yield of 7100 photons/MeV and an energy resolution of 11.7% at 662 keV. The pulse height spectra under ^{137}Cs gamma-ray irradiation are shown in Fig. 6. Although the scintillation light yield decreases from 9800 for un-loaded to 5400 photons/MeV for 30 wt% Sn-1 loading ratio, the photopeak can be well-resolved in all Sn-1 loaded

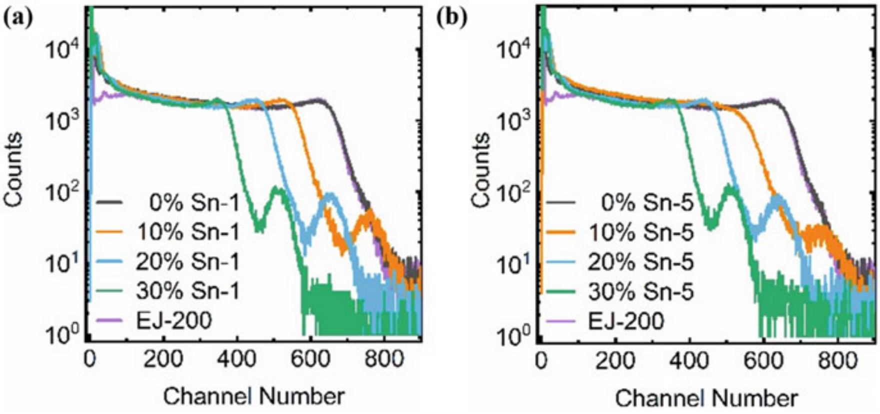

Fig. 6 Pulse height spectra of (**a**) Sn-1 loaded and (**b**) Sn-5 loaded plastic scintillators under ^{137}Cs irradiation

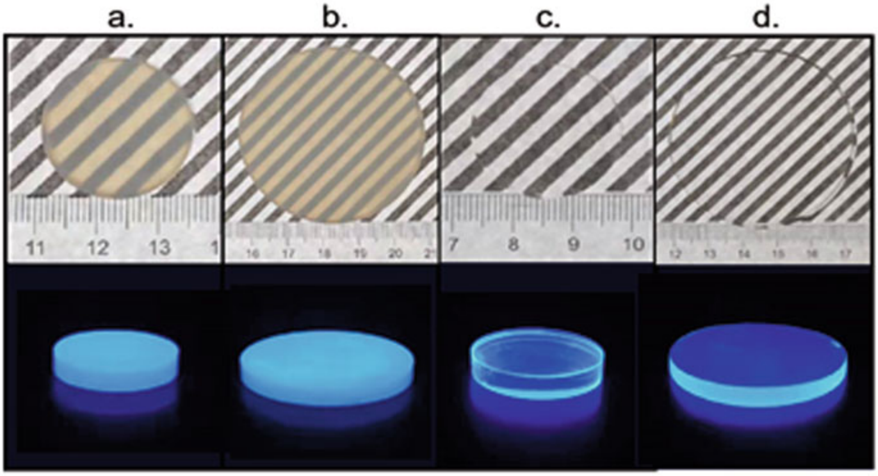

Fig. 7 Plastics loaded with 30 wt% Sn-1 under day light and 365 nm UV illumination: (**a**) Φ25 mm × 5 mm, (**b**) Φ51 mm × 5 mm. Plastics loaded with 30 wt% Sn-5 under day light and 365 nm UV illumination: (**c**) Φ25 mm × 5 mm, (**d**) Φ51 mm × 5 mm

samples (Fig. 6a). As shown in Fig. 6b, the photopeaks can also be well identified for all Sn-5 loaded plastics. Like Sn-1 loaded samples, the light yield decreases with the increase of Sn-5 loading concentration.

To investigate the practical application of these organotin compounds loaded plastics, 1 and 2 in. diameter plastic scintillators containing 30 wt% Sn-1 and Sn-5 were synthesized, respectively. Plastics under day light and 365 nm UV illumination are shown in Fig. 7. It is clear that the optical quality of plastics loaded with Sn-5 is better than that of Sn-1 loaded one.

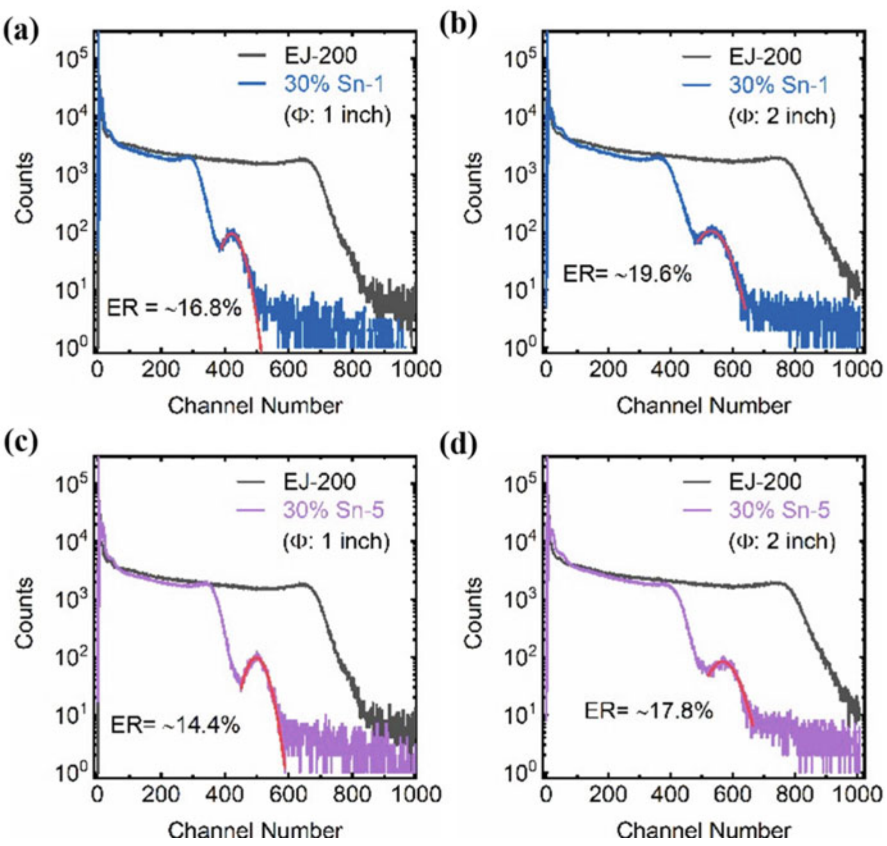

Fig. 8 The ^{137}Cs gamma spectrum of 30 wt% Sn-1 loaded samples with a size of: (**a**) Φ25 mm × 5 mm, and (**b**) Φ51 mm × 5 mm. The ^{137}Cs gamma spectrum of 30 wt% Sn-5 loaded samples with a size of: (**c**) Φ25 mm × 5 mm, (**d**) Φ51 mm × 5 mm

Figure 8 shows the pulse height spectra of 1 and 2 in. diameter plastic scintillators loaded with 30 wt% Sn-1 and Sn-5 under ^{137}Cs irradiation. All samples show a well-resolved photopeak. The light yield of 1 and 2 in. diameter plastics loaded with 30 wt% Sn-1 was estimated as 4700 and 4600 photons/MeV, respectively. The EJ-200 with a light yield of 10,000 photons/MeV was used as a reference. When the size of Sn-1 loaded plastic increased from 1 to 2 in. diameter, its energy resolution degraded from 16.8% to 19.6% at 662 keV. For 30 wt% Sn-5 loaded plastics, 1 in. diameter sample has a light yield of 5400 photons/MeV and an energy resolution of 14.4% at 662 keV. When being scaled up to 2 in. diameter, the light yield and energy resolution of the Sn-5 loaded plastic decreased to 5100 photons/MeV and 17.8% at 662 keV, respectively. Thus, compared with plastics loaded with Sn-1, Sn-5 loaded samples perform better in terms of gamma spectroscopy capability. It is associated with a higher transparency of the larger size sample.

5 Phosphorescent Sensitizers-Loaded Plastic Scintillators

In traditional plastic scintillators, ionizing radiation produces both singlet (25%) and triplet excitations (75%) [39]. The proportion of triplet excitations is largely increased in particular for the organometallics loaded plastics. Triplet state radiative decay is a forbidden transition, so triplet state tends to be long-lived and overall more susceptible to undergo non-radiative decay [40]. Heavy metal organic phosphorescent compounds can harvest both singlet and triplet excitons to enhance quantum efficiency [41–43]. Thus, the attempt on plastic scintillators loaded with phosphorescent sensitizers is currently an effective route to enhance both scintillation light yield and Z_{eff}.

In 2007, Campbell and Crone proposed plastic scintillators with iridium(III)tris[2-(4-totyl)pyridinato-NC^2] [Ir(mppy)$_3$] as phosphorescent sensitizers [44]. The scintillation light yield is improved to 32,000 photons/MeV. However, due to the limited solubility of Ir(mppy)$_3$, it can only be used in the form of thin film (thickness <5 μm), and thus cannot meet the practical application requirements of detectors. In addition to iridium complexes, plastic scintillator films with tris(dibenzoylmethane)mono(1,10-phenanthroline)europium(III) (Eu[DBM]$_3$phen) complex as phosphorescent dopants demonstrate a moderate scintillation yield of 5650 photons/MeV, but with a penalizing undesired long scintillation decay of 469 μs [45]. Quite a few efforts were devoted to finding low-cost metal compounds to replace iridium compounds toward cost-efficient and high-performance luminescence of organocopper complexes or fully organic systems [46–48]. In particular, blue-emitting cuprous compounds have attracted extensive attention, and some cuprous compounds have shown thermally activated delayed fluorescence (TADF) and effective singlet emitting in OLEDs [49–51]. Motivated by the excellent performance of Cu(I) complexes as luminescent emitters, we aim to study the effects of organic copper compounds with high photoluminescence quantum yield (PLQY) on the optical and scintillation properties of plastics for radiation detection applications. Though cuprous compounds can advantageously replace iridium ones in OLED systems, to the best of our knowledge, there is only a single publication which reports the use of a chlorine-loaded copper iodide phosphor in a composite scintillator [52].

Recently, we reported novel plastic scintillators loaded with deep-blue-emitting phosphorescent sensitizer CuI(PPh$_3$)$_2$(*t*-BuPy) (high PLQY up to 100%) [53], where PPh$_3$ and *t*-BuPy stand for triphenylphosphine and 4-*tert*-butylpyridine, respectively. Transparent plastic scintillators with varying concentrations of CuI(PPh$_3$)$_2$(*t*-BuPy) from 0.5 to 3 wt% have been synthesized, with high optical transmittance of over 80%. We explored the γ-ray response of CuI(PPh$_3$)$_2$(*t*-BuPy)-loaded plastic scintillators under ^{137}Cs source. The light yield significantly decreased from 9800 to 3800 photons/MeV with increasing CuI(PPh$_3$)$_2$(*t*-BuPy) concentration. We further studied the scintillation response of CuI(PPh$_3$)$_2$(*t*-BuPy)-loaded plastic scintillators under alpha-particle irradiation. The light yield decreased from 380 to 130 photons/MeV with increasing CuI(PPh$_3$)$_2$(*t*-BuPy)

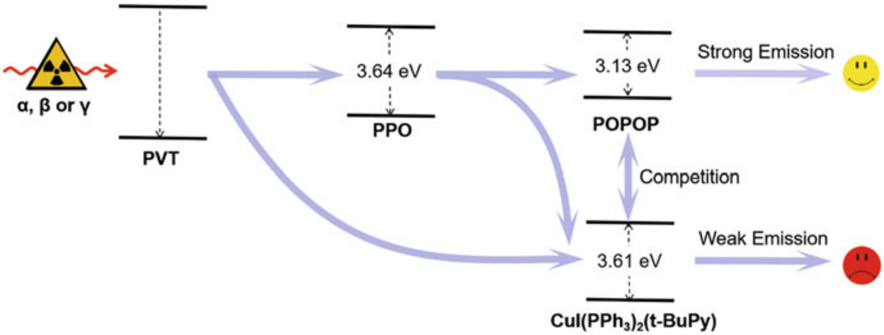

Fig. 9 Schematic illustration of energy transfer processes in CuI(PPh_3)$_2$(*t*-BuPy)-loaded PVT plastic scintillators

loading concentration. The scintillation yield deterioration under ^{137}Cs and ^{239}Pu irradiation is probably associated with inefficient energy transfer from PVT to CuI(PPh_3)$_2$(*t*-BuPy) and from PPO to CuI(PPh_3)$_2$(*t*-BuPy), and the low-efficiency emission of CuI(PPh_3)$_2$(*t*-BuPy).

Based on the photoluminescence and scintillation properties of CuI(PPh_3)$_2$(*t*-BuPy) loaded plastics, the possible energy transfer paths were proposed in this system (Fig. 9): (1) PVT → PPO → POPOP, (2) PVT → CuI(PPh_3)$_2$(*t*-BuPy), and (3) PVT → PPO → CuI(PPh_3)$_2$(*t*-BuPy). These three paths are co-existent. In this system, the emission of CuI(PPh_3)$_2$(*t*-BuPy) is very weak, and the energy transfer from CuI(PPh_3)$_2$(*t*-BuPy) to POPOP is not favorable considering their respective emission and absorptions. Thus, (2) and (3) energy transfer paths account for energy loss due to inefficient energy transfer. Furthermore, it is interesting that plastic scintillator containing CuI(PPh_3)$_2$(*t*-BuPy) also showed α/γ PSD performance due to its triplet harvesting capability.

6 Summary and Outlook

The incorporation of heavy metal elements to plastic scintillators has been accomplished through the form of organometallics. Toward gamma spectroscopy applications, this chapter briefly reviews several representative examples of heavy metal loaded plastic scintillators, such as Sn, Pb and Bi loading. Despite substantial progresses have been made in the development of organometallic loaded plastic scintillators, due to the quenching effect of organometallics additives, there is always a tradeoff between the desired gamma spectroscopy performance, such as light yield, energy resolution, and gamma detection sensitivity. A recent case that combination of organobismuth and iridium complex (triplet-harvesting fluors) loaded plastic scintillators provides a new horizon to achieve decent scintillation yield and high gamma sensitivity simultaneously. Therefore, bimetallic system compounds composed of two organometallics, namely one has a high Z_{eff} and the other has a triplet-harvesting capability, deserve to be explored further.

References

1. Moser, S. W., Harder, W. F., Hurlbut, C. R., & Kusner, M. R. (1993). Principles and practice of plastic scintillator design. *Radiation Physics and Chemistry, 41*, 31–36.
2. Nikl, M., & Yoshikawa, A. (2015). Recent R&D trends in inorganic single-crystal scintillator materials for radiation detection. *Advanced Optical Materials, 3*, 463–481.
3. Milbrath, B. D., Peurrung, A. J., Bliss, M., & Weber, W. J. (2008). Radiation detector materials: An overview. *Journal of Materials Research, 23*, 2561–2581.
4. Weber, M. J. (2002). Inorganic scintillators: Today and tomorrow. *Journal of Luminescence, 100*, 35–45.
5. Stromswold, D. C., et al. (2004). Field tests of a NaI(Tl)-based vehicle portal monitor at border crossings. In *IEEE symposium conference record nuclear science 2004* (pp. 196–200). IEEE.
6. Sciliano, E. R., Ely, J. H., Kouzes, R. T., Milbrath, B. D., Schweppe, J. E., & Stromswold, D. C. (2005). Comparison of PVT and NaI(Tl) scintillators for vehicle portal monitor applications. *Nuclear Instruments and Methods in Physics Research Section A, 550*, 647–674.
7. Simmax Techonology. *Radiation monitoring system for large passageway vehicle provided by Shanghai Simmax Techonology Co., Ltd.* http://www.simaxtechnology.com/product-item-384049.html
8. Watanabe, M., Katsumata, M., Ono, H., Suzuki, T., Miyata, H., Itoh, Y., Ishida, K., Tamura, M., & Yamaguchi, Y. (2015). First performance test of newly developed plastic scintillator for radiation detection. *Nuclear Instruments and Methods in Physics Research Section A, 770*, 197–202.
9. van Loef, E., Markosyan, G., Shirwadkar, U., McClish, M., & Shah, K. (2015). Gamma-ray spectroscopy and pulse shape discrimination with a plastic scintillator. *Nuclear Instruments and Methods in Physics Research Section A, 788*, 71–72.
10. Saito, E., Miyata, H., Katsumata, M., Karasawa, Y., Koike, T., Ono, H., Watanabe, M., Sato, M., Umeyama, A., Suzuki, T., & Tamura, M. (2020). Light yield, long-term stability, and attenuation length of a new plastic scintillator cured at room temperature. *Nuclear Instruments and Methods in Physics Research Section A, 953*, 162885.
11. Rahmanifard, R., Katebi, F., Zahedi, A. R., & Gholipour-Peyvandi, R. (2018). Synthesis and development of a vinyltoluene-based plastic scintillator. *Journal of Luminescence, 194*, 456–460.
12. Ely, J., Kouzes, R., Schweppe, J., Siciliano, E., Strachan, D., & Weier, D. (2006). The use of energy windowing to discriminate SNM from NORM in radiation portal monitors. *Nuclear Instruments and Methods in Physics Research Section A, 560*, 373–387.
13. Simmax Techonology. *A handheld radioisotope identification device based on a ~2 in.^{3}NaI:Tl scintillator crystal*. http://www.simaxtechnology.com/product-item-384055.html
14. Inspection Detection. *Portal monitors*. https://inspection-detection.com/product/portal-monitors/
15. Dynes, R. (2009). *Evaluating testing, costs, and benefits of advanced spectroscopic portals for screening cargo at ports of entry: Interim report (abbreviated version)*. National Academies Press. http://nap.edu/12699. https://doi.org/10.17226/12699
16. Hajagos, T. J., Liu, C., Cherepy, N. J., & Pei, Q. (2018). High-Z sensitized plastic scintillators: A review. *Advanced Materials, 30*, 1–13.
17. Hyman, M., & Ryan, J. J. (1958). Heavy elements in plastic scintillators. *IEEE Transactions on Nuclear Science, 5*, 87–90.

18. Sandler, S. R., & Tsou, K. C. (1964). Evaluation of organometallics in plastic scintillators toward gamma radiation. *International Journal of Applied Radiation and Isotopes, 15*, 419–426.
19. Hamel, M. (2021). *Plastic scintillators* (p. 140). Springer. https://doi.org/10.1007/978-3-030-73488-6
20. Bertrand, G. H. V., Dumazert, J., Sguerra, F., Coulon, R., Corre, G., & Hamel, M. (2015). Understanding the behaviour of different metals in loaded scintillators: Discrepancy between gadolinium and bismuth. *Journal of Materials Chemistry C, 3*, 6006–6011.
21. Cherepy, N. J., Payne, S. A., Sturm, B. W., O'Neal, S. P., Seeley, Z. M., Drury, O. B., Haselhorst, L. K., Rupert, B. L., Sanner, R. D., Thelin, P. A., Fisher, S. E., Hawrami, R., Shah, K. S., Burger, A., Ramey, J. O., & Boatner, L. A. (2011). Performance of europium-doped strontium iodide, transparent ceramics and bismuth-loaded polymer scintillators. *SPIE Optical Engineering + Applications, 8142*, 81420W.
22. Cherepy, N. J., et al. (2012). Bismuth-loaded plastic scintillators for gamma spectroscopy and neutron active interrogation. In *2012 IEEE nuclear science symposium and medical imaging conference record (NSS/MIC)* (pp. 1972–1973). IEEE.
23. Sato, A., Magi, A., Koshimizu, M., Fujimoto, Y., Kishimoto, S., & Asai, K. (2021). Photoluminescence and scintillation characteristics of Bi-loaded PVK-based plastic scintillators for the high counting-rate measurement of high-energy X-rays. *RSC Advances, 11*, 15581–15589.
24. Rupert, B. L., Cherepy, N. J., Sturm, B. W., Sanner, R. D., & Payne, S. A. (2012). Bismuth-loaded plastic scintillators for gamma-ray spectroscopy. *Europhysics Letters, 97*, 22002.
25. Bertrand, G. H. V., et al. (2014). Influence of bismuth loading in polystyrene-based plastic scintillators for low energy gamma spectroscopy. *Journal of Materials Chemistry C, 2*, 7304–7312.
26. Cherepy, N. J., Sanner, R. D., Beck, P. R., et al. (2015). Bismuth- and lithium-loaded plastic scintillators for gamma and neutron detection. *Nuclear Instruments and Methods in Physics Research Section A, 778*, 126–132.
27. O'Neal, S., Cherepy, N., Hok, S., & Payne, S. (2020). Performance of high stopping power bismuth-loaded plastic scintillators for radiation portal monitors. *IEEE Transactions on Nuclear Science, 67*(4), 746.
28. Dannin, J., Sandlert, S. R., & Baum, B. (1965). The use of organometallic plastic scintillators compounds in for the detection and resolution of gamma rays. *International Journal of Applied Radiation and Isotopes, 16*, 509–597.
29. Cho, Z. H., & Tsai, C. M. (1975). Tin and lead loaded plastic scintillators for low energy gamma-ray detection with particular application to high rate detection. *IEEE Transactions on Nuclear Science, 22*, 72–80.
30. Bressani, T., Macciotta, P., & Muntoni, C. (1983). Further improvements in Mossbauer spectroscopy with lead loaded plastic scintillators. *Nuclear Instruments and Methods in Physics Research, 211*, 231–233.
31. Britvich, G. I., Vasil'chenko, V. G., Lapshin, V. G., et al. (2000). New heavy plastic scintillators. *Instruments and Experimental Techniques, 43*, 36–39.
32. Hamel, M., Turk, G., Rousseau, A., et al. (2011). Preparation and characterization of highly lead-loaded red plastic scintillators under low energy x-rays. *Nuclear Instruments and Methods in Physics Research Section A, 660*, 57–63.
33. van Loef, E. V., Markosyan, G., Shirwadkar, U., et al. (2015). Gamma-ray spectroscopy and pulse shape discrimination with a plastic scintillator. *Nuclear Instruments and Methods in Physics Research Section A, 788*, 71–72.
34. Becker, J., Eriksson, L., Moberg, L. C., & Cho, Z. H. (1975). On the use of tin-loaded plastic scintillators in Mössbauer spectroscopy. *Nuclear Instruments and Methods in Physics Research, 123*, 199–201.
35. Feng, P. L., Mengesha, W., Anstey, M. R., et al. (2016). Distance dependent quenching and gamma-ray spectroscopy in tin-loaded polystyrene scintillators. *IEEE Transactions on Nuclear Science, 63*, 407–415.

36. van Loef, E. V., Feng, P., Markosyan, G., et al. (2016). High energy resolution plastic scintillator. *Proceedings of SPIE, 9968*, 996803.
37. Radiation Monitoring Devices, Inc. *Tin-loaded plastics*. https://www.rmdinc.com/research/scintillators/tin-loaded-plastic-scintillators/. Accessed 30 Sept 2022.
38. Li, W., Li, Y., & Wu, Y. (2022). Novel organotin-loaded plastic scintillators toward gamma spectroscopy applications. *IEEE Transactions on Nuclear Science, 69*, 2089–2094.
39. Adadurov, A. F., Zhmurin, P. N., Lebedev, V. N., et al. (2010). Plastic scintillator with phosphorescent dopants for α-particles registration. *Nuclear Instruments and Methods in Physics Research Section A, 621*, 354–357.
40. Griffiths, D. J., & Schroeter, D. F. (2005). *Introduction to quantum mechanics*. Cambridge University Press.
41. Baldo, M. A., Thompson, M. E., & Forrest, S. R. (2000). High-efficiency fluorescent organic light-emitting devices using a phosphorescent sensitizer. *Nature, 403*, 750–753.
42. Adachi, C., Baldo, M. A., Thompson, M. E., & Forrest, S. R. (2001). Nearly 100% internal phosphorescence efficiency in an organic light emitting device. *Journal of Applied Physics, 90*, 5048–5051.
43. Yersin, H., Rausch, A. F., Czerwieniec, R., Hofbeck, T., & Fischer, T. (2011). The triplet state of organo-transition metal compounds. Triplet harvesting and singlet harvesting for efficient OLEDs. *Coordination Chemistry Reviews, 255*, 2622–2652.
44. Campbell, I. H., & Crone, B. K. (2007). Efficient plastic scintillators utilizing phosphorescent dopants. *Applied Physics Letters, 90*, 012117.
45. Adadurov, A. F., Zhmurin, P. N., Lebedev, V. N., & Kovalenko, V. N. (2011). Plastic scintillators with β-diketone Eu complexes for high ionizing radiation detection. *Applied Radiation and Isotopes, 69*, 1475–1478.
46. Torres Ziegenbein, C., Fröbel, S., Glöß, M., Nobuyasu, R. S., Data, P., Monkman, A., & Gilch, P. (2017). Triplet harvesting with a simple aromatic carbonyl. *ChemPhysChem, 18*, 2314–2317.
47. Huitorel, B., El Moll, H., Utrera-Melero, R., Cordier, M., Fargues, A., Garcia, A., Massuyeau, F., Martineau-Corcos, C., Fayon, F., Rakhmatullin, A., Kahlal, S., Saillard, J.-Y., Gacoin, T., & Perruchas, S. (2018). Evaluation of ligands effect on the photophysical properties of copper iodide clusters. *Inorganic Chemistry, 57*, 4328–4339.
48. Elie, M., Sguerra, F., Di Meo, F., Weber, M. D., Marion, R., Grimault, A., Lohier, J., Stallivieri, A., Brosseau, A., Pansu, R. B., Renaud, J., Linares, M., Hamel, M., Costa, R. D., & Gaillard, S. (2016). Designing NHC–copper(I) dipyridylamine complexes for blue light-emitting electrochemical cells. *ACS Applied Materials & Interfaces, 8*, 14678–14691.
49. Czerwieniec, R., Yu, J., & Yersin, H. (2011). Blue-light emission of Cu(I) complexes and singlet harvesting. *Inorganic Chemistry, 50*, 8293–8301.
50. Egly, J., Bissessar, D., Achard, T., Heinrich, B., Steffanut, P., Mauro, M., & Bellemin-Laponnaz, S. (2021). Copper(I) complexes with remotely functionalized phosphine ligands: Synthesis, structural variety, photophysics and effect onto the optical properties. *Inorganica Chimica Acta, 514*, 119971.
51. Chen, X.-L., Yu, R., Zhang, Q.-K., Zhou, L.-J., Wu, X.-Y., Zhang, Q., & Lu, C.-Z. (2013). Rational design of strongly blue-emitting cuprous complexes with thermally activated delayed fluorescence and application in solution-processed OLEDs. *Chemistry of Materials, 25*, 3910–3920.
52. Hao, S., Liu, X., Gu, M., Li, Q., Huang, M., & Yang, H. (2021). Development of CuI:Cl-PS composite scintillator. *Journal of Luminescence, 240*, 118449.
53. Li, W., Li, Y., Nikl, M., Hamel, M., Wu, H., Qian, S., Kucerkova, R., Babin, V., Ren, G., & Wu, Y. (2022). Preparation and performance of plastic scintillators with copper iodide complex-loaded for radiation detection. *Polymer, 249*, 124832.

Index

A
Absorber detector, 67, 68, 72–83, 88, 167, 168, 175
Analog electronics, 1, 3, 4, 10, 18, 157
Angular resolution, 65, 66, 68–70, 80, 81, 88, 112–116, 123, 124, 126, 128–130
Astrophysics, 66, 73, 81, 103–131

B
Back-projection, 22, 55, 62
BuPy, 239, 240

C
Cadmium Selenide (CdSe), 185, 212, 216, 217
Cadmium zinc telluride (CZT), 2, 5, 70, 75, 80, 82, 89–96, 112, 121, 127, 149, 153–157, 159, 195, 196
Cascade gamma emission, 43–62, 173
CdS, 216, 217
Coded aperture, 88, 112, 129, 166
Coincidence detection, 49, 58, 139
Coincidence events, 11, 12, 21, 46–62, 144, 148, 149, 154, 157
Coincidence imaging, 44–47, 55, 57, 58, 61
Coincidence technique, 7, 154
Comprehensive Nuclear-Test-Ban Treaty (CTBT), 137, 142, 147, 148, 154
Comprehensive Nuclear-Test-Ban Treaty Organization (CTBTO), 137, 142, 147, 148
Compton camera, 65–82, 115, 129, 166–168
Compton scatter, 46, 50, 67, 71, 73, 80, 81, 83, 88, 89, 108, 109, 113, 114, 124, 165–178, 213
Correlation, 7–8, 18, 45, 49, 55, 61, 187
Crystal growth, 157, 159, 184, 186, 187, 192
CuI, 239, 240

D
Decommissioning, 165, 166
Deep learning, 26, 32–37, 68
Detector electronics, 47, 124, 153
Digital signal processing, 1–18
Directional gamma-ray detector, 165–178

E
Efficiency, 2, 12, 22, 27, 49, 51, 52, 55, 57–62, 65, 66, 68, 69, 73–83, 87, 95, 108, 117, 118, 120, 142, 143, 146–148, 150, 153–157, 159, 169, 173, 178, 189, 191, 192, 194, 212, 213, 216–218, 223, 226, 231, 234, 239
Energy resolution, 2, 3, 5, 6, 18, 45–47, 65, 68–70, 72, 74, 80, 88, 110, 114, 119, 124–130, 146, 149, 152–156, 159, 169–171, 183, 184, 190, 214, 218, 220, 225, 232, 234–236, 238, 240

F
Fukushima Daiichi Nuclear Power Station (FDNPS), 165, 166, 168

© The Editor(s) (if applicable) and The Author(s), under exclusive license to Springer Nature Switzerland AG 2023

J. Du, K. (K.) Iniewski (eds.), *Gamma Ray Imaging*,
https://doi.org/10.1007/978-3-031-30666-2

G
Gamma detection, 150, 152, 210, 213, 240
Gamma-ray imaging (GRI), 87, 97, 101, 113, 166
Gamma rays, 1–18, 65–67, 69–71, 73, 74, 77–78, 81, 87, 88, 103–131, 140, 165–178, 181, 188–197, 210, 220, 232, 234–236
Gamma-ray source, 67, 70, 78, 105, 107, 167
Gamma-ray spectroscopy, 1–18, 232, 236
Gamma spectroscopy, 144, 231–241
GEANT4, 73, 74, 81, 156, 171, 173, 175, 176, 221

H
High-Z, 88, 110, 116, 149, 153, 154, 156, 159, 194, 211, 213, 214, 216, 219, 221, 222, 232
Homeland security, 87–101, 182, 190, 231

I
Illicit nuclear materials, 88
Image reconstruction, 21–37, 46, 59–62, 67, 68, 80, 209, 225
International Monitoring System (IMS), 137–139, 142, 157
Iterative reconstruction, 32, 34–36, 55, 61, 62

L
Level schemes, 7, 8, 15
Lifetime measurements, 8–11, 14, 18

M
Machine learning, 30, 32, 36, 89, 94–96, 98, 225
Material engineering, 189
Maximum-likelihood expectation-maximization method (MLEM), 24, 28, 55–57, 61
Memory effect, 143, 146, 147, 152–155, 157, 159
Metal-loading, 231–241
Metascintillators, 209–227
Minimum detectable concentration (MDC), 142–143, 146–148, 152, 153, 155–159
Monte Carlo simulation, 26, 53, 58, 73, 171, 221
MURA mask, 88

N
Nanoplatelets, 215–217, 224
Nuclear explosion monitoring, 137–159
Nuclear isomers, 11, 14
Nuclear shapes and symmetries, 11, 14
Nuclear structure, 1–18
Nuclear tests, 141

P
Perovskites, 197–199, 212, 223
Photonic crystals, 217, 218, 224–225
Pinhole camera, 66, 165–168
Pixelated arrays, 87–89
Plastic scintillators, 108, 118, 125, 143, 146–149, 152, 154, 155, 193, 212, 214, 215, 231–241
Positron emission tomography (PET), 21–37, 43, 47, 49–52, 57–59, 61, 65, 66, 209–215, 221–223, 225, 226

R
Radiation detection, 1, 119, 144, 182, 184, 186, 188, 190, 192, 197, 199, 239
Radiation detectors, 1, 3, 18, 73, 101, 117–119, 182–190, 192, 194, 197, 199, 216, 231
Radiation monitoring devices, 235
Radioactive sources, 4, 18, 65, 75, 76, 78, 82, 87–101, 168, 231
Radiopharmaceutical therapy, 44
Radioxenon, 137–159
Read-out, 3, 118, 119, 122–124, 126–128, 210, 216, 218–221, 226

S
Scanners, 21, 22, 25–28, 58, 210, 221
Scatterer detector, 67–70, 72–76, 78–83, 167, 168, 170, 175
Scintillation media, 150
Scintillators, 2, 26, 49, 89, 108, 143, 170, 182, 209, 231
Semiconductor detectors, 1–6, 17, 18, 65–83, 89, 117, 119, 120, 124, 127, 130, 193, 194, 197
Semiconductors, 1–6, 17, 18, 65–83, 112, 116, 117, 119–121, 124, 127, 130, 154–157, 159, 181, 187, 188, 193–198, 216
Sensitivity, 2, 24, 25, 27, 60, 68, 73–81, 88, 105, 123, 130, 139, 142, 152, 155, 157, 159, 209, 210, 215, 221, 222, 226, 232, 235, 240

Sensor materials, 181, 184, 188–197
Silicon drift detector (SDD), 170, 172, 175–178
Single-photon emission computerized tomography (SPECT), 43, 47, 49, 52, 54, 57, 59, 61, 65, 66, 81
Small-angle Compton scattering, 165–178
Solid state detection, 150, 153, 159
Solid state detectors, 103–131
Space, 2, 27, 51, 53, 55, 60, 67, 87, 95, 101, 103–131, 165, 194
Spatial resolution, 22, 24, 25, 27, 57–62, 65, 68, 69, 81, 112, 114, 117–119, 122, 126, 127, 129–131, 168
Spectroscopy, 1–18, 90, 91, 110, 121, 124, 127, 131, 144, 148, 185–187, 193, 231–241

T
Time-of-flight (TOF), 24, 27, 28, 33, 34, 61, 66, 115, 209–210, 212, 215, 226
Time window, 50, 54, 95, 144
Tin (Sn), 234–238, 240